école normale supérieure paris—saclay

Habilitation à diriger les recherches

# Contributions aux méthodes de modélisation de la propagation des ondes acoustiques et élastiques dans des domaines de grande taille par méthodes d'éléments de frontière

Habilitation à diriger les recherches
de l'École normale supérieure Paris-Saclay
(École normale supérieure de Cachan)

Spécialité: Mécanique - Génie Mécanique - Génie civil

Thèse présentée et soutenue à Palaiseau, le 29 Mars 2019, par

**Stéphanie CHAILLAT**

Composition du jury:

| | |
|---|---|
| Olivier Allix<br>Prof. ENS Paris-Saclay — LMT | Examinateur, garant |
| Xavier Antoine<br>Prof. Université de Lorraine — IECL | Rapporteur |
| Oscar Bruno<br>Prof. Caltech— Applied and Computational Mathematics | Rapporteur |
| Ludovic Chamoin<br>Prof. ENS Paris-Saclay — LMT | Examinateur |
| Geert Degrande<br>Prof. KU Leuven — Civil Engineering | Rapporteur |
| Mahadevan Ganesh<br>Prof. Colorado School of Mines — Math. & Comp. Sciences | Examinateur |
| Laura Grigori<br>Directrice de recherche INRIA – Equipe ALPINES | Examinateur |
| Jean-François Molinari<br>Prof. EPFL — LSMS | Président |

université PARIS-SACLAY

**Titre:** Contributions aux méthodes de modélisation de la propagation des ondes acoustiques et élastiques dans des domaines de grande taille par des méthodes d'éléments de frontière

**Mots clés:** Acoustique, Elastodynamique, Propagation d'ondes, Solveurs Rapides, Méthodes des éléments de frontière

**Résumé:** Le principal avantage de la méthode des éléments de frontière (BEM) est de ne nécessiter la discrétisation que de la frontière du domaine (et éventuellement les interfaces) et donc de réduire drastiquement le nombre total de degrés de liberté. Dans sa mise en oeuvre traditionnelle, cet avantage par rapport aux méthodes volumiques est contre-balancé par le caractère plein de la matrice du système, les temps d'assemblage et de résolution augmentant rapidement avec la taille du problème. Au cours des dernières années, des BEMs rapides ont été proposées pour contourner les inconvénients provenant de la matrice pleine. La méthode multipôle rapide (FMM) est une méthode rapide, fiable et approchée pour calculer l'opérateur intégral lors d'une résolution itérative du système BEM. L'efficacité de la méthode a été démontrée pour les problèmes de propagation d'ondes dans des domaines 3D. Cependant, le nombre d'itérations est maintenant le principal facteur limitant de la méthode pour considérer des configurations réalistes. Il existe d'autres BEMs rapides basées par exemple sur la notion de matrices hiérarchiques. Combinée à des approximations de rang faible de certains blocs de la matrice, cette approche permet une représentation data-sparse de la matrice initiale. Contrairement à la FM-BEM, il s'agit d'une méthode purement algébrique qui ne nécessite pas la connaissance a priori de l'expression analytique des solutions fondamentales et qui permet ainsi de définir des solveurs itératifs ou directs. L'adaptation de maillage est une technique supplémentaire pour réduire le coût de calcul des BEMs. Le principe est d'optimiser (ou du moins d'améliorer) le positionnement d'un nombre donné de degrés de liberté, afin d'obtenir des simulations plus précises que celles obtenues via l'utilisation d'un maillage uniforme. Dans ce document, je donne un aperçu de travaux récents menés pour accélérer la solution des BEMs en acoustique et élastodynamique 3D.

**Title:** Contributions to the modelling of acoustic and elastic wave propagation in large-scale domains with boundary element methods (BEMs)

**Keywords:** Acoustics, Elastodynamics, Wave propagation, Fast Solvers, Boundary Element Method

**Abstract:** The main advantage of the BEM is that only the domain boundaries (and possibly interfaces) are discretized leading to a drastic reduction of the total number of degrees of freedom. In traditional BE implementation the dimensional advantage with respect to domain discretization methods is offset by the fully-populated nature of the BEM matrix, with set-up and solution times rapidly increasing with the problem size. In the last couple of years, fast BEMs have been proposed to overcome the drawback of the fully populated matrix. The Fast Multipole Method (FMM) is a fast, reliable and approximate method to compute the linear integral operator and is defined together with an iterative solver. The efficiency of the method has been demonstrated for 3D wave problems. However, the iteration count becomes the main limitation to consider realistic problems. Other accelerated BEMs are based on hierarchical matrices. When used in conjunction with an efficient rank revealing algorithm, it leads to a data-sparse and memory efficient approximation of the original matrix. Contrary to the FM-BEM it is a purely algebraic tool which does not require a priori knowledge of the closed-form expression of the fundamental solutions and it is possible to define iterative or direct solvers. Mesh adaptation is an additional technique to reduce the computational cost of the BEM. The principle is to optimize (or at least improve) the positioning of a given number of degrees of freedom on the geometry of the obstacle, in order to yield simulations with superior accuracy compared to those obtained via the use of uniform meshes. If an extensive literature is available for volume methods, much less attention has been devoted to BEMs. In this document, I give an overview of recent works to speed-up the solution of 3D acoustic and elastodynamic BEMs.

École normale supérieure Paris-Saclay
61, avenue du Président Wilson
94235 Cachan, France

# Contents

# Introduction

Understanding the propagation of acoustic and elastic waves is of paramount importance in many fields such as the automotive industry, aeronautics, medical imaging or seismology. The aims of the numerical simulation are, on the one hand, to be as close as possible to the reality of the physical phenomenon despite its complexity and on the other hand to be fast. The advantage of the numerical simulation of wave propagation is the prediction of large-scale complex phenomena. However, this is an advantage only if the computational cost is moderate. In this case, it will be possible to test different scenarios and the use of the numerical simulation will be justified. If experimental methods naturally take into account all the complexity of the physics, numerical methods require theoretical and numerical developments to achieve the same degree of fidelity. It is therefore necessary to develop numerical methods capable of taking into account complex configurations, both in terms of geometry and model. My main research axis is the development of numerical methods to simulate the propagation of acoustic and elastic waves which are **fast** and more and more **realistic** to be complementary to experimental methods. One important application of these methods is the modelling of the amplification of the seismic motion while traveling the different layers of the soil in order to understand *site effects* [Semblat 2009] (see Fig. 1) and *soil-structure interactions*. To achieve these goals, I am collaborating with computer scientists, geophysicists, geologists, experts of engineering seismology, engineers and mathematicians. All my research is capitalised in a in-house fast solver (COFFEE) devoted to the simulation of the propagation of acoustic and elastic waves.

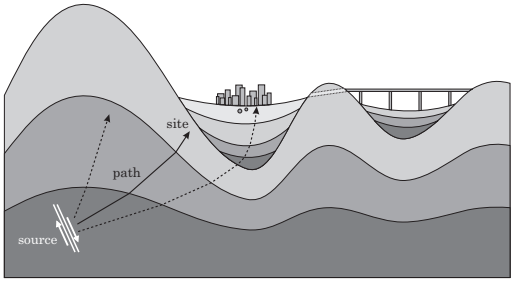


***Figure 1:*** *The seismic waves can be amplified by the geological and topographical structure of the soil (site effects) and this amplified motion interacts with the structures in the city (soil-structure interactions) (figure from [Semblat 2009]).*

The propagation of acoustic and elastic waves can be simulated by means of various numerical methods: finite element method (FEM), finite difference method, spectral element method, Discontinuous Galerkin method, Boundary Element Method (BEM), ... The latter, which corresponds to the numerical solution of boundary integral equations, has the advantages of necessitating only the discretization of the boundary of the computational domain and intrinsically taking into account radiation conditions in the formulation. The main drawbacks of the BEM are: (i) that it requires

the knowledge or numerical evaluation of the fundamental solution and (ii) that it leads to a smaller size problem (compared to volume methods) but with a fully-populated linear system. My work has mainly concerned the acceleration of the BEM for frequency-domain wave propagation problems. Indeed, the BEM system can be solved with either direct or iterative solvers. On the one hand, direct solvers such as the LU factorization have a complexity of the order of $\mathcal{O}(N^3)$ in terms of computational times and $\mathcal{O}(N^2)$ in terms of memory requirements ($N$ being the number of degrees of freedom on the domain boundary). They have therefore a prohibitive cost as soon as $N$ becomes large. On the other hand, iterative solvers construct sequences of solution candidates converging towards the solution. The complexity is then reduced to the order of $\mathcal{O}(N^2)$ in terms of memory and $\mathcal{O}(n_{\text{iter}} \times N^2)$ in terms of time, with $n_{\text{iter}}$ the number of iterations to achieve convergence. Memory requirements are still prohibitive to apply BEMs to very large-scale problems. The solution of realistic configurations in terms of geometry, heterogeneity, frequency range, ... is therefore limited by the number of degrees of freedom that the solver can handle on a given computer. For all these reasons, fast BEMs have undergone intense development in the last 30 years. The principle of fast BEMs such as the fast multipole accelerated BEM (FM-BEM) or the $\mathcal{H}$-matrix based BEM ($\mathcal{H}$-BEM) is to speed up the integral operator evaluations entailed by matrix-vector products. My work concerns the improvement of fast BEMs both in terms of computational efficiency, ability to deal with realistic configurations, and certification through error estimation.

In this manuscript, I synthesise my research as a full time researcher at CNRS since December 2010. During this period, I have co-advised 4 PhD students and 3 Postdocs.

Dec. 2017- : **Damien Mavaleix-Marchessoux**, PhD co-supervised at 40% with M. Bonnet (POEMS) and B. Leblé (Naval Group), on *Modelling the fluid-structure interaction during an underwater explosion* (CIFRE grant with Naval Group).

Dec. 2014- May 2018 : **Zouhaïr Adnani**, PhD co-supervised at 40% with M. Bonnet (POEMS) and V. Alves Fernandez (EDF), on *Fast Multipole Boundary Element Method for site effects and soil-structure interactions* [Adnani 2018] (CIFRE grant with EDF). Publication [21] is related to this work.

Oct. 2013-Jan. 2017 : **Luca Desiderio**, PhD co-supervised at 75% with P. Ciarlet (POEMS), on *$\mathcal{H}$-matrix based Solvers for 3D Elastodynamic Boundary Integral Equations* [Desiderio 2017] (funded by Shell). Publication [2] is related to this work.

2013-2016 : **Marc Bakry**, PhD co-supervised at 10% with P. Ciarlet (POEMS) and S. Pernet (ONERA), on *the development of error estimates for the Boundary Integral Equations* [Bakry 2016] (funded by ANR).

Oct. 2017 - : **Félix Kpadonou**, Postdoc supervised at 75% with P. Ciarlet (POEMS), on *the development of efficient preconditioners for the iterative solution of the BEM*. Publication [19] is related to this work.

Oct. 2016-Dec. 2018 : **Faisal Amlani**, Postdoc supervised at 50% with A. Loseille (INRIA GAMMA3), on *High Order Anisotropic mesh adaptation for Boundary Element Methods*. Publication [20] is related to this work.

2016 : **Samuel Groth**, Postdoc supervised at 50% with A. Loseille (INRIA GAMMA3), on *Anisotropic mesh adaptation for Boundary Element Methods*. Publication [1] is related to this work.

I have also participated informally to the following PhD works:

2017 : **Pierre Romanet**, PhD student of Harsha Bhat (ENS Ulm), on *Fast algorithms to model quasi-dynamic earthquake cycles in complex fault networks* [Romanet 2018]. Publication [18] is related to this collaboration.

2011 : **Eva Grasso**, PhD student of Marc Bonnet (POEMS) and Jean-François Semblat (IFSTTAR), on *Modelling visco-elastic seismic wave propagation: a fast-multipole boundary element method and its coupling with finite elements* [Grasso 2012]. Publication [9] is related to this collaboration.

All my different projects being connected, I have chosen to give in this manuscript a large overview of my research rather than providing detailed presentations of specific achievements. It is organised as follows.

**In Chapter 1,** I recall the basic principles of standard and fast BEMs for seismic wave propagation problems. The capabilities of fast BEMs (based on the Fast Multipole Method, FMM) are illustrated on two idealized configurations representative of phenomena we want to simulate: *site effects* and *soil-structure interations*. While fast BEMs are seen to be an interesting tool to understand the physics of these large scale phenomena, these test problems also show the limitations of the available tools: a large portion of the degrees of freedom (DOFs) are used to impose the traction free condition on the free surface, a large number of iterations are required in the iterative solver, there is no tool to certify the results. These observations have motivated the research axes presented in Chapters 2-5 and synthesized in Figure 2[1].

**In Chapter 2,** I present the improvement of the capabilities of the FMM to model seismic wave propagation in the soil by the development of (i) a new FM-BEM based on the elastic half-space fundamental solutions and (ii) a new FM-BEM for wave propagation stable at all frequencies.

**Chapter 3** is concerned with the proposition of analytic preconditioners for the 3D elastodynamic FM-BEM.

**In Chapter 4,** I show the capabilities of fast BEM solvers based on hierarchical matrices for wave propagation problems.

**Chapter 5** presents some tools to guarantee a given level of accuracy of the BEM results and a metric-based anisotropic mesh adaptation strategy for BEMs.

**Chapter 6** concludes this document with the new orientations I intend to give my research in the next few years in addition to the direct perspectives given in Chapters 2-5.

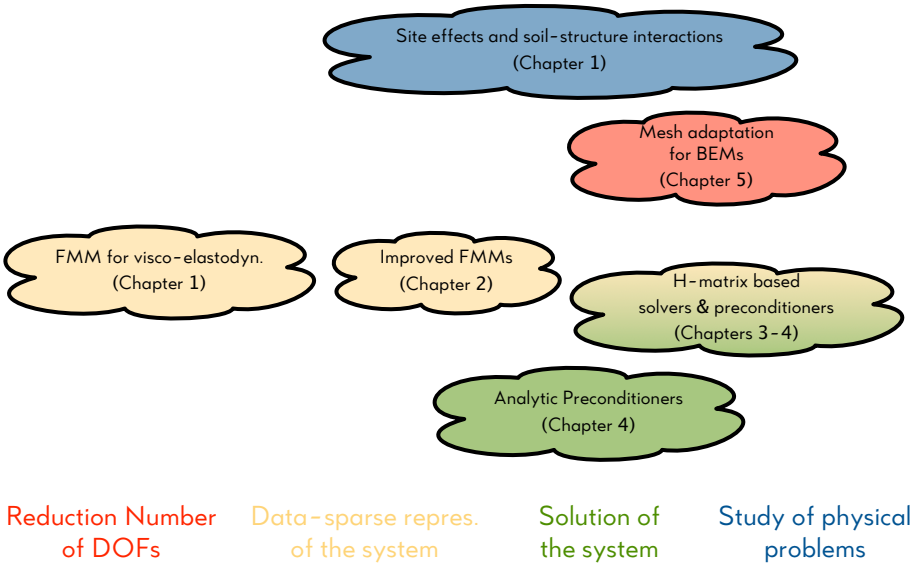


***Figure 2:*** *My research concerns mainly three levels of improvement of fast BEM solvers: the optimization of the number of DOFs (in red), the data-sparse representation of the system matrix (in yellow) and the acceleration of the system solution (in green).*

[1] A more complete description of Chapters 2-5 is given at the end of Chapter 1.

# CHAPTER 1

# Why improving fast Boundary Element Methods for wave propagation problems?

## Contents



As stated in the introduction, the aim of my research is to develop a BEM solver to simulate the propagation of acoustic and elastic waves in realistic configurations. For sure, the BEM cannot be applied to all realistic configurations but there are some cases where the domain can be approximated (at least as a first attempt) as a homogeneous or piecewise homogeneous domain. If in addition the domain is very large-scale, the BEM has many advantages. We can think for example to acoustic scattering problems. For seismic wave propagation, it is relevant to understand the effect of the soil layering even without taking into account the heterogeneities in each layer. We can also imagine that in the long-term future these simplified configurations can be used to speed-up the solution of problems in more heterogeneous domains.

In Section 1.1, I recall the classical principles of 3D time-harmonic elastodynamic BEMs. Note that the 3D acoustic BEM is only a simplification of this case. Due to the high computational costs associated with the standard BEM, the method has lost popularity in the eighties, in favour of volume methods. To consider realistic configurations, acceleration and memory reduction techniques have then been proposed leading to a new interest in BEMs.

There exists various fast BEMs with complementary advantages and drawbacks. Depending on the application considered, one method is more adapted than another. We can mention FFT acceleration or spectral based techniques, e.g. [Bruno 2001, Bruno 2018, Ganesh 2004, Xu 2001, Le Louër 2014]. These methods have the advantages to be very accurate and stable with respect to the frequency. They are especially efficient in the very high-frequency regime. However, they can suffer from some restrictions with respect to the geometric complexities that can be considered (e.g. spectral methods require a regular parameterization of the surface in spherical coordinates). Another class of method is based on the concept of hierarchical matrices. The principle is to perform low rank approximations of some blocks of the BEM matrix. We will see in Chapter 4 that while

they allow a drastic reduction of the memory requirements and computational time, they are not optimal for wave problems. The most appropriate method to simulate seismic wave propagation problems in the low to mid-frequency regime is the FMM. It is based on a reformulation of the fundamental solutions (with a plane wave expansion in our case) allowing for a factorization while evaluating the integral operators.

In Section 1.2, I recall the principal results on FM-BEMs for (visco)-elastodynamic problems obtained during my PhD and the PhD of Eva Grasso. Once the numerical efficiency of the FM-BEM to simulate (visco-)elastic wave propagation in sedimentary basins is illustrated for academic examples, the method is applied to more realistic (but still simplified) configurations.

In Section 1.3, I summarize the results obtained with Kristel Meza-Fajardo and Jean-François Semblat (previously at IFSTTAR now respectively at BRGM and UME, ENSTA Paristech) to study site effects (Fig. 1), i.e. the amplification of the seismic motion while traveling in the different layers of the soil. In Section 1.4, the FM-BEM is used to study the contribution of site effects to soil-structure interaction in an industrial context (with EDF's R&D, French electricity supplier). The main objective of this Chapter is twofold: (i) to present the potentialities of fast BEMs for some realistic configurations in engineering seismology and (ii) to show the main limitations observed when applying the FM-BEM to these applications.

This Chapter ends with a detailed outline of the document following from the limitations pointed out in Sections 1.3 and 1.4.

## 1.1 The Boundary Element Method for elastic waves and its Fast Multipole acceleration

We denote in this work $\Omega \subset \mathbb{R}^3$ the region of space occupied by a three-dimensional elastic solid with constitutive properties defined by the fourth-order elasticity tensor $\boldsymbol{\mathcal{C}}$ and the mass density $\rho$. The propagation of time-harmonic waves in a three-dimensional homogeneous elastic medium is modelled by the homogeneous Navier equation

$$\mathcal{L}(\boldsymbol{u}) := \operatorname{div} \sigma(\boldsymbol{u}) + \rho\omega^2 \boldsymbol{u} = 0 \tag{1.1}$$

where $\omega > 0$ is the angular frequency. In the case of an isotropic homogeneous domain, the fourth-order elasticity tensor $\boldsymbol{\mathcal{C}}$ is given by

$$\boldsymbol{\mathcal{C}} = 2\mu\Big[\frac{\nu}{1-2\nu}\boldsymbol{I}\otimes\boldsymbol{I} + \boldsymbol{\mathcal{I}}\Big], \tag{1.2}$$

where $\mu$ and $\nu$ are the shear modulus and the Poisson's ratio of the material, $\boldsymbol{I}$ being the second-order identity tensor and $\boldsymbol{\mathcal{I}}$ the symmetric fourth-order identity tensor. The stress and strain tensors are then given by $\sigma(\boldsymbol{u}) = \lambda(\operatorname{div}\boldsymbol{u})\mathbf{I} + 2\mu\varepsilon(\boldsymbol{u})$ and $\varepsilon(\boldsymbol{u}) = \frac{1}{2}\big([\boldsymbol{\nabla u}] + [\boldsymbol{\nabla u}]^{\mathsf{T}}\big)$ respectively, where $[\boldsymbol{\nabla u}]$ is the matrix whose $j$-th column is the gradient of the $j$-th component of $\boldsymbol{u}$. The field $\boldsymbol{u}$ can be decomposed into a longitudinal field $\boldsymbol{u}_p = \boldsymbol{\nabla}\psi_p$ and a transverse field $\boldsymbol{u}_s = \boldsymbol{u} - \boldsymbol{u}_p = \mathbf{curl}\,\boldsymbol{\psi}_s$. The scalar and vector Lamé potentials $\psi_p$ and $\boldsymbol{\psi}_s$ satisfy respectively

$$\begin{cases} \psi_p = -\kappa_p^{-2}\operatorname{div}\boldsymbol{u} \\ \Delta\psi_p + \kappa_p^2\psi_p = 0 \end{cases} \quad \text{and} \quad \begin{cases} \boldsymbol{\psi}_s = \kappa_s^{-2}\,\mathbf{curl}\,\boldsymbol{u} \\ \boldsymbol{\Delta\psi}_s + \kappa_s^2\boldsymbol{\psi}_s = 0 \end{cases} \tag{1.3}$$

where $\kappa_p^2 = \rho\omega^2(\lambda+2\mu)^{-1}$, $\kappa_s^2 = \rho\omega^2\mu^{-1}$ are the P and S wavenumbers and $\kappa_{\mathrm{P}} = \gamma\kappa_{\mathrm{S}}$, with $\gamma^2 = \frac{1-2\nu}{2(1-\nu)}$. The wavelengths are defined by $\lambda_\alpha = 2\pi/\kappa_\alpha$ $(\alpha = s, p)$.

We denote by $H^s_{loc}(\Omega)$ and $H^s(\Gamma)$ the standard (local in the case of the exterior domain) complex valued Hilbertian Sobolev spaces of order $s \in \mathbb{R}$ defined on $\Omega$ and $\Gamma$ respectively (with the convention $H^0 = L^2$). Spaces of vector functions will be denoted by boldface letters, thus $\boldsymbol{H}^s = (H^s)^3$. We set $\Delta^*\boldsymbol{u} := \operatorname{div}\sigma(\boldsymbol{u}) = (\lambda+2\mu)\boldsymbol{\nabla}\operatorname{div}\boldsymbol{u} - \mu\,\mathbf{curl}\,\mathbf{curl}\,\boldsymbol{u}$ and introduce the energy space $\boldsymbol{H}^1(\Delta^*) := \big\{\boldsymbol{u} \in \boldsymbol{H}^1_{loc}(\Omega) :\ \Delta^*\boldsymbol{u} \in \boldsymbol{L}^2_{loc}(\Omega)\big\}$. The Neumann trace, defined by $\boldsymbol{t}_{|\Gamma} := \mathbf{T}\boldsymbol{u}$, is given by the traction operator

$$\mathbf{T} = \mathbf{2}\mu\frac{\partial}{\partial\boldsymbol{n}} + \lambda\boldsymbol{n}\operatorname{div} + \mu\,\boldsymbol{n}\times\mathbf{curl}\,.$$

We recall that we have $\boldsymbol{u}_{|\Gamma} \in \boldsymbol{H}^{\frac{1}{2}}(\Gamma)$ and $\boldsymbol{t}_{|\Gamma} \in \boldsymbol{H}^{-\frac{1}{2}}(\Gamma)$ for any $\boldsymbol{u} \in \boldsymbol{H}^1(\Delta^*)$. We will also use surface differential operators [Nédélec 2001, pages 68-75]: the tangential gradient $\boldsymbol{\nabla}_\Gamma$, the surface divergence $\mathrm{div}_\Gamma$, the surface scalar curl $\mathbf{curl}_\Gamma$, the tangential vector curl $\mathbf{curl}_\Gamma$, the scalar Laplace-Beltrami operator $\Delta_\Gamma$ and the vector Laplace-Beltrami operator $\boldsymbol{\Delta}_\Gamma$.

In this work, we will look for a field $\boldsymbol{u}$ that satisfies the Kupradze radiation conditions at infinity

$$\lim_{r\to\infty} r\left(\frac{\partial \psi_p}{\partial r} - i\kappa_p \psi_p\right) = 0, \qquad \lim_{r\to\infty} r\left(\frac{\partial \boldsymbol{\psi}_s}{\partial r} - i\kappa_s \boldsymbol{\psi}_s\right) = 0, \quad r = |\boldsymbol{x}|, \tag{1.4}$$

uniformly in all directions. Such a field can be generated by an incident field traveling in a perturbated reference homogeneous medium or produced by a source with a compact support. We will see more practical examples in this Chapter.

**Boundary integral representation and boundary integral equation (BIE).** The BIE formulation for frequency-domain elastodynamics is summarized in its basic form, as it defines a convenient framework and notational setting for starting the discussion of fast BEMs for waves. Assume for definiteness that time-harmonic motions, with circular frequency $\omega$, are induced by a prescribed traction distribution $\boldsymbol{t}^{\mathrm{D}}$ on the boundary $\partial\Omega$ and in the absence of body forces (with straightforward modifications allowing the discussion of other boundary conditions or other integral formulations). The displacement $\boldsymbol{u}$ is given at an interior point $\boldsymbol{x} \in \Omega$ by the following well-known representation formula [Eringen 1975]:

$$\boldsymbol{u}(\boldsymbol{x}) = -\int_{\partial\Omega} \boldsymbol{u}(\boldsymbol{y})\cdot\boldsymbol{T}(\boldsymbol{x},\boldsymbol{y})\,\mathrm{d}S_y + \int_{\partial\Omega} \boldsymbol{t}^{\mathrm{D}}(\boldsymbol{y})\cdot\boldsymbol{U}(\boldsymbol{x},\boldsymbol{y})\,\mathrm{d}S_y \qquad (\boldsymbol{x}\in\Omega), \tag{1.5}$$

where $\boldsymbol{U}(\boldsymbol{x},\boldsymbol{y})$ and $\boldsymbol{T}(\boldsymbol{x},\boldsymbol{y})$ denote an elastodynamic Green's tensor, defined such that $\boldsymbol{U}\cdot\boldsymbol{F}$ and $\boldsymbol{T}\cdot\boldsymbol{F}$ are the displacement and traction vector, respectively, generated at any point $\boldsymbol{y}$ of a region $\mathcal{O} \subset \mathbb{R}^3$ by a unit point force $\boldsymbol{F}$ applied at $\boldsymbol{x} \in \mathcal{O}$. The region $\mathcal{O}$ must contain $\Omega$, and Green's tensors may then be defined according to the choice of $\mathcal{O} \supset \Omega$ and boundary conditions on $\partial\mathcal{O}$. The simplest, and most commonly used, Green's tensor corresponds to the isotropic full-space, i.e. $\mathcal{O} = \mathbb{R}^3$. In this case, one has:

$$\begin{aligned} \boldsymbol{U}(\boldsymbol{x},\boldsymbol{y}) &= \frac{1}{\kappa_{\mathrm{S}}^2\mu}\Big[\big(\boldsymbol{I}\Delta - \boldsymbol{\nabla}_y\boldsymbol{\nabla}_x\big)G(|\boldsymbol{y}-\boldsymbol{x}|;\kappa_{\mathrm{S}}) + \boldsymbol{\nabla}_x\boldsymbol{\nabla}_y G(|\boldsymbol{y}-\boldsymbol{x}|;\kappa_{\mathrm{P}})\Big], \\ \boldsymbol{T}(\boldsymbol{x},\boldsymbol{y}) &= \boldsymbol{n}(\boldsymbol{y})\cdot\boldsymbol{\mathcal{C}}:\boldsymbol{\nabla}_y\boldsymbol{U}(\boldsymbol{x},\boldsymbol{y}), \end{aligned} \tag{1.6}$$

where $\boldsymbol{n}(\boldsymbol{y})$ is the unit normal to $\partial\Omega$ directed outwards of $\Omega$ and $G(\cdot;\kappa)$ is the free-space fundamental solution for the Helmholtz equation with wavenumber $\kappa$, given by

$$G(r;\kappa) = \frac{\exp(\mathrm{i}\kappa r)}{4\pi r}, \quad \text{with } r = ||\boldsymbol{x}-\boldsymbol{y}||. \tag{1.7}$$

Well-known results on the limiting values of elastic potentials as the point $\boldsymbol{x}$ reaches the boundary [Kupradze 1963] allow to deduce from (1.5) the boundary integral equation

$$\boldsymbol{\mathcal{K}}[\boldsymbol{u}](\boldsymbol{x}) = \boldsymbol{\mathcal{S}}[\boldsymbol{t}^{\mathrm{D}}](\boldsymbol{x}) \quad (\boldsymbol{x}\in\partial\Omega) \qquad \text{with } \boldsymbol{\mathcal{K}}[\boldsymbol{u}](\boldsymbol{x}) := \boldsymbol{\mathcal{D}}[\boldsymbol{u}](\boldsymbol{x}) + \boldsymbol{c}(\boldsymbol{x})\cdot\boldsymbol{u}(\boldsymbol{x}), \tag{1.8}$$

where the right-hand side and the linear operator $\boldsymbol{\mathcal{K}}$ respectively involve the single-layer integral operator $\boldsymbol{\mathcal{S}}$ and the double-layer integral operator $\boldsymbol{\mathcal{D}}$, defined by

$$\boldsymbol{\mathcal{S}}[\boldsymbol{t}](\boldsymbol{x}) := \int_{\partial\Omega} \boldsymbol{t}(\boldsymbol{y})\cdot\boldsymbol{U}(\boldsymbol{x},\boldsymbol{y})\,\mathrm{d}S_y, \quad \boldsymbol{\mathcal{D}}[\boldsymbol{u}](\boldsymbol{x}) := (\mathrm{P.V.})\int_{\partial\Omega} \boldsymbol{u}(\boldsymbol{y})\cdot\boldsymbol{T}(\boldsymbol{x},\boldsymbol{y})\,\mathrm{d}S_y, \quad \boldsymbol{x}\in\partial\Omega. \tag{1.9}$$

Due to the strong singularity of $\boldsymbol{T}$ for $\boldsymbol{y}=\boldsymbol{x}$, the integral defining $\boldsymbol{\mathcal{D}}$ is understood in the Cauchy principal value (CPV) sense (as indicated by the notation P.V.) while a *free-term* $\boldsymbol{c}(\boldsymbol{x})$ arose from the limit-to-the-boundary process. The latter is equal to $0.5\boldsymbol{I}$ in the usual case where $\partial\Omega$ is smooth at $\boldsymbol{x}$, and is otherwise a known (second-order tensor-valued) function of the local geometry of $\partial\Omega$ at $\boldsymbol{x}$. Kernel singularities are extensively studied in the literature in terms of their consequences on the fundamental properties of integral operators [Hsiao 2008, Nédélec 2001] and the specialized numerical quadrature methods allowing to handle them in implementing the BEM [Guiggiani 1990, Tanaka 1994].

**Boundary Element Method.** The main ingredients of the numerical solution of boundary integral equation (1.8), e.g. [Bonnet 1999], are a transposition of the concepts developed for the Finite Element Method. In this work, it is based on a discretization of the surface $\partial\Omega$ into $N_E$ isoparametric boundary elements of order one, i.e. three-node triangular elements. Higher order discretizations are also possible (but only used in Chapter 5). Each physical element $E_e$ on the approximate boundary is mapped onto a reference element $\Delta_e$ via an affine mapping

$$\boldsymbol{\xi} \in \Delta_e \to \boldsymbol{y}(\boldsymbol{\xi}) \in E_e, \quad 1 \leq e \leq N_e.$$

$\Delta_e$ is the reference triangle in the $(\xi_1, \xi_2)$-plane. The $N$ interpolation points $\boldsymbol{y}_1, \ldots, \boldsymbol{y}_N$ are chosen as the vertices of the mesh. Each component of the displacement field is approximated with globally continuous, piecewise-linear shape functions $(v_i(\boldsymbol{y}))_{1\leq i\leq N}$: $v_i(\boldsymbol{y}_j) = \delta_{ij}$ for $1 \leq i, j \leq N$. A boundary element $E_e$ contains exactly 3 interpolation nodes $(\boldsymbol{y}_k^e)_{1\leq k\leq 3}$ associated with 3 basis functions $(v_k^e)_{1\leq k\leq 3}$. These basis functions are related to the canonical basis $(\hat{v}_k)_{1\leq k\leq 3}$ defined on the reference element $\Delta_e$ by $v_k^e(\boldsymbol{y}(\boldsymbol{\xi})) = \hat{v}_k(\boldsymbol{\xi})$. Each component of the displacement field $\boldsymbol{u}(\boldsymbol{y})$ is approximated on the element $E_e$ by

$$\boldsymbol{u}_\alpha(\boldsymbol{y}) \approx \sum_{k=1}^{3} u_\alpha^k v_k^e(\boldsymbol{y}) \quad (1 \leq \alpha \leq 3),$$

where $u_\alpha^k$ denotes the approximation of the nodal value of the component $\alpha$ of the vector $\boldsymbol{u}(\boldsymbol{y}_k)$. The discretization process of the boundary integral equation (1.8) is either based on a nodal collocation [Bonnet 1999] or on a Galerkin approach [Sauter 2011]. In this work, we consider only the collocation approach but most of the algorithms presented can be extended straightforwardly to the Galerkin approach. The collocation consists in enforcing the equation at a finite number of collocation points $\boldsymbol{x}$. To have a solvable discrete problem, one has to choose $N$ collocation points. The $N$ displacement approximation nodes thus defined also serve as collocation points, i.e. $(\boldsymbol{x}_i)_i = (\boldsymbol{y}_j)_j$. This discretization process transforms (1.8) into a square complex-valued linear system of size $3N$ of the form

$$\mathbb{K}\mathbf{u} = \mathbf{f}, \tag{1.10}$$

where the $3N$-vector $\mathbf{u}$ collects the sought degrees of freedom (DOFs), namely the nodal displacement components, $\mathbb{K}$ is the $3N \times 3N$ influence matrix and the $3N$-vector $\mathbf{f}$ arises from the discretization of $\boldsymbol{\mathcal{S}}[\boldsymbol{t}^{\mathrm{D}}]$. Setting up the matrix $\mathbb{K}$ classically requires the computation of all element integrals for each collocation point, or of double integrals over all products of elements in the Galerkin approach, thus needing $\mathcal{O}(N^2)$ arithmetic operations (i.e. they have a $\mathcal{O}(N^2)$ complexity).

The important and limiting aspect in the BEM is that the influence matrix $\mathbb{K}$ is fully-populated. Usual direct solvers, such as the LU factorization, then have a complexity of $\mathcal{O}(N^3)$ in terms of computational times and of $\mathcal{O}(N^2)$ in terms of memory requirements, limiting the applicability of the traditional BEM to moderately-sized models. BEM problems of larger size are preferably solved by means of iterative algorithms (GMRES [Saad 1986] for example), which build sequences $(\mathbf{u}^{(k)})_{k\in\mathbb{N}}$ of solution candidates until $\|\mathbb{K}\mathbf{u}^{(k)} - \mathbf{f}\|/\|\mathbf{f}\|$ is less that a predefined tolerance. Each GMRES iteration requires one evaluation of $\mathbb{K}\mathbf{w}$ for given $\mathbf{w}$, a task of computational complexity $\mathcal{O}(N^2)$ whether $\mathbb{K}$ is set up and stored prior to the iterations, or $\mathbb{K}\mathbf{w}$ is evaluated directly by means of standard BEM numerical integration and assembly procedures.

**Fast BEMs for frequency-domain wave propagation.** Applications of the BEM to large models thus require evaluation procedures for $\mathbb{K}\mathbf{w}$ whose complexity is lower than $\mathcal{O}(N^2)$ and which do not require explicit setup and storage of $\mathbb{K}$. Several approaches, collectively referred to as fast BEMs, have been proposed and developed towards meeting these requirements on complexity. They are briefly reviewed in this section, with emphasis on applications to elastodynamics. A more complete review is available in [8].

One notes that $\mathbf{w} \mapsto \mathbb{K}\mathbf{w}$ is (up to the additive free term) a discretized version of the double-layer integral operator $\boldsymbol{w} \mapsto \boldsymbol{\mathcal{D}}[\boldsymbol{w}]$, so that fast BEMs essentially consist in accelerated methods for the evaluation of discretized integral operators on given densities. To reduce the complexity incurred by matrix-vector products $\mathbb{K}\mathbf{w}$, one needs to define an approximation $\mathbb{K}_\varepsilon$ of $\mathbb{K}$ such that (a) $\|\mathbb{K} - \mathbb{K}_\varepsilon\| \leq \varepsilon\|\mathbb{K}\|$ (where $\varepsilon$ is a preset desired relative accuracy) and (b) $\mathbb{K}_\varepsilon$ is increasingly

data-sparse as $N$ grows, so that the computational cost of evaluating good approximations $\mathbb{K}_\varepsilon \mathbf{w}$ of $\mathbb{K}\mathbf{w}$ grows at a rate lower than $\mathcal{O}(N^2)$. The fast BEMs essentially differ in how $\mathbb{K}_\varepsilon$ is defined.

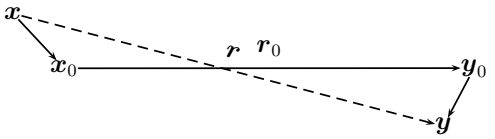


***Figure 1.1:*** *Decomposition of the position vector: notation.*

The first category of fast BEMs is using the **Fast Multipole Method (FMM) based on an explicit kernel decomposition.** The FMM consists in formulating sparse approximations of integral operators such as $\boldsymbol{\mathcal{K}}$ by recasting the fundamental solutions, e.g. $\boldsymbol{U}(\boldsymbol{x},\boldsymbol{y})$, $\boldsymbol{T}(\boldsymbol{x},\boldsymbol{y})$ in (1.5), in terms of products of functions of $\boldsymbol{x}$ and of $\boldsymbol{y}$. On recasting the position vector $\boldsymbol{r} = \boldsymbol{y} - \boldsymbol{x}$ in the form $\boldsymbol{r} = \tilde{\boldsymbol{y}} - \tilde{\boldsymbol{x}} + \boldsymbol{r}_0$, having set $\tilde{\boldsymbol{y}} := \boldsymbol{y} - \boldsymbol{y}_0$, $\tilde{\boldsymbol{x}} := \boldsymbol{x} - \boldsymbol{x}_0$ and $\boldsymbol{r}_0 := \boldsymbol{y}_0 - \boldsymbol{x}_0$ in terms of two chosen poles $\boldsymbol{x}_0$, $\boldsymbol{y}_0$ (Fig. 1.1), decompositions of the form

$$K(\boldsymbol{x},\boldsymbol{y}) = \sum_{n=1}^{p} T_n(\boldsymbol{r}_0) X_n(\tilde{\boldsymbol{x}}) Y_n(\tilde{\boldsymbol{y}}) + E(p), \tag{1.11}$$

called separated decompositions, are sought for generic fundamental solutions $K(\boldsymbol{x},\boldsymbol{y})$ (with $E(p)$ denoting the truncation error). Selecting a truncation level $p$ such that $E(p) < \varepsilon$ and substituting the above kernel approximation into the relevant integral operators, the resulting BE-discretized influence matrix $\mathbb{K}_\varepsilon$ is seen to be of rank at most $p$. The desired data-sparsity of $\mathbb{K}_\varepsilon$ is thus achieved if $p$ is small enough. Note also that the separated character of expansion (1.11) allows to re-use integrations with respect to $\boldsymbol{y}$ when the collocation point $\boldsymbol{x}$ is changed. This defining feature of the FMM is one of the main mechanisms for lowering the $\mathcal{O}(N^2)$ complexity per iteration entailed by standard BEMs (see Fig. 1.2), and was in particular at the heart of the original fast summation method for electrostatics [Greengard 1987] (wherein $K(\boldsymbol{x},\boldsymbol{y}) = C\|\boldsymbol{y}-\boldsymbol{x}\|^{-1}$).

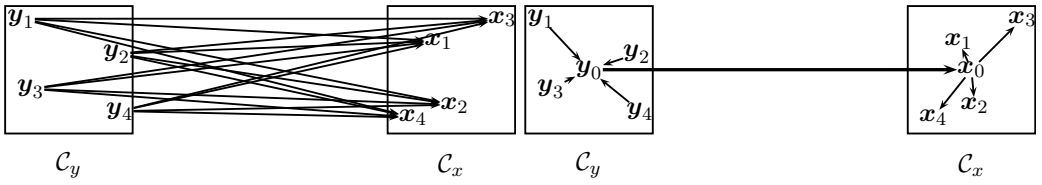


***(a)*** *Standard BEM* ***(b)*** *FM-BEM*

***Figure 1.2:*** *Matrix-vector product with Standard BEM and FM-BEM. The use of the FMM drastically reduces the number of operations necessary to calculate the influence of the source points $y_i$ located in the cell $\mathcal{C}_y$ on the observation points $x_i$ in the cell $\mathcal{C}_x$.*

The truncation error $E(p)$ is in general such that it is controllable, and moderate values of $p$ sufficient (i.e low-rank approximations of $K$ are accurate enough), when $\|\tilde{\boldsymbol{x}}\|$, $\|\tilde{\boldsymbol{y}}\|$ are sufficiently small compared to $\|\boldsymbol{r}_0\|$ (e.g. $\|\tilde{\boldsymbol{x}} - \tilde{\boldsymbol{y}}\|/\|\boldsymbol{r}_0\| \leq 2/\sqrt{5}$ for the Helmholtz-type kernels of frequency-domain acoustics or elastodynamics). This naturally leads to subdividing the (collocation, integration) points involved in the BE-discretized integral equation into clusters and applying decompositions of type (1.11) to well-separated clusters. This subdivision is usually performed by means of a 3D cubic grid of linear spacing $d$ embedding the geometrical support $\partial\Omega$ of (1.5), so that $\partial\Omega$ is enclosed in a set of cubic cells. The FMM basically consists in using (1.11), with the poles $\boldsymbol{x_0}$ and $\boldsymbol{y_0}$ chosen as the cell centers, whenever $\boldsymbol{x}$ and $\boldsymbol{y}$ belong to *non-adjacent* cubic cells. When $\boldsymbol{x}$ and $\boldsymbol{y}$ belong to adjacent cells, the original (i.e. non-separated) definitions of the kernels (e.g. (1.6) with (1.7)) are used together with classical BEM element integration techniques. To further improve the computational efficiency of the FM-BEM, standard (i.e. non-FMM) calculations must be confined to

the smallest possible spatial regions while retaining the advantage of clustering the computation of influence terms into non-adjacent large groups whenever possible. This is achieved by recursively subdividing cubic cells into eight smaller cubic cells. New pairs of non-adjacent smaller cells, to which expansion (1.11) is applicable, are thus obtained from the subdivision of pairs of adjacent cells. The cell-subdivision approach is systematized by means of an octree structure of cells. At each level $\ell$, the linear cell size is denoted $d^\ell$. The level $\ell = 0$, composed of only one cubic cell containing the whole surface $\partial\Omega$, is the tree root. The subdivision process is further repeated until the finest level $\ell = \bar{\ell}$, implicitly defined by a preset subdivision-stopping criterion ($d^{\bar{\ell}} \geq d^{\min}$), is reached. Level-$\bar{\ell}$ cells are usually termed leaf cells. This octree-based recursive clustering, which defines the so-called multi-level FMM, is the other main mechanism for lowering the complexity of BEMs. The theoretical complexity of the multi-level FMM for Helmholtz-type kernels is in fact known to be $\mathcal{O}(N \log N)$ per GMRES iteration both for CPU time and memory [Song 1995].

FMMs for (acoustic, electromagnetic, elastic) waves are often based on the fact that the Helmholtz Green's function (1.7) is known [Epton 1995, Darve 2000a] to admit the separated decomposition

$$G(|\boldsymbol{r}|;\kappa) = \lim_{L\to+\infty} G_L(|\boldsymbol{r}|;\kappa), \quad \text{with } G_L(|\boldsymbol{r}|;\kappa) := \int_{\hat{S}} e^{\mathrm{i}\kappa\hat{\boldsymbol{s}}\cdot\tilde{\boldsymbol{y}}}\mathcal{G}_L(\hat{\boldsymbol{s}};\boldsymbol{r}_0;\kappa)e^{-\mathrm{i}\kappa\hat{\boldsymbol{s}}\cdot\tilde{\boldsymbol{x}}}\,\mathrm{d}\hat{\boldsymbol{s}}, \tag{1.12}$$

where $\hat{S} \subset \mathbb{R}^3$ is the unit sphere and the *transfer function* $\mathcal{G}_L(\hat{\boldsymbol{s}};\boldsymbol{r}_0;\kappa)$ is defined in terms of the Legendre polynomials $P_n$ and the spherical Hankel functions of the first kind $h_n^{(1)}$ by:

$$\mathcal{G}_L(\hat{\boldsymbol{s}};\boldsymbol{r}_0;\kappa) = \frac{\mathrm{i}\kappa}{16\pi^2}\sum_{0\leq n\leq L}(2p+1)\mathrm{i}^n h_n^{(1)}(\kappa|\boldsymbol{r}_0|)P_n\big(\cos(\hat{\boldsymbol{s}},\boldsymbol{r}_0)\big). \tag{1.13}$$

Replacing the integration over $\hat{S}$ with a numerical quadrature then yields a decomposition of the type (1.11). This is the approach used in this work.

The second category of fast BEMs is using the **kernel-independent FMM.** While kernel-dependent FMMs rely on analytical identities giving separable decompositions of specific kernels, kernel-independent FMM are based on kernel decompositions of the form

$$K(\boldsymbol{x},\boldsymbol{y}) = \sum_{m,n=1}^{p} K(\boldsymbol{x}_m,\boldsymbol{y}_n)I_m(\boldsymbol{x})I_n(\boldsymbol{y}) + E(p)$$

where $I_n$ is a family of chosen interpolation functions (e.g. Lagrange or Chebyshev polynomials) and $\boldsymbol{x}_m, \boldsymbol{y}_n$ are interpolation nodes [Fong 2009]. The main conceptual advantage over kernel-dependent decompositions is that the only required knowledge about the kernel is a procedure allowing its evaluation at chosen points. Oscillatory kernels of type (1.7) are considered in [Engquist 2007, Messner 2012]. Another kernel-independent approach exploits the fact that integral operators of convolutional form (i.e. whose kernels are translation-invariant, which includes all full-space fundamental solutions) can be evaluated in $\mathcal{O}(N \log N)$ time using the FFT. As in the FMM, an octree is introduced, with each cell discretized into a Cartesian grid that supports FFT operations. Transfers between non-uniform BE meshes and Cartesian grids are effected using sparse anterpolation and interpolation matrices. This approach has been successfully applied to 3D frequency-domain elastodynamics [Yan 2010] and to a time-frequency treatment of transient elastodynamics [Xiao 2012].

## 1.2 Kernel-dependent FMM for frequency-domain (visco)-elastodynamics

Since the elastodynamic Green's tensors $\boldsymbol{U}(\boldsymbol{x},\boldsymbol{y})$, $\boldsymbol{T}(\boldsymbol{x},\boldsymbol{y})$ given by (1.6) are linear combinations of derivatives of the Green's function (1.7), they are amenable to a decomposition similar to (1.12). An initial series of investigations on the elastodynamic FMM [15, 14, 17] has concentrated on the kernel-dependent approach based on the full-space Green's tensor (1.6). The acceleration was based on separated decompositions of (1.6) obtained by substituting decomposition (1.12)

into (1.6). Many implementation issues arising in this elastodynamic FM-BEM revolve around how to choose the truncation level $L$ in (1.13) so that (1.12) is sufficiently accurate. The overall computational cost indeed is strongly dependent on $L$ through not only the number of terms in the transfer function (1.13), but also the correct number $Q$ of quadrature points on $\hat{S}$, with $Q = O(L^2)$. Selection rules for $L$ in all Helmholtz-type FMMs rest on a key error analysis result [Darve 2000a], which states that there exist four constants $C_1, C_2, C_3, C_4$ such that

$$L = C_1 + C_2\kappa|\boldsymbol{r} - \boldsymbol{r}_0| + C_3 \ln(\kappa|\boldsymbol{r} - \boldsymbol{r}_0|) + C_4 \ln \epsilon^{-1} \Longrightarrow \left|G(|\boldsymbol{r}|;\kappa) - G_L(|\boldsymbol{r}|;\kappa)\right| < \epsilon \qquad (1.14)$$

for any chosen error level $\epsilon < 1$, whenever $\|\boldsymbol{r} - \boldsymbol{r}_0\|/\|\boldsymbol{r}_0\| \leq 2/\sqrt{5}$. First, noting that the magnitude of $\|\boldsymbol{r} - \boldsymbol{r}_0\|$ and $\|\boldsymbol{r}_0\|$ depend on the level (through the linear size of cells for that level), estimate (1.14) dictates that suitable values of $L$ in (1.12) are level-dependent. The following selection rule for $L$ (whose form is known from previous studies on FMMs for Maxwell equations [Darve 2000b]), inspired by (1.14), proved satisfactory:

$$L_\alpha(d) = \sqrt{3}\kappa_\alpha d + C_\epsilon \log_{10}(\sqrt{3}\kappa_\alpha d + \pi), \qquad \alpha = \mathrm{P,S} \qquad (1.15)$$

(with $d$ denoting the linear size of a cell, making the rule level-dependent). Note that the recommended value of $L$ depends on whether it is used for the contribution of $G(\cdot;\kappa_\mathrm{P})$ or $G(\cdot;\kappa_\mathrm{S})$ to (1.6). Empirical tuning of (1.15) by means of numerical experiments led to set $C_\epsilon = 7.5$ as the best trade-off between accuracy and efficiency. The version of the elastodynamic FM-BEM incorporating the above-described features was shown (both theoretically and numerically) to conform to the expected $\mathcal{O}(N \log N)$ per GMRES iteration computational complexity. Figure 1.3 (from [14]) represents the horizontal and vertical displacements computed with the FM-BEM for the test problem of the diffraction of an oblique incident plane P-wave by a semi-ellipsoidal canyon. These studies have shown the potentialities of the method to model elastic wave propagation in the geological structures.

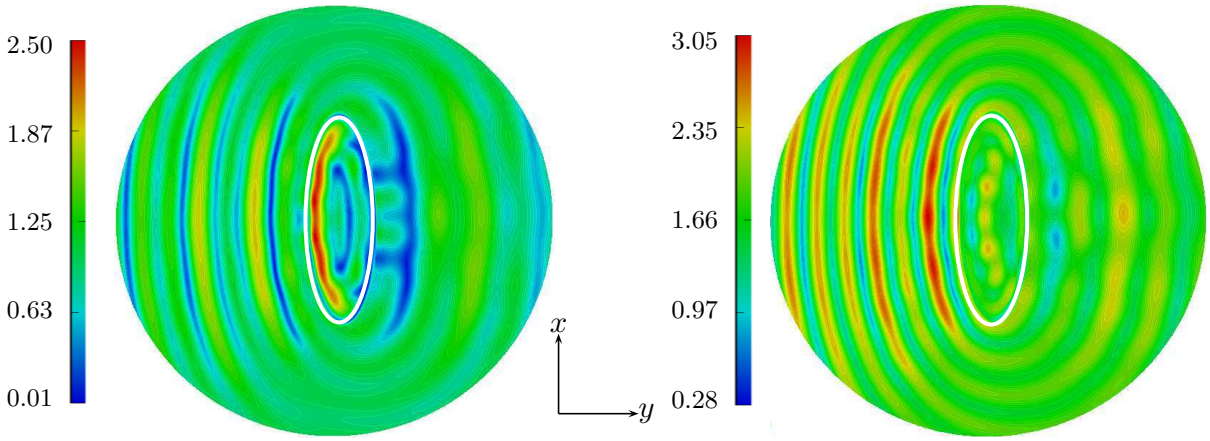


***Figure 1.3:*** *Diffraction of an oblique incident plane P-wave by a semi-ellipsoidal canyon: horizontal (left) and vertical (right) computed displacement on canyon surface and meshed part of free surface (normalized frequency $\kappa_s a/\pi = 2$); from [14]. The white ellipse depicts the canyon edge.*

The previous treatment has been expanded in [13] so as to allow piecewise-homogeneous media, by coupling integral equations arising from writing (1.5) separately for each homogeneous component (of course using the Green's tensor with the corresponding material parameters). Then, perfect-bonding transmission conditions were used in weighted combinations of the integral equations obtained for each subdomain, reducing the unknowns to one displacement field and one traction field on each interface. This formulation has been tested on 3D examples including a two-layered semi-spherical basin embedded in an infinite half-space (Fig. 1.4). As an illustration of the capacities of the method, in Fig. 1.5 the results for a two-layered semi-spherical basin

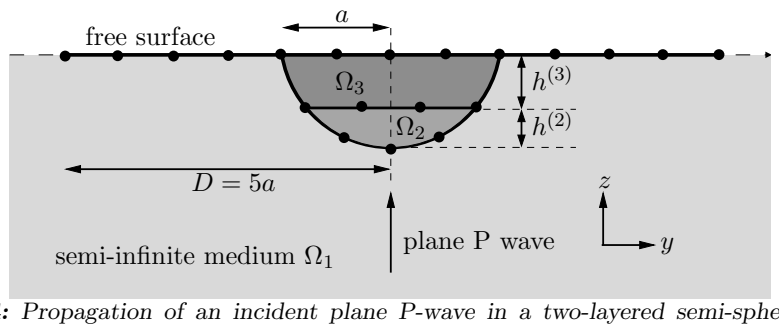


***Figure 1.4:*** *Propagation of an incident plane P-wave in a two-layered semi-spherical basin: notation.*

are compared to those for a single-layered basin. In example (a), mechanical properties are defined so that the velocity contrasts between $\Omega_1, \Omega_2$ and $\Omega_2, \Omega_3$ are the same for S-waves (and as in [Sánchez-Sesma 1983]):

$$\frac{\rho^{(2)}}{\rho^{(1)}} = \frac{\rho^{(3)}}{\rho^{(2)}} = 0.6; \qquad \frac{\mu^{(2)}}{\mu^{(1)}} = \frac{\mu^{(3)}}{\mu^{(2)}} = 0.3; \qquad \nu^{(1)} = 0.25; \qquad \nu^{(2)} = \nu^{(3)} = 0.30. \tag{1.16}$$

In example (b), the velocity contrasts between $\Omega_1, \Omega_2$ and $\Omega_2, \Omega_3$ are the same for P- and S-waves:

$$\frac{\rho^{(2)}}{\rho^{(1)}} = \frac{\rho^{(3)}}{\rho^{(2)}} = 0.6; \qquad \frac{\mu^{(2)}}{\mu^{(1)}} = \frac{\mu^{(3)}}{\mu^{(2)}} = 0.3; \qquad \nu^{(1)} = 0.25; \qquad \nu^{(2)} = 0.30; \qquad \nu^{(3)} = 0.34. \tag{1.17}$$

The thickness, $h^{(2)}$ and $h^{(3)}$ of the layers $\Omega_2$ and $\Omega_3$ are adjusted to the wavelengths:

$$h^{(2)}/\lambda_S^{(2)} = h^{(3)}/\lambda_S^{(3)} \qquad \Rightarrow \qquad h^{(2)} = \sqrt{2}h^{(3)} = (2-\sqrt{2})a. \tag{1.18}$$

The study is performed at normalized frequency $\kappa_P^{(1)} a/\pi = 1$, using a truncation radius $D = 5a$. The mesh features $N = 91\ 893$ DOFs. The computations required 255 and 272 iterations for example (a) and (b). The introduction of the layer $\Omega_3$ leads to stronger amplification (up to 7 for (a) or 6.5 for (b) instead of 3 for the single-layered basin, the free-surface effects being removed), with shorter wavelengths in the basin. We also see on this example the effect of the value of $\nu^{(3)}$: a higher value of $\nu^{(3)}$ leads to a smaller increase of the maximum amplification.

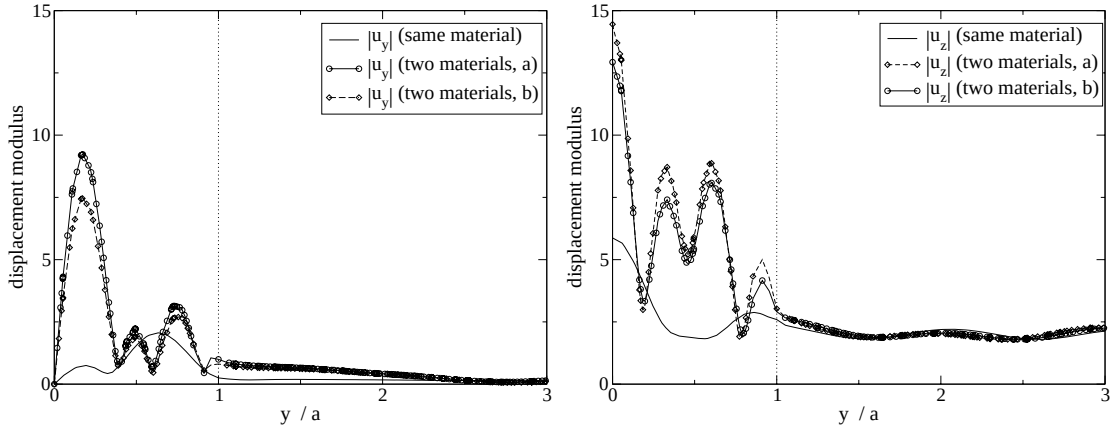


***Figure 1.5:*** *Propagation of an incident plane P-wave in a two-layered semi-spherical basin (with mechanical properties (1.16) and (1.17) , $\kappa_P^{(1)} a/\pi = 1$).*

The applicability of the single-domain and multi-domain elastodynamic FM-BEM formulations to weakly dissipative visco-elastic media characterized (for fixed frequency) by complex-valued wavenumbers $\kappa_\alpha^\star = \kappa_\alpha(1 + \mathrm{i}\beta_\alpha)$ ($\alpha$ = P,S), where $\kappa_\alpha^\star$ are the elastic pressure and shear complex wavenumbers and $\beta_\alpha \ll 1$ are the damping ratios, has been examined in [9]. In particular, the validity of selection rules such as (1.15) in the complex-wavenumber case, an issue only sparingly addressed in the available literature, was examined. In contrast to the already-mentioned real-wavenumber case, no mathematical error analysis is available. An empirical study based on numerical simulations has shown that a slightly altered version of (1.15) performs satisfactorily, leading to the adoption of the following damping-dependent selection rule:

$$L_\alpha(d;\beta_\alpha) = \kappa_\alpha^\star d + (C_\epsilon + C\beta_\alpha)\log_{10}(\kappa_\alpha^\star d + \pi), \qquad \alpha = \mathrm{P,S} \tag{1.19}$$

with $C_\epsilon = 7.5$ as before and $C = 60$. This multi-domain visco-elastodynamic FM-BEM has been applied to the problem of a wave propagating in a semi-infinite medium with a lossy semi-spherical inclusion (seismic wave in alluvial basin). Contour maps for the vertical and horizontal displacements, $u_z$ and $u_y$, on the free surface are shown in Fig. 1.6 (from [9]) for three levels of damping $\beta$, illustrating the effect of damping on the basin response.

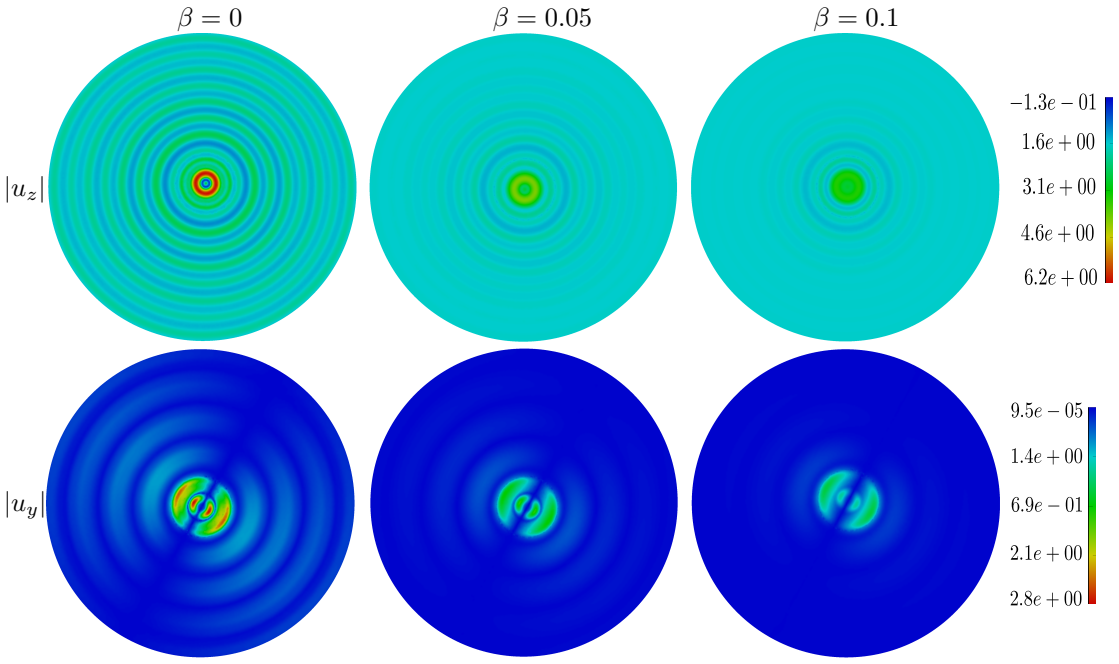


***Figure 1.6:*** *Vertically incident P-wave in a viscoelastic half-space containing a semi-spherical soft basin: contour maps of $|u_z|$ and $|u_y|$ at $\kappa_P^{(1)} R/\pi = 2$ for three levels of damping in both media ($\beta_1 = \beta_2 = \beta$): $\beta = 0$ (purely elastic case), $\beta = 0.05$ and $\beta = 0.1$; from [9].*

The next two Sections are devoted to the illustration of some typical configurations that can be considered with the fast BEM developed during my PhD and extended during the PhD of Eva Grasso. The limitations observed with these direct applications of the FM-BEM have motivated the research topics I have considered since then.

## 1.3 On the efficiency of the FM-BEM to study site effects

**Amplification of seismic waves in alluvial deposits.** It is well-known that the amplification of seismic waves in alluvial deposits is strongly influenced by the geometry and mechanical properties of the surficial layers. The estimation of this amplification is mainly performed through simplified 1D approaches. However the amplification process can significantly differ between the 1D (horizontal layering) and the 2D/3D cases because of focusing effects and waves generated at basin edges, (e.g., [Paolucci 1999]). Some analytical and numerical results have been already derived by various authors for the response of basins with simple geometries to incident seismic waves. [Bard 1985] considers rectangular and sine-shaped soft layers embedded in a rigid half-space considering incident plane SH-waves. The propagation of plane vertical SH-waves in 2D cylindrical basins is analysed in [Semblat 2010] using the BEM in the frequency domain. [Rodríguez-Zúñiga 1995] studies the case of a 3D cylindrical basin having a rectangular vertical cross-section. In that case, a large difference between the 2D and 3D response at the center of the basin is observed. In [Bard 1985] and [Jiang 1988], it is reported that the fundamental frequencies of the basins only depend on the aspect ratio and the 1D fundamental frequency at the center of the valley. The 3D wave diffraction by a semi-spherical canyon has been studied [Lee 1978, Kim 1993, Yokoi 2003, Liao 2004, 14] and 3D wave amplification due to surface heterogeneities has also been quantified [Sánchez-Sesma 1995, Komatitsch 1998, Dravinski 2003, Moczo 2002]. [Smerzini 2011] makes comparisons of 3D, 2D and 1D amplification using the Spectral Element Method with a 3D model of the Gubbio plain in Italy. [Olsen 2000] shows differences among 3D/2.5D/1D amplification and duration with a 3D finite difference model of the Upper Borrego Valley, California. The originality of our work with K. Meja Fajardo and J.F. Semblat [4] consists in estimating the 3D/1D amplification factors in different 3D configurations.

**Numerical models for the parametric study.** We use the capabilities of the FM-BEM solver to model the amplification of seismic waves in 3D basins with canonical geometries subjected to incident plane waves. In particular, we quantify how the 3D amplification differs from the 1D case consisting of an equivalent horizontal layering. We consider a basin embedded in a half-space, which is subjected to an incident field of plane P or S waves. Following the same notations than in Fig. 1.4 but with the same mechanical properties in $\Omega_2$ and $\Omega_3$, we set:

$$\frac{\rho^{(2)}}{\rho^{(1)}} = 0.6; \quad \nu^{(1)} = 0.25; \quad \nu^{(2)} = 0.30; \quad \chi = \frac{c_S^{(1)}}{c_S^{(2)}}; \quad h = h^{(2)} + h^{(3)}. \tag{1.20}$$

The free surface is again truncated at a distance $D = 5a$ and the interface between the basin and the underlying bedrock is defined by

$$\left(\frac{x}{a}\right)^2 + \left(\frac{y}{a}\right)^2 + \left(\frac{z}{a}\right)^2 = 1, \quad z \leq 0,$$

i.e. the study is not limited to semi-spherical basins. Several values of horizontal aspect ratio are considered $\frac{a}{h} = 0.5,\ 1,\ 2,\ 3$, i.e. ranging from deep to shallow basins. Different velocity ratios are also considered, $\chi = 2,\ 3,\ 4,\ 6$, the higher the value of $\chi$, the softer the basin. We also consider incident P and S waves, at incidence angles $\theta = 45°,\ 30°$ and $0°$ (vertical incidence). The size of the resulting numerical models ranged from 16 461 to 92 565 DOFs (i.e. moderate size problems for the FM-BEM such that a parametric study is easily performed). Basin models with and without attenuation due to material damping are also considered.

**Main results of the study.** We first examine the relationship between the amplification level and the most relevant physical parameters of the problem: impedance contrast, 3D aspect ratio, vertical and oblique incidence of plane waves. Our main results, reported in Figure 1.7 show that the largest amplification levels correspond to the deepest and softest basins.

We have also studied the effect of the 3D basin shape. We have considered three usual geometries: an ellipsoidal shape, a super-ellipsoid of fifth degree and a 3D cosine shape (Fig. 1.8). Introducing the "equivalent shape ratio" $l_0/h$ used by [Jiang 1988], where $l_0$ is the half width over

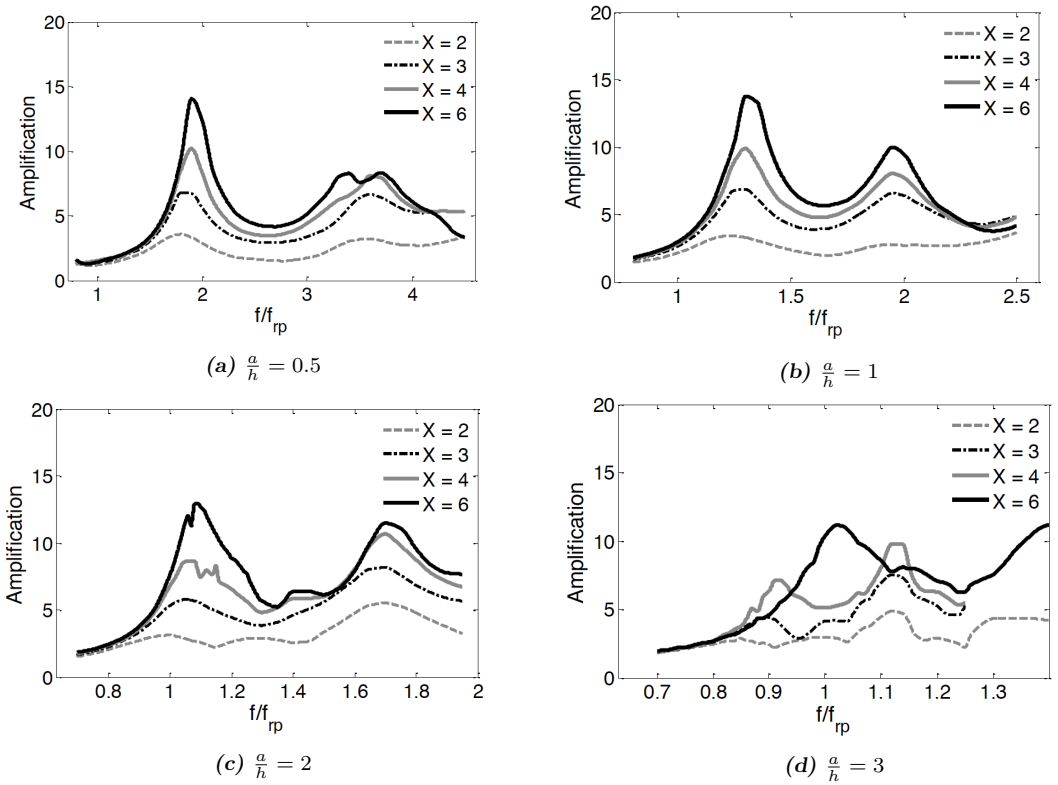


*(a)* $\frac{a}{h} = 0.5$ *(b)* $\frac{a}{h} = 1$

*(c)* $\frac{a}{h} = 2$ *(d)* $\frac{a}{h} = 3$

***Figure 1.7:*** *Amplification at the top of the 3D basin (5% damping in the basin and 0.5% damping in the half-space) due to vertically incident P-waves for several velocity contrasts $\chi$ and several aspect ratios. The amplification factor is represented with respect to the normalised frequency $f/f_{rp}$ where $f_{rp} = c_P^{(2)}/4h$ is the 1D resonance frequency at the center of the basin (from [4]).*

which the depth of the basin is half its maximum value, we can take into account the difference in thickness of the three basin shapes. Even though the three shapes have the same aspect ratio $a/h$, the cosine shape has the lowest equivalent shape ratio. In Fig. 1.9, the amplification level for the ellipsoidal shapes remains almost the same, both for the horizontal and vertical components; however the different shapes lead to different fundamental and dominant frequencies. On the other hand, we can see slightly higher amplification factors for the fundamental frequency in the case of the basin with cosine shape, a result that was expected, since there are strong basin edge effects and there is more trapped waves due to the lower thickness of the basin.

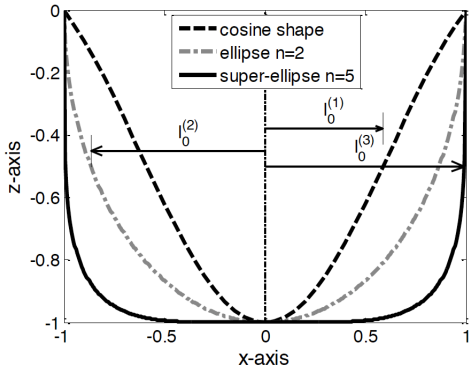


***Figure 1.8:*** *Cross section of the basin shapes in the* **x-z** *plane (from [4]).*

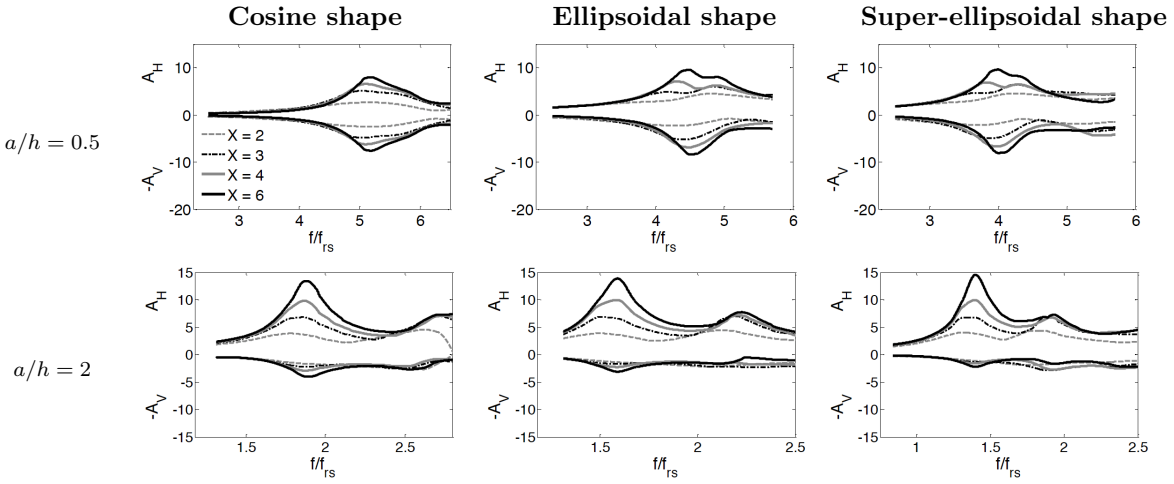


***Figure 1.9:*** *Amplification at the top of the 3D basin (with 5% damping) due to vertically incident S-waves with different equivalent shape ratios (from [4]).*

**Simple rules to assess 3D basin effects.** Using the capabilities of the FM-BEM, we have performed a parametric study. Such a study would not have been possible with the standard BEM due to the computational costs. The numerical results show that the most important parameters for wave amplification are the impedance contrast and the "equivalent shape ratio". Using these two parameters, simple rules are derived to compute the fundamental frequency for various 3D basin shapes and the corresponding 3D/1D amplification factor for 5% damping. The proposed equations are expressed only in terms of the "equivalent shape ratio", the basin/bedrock impedance contrast and the damping ratios. These numerical results are in good agreement with the partial results proposed in the previous studies and have shown the efficiency and usefulness of fast BEMs to study site effects.

However, to be more complete the study should also include the effects of the soil layering for higher frequencies. So far the proposed FM-BEM is more efficient to model homogeneous or piecewise homogeneous domains (with a modest number of layers) than to model vertically stratified models since only the full-space Green's tensors have been accelerated with the FMM. It is thus necessary to discretize the complete free surface to impose the traction free condition. This study has also shown that the computational time per iteration is no longer the main issue to apply BEM to realistic configurations, but the total number of iterations is now the major limiting factor.

## 1.4 Using the capabilities of the FM-BEM to take into account site effects in soil-structure interaction

The understanding and prediction of the dynamic behaviour of large and heavy structures in several limit states is a major societal issue. The structure may include bridges, dams, power plants, etc. and the excitation may come from an earthquake, a nearby blast, vibrations induced by transportation systems, etc. With the improvement of computational resources, numerical methods simulating on computers the propagation of elastic waves from the source to the structures provide a unique framework to help designing safe buildings. Obviously the study of the structure response is important. But, experimental and numerical evidence shows that, due to the propagation of elastic waves, there also exist interactions between the structure and the soil [Wirgin 1996] that need to be taken into account. The simulation of Soil-structure interaction problems is an active area of research [Clouteau 2013] and EDF (French Electricity operator) is currently defining new seismic risk assessments of the existing power production sites.

Once the capabilities of fast BEMs demonstrated to simulate site effects, we have used the FM-BEM to incorporate site effects in the simulation of soil-structure interactions. This work has been done in the context of the PhD of Zouhair Adnani [Adnani 2018] funded by EDF R&D and in collaboration with Marc Bonnet (POEMS) and Vinicius Alves Fernandes (EDF R&D).

**Modeling Soil-Structure Interactions.** Soil-Structure Interaction problems can be solved either by a direct approach [Jingbo 1998, Yang 1992, Seo 2007, Choi 2001, Isbiliroglu 2015] which consists in applying a single numerical method (generally the FEM) to the complete problem and thus necessitating to use a non-reflecting boundary condition in the soil to ensure the radiation condition. Alternatively, a substructuring approach [Clouteau 2001, Nieto-Ferro 2013] (which is similar to a domain decomposition method) can be applied. In that case, the whole computational domain is subdivided into several subdomains and in each subdomain the method that is the best suited is applied. Because of the complementary specificities of the FEM and the BEM, it is natural to use the BEM to model the underground environment and the FEM to model the bounded domain, i.e. the structure and possibly its close-range environment (see Fig. 1.10). There exist then various numerical methods to perform a FEM-BEM coupling, see e.g. [Beskos 1993, Clouteau 2013, Lin 1996, Elleithy 2003, Hsiao 1990, Coulier 2014a, François 2015, Caudron 2018].

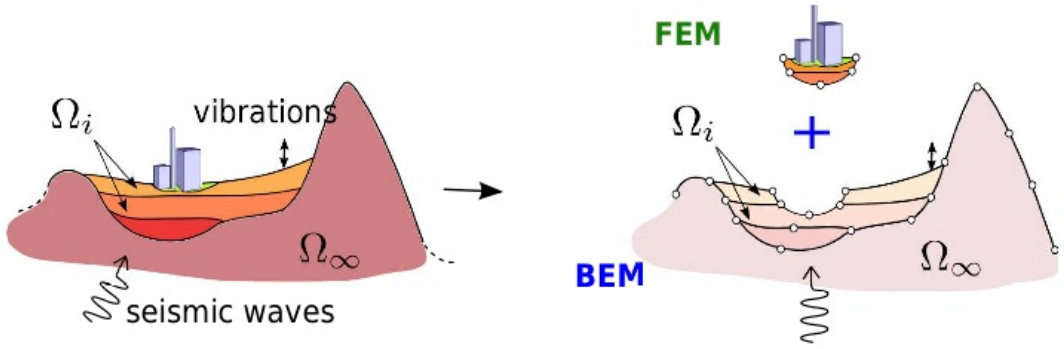


***Figure 1.10:*** *Coupling between the Finite Element and the Boundary Element Methods to combine the advantages of both methods in the context of soil-structure problems.*

More recently, some fast BEM-FEM coupling strategies have been proposed. An exhaustive study of BEM-FEM coupling strategies for the solution of dynamic soil-structure interaction problems is proposed in [Coulier 2014b]. The application of hierarchical matrices in the boundary element formulation is used to accelerate the solution of the BEM. Fischer et al. [Fischer 2005] propose a coupling algorithm based on Lagrange multipliers in the time-harmonic domain.

During the PhD of Eva Grasso [Grasso 2012] (in collaboration with Marc Bonnet and Jean-François Semblat), we have proposed an approach to couple the FEM and the FM-BEM to model three-dimensional time-harmonic visco-elastodynamics problems in unbounded domains. Two classical strategies of coupling are considered. The first one is an iterative procedure based on a sequential interface relaxation method. This method is tested on simple geometries with homogeneous materials. The second strategy is a simultaneous approach. The algorithm is based on the fast solution of the BEM global system of equations and by an implicit condensation of the FEM internal degrees of freedom performed at each global iteration of the iterative solver. The simultaneous approach algorithm is shown to be stable for models with simple shapes. The main drawbacks of these approaches in an industrial context is the use of a global iterative solver for which the convergence behaviour has not been yet studied.

The originality of the PhD work of Zouhair Adnani is to formulate, implement, and evaluate on simple soil-structure oriented examples, a computational strategy that combines the FM-BEM (with the solver *COFFEE*), and the FEM (with the EDF in-house code *Code Aster*) with a substructuring approach and without the need of a global iterative solver. So far at EDF, the substructuring approach for solving SSI problems is implemented but with a coupling between the standard BEM (solver Miss3D, developed by D. Clouteau [Clouteau 2003]) and the FEM (with *Code_Aster*).

In this industrial context, the BEM-FEM coupling is performed with the substructuring method by computing the soil impedance (i.e. elastodynamic Poincaré-Steklov) operator relating forces to displacements on the FEM-BEM coupling interface. This approach has the important advantage to be a black box approach such that it is not intrusive in the industrial code. But the current approach used at EDF presents two main limitations.

1. First it is limited in terms of problem size that can be considered since no acceleration technique is used for the BEM solver.
2. Secondly, since it is based on the layered half-space Green's tensor, it is only possible to consider the effect of a vertical stratification of the soil. Sedimentary basins c and 3D site effects are not considered with this approach.

Following this remark, the aim during the PhD of Z. Adnani was to determine the capabilities of the coupling of the multi-domain FM-BEM (based on the full-space fundamental solutions in order to model non-horizontal layering) with the FEM in an industrial context. Obviously, other approaches could be used to perform the coupling but the industrial partner preferred to retain the approach based on the computation of the soil impedance operator.

**FEM-BEM coupling with the soil impedance operator: summary.** We follow the notations presented in Fig. 1.11. $\Omega_b$ is a bounded domain and $\Omega_s$ is the unbounded domain. The two domains are connected through the interface $\Gamma$. The finite element approximation of $\Omega_b$ is based on the usual weak formulation, written in the frequency domain:

$$\int_{\Omega_b} \boldsymbol{\sigma}_b(\boldsymbol{u}_b) : \boldsymbol{\varepsilon}(\boldsymbol{w}) dV - \omega^2 \int_{\Omega_b} \rho_b \boldsymbol{u}_b . \boldsymbol{w} dV = F(\boldsymbol{w}) + \langle \boldsymbol{t}_{\boldsymbol{n}_b}(\boldsymbol{u}_b), \boldsymbol{w} \rangle_\Gamma, \quad \forall \boldsymbol{w} \in \mathcal{W} \tag{1.21}$$

where $\boldsymbol{u}_b$ is the displacement vector in $\Omega_b$, $\mathcal{W}$ is the space of kinematically admissible virtual displacements in $\Omega_b$, $\boldsymbol{\sigma}_b(\boldsymbol{u}_b)$ is the stress tensor associated to $\boldsymbol{u}_b$ in $\Omega_b$, and $\boldsymbol{t}_{\boldsymbol{n}_b}$ represents the stress vector relative to $\Omega_b$ on $\Gamma$, i.e. $\boldsymbol{t}_{\boldsymbol{n}_b}(\boldsymbol{u}_b) = \boldsymbol{\sigma}_b(\boldsymbol{u}_b).\boldsymbol{n}_b$. The linear functional $F : \mathcal{W} \to \mathbb{R}$ synthesizes all loadings applied to $\Omega_b$ on the interface $\Gamma$.

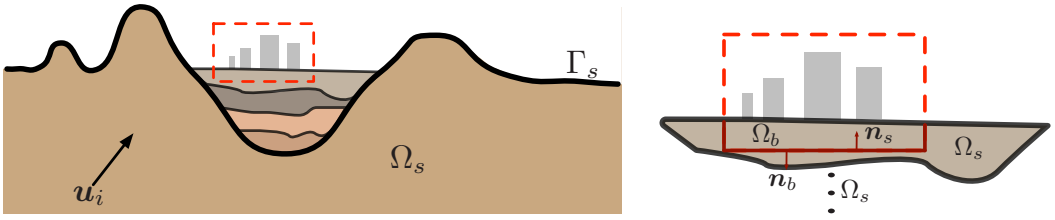


***Figure 1.11:*** *FEM-BEM coupling: notations.*

The field $\boldsymbol{u}_s$ in $\Omega_s$, corresponding to the displacement in the soil, satisfies the following system

$$\mathcal{L}_s(\boldsymbol{u}_s) := \mathrm{div}(\boldsymbol{\sigma}_s(\boldsymbol{u}_s)) + \rho_s \omega^2 \boldsymbol{u}_s = \boldsymbol{0} \text{ and } \boldsymbol{t}_{\boldsymbol{n}_s}(\boldsymbol{u}_s) = \boldsymbol{0} \text{ on } \Gamma_0 = \partial\Omega_s \setminus \Gamma \text{ (free surface condition).}$$

The coupling between the domains $\Omega_s$ and $\Omega_b$ is done with the transmission conditions

$$\boldsymbol{u}_b = \boldsymbol{u}_s \text{ and } \quad \boldsymbol{t}_{\boldsymbol{n}_b}(\boldsymbol{u}_b) + \boldsymbol{t}_{\boldsymbol{n}_s}(\boldsymbol{u}_s) = \boldsymbol{0} \qquad \text{on } \Gamma.$$

To simplify the solution, the displacement in $\Omega_s$ is decomposed as

$$\boldsymbol{u}_s = \boldsymbol{u}_i + \boldsymbol{u}_r + \boldsymbol{u}_c,$$

where:

(i) $\boldsymbol{u}_i$ is the given incident field, i.e. $\mathcal{L}_s(\boldsymbol{u}_i) = \boldsymbol{0}$ in $\Omega_0$ (in the absence of any topographic perturbation), and $\boldsymbol{t}_{\boldsymbol{n}_s}(\boldsymbol{u}_i) = \boldsymbol{0}$ on $\Gamma_0$;

(ii) $\boldsymbol{u}_r$ is the diffracted field due to topographic perturbation, i.e. $\mathcal{L}_s(\boldsymbol{u}_r) = \boldsymbol{0}$ in $\Omega_s$, $\boldsymbol{u}_i + \boldsymbol{u}_r = \boldsymbol{0}$ on $\Gamma$ and $\boldsymbol{t}_{\boldsymbol{n}_s}(\boldsymbol{u}_r) = \boldsymbol{0}$ on $\Gamma_s$;

(iii) $\boldsymbol{u}_c$ is the radiated displacement in $\Omega_s$ resulting from the motion of $\Omega_b$, transmitted through the interface $\Gamma$, i.e. $\boldsymbol{u}_b = \boldsymbol{u}_c$ on $\Gamma$.

$\langle \boldsymbol{t}_{\boldsymbol{n}_b}(\boldsymbol{u}_b), \boldsymbol{w}\rangle_\Gamma$ in (1.21) is then expanded by taking into account the decomposition of $\boldsymbol{u}_s$ such that:

$$\langle \boldsymbol{t}_{\boldsymbol{n}_b}(\boldsymbol{u}_b), \boldsymbol{w}\rangle_\Gamma = \langle \boldsymbol{f}_s, \boldsymbol{w}\rangle_\Gamma - \langle \boldsymbol{t}_{\boldsymbol{n}_s}(\boldsymbol{u}_c), \boldsymbol{w}\rangle_\Gamma, \tag{1.22}$$

where we have introduced the *seismic force density* $\boldsymbol{f}_s := -\boldsymbol{t}_{\boldsymbol{n}_s}(\boldsymbol{u}_i + \boldsymbol{u}_r)$ on $\Gamma$ resulting only from the presence of an incident field. The field $\boldsymbol{u}_s = \boldsymbol{u}_s[\boldsymbol{v}]$ in $\Omega_s$ resulting from a prescribed displacement $\boldsymbol{v}$ on the interface is defined by:

$$\mathcal{L}_s(\boldsymbol{u}_s) = \boldsymbol{0} \text{ in } \Omega_s, \quad \boldsymbol{t}_{\boldsymbol{n}_s}(\boldsymbol{u}_s) = \boldsymbol{0} \text{ on } \Gamma_s, \quad \boldsymbol{u}_s = \boldsymbol{v} \text{ on } \Gamma. \tag{1.23}$$

With this definition, it follows that $\boldsymbol{u}_r = -\boldsymbol{u}_s[\boldsymbol{u}_i]$ and the computation of the seismic force $\boldsymbol{f}_s$ then requires the solution of (1.23) with $\boldsymbol{v} = -\boldsymbol{u}_i$. Let $\mathcal{Z}$ be the linear impedance operator such that

$$\boldsymbol{t}_{\boldsymbol{n}_s}(\boldsymbol{u}_s[\boldsymbol{v}]) = \mathcal{Z}\boldsymbol{v} \qquad \text{on } \Gamma. \tag{1.24}$$

The operator $\mathcal{Z}$ operates the condensation of the unbounded soil region $\Omega_s$ on the interface $\Gamma$. Since $\boldsymbol{u}_b = \boldsymbol{u}_c$ on $\Gamma$, (1.22) becomes

$$\langle \boldsymbol{t}_{\boldsymbol{n}_b}(\boldsymbol{u}_b), \boldsymbol{w}\rangle_\Gamma = \langle \boldsymbol{f}_s, \boldsymbol{w}\rangle_\Gamma - \langle \mathcal{Z}\boldsymbol{u}_b, \boldsymbol{w}\rangle_\Gamma. \tag{1.25}$$

An approximation space in the form of $\mathcal{W}_h = \text{Span}\big( (\boldsymbol{\Phi}_i)_{1\le i\le n}\,, (\boldsymbol{\Psi}_j)_{1\le j\le m} \big) \subset \mathcal{W}$ is then considered, such that each (vector) basis function $\boldsymbol{\Phi}_i$ has a vanishing trace on $\Gamma$. To evaluate the contribution of $\langle \boldsymbol{t}_{\boldsymbol{n}_b}(\boldsymbol{u}_b), \boldsymbol{w}\rangle_\Gamma$ to the weak formulation (1.21), we approximate $\boldsymbol{u}_b$ on $\Gamma$ as $\boldsymbol{u}_b = \sum_j u_b^j \boldsymbol{\Psi}_j$, while virtual displacements $\boldsymbol{w}$ are chosen as $\boldsymbol{w} = \boldsymbol{\Psi}_k$ $(1 \le k \le m)$, which gives

$$\langle \mathcal{Z}\boldsymbol{u}_b, \boldsymbol{w}\rangle_\Gamma = \sum_j u_b^j \langle \boldsymbol{t}_{\boldsymbol{n}_s}(\boldsymbol{\Psi}_j), \boldsymbol{\Psi}_k\rangle_\Gamma = \sum_j u_b^j \langle \mathcal{Z}\boldsymbol{\Psi}_j, \boldsymbol{\Psi}_k\rangle_\Gamma = \sum_j u_b^j Z_{kj}, \tag{1.26}$$

$$\text{and } \langle \boldsymbol{f}_s, \boldsymbol{w}\rangle_\Gamma = \langle \boldsymbol{f}_s, \boldsymbol{\Psi}_k\rangle_\Gamma = \langle -\boldsymbol{t}_{\boldsymbol{n}_s}(\boldsymbol{u}_i + \boldsymbol{u}_r), \boldsymbol{\Psi}_k\rangle_\Gamma = f_{sk}. \tag{1.27}$$

The solution of the weak formulation by the FEM requires the computation of the impedance operator $\mathcal{Z}$ and the seismic force $\boldsymbol{f}_s$ projected on $\mathcal{W}_h$, i.e. the $Z_{kj}$ coefficients defined by (1.26) and the $f_{sk}$ coefficients defined by (1.27).

The discretization of the impedance operator $\mathcal{Z}$ would require the iterative solution of $m$ systems. To reduce the computational costs, we compute the projection of the impedance operator $\mathcal{Z}$ on a reduced basis of interface modes. The number of FM-BEM calculations is thus reduced to the "small" number interface modes selected.

**Validation of the coupling approach.** In all the numerical results, the reduced basis is composed only of rigid body modes of the footing. They consist in kinematically admissible displacements with no deformation of the footing: the three possible translations and the three rotations for a rigid body. The impedance operator and the seismic force (obtained with the FM-BEM only) have been compared to reference solutions and validated for (circular) superficial and buried foundations on homogeneous or piecewise homogeneous soils.

As an illustration, the case of a hemispherical basin in an elastic half-space is reported. The mechanical properties are set in the half-space to $c_s = 1740$ m/s , $c_p = 3455$ m/s, $\nu = 0.33$ and in the basin to $c_s = 870$ m/s , $c_p = 1727$ m/s, $\nu = 0.33$ . The impedances are normalised by the static stiffness of an infinite half-space with the mechanical characteristics of the hemispherical basin. The impedances for a circular surface footing in a half-space [Sieffert 1992], are also plotted to see the impact of the velocity contrast on the impedance. Figure 1.12 represents the real and imaginary parts of the impedance operator with respect to the non-dimensional circular frequency defined by $a_0 = \omega r/c_s$ for the case of a circular surface footing and Figure 1.13 for the case of an embedded cylindrical footing. The footings have a radius of $r = 30$ m and the embedded footing a depth of 31 m. The free surface is truncated at a distance equal to $4r$ and the basin has a radius of 100 m. The frequency range of interest is [0.2Hz, 24Hz]. The numerical results obtained with our new approach are in good agreement with the existing numerical results. The main differences are observed for high frequencies where the FEM code *Code_Aster* is known to be less accurate for the mesh used. Finally, Figure 1.14 gives the seismic forces in the case of the circular surface

footing. Again, we obtain a good agreement between our results and previous results obtained at EDF, validating the efficiency of our new approach. The point here is not to explain the observed differences (see [Adnani 2018] for more details) but rather to illustrate the possibility to use the FM-BEM to introduce site effects in soil-structure interaction problems.

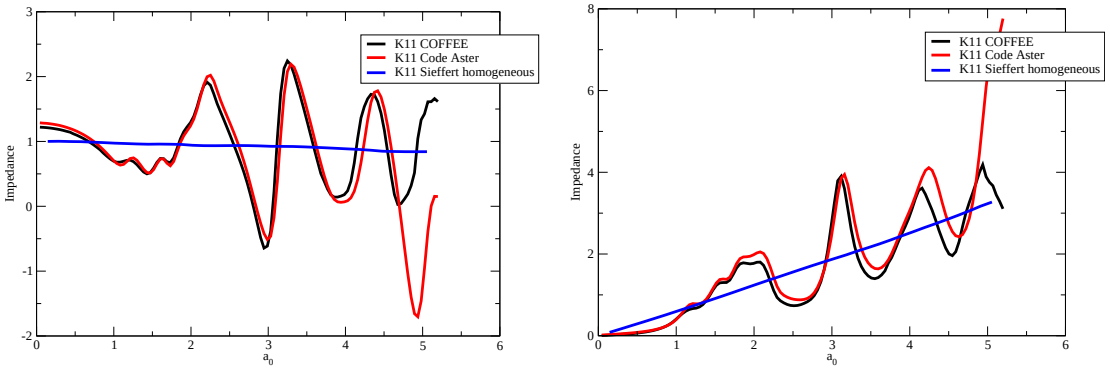


Real part Imaginary part

***Figure 1.12:*** *Circular surface footing on a hemispherical basin. Computation of the normalised impedance ($K_{11}$): comparison of the FM-BEM (COFFEE), FEM-BEM coupling (Code_Aster) solutions and the reference solution from [Sieffert 1992] (Sieffert homogeneous) for a half-space.*

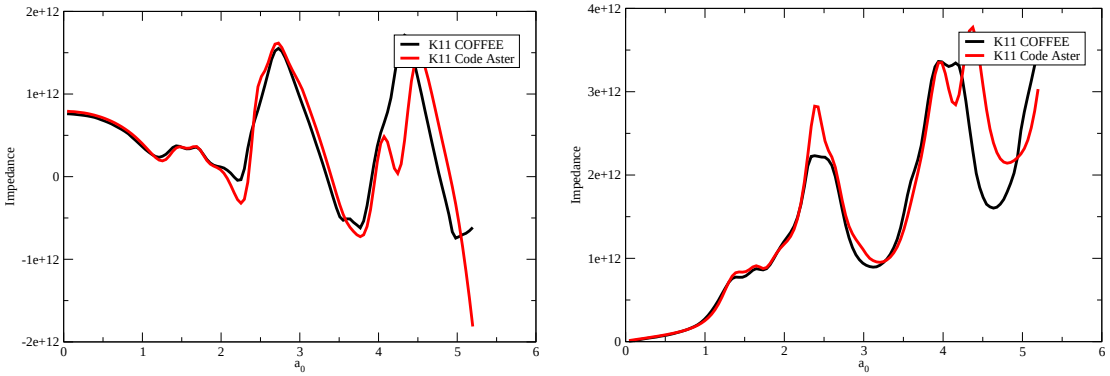


Real part Imaginary part

***Figure 1.13:*** *Embedded cylindrical footing on a hemispherical basin. Computation of the impedance ($K_{11}$): comparison of the FM-BEM and the FEM-BEM coupling solutions.*

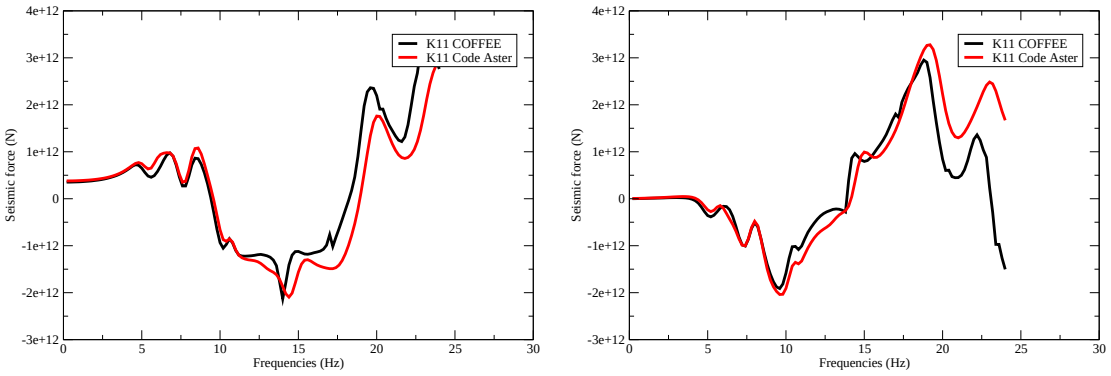


Real part Imaginary part

***Figure 1.14:*** *Validation of the computation of the seismic force for the coupling of SV-wave with the horizontal mode $f_{11}$: comparison of the FM-BEM and FEM-BEM coupling solutions.*

**Issues encountered to apply the method to a more challenging geometry.** This industrial collaboration with EDF aimed at exploiting the capabilities of the FM-BEM to assess the consequences of site effects on soil-structure interactions. Once the coupling strategy validated on simplified configurations, we have considered the case of a realistic site: the sedimentary basin around the city of Grenoble. The Grenoble valley has the advantage to present the three kinds of site effects (see Fig. 1.15): topographical effects due to the complex topography, lithologic effects due to the different layers in the basin, and geometric effects due to the Y shape of the basin. It is therefore a good scenario to quantify the influence of site effects on the response of a building. The Grenoble valley has already been considered with FM-BEM [10]. The main differences is that the topography was not taken into account (as the free surface was considered horizontal), the sedimentary basin was homogeneous (while it is layered here) and the analysis was performed for two frequencies of 0.3 Hz and 0.6 Hz. In this work, the ambition is to better take into account the topography and the layers inside the sedimentary basin, as well as to treat higher frequencies.

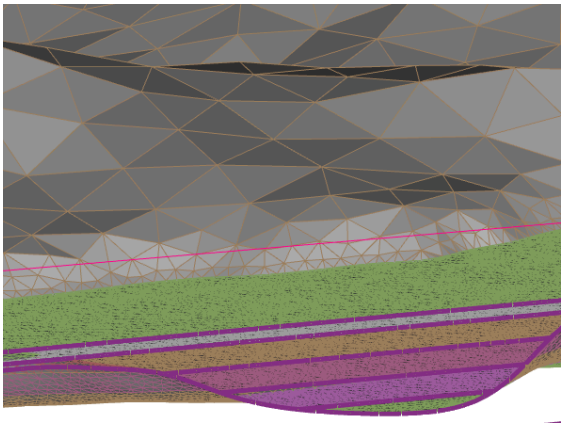

***(a)*** *Layers in Grenoble basin*

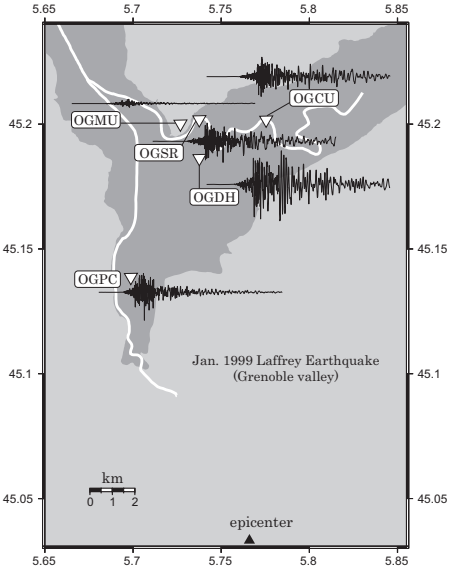


***(b)*** *Shape of the Grenoble basin from [Semblat 2009]*

***Figure 1.15:*** *Grenoble basin: layers and shape of the basin.*

The mechanical parameters of the bedrock and sedimentary basin models are as proposed in [Chaljub 2010]. Since the use of a BEM imposes a piecewise homogeneous domain, the sedi-

mentary basin is nevertheless decomposed into five homogeneous layers. The BE mesh has been provided by Adrien Loseille from INRIA Saclay. Each homogeneous layer is meshed in order to have at least ten points per S-wavelength at the frequency of 1 Hz. The model thus consists of 890 000 DOFs. Two cases have been considered: the response of the alluvial basin without any structure to quantify the site effects and then, the response of the basin with a structure.

While, the treatment of large simplified soil-structure interaction problems has been easy performed, the treatment of this realistic configuration has shown two main issues.

- The first difficulty is due to the use of conforming meshes on domains with large velocity contrasts. The mesh conformity requirement at interfaces implies a density of about ten points per S-wavelength on interfaces. Since two domains with different velocities share the same interface, the mesh density is defined by the smallest S-wavelength. As a result, the interface between two layers is adapted to one domain but is too dense for the other domain. This situation is sub-optimal for the FM-BEM [10]. It is known that the efficiency of the method is subjected to the use of a uniform mesh with a moderate (about 10) density of points per wavelength. The system is artificially a "too" large matrix for the near contributions. The consequence is that the memory requirements and computational times are too large to consider this problem even if a fast BEM is used. We give in the following some ideas to avoid this problem and be able to consider such large-scale problems with high velocity contrasts.
- The second difficulty is again due to the use of an iterative solver (similarly to the observations in Section 1.3). Hence, one specificity of the FM-BEM is the intrinsic iterative nature of the method. Even though the computational time per iteration is optimal, the number of iterations becomes the limiting factor. In practice, we have observed that some frequencies have required more than 5 000 iterations to converge for realistic configurations. We will see in the following that the preconditioning of the FM-BEM is a crucial issue.

## 1.5 My contributions on the improvement of fast BEMs to deal with realistic configurations

At this stage we understand that the FM-BEM is only partially answering the issues raised in the introduction. The FM-BEM is a fast method but it is facing some important limitations to be used for realistic problems. My research since 2011 has been devoted to the improvement of fast BEM solvers in several ways. Each Chapter of this document is devoted to one of these important aspects.

**Chapter 2:** Improving acoustic and visco-elastodynamic FM-BEMs for specific configurations.

The size of the BEM matrix is related to the choice of the Green's tensors used in the Boundary Integral Equation. These tensors take into account the geometry of the domain (infinite space, half-space, ...) and the mechanical properties (homogeneous or layered domains, ...). In some configurations, they are known analytically or semi-analytically [Kausel 2006]. Initially, the FM-BEM was developed for the Green's tensors of an infinite elastic space. But the use of the elastodynamic half-space Green's tensor is a very promising avenue for enhancing the computational performances of BEMs to study soil-structure interaction or seismology oriented problems. Thus, the BIE formulated with the half-space Green's tensors directly takes into account the free surface condition (zero traction on the surface). And it is no longer necessary to discretize the complete free surface (Fig 1.16a) but only the irregularities (Fig 1.16b). In [7, 8], we have proposed with Marc Bonnet (POEMS) a formulation and an algorithm for the evaluation of the elastodynamic Green's tensor for the configuration of the traction-free half-space, allowing its use within a FM-BEM.

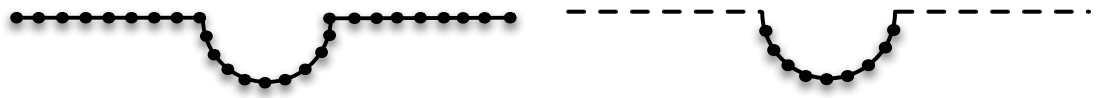

*(a) Mesh: Full-space Green's tensors* *(b) Mesh: Half-space Green's tensors*

***Figure 1.16:*** *Required meshes if the full-space or half-space Green's tensors are used.*

The definition of a FM-BEM for problems in an elastic half-space is not the only improvement I have considered. Thus decomposition (1.12), often called the diagonal form decomposition of the full-space fundamental solution, is known to fail in the low-frequency limit [Darve 2000a]. Other decompositions that are well-behaved at low frequencies are available, based on either the Gegenbauer addition theorem [Zhao 1999] or Fourier transforms along coordinate planes [Greengard 1998, Darve 2004b]. So-called wideband FMMs have then be proposed, combining kernel expansions appropriate for low frequencies with the diagonal-form decomposition for higher frequencies [Cheng 2006]. The main drawback of these wideband FMMs is the involved numerical implementation that they require. With Francis Collino (external collaborator at POEMS), we have proposed in [6] a new wideband FMM that is stable at all frequencies and easier to implement than previous formulations.

**Chapter 3:** Reduction of the number of iterations in the FM-BEM with efficient preconditioners.

The FMM accelerates the iterative solution of the BEM system by evaluating in a fast and approximate way the matrix-vector product necessary at each iteration. The number of operations per iteration is thus reduced to $\mathcal{O}(N \log N)$. However, the number of iterations in GMRES can significantly hinder the overall efficiency of the FM-BEM. A crucial step in accelerating an iterative solver is thus to define an efficient preconditioner, i.e. a matrix that permits to modify the spectral properties of the initial system.

The proposition of an appropriate preconditioner is today the key point to increase the capabilities of fast BEMs for wave propagation problems. However, it is a delicate task in the framework of the FMM since the system matrix is never explicitly formed. With Marion Darbas (LAMFA, Université de Picardie) and Frédérique Le Louër (LMAC, Université de Technologie de Compiègne) we have proposed an analytic preconditioner to deal with scattering problems of time-harmonic elastic waves by 3-D rigid obstacles [3, 5].

**Chapter 4:** Study of the potentialities of fast BEMs based on hierarchical matrices for wave propagation problems.

Analytic preconditioners are very efficient for 3D elastic exterior Dirichlet problems with homogeneous properties. But these preconditioners are very intrusive in the code since they require to modify the BIE, and are problem-dependent. The extension of these analytic preconditioners to complex geological configurations with many layers or to anisotropic media is far from straightforward. FM-BEMs are however not the only possible fast BEMs, other accelerated BEMs based on hierarchical matrices ($\mathcal{H}$-matrices) have been proposed in the literature [Hackbusch 1999]. $\mathcal{H}$-matrices permit to approximate the fully-populated BEM system by a data-sparse matrix. To reduce storage requirements only the most significant and non redundant pieces of information are kept. Contrary to the FM-BEM, it is a purely algebraic tool which does not require an *a priori* knowledge of the closed-form expression of the fundamental tensors. In [2], we have studied (with Patrick Ciarlet and during the PhD of Luca Desiderio, POEMS) the capabilities of the $\mathcal{H}$-matrix based iterative and direct solvers for 3D elasticity.

**Chapter 5:** Anisotropic mesh adaptation for BEMs.

So far, most of the effort in the BEM community has been dedicated to the speed-up of the solution of the BIEs. Now that fast BEMs are well developed, it is necessary to propose tools to guarantee a given level of accuracy of the numerical results. With Samuel Groth, Faisal Amlani and in collaboration with Adrien Loseille (INRIA team Gamma3), we have introduced a metric-based anisotropic mesh adaptation strategy [Loseille 2010] for the FM-BEM for the three-dimensional

Helmholtz equation [1]. The methodology is independent of the discretization technique and iteratively constructs meshes refined in size, shape and orientation according to an optimal metric reliant on a reconstructed Hessian of the boundary solution. This strategy allows to recover the optimal convergence rate with respect to the number of DOFs.

# CHAPTER 2

# Improving acoustic and visco-elastodynamic FM-BEMs for specific configurations

## Contents



The FMM corresponds to a class of fast algorithms to perform a matrix-vector product involving a fundamental solution. We have made the choice to use kernel-dependent FMMs tailored for wave propagation problems. However, there are still needs for improvements to apply these methods to model the propagation of seismic waves in sedimentary basins.

This Chapter is devoted to two important aspects when considering seismic wave propagation. The first point is the reduction of the problem size (i.e. the number of DOFs on the domain boundary) by using a formulation based on the half-space fundamental solutions. For Helmholtz problems, these fundamental solutions and the corresponding FM-BEM are easily obtained by applying the method of images. But in 3D elastodynamics, the method of images is not sufficient to obtain a traction free condition on the free surface due to the vector nature of the problem. The derivation of these fundamental solutions and the proposition of the corresponding FM-BEM require more numerical developments presented in Section 2.1.

Another important limitation of the FM-BEM presented in Chapter 1 is that it is efficient only in the mid- to high-frequency regime. It is a major drawback if we want to consider a non-uniform mesh, e.g. coming from a mesh adaptation strategy (see Chapter 5) or a geometry with complex details. Section 2.2 presents an approach stable and efficient at all frequencies. This Chapter ends in Section 2.3 with some other challenging aspects of FM-BEM for wave propagation problems that need to be improved.

## 2.1 Fast Multipole Method for problems in an elastic half-space

(Visco)elastodynamic FM-BEMs presented in Chapter 1 are based on the full-space Green's tensor. However, many applications in e.g. civil engineering or geophysics involve semi-infinite media, and therefore entail a costly BE discretization of a portion of the free surface within a truncation distance that is sufficiently larger than the region of interest (see [Arias 2004] for the 2D case, where the Rayleigh-wave part of the solution is accounted for beyond the truncation distance). To avoid both this additional computational burden and accuracy control issues raised by the truncation, a natural idea is to use the Green's tensor $\boldsymbol{U}_{\rm HS}, \boldsymbol{T}_{\rm HS}$ satisfying the traction-free boundary condition

$$\boldsymbol{T}_{\rm HS}(\boldsymbol{x},\boldsymbol{y}) := \boldsymbol{e}_3 \cdot \boldsymbol{\mathcal{C}} \cdot \nabla_y \boldsymbol{U}_{\rm HS}(\boldsymbol{x},\boldsymbol{y}) = \boldsymbol{0} \quad (\boldsymbol{y} \in \Gamma_F), \tag{2.1}$$

on the planar infinite surface $\Gamma_F := \{\boldsymbol{y} \,|\, y_3 = 0\}$ bounding the half-space $\Omega_F := \{\boldsymbol{y} = (y_1, y_2, y_3) \,|\, y_3 < 0\}$ (in (2.1) and thereafter, the gradient operator $'\boldsymbol{\nabla}'$ conventionally adds one tensorial order from the left, i.e. (for example) $(\boldsymbol{\nabla}\boldsymbol{U})_{kij} = \partial_k U_{ij}$). This choice of Green's tensor is well suited to semi-infinite configurations that feature wave scattering by topographic irregularities or buried objects, modelled as semi-infinite domains $\Omega$ which deviate from the half-space $\Omega_F$ only in a region of finite size. Here, the boundary $\partial\Omega$ is assumed of the form $\partial\Omega = S \cup \Gamma_0$, where the bounded (and possibly non-connected) surface $S := \partial\Omega \setminus (\partial\Omega \cap \Gamma_F)$ defines topographic irregularities or buried obstacles and $\Gamma_0 \subset \Gamma_F$ is the unbounded planar component of the traction-free surface (Fig. 2.1). In this setting, the integral equation (1.8) takes the form (with collocation now needed on $S$ only)

$$\boldsymbol{\mathcal{K}}_{\rm HS}[\boldsymbol{u}](\boldsymbol{x}) = \boldsymbol{\mathcal{S}}_{\rm HS}[\boldsymbol{t}^{\rm D}](\boldsymbol{x}) \quad (\boldsymbol{x} \in S) \qquad \text{with } \boldsymbol{\mathcal{K}}_{\rm HS}[\boldsymbol{u}](\boldsymbol{x}) := \boldsymbol{\mathcal{D}}_{\rm HS}[\boldsymbol{u}](\boldsymbol{x}) + \boldsymbol{c}(\boldsymbol{x}) \cdot \boldsymbol{u}(\boldsymbol{x}), \tag{2.2}$$

where the single-layer and double-layer integral operators $\boldsymbol{\mathcal{S}}_{\rm HS}$ and $\boldsymbol{\mathcal{D}}_{\rm HS}$ defined by

$$\begin{aligned} \boldsymbol{\mathcal{S}}_{\rm HS}[\boldsymbol{t}](\boldsymbol{x}) &:= \int_S \boldsymbol{t}(\boldsymbol{y}) \cdot \boldsymbol{U}_{\rm HS}(\boldsymbol{x},\boldsymbol{y}) \, {\rm d}S_y, \\ \boldsymbol{\mathcal{D}}_{\rm HS}[\boldsymbol{u}](\boldsymbol{x}) &:= ({\rm P.V.}) \int_S \boldsymbol{u}(\boldsymbol{y}) \cdot \boldsymbol{T}_{\rm HS}(\boldsymbol{x},\boldsymbol{y}) \, {\rm d}S_y, \end{aligned} \qquad (\boldsymbol{x} \in S). \tag{2.3}$$

The overall size of the BE model is therefore much smaller than using the full-space Green's tensor (1.6) since the planar part $\Gamma_0$ of the free surface is no longer discretized. The derivation and implementation of $\boldsymbol{U}_{\rm HS}, \boldsymbol{T}_{\rm HS}$ are however involved [Pan 1998]. In particular, $\boldsymbol{U}_{\rm HS}$ and $\boldsymbol{T}_{\rm HS}$ cannot be expressed in the fashion of (1.6) in terms of simpler kernels having already-known plane-wave expansions, and a specific approach is needed.

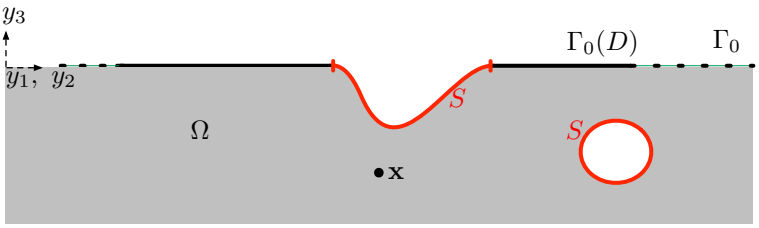


***Figure 2.1:*** *Elastic semi-infinite medium: geometry and notations.*

### 2.1.1 Plane wave expansions of the half-space Green's tensor

**Complementary displacement Green's tensor.** The formulation of a plane wave expansion for $\boldsymbol{U}_{\rm HS}$ has been addressed in [7, 8] (in collaboration with Marc Bonnet, POEMS). It exploits the additive decomposition

$$\boldsymbol{U}_{\rm HS}(\boldsymbol{x},\boldsymbol{y}) = \boldsymbol{U}(\boldsymbol{x},\boldsymbol{y}) + \widetilde{\boldsymbol{U}}(\boldsymbol{x},\boldsymbol{y}) + \boldsymbol{U}_{\rm C}(\boldsymbol{x},\boldsymbol{y}), \tag{2.4}$$

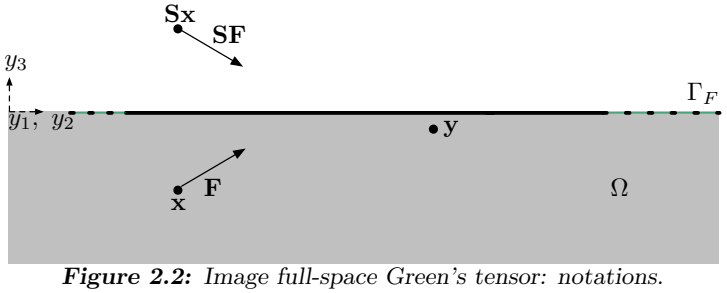


***Figure 2.2:*** *Image full-space Green's tensor: notations.*

where $\boldsymbol{U}$ is the full-space Green's tensor (1.6) and $\widetilde{\boldsymbol{U}}$ is the image full-space Green's tensor corresponding to an image point force $\boldsymbol{S}\cdot\boldsymbol{F}$ applied at the mirror image source point $\boldsymbol{S}\cdot\boldsymbol{x}$ (Fig. 2.2), i.e.

$$\widetilde{\boldsymbol{U}}(\boldsymbol{x},\boldsymbol{y}) := \boldsymbol{U}(\boldsymbol{S}\cdot\boldsymbol{x},\boldsymbol{y})\cdot\boldsymbol{S}, \tag{2.5}$$

with $\boldsymbol{S} := \boldsymbol{I} - 2\boldsymbol{e}_3\otimes\boldsymbol{e}_3$ denoting the symmetry with respect to the free surface $y_3 = 0$. The complementary Green's tensor $\boldsymbol{U}_{\mathrm{C}}$ must then satisfy the homogeneous field equation and be such that $\boldsymbol{U}_{\mathrm{HS}}$ given by (2.4) satisfies the free-surface condition (2.1). A separated representation of $\boldsymbol{U}_{\mathrm{C}}$ was found [7] in the form of an inverse partial Fourier transform:

$$\boldsymbol{U}_{\mathrm{C}}(\boldsymbol{x},\boldsymbol{y}) = \int_{\mathbb{R}^2} e^{\mathrm{i}(\xi_1 y_1+\xi_2 y_2)}\,\hat{\boldsymbol{U}}_{\mathrm{C}}(\boldsymbol{\xi},y_3;\boldsymbol{x})\,\mathrm{d}\xi_1\mathrm{d}\xi_2, \tag{2.6}$$

where $\boldsymbol{\xi} := (\xi_1,\xi_2)\in\mathbb{R}^2$ are the transformed coordinates associated with $(y_1,y_2)$ and with

$$\hat{\boldsymbol{U}}_{\mathrm{C}}(\boldsymbol{\xi},y_3;\boldsymbol{x}) = \frac{1}{4\pi^2\mu\kappa_{\mathrm{S}}^2}\frac{s_{\mathrm{P}}(\xi)}{\delta(\xi)}\big[2\boldsymbol{V}_{\mathrm{S}}^{+}(\boldsymbol{\xi})e^{s_{\mathrm{S}}(\xi)y_3}+\beta(\xi)\boldsymbol{V}_{\mathrm{P}}^{+}(\boldsymbol{\xi})e^{s_{\mathrm{P}}(\xi)y_3}\big] \otimes\big[2\boldsymbol{V}_{\mathrm{S}}^{-}(\boldsymbol{\xi})\,e^{\boldsymbol{q}_{\mathrm{S}}^{-}(\boldsymbol{\xi})\cdot\boldsymbol{x}}+\beta(\xi)\boldsymbol{V}_{\mathrm{P}}^{-}(\boldsymbol{\xi})\,e^{\boldsymbol{q}_{\mathrm{P}}^{-}(\boldsymbol{\xi})\cdot\boldsymbol{x}}\big]. \tag{2.7}$$

In addition, the various scalar or vector functions appearing in (2.7) are defined by

$$\begin{aligned}
\boldsymbol{q}_a^{\pm}(\boldsymbol{\xi}) &= \pm\mathrm{i}\boldsymbol{\xi}+s_a(\xi)\boldsymbol{e}_3, & s_a(\xi) &= \sqrt{\xi^2-\kappa_a^2} & (a=\mathrm{P,S}),\\
\beta(\xi) &= \kappa_{\mathrm{S}}^2-2\xi^2 = -(s_{\mathrm{S}}^2(\xi)+\xi^2), & \delta(\xi) &= \beta^2(\xi)-4\xi^2 s_{\mathrm{P}}(\xi)s_{\mathrm{S}}(\xi),\\
\boldsymbol{V}_{\mathrm{S}}^{\pm}(\boldsymbol{\xi}) &= \pm\big[\,s_{\mathrm{S}}(\xi)\,\boldsymbol{q}_{\mathrm{S}}^{\pm}(\boldsymbol{\xi})+\kappa_{\mathrm{S}}^2\boldsymbol{e}_3\,\big], & \boldsymbol{V}_{\mathrm{P}}^{\pm}(\boldsymbol{\xi}) &= \pm s_{\mathrm{P}}^{-1}(\xi)\boldsymbol{q}_{\mathrm{P}}^{\pm}(\boldsymbol{\xi})
\end{aligned}$$

with $\xi := |\boldsymbol{\xi}| = (\xi_1^2+\xi_2^2)^{1/2}$. Upon inserting (2.7) into (2.6), introducing polar coordinates in the Fourier space (i.e. setting $\boldsymbol{\xi} = (\xi_1,\xi_2) = \xi(\cos\alpha,\sin\alpha)$) and rearranging terms, the above formula can be recast in the following form:

$$\boldsymbol{U}_{\mathrm{C}}(\boldsymbol{x},\boldsymbol{y}) = \frac{1}{4\pi^2\kappa_{\mathrm{S}}^2\mu}\sum_{a,b=\mathrm{P,S}}\int_0^{+\infty}\xi s_{\mathrm{P}}(\xi)A_{ab}(\xi)\bigg\{\int_0^{2\pi}\big[\,\exp(\boldsymbol{q}_a^{+}(\xi,\alpha)\cdot\boldsymbol{y})\,\boldsymbol{V}_a^{+}(\xi,\alpha)\,\big] \otimes\big[\,\exp(\boldsymbol{q}_b^{-}(\xi,\alpha)\cdot\boldsymbol{x})\,\boldsymbol{V}_b^{-}(\xi,\alpha)\,\big]\,\mathrm{d}\alpha\bigg\}\,\mathrm{d}\xi \tag{2.8}$$

with

$$A_{\mathrm{PP}}(\xi) := \frac{\beta^2(\xi)}{\delta(\xi)},\quad A_{\mathrm{PS}}(\xi) = A_{\mathrm{SP}}(\xi) := \frac{2\beta(\xi)}{\delta(\xi)},\quad A_{\mathrm{SS}}(\xi) := \frac{4}{\delta(\xi)}.$$

Decomposition (2.8) is separated, and has a structure reminiscent of the diagonal form (1.12).

**Complementary traction Green's tensor.** Most integral equations for semi-infinite media, such as (2.2), also require the complementary traction Green's tensor $\boldsymbol{T}_{\mathrm{C}}$, which is addressed in [8]. To this aim, the complementary stress Green's tensor $\boldsymbol{\Sigma}_{\mathrm{C}} := \boldsymbol{\mathcal{C}}:\boldsymbol{\nabla}_y\boldsymbol{U}_{\mathrm{C}}$ is first derived by invoking Hooke's law (1.2) and noting that

$$\widehat{\nabla\boldsymbol{U}}_{\mathrm{C}}(\boldsymbol{\xi},y_3;\boldsymbol{x}) = \mathrm{i}\boldsymbol{\xi}\otimes\hat{\boldsymbol{U}}_{\mathrm{C}}(\boldsymbol{\xi},y_3;\boldsymbol{x})+\boldsymbol{e}_3\otimes\hat{\boldsymbol{U}}'_{\mathrm{C}}(\boldsymbol{\xi},y_3;\boldsymbol{x}) \tag{2.9}$$

(with the prime ($'$) symbol denoting partial derivatives with respect to $y_3$) as a consequence of the partial Fourier representation (2.6) of $\boldsymbol{U}_{\mathrm{C}}$, to obtain

$$\hat{\boldsymbol{\Sigma}}_{\mathrm{C}}(\boldsymbol{\xi},y_3;\boldsymbol{x}) = \mu(\gamma^{-2}-2)\boldsymbol{I}\otimes\big[\mathrm{i}\boldsymbol{\xi}\cdot\hat{\boldsymbol{U}}(\boldsymbol{\xi},y_3;\boldsymbol{x}) + \boldsymbol{e}_3\cdot\hat{\boldsymbol{U}}'_{\mathrm{C}}(\boldsymbol{\xi},y_3;\boldsymbol{x})\big] + 2\mu\widehat{\nabla\boldsymbol{U}}^{\mathrm{sym}}_{\mathrm{C}}(\boldsymbol{\xi},y_3;\boldsymbol{x})$$

(with $\gamma^2 = \frac{1-2\nu}{2(1-\nu)}$, and where "sym" indicates symmetrization with respect to the first two indices, noting that $\widehat{\nabla\boldsymbol{U}}$ is a third-order tensor). Substituting expression (2.7) into the above formula, performing straightforward derivations and rearranging terms, one arrives at the explicit formula

$$\begin{aligned}\hat{\boldsymbol{\Sigma}}_{\mathrm{C}}(\boldsymbol{\xi},y_3;\boldsymbol{x}) = \frac{1}{4\pi^2\kappa_{\mathrm{S}}^2\delta(\xi)}\Big(&\beta(\xi)e^{s_{\mathrm{P}}(\xi)y_3}\big[2\boldsymbol{q}^+_{\mathrm{P}}(\boldsymbol{\xi})\otimes\boldsymbol{q}^+_{\mathrm{P}}(\boldsymbol{\xi}) + (2\gamma^2-1)\kappa_{\mathrm{S}}^2\boldsymbol{I}\big]\\ &+ 2s_{\mathrm{P}}(\xi)e^{s_{\mathrm{S}}(\xi)y_3}\big[2s_{\mathrm{S}}(\xi)\,\boldsymbol{q}^+_{\mathrm{S}}(\boldsymbol{\xi})\otimes\boldsymbol{q}^+_{\mathrm{S}}(\boldsymbol{\xi}) + \kappa_{\mathrm{S}}^2\big(\boldsymbol{e}_3\otimes\boldsymbol{q}^+_{\mathrm{S}}(\boldsymbol{\xi}) + \boldsymbol{q}^+_{\mathrm{S}}(\boldsymbol{\xi})\otimes\boldsymbol{e}_3\big)\,\big]\Big)\\ &\otimes\Big(2\boldsymbol{V}^-_{\mathrm{S}}(\boldsymbol{\xi})\,e^{\boldsymbol{q}^-_{\mathrm{S}}(\boldsymbol{\xi})\cdot\boldsymbol{x}} + \beta(\xi)\boldsymbol{V}^-_{\mathrm{P}}(\boldsymbol{\xi})\,e^{\boldsymbol{q}^-_{\mathrm{P}}(\boldsymbol{\xi})\cdot\boldsymbol{x}}\Big)\end{aligned} \tag{2.10}$$

Finally, the traction Green's tensor $\boldsymbol{T}_{\mathrm{C}} := \boldsymbol{n}\cdot\boldsymbol{\Sigma}_{\mathrm{C}}$ for a given unit normal $\boldsymbol{n}$ is obtained in Fourier form as

$$\begin{aligned}\hat{\boldsymbol{T}}_{\mathrm{C}}(\boldsymbol{\xi},y_3;\boldsymbol{x}) = \frac{1}{4\pi^2\kappa_{\mathrm{S}}^2\delta(\xi)}&\Big(2\boldsymbol{W}_{\mathrm{S}}(\boldsymbol{\xi})e^{s_{\mathrm{S}}(\xi)y_3} + \beta(\xi)\boldsymbol{W}_{\mathrm{P}}(\boldsymbol{\xi})e^{s_{\mathrm{P}}(\xi)y_3}\Big)\\ &\otimes\Big(2\boldsymbol{V}^-_{\mathrm{S}}(\boldsymbol{\xi})\,e^{\boldsymbol{q}^-_{\mathrm{S}}(\boldsymbol{\xi})\cdot\boldsymbol{x}} + \beta(\xi)\boldsymbol{V}^-_{\mathrm{P}}(\boldsymbol{\xi})\,e^{\boldsymbol{q}^-_{\mathrm{P}}(\boldsymbol{\xi})\cdot\boldsymbol{x}}\Big)\end{aligned} \tag{2.11}$$

with the vector functions $\boldsymbol{W}_{\mathrm{S}}$ and $\boldsymbol{W}_{\mathrm{P}}$ given by

$$\begin{aligned}\boldsymbol{W}_{\mathrm{S}}(\boldsymbol{\xi}) &:= s_{\mathrm{P}}(\xi)\big(\boldsymbol{q}^+_{\mathrm{S}}(\boldsymbol{\xi})\cdot\boldsymbol{n}\big)\big[2s_{\mathrm{S}}(\xi)\boldsymbol{q}^+_{\mathrm{S}}(\boldsymbol{\xi}) + \kappa_{\mathrm{S}}^2\boldsymbol{e}_3\big] + \kappa_{\mathrm{S}}^2 s_{\mathrm{P}}(\xi)(\boldsymbol{n}\cdot\boldsymbol{e}_3)\boldsymbol{q}^+_{\mathrm{S}}(\boldsymbol{\xi}),\\ \boldsymbol{W}_{\mathrm{P}}(\boldsymbol{\xi}) &:= 2\big(\boldsymbol{q}^+_{\mathrm{S}}(\boldsymbol{\xi})\cdot\boldsymbol{n}\big)\boldsymbol{q}^+_{\mathrm{S}}(\boldsymbol{\xi}) + (2\gamma^2-1)\kappa_{\mathrm{S}}^2\boldsymbol{n}.\end{aligned}$$

One notes the formal analogy between the partial Fourier expressions (2.7) of $\hat{\boldsymbol{U}}_{\mathrm{C}}$ and (2.11) of $\hat{\boldsymbol{T}}_{\mathrm{C}}$, the only difference lying in $\boldsymbol{V}^+_{\mathrm{S}}, \boldsymbol{V}^+_{\mathrm{P}}$ being replaced by $\boldsymbol{W}_{\mathrm{S}}, \boldsymbol{W}_{\mathrm{P}}$. Now, expressing $\boldsymbol{T}_{\mathrm{C}}$ in terms of physical coordinates as the inverse partial Fourier transform (2.6) with $\hat{\boldsymbol{U}}_{\mathrm{C}}$ replaced by $\hat{\boldsymbol{T}}_{\mathrm{C}}$ and using polar coordinates in the Fourier space, one finally obtains

$$\begin{aligned}\boldsymbol{T}_{\mathrm{C}}(\boldsymbol{x},\boldsymbol{y}) = \frac{1}{4\pi^2\kappa_{\mathrm{S}}^2}\sum_{a,b=\mathrm{P,S}}\int_0^{+\infty}\xi A_{ab}(\xi)\Big\{\int_0^{2\pi}&\big[\,\exp(\boldsymbol{q}^+_a(\xi,\alpha)\cdot\boldsymbol{y})\,\boldsymbol{W}_a(\xi,\alpha)\,\big]\\ &\otimes\big[\,\exp(\boldsymbol{q}^-_b(\xi,\alpha)\cdot\boldsymbol{x})\,\boldsymbol{V}^-_b(\xi,\alpha)\,\big]\,\mathrm{d}\alpha\Big\}\,\mathrm{d}\xi\end{aligned} \tag{2.12}$$

with the $A_{ab}(\xi)$ again as defined for (2.8).

### 2.1.2 Fast multipole algorithm for the half-space Green's tensor

The single-layer and double-layer operators $\boldsymbol{\mathcal{S}}[\boldsymbol{t}]$, $\boldsymbol{\mathcal{D}}[\boldsymbol{u}]$ applied to given densities $\boldsymbol{t}$, $\boldsymbol{u}$ can then be, following (2.4) and using obvious notation, additively decomposed as

$$\boldsymbol{\mathcal{S}}_{\mathrm{HS}}[\boldsymbol{t}](\boldsymbol{x}) = \boldsymbol{\mathcal{S}}[\boldsymbol{t}](\boldsymbol{x}) + \widetilde{\boldsymbol{\mathcal{S}}}[\boldsymbol{t}](\boldsymbol{x}) + \boldsymbol{\mathcal{S}}_{\mathrm{C}}[\boldsymbol{t}](\boldsymbol{x}), \tag{2.13}$$

$$\boldsymbol{\mathcal{D}}_{\mathrm{HS}}[\boldsymbol{t}](\boldsymbol{x}) = \boldsymbol{\mathcal{D}}[\boldsymbol{t}](\boldsymbol{x}) + \widetilde{\boldsymbol{\mathcal{D}}}[\boldsymbol{t}](\boldsymbol{x}) + \boldsymbol{\mathcal{D}}_{\mathrm{C}}[\boldsymbol{t}](\boldsymbol{x}). \tag{2.14}$$

The contributions $\boldsymbol{\mathcal{S}}[\boldsymbol{t}](\boldsymbol{x})$, $\widetilde{\boldsymbol{\mathcal{S}}}[\boldsymbol{t}](\boldsymbol{x})$ and $\boldsymbol{\mathcal{D}}[\boldsymbol{u}](\boldsymbol{x})$, $\widetilde{\boldsymbol{\mathcal{D}}}[\boldsymbol{u}](\boldsymbol{x})$ are then evaluated using the standard diagonal-form FMM presented in Chapter 1, whereas the complementary operators $\boldsymbol{\mathcal{S}}_{\mathrm{C}}$, $\boldsymbol{\mathcal{D}}_{\mathrm{C}}$ requires a specific treatment. The case of $\boldsymbol{\mathcal{S}}_{\mathrm{C}}$ is treated in detail in [7], and the case of $\boldsymbol{\mathcal{D}}_{\mathrm{C}}[\boldsymbol{t}](\boldsymbol{x})$ in [8] and is recalled in the following.

Substituting the representation (2.12) of $\boldsymbol{T}_{\mathrm{C}}$ into the definition of $\boldsymbol{\mathcal{D}}_{\mathrm{C}}[\boldsymbol{t}](\boldsymbol{x})$ and rearranging terms, the complementary double-layer operator is given by

$$\boldsymbol{\mathcal{D}}_{\mathrm{C}}[\boldsymbol{t}](\boldsymbol{x}) = \frac{1}{4\pi^2\kappa_{\mathrm{S}}^2}\sum_{a,b=\mathrm{P,S}}\int_0^{+\infty}\xi A_{ab}(\xi)\Big\{\int_0^{2\pi}\mathcal{R}^u_a(\xi,\alpha)\big[\,\exp(\boldsymbol{q}^-_b(\xi,\alpha)\cdot\boldsymbol{x})\,\boldsymbol{V}^-_b(\xi,\alpha)\,\big]\,\mathrm{d}\alpha\Big\}\,\mathrm{d}\xi \tag{2.15}$$

where the multipole moments are given by

$$\mathcal{R}^t_a(\xi,\alpha) := \Big\{\int_S \exp(\boldsymbol{q}^+_a(\xi,\alpha)\cdot\boldsymbol{y})\,\boldsymbol{t}(\boldsymbol{y})\,\mathrm{d}S_y\Big\}\cdot\boldsymbol{W}_a(\xi,\alpha). \tag{2.16}$$

**Convergence of radial integral.** The radial integral in (2.15) is convergent whenever $x_3+y_3 < 0$ due to the exponential decay of the integrand as $\xi \to +\infty$. On the other hand, noting that $\boldsymbol{W}_{\mathrm{S}} = O(\xi^4)$, $\boldsymbol{W}_{\mathrm{P}} = O(\xi^2)$, $\boldsymbol{V}_{\mathrm{S}}^- = O(\xi^2)$, $\boldsymbol{V}_{\mathrm{P}}^- = O(1)$, $\beta(\xi) = O(\xi^2)$ and $\delta(\xi) = O(\xi^2)$ (the latter estimate requiring straightforward derivations) for large $\xi$, the integrand of (2.15) is thus $O(\xi^5)$ if $x_3 + y_3 = 0$, making the radial integral divergent. The proposed acceleration approach is thus subject to the restriction $x_3 + y_3 < 0$, and is not applicable when $x_3 + y_3 = 0$ (i.e. for integration and collocation points both lying on $\Gamma_F$).

**Clustering.** If convergent (i.e. whenever $x_3 + y_3 < 0$), integral (2.15) can be evaluated accurately. In particular, unlike for more usual forms of the FMM, the representation (2.15) of $\boldsymbol{T}_{\mathrm{C}}$ is valid without requiring that clusters of source and collocation points be well-separated, making it unnecessary to subdivide the spatial region of interest into cells. The simplest option of applying (2.15) to all source and collocation points at once (i.e. of enclosing all points in one single cell) is permitted, and is used here.

**Quadrature in Fourier space.** The radial integration featured in (2.15) requires a quadrature rule that is suitable for a limited set of $L$ integrals of the form

$$I_\ell(\boldsymbol{p}) = \int_0^{\xi\max} f_\ell(\xi;\boldsymbol{p})\,\mathrm{d}\xi \qquad (1 \le \ell \le L,\ \boldsymbol{p} \in \mathcal{P})$$

where $(f_\ell)_{1\le\ell\le L}$ are real-valued square-integrable functions, whose (singular, oscillatory...) behavior may make numerical quadrature difficult (or *a priori* expensive). The $f_\ell$ are chosen so that all integrands appearing in (2.15) are linear combinations of them, while the parameters gathered in $\boldsymbol{p}$ are the frequency $\omega$ and the source and observation points $\boldsymbol{x}, \boldsymbol{y}$. The quadrature rule then must accurately evaluate all integrals $I_\ell(\boldsymbol{p})$ for all values of $\boldsymbol{p}$ in a given parameter domain $\mathcal{P}$, whose definition reflects the clusters of source and observation points used in $\boldsymbol{T}_{\mathrm{C}}(\boldsymbol{x},\boldsymbol{y})$ and the frequencies of interest. To this aim, generalized Gaussian quadrature (GGQ) rules that are specific to the set of integrals $I_\ell(\boldsymbol{p})$ are computed by means of the GGQ generation methodology proposed in [Bremer 2010]. Its implementation for $\boldsymbol{U}_{\mathrm{C}}$ is described in detail in [7]; and for (2.15) in [8] by appropriately choosing the choice of input functions $f_\ell$.

As an example, the Fourier integral (2.15) is evaluated by means of a product quadrature rule in $(\xi,\alpha)$-space of the form

$$\boldsymbol{\mathcal{D}}_{\mathrm{C}}[\boldsymbol{u}](\boldsymbol{x}) = \frac{1}{4\pi^2\kappa_{\mathrm{S}}^2} \sum_{a,b=\mathrm{P,S}} \sum_{i=1}^{n_\xi} w_i^\xi \xi_i A_{ab}(\xi_i) \left\{ \sum_{j=1}^{n_\alpha} w_j^\alpha \mathcal{R}_a^u(\xi_i,\alpha_j) \big[\, \exp(\boldsymbol{q}_b^-(\xi_i,\alpha_j)\cdot\boldsymbol{x})\, \boldsymbol{V}_b^-(\xi_i,\alpha_j) \,\big] \right\} + E(n_\xi, n_\alpha) \quad (2.17)$$

where $(\xi_i, w_i^\xi)_{1\le i\le n_\xi}$ are the $n_\xi$ GGQ nodes and weights for the radial integration, obtained by the procedure outlined above, $(\alpha_j, w_j^\alpha)_{1\le j\le n_\alpha}$ are the $n_\alpha$ nodes and weights corresponding to a simple trapezoidal rule for the angular quadrature, and $E(n_\xi, n_\alpha)$ is the quadrature error. Finally, the simultaneous evaluation of both complementary operators $\boldsymbol{\mathcal{S}}_{\mathrm{C}}[\boldsymbol{t}]$ and $\boldsymbol{\mathcal{D}}_{\mathrm{C}}[\boldsymbol{u}]$ is decomposed into two steps: (i) computation of multipole moments $(a, b = \mathrm{P,S})$

$$\mathcal{R}_a^t(\xi_i,\alpha_j) := \frac{1}{4\pi^2\kappa_{\mathrm{S}}^2\mu} \left\{ \int_S \exp(\boldsymbol{q}_a^+(\xi_i,\alpha_j)\cdot\boldsymbol{y})\, \boldsymbol{t}(\boldsymbol{y})\,\mathrm{d}S_{\boldsymbol{y}} \right\} \cdot \boldsymbol{V}_a^+(\xi_i,\alpha_j),$$
$$\mathcal{R}_a^u(\xi_i,\alpha_j) := \frac{1}{4\pi^2\kappa_{\mathrm{S}}^2} \left\{ \int_S \exp(\boldsymbol{q}_a^+(\xi_i,\alpha_j)\cdot\boldsymbol{y})\, \boldsymbol{u}(\boldsymbol{y})\,\mathrm{d}S_{\boldsymbol{y}} \right\} \cdot \boldsymbol{W}_a(\xi_i,\alpha_j),$$

and (ii) operator evaluation at collocation points (quadrature in Fourier space)

$$\boldsymbol{\mathcal{S}}_{\mathrm{C}}[\boldsymbol{t}](\boldsymbol{x}) = \sum_{a,b=\mathrm{P,S}} \sum_{i=1}^{n_\xi^t} w_i^t \xi_i^t A_{ab}(\xi_i^t) \Big\{ \sum_{j=1}^{n_\alpha} w_j^\alpha \mathcal{R}_a^t(\xi_i^t,\alpha_j) \big[ \exp(\boldsymbol{q}_b^-(\xi_i^t,\alpha_j)\cdot\boldsymbol{x})\, \boldsymbol{V}_b^-(\xi_i^t,\alpha_j) \big] \Big\},$$

$$\boldsymbol{\mathcal{D}}_{\mathrm{C}}[\boldsymbol{u}](\boldsymbol{x}) = \sum_{a,b=\mathrm{P,S}} \sum_{i=1}^{n_\xi^u} w_i^u \xi_i^u B_{ab}(\xi_i^u) \Big\{ \sum_{j=1}^{n_\alpha} w_j^\alpha \mathcal{R}_a^u(\xi_i^u,\alpha_j) \big[ \exp(\boldsymbol{q}_b^-(\xi_i^u,\alpha_j)\cdot\boldsymbol{x})\, \boldsymbol{V}_b^-(\xi_i^u,\alpha_j) \big] \Big\}.$$

Note that to minimize the overall quadrature work, separate GGQ rules $(\xi_i^t, w_i^t)_{1\le i\le n_\xi^t}$ and $(\xi_i^u, w_i^u)_{1\le i\le n_\xi^u}$ are generated and used for $\boldsymbol{\mathcal{S}}_{\mathrm{C}}[\boldsymbol{t}]$ and $\boldsymbol{\mathcal{D}}_{\mathrm{C}}[\boldsymbol{u}]$.

**Extension to visco-elastodynamics.** The extension of the FM-BEM for the elastic half-space Green's tensors to visco-elastodynamics is again done by introducing complex wavenumbers $\kappa_\alpha^\star = \kappa_\alpha(1+\mathrm{i}\zeta_\alpha)$ ($\alpha = \mathrm{P,S}$), where $0 \le \zeta_\alpha \ll 1$ are the damping ratios. This modification does not affect the above methodology and results in any essential way. The only significant change caused by the switch to complex-valued wavenumbers consists in the redefinition of the collection of real-valued input functions that are used for generating the GGQ rule.

### 2.1.3 Example: scattering of incident plane P waves by a spherical cavity in a half-space

To check the accuracy of this new FM-BEM based on the elastic half-space Green's tensors, the scattering of vertical incident plane P waves by a spherical cavity bounded by the sphere $S$ of radius $r$ centered at $(0,0,-3r)$, embedded in an elastic half-space $y_3 \le 0$, is considered. We assume material characteristics such that $\mu = 3$, $\rho = 1$ (in arbitrary units) and $\nu = 0.25$. This problem may be formulated by means of either the integral equation for the total field $\boldsymbol{u}$

$$\boldsymbol{\mathcal{K}}_{\mathrm{HS}}[\boldsymbol{u}](\boldsymbol{x}) = \boldsymbol{u}^F(\boldsymbol{x}) \quad (\boldsymbol{x} \in S) \tag{2.18}$$

based on the half-space Green's tensor, or the integral equation for the scattered field $\boldsymbol{u}^S := \boldsymbol{u} - \boldsymbol{u}^F$

$$\boldsymbol{\mathcal{K}}[\boldsymbol{u}^S](\boldsymbol{x}) = -\boldsymbol{\mathcal{S}}[\boldsymbol{t}^F](\boldsymbol{x}) \quad (\boldsymbol{x} \in S \cup \Gamma_0) \tag{2.19}$$

based on the full-space Green's tensor and having set $\boldsymbol{t}^F = \boldsymbol{n}\cdot\boldsymbol{\mathcal{C}} : \boldsymbol{\nabla}\boldsymbol{u}^F$. Note that (2.18) results from the well-known expedient of applying the integral representation theorem to $\boldsymbol{u}^F$ inside $S$ and combining the resulting identity with (2.2), and as a result involves only the double-layer integral operator $\boldsymbol{\mathcal{D}}_{\mathrm{HS}}$. Moreover, the given free field $\boldsymbol{u}^F$ is a known seismic wave in the reference half-space, here composed of the incident plane P wave and the wave reflected by the free surface $\Gamma_F$.

Results from FM-BEM formulations based on either (2.18) or (2.19) are compared in Fig. 2.3. Formulation (2.19) required the meshing of a disk-shaped truncated free surface $\Gamma_0(D)$, with the truncation radius set to $D = 5r$, while formulation (2.18) needed only a mesh of the cavity surface $S$. Enforcing a uniform, and identical, mesh density in both formulations (here set to 10 BE nodes per $S$ wavelength), the number of DOFs for the full-space BIE formulation ($N_{\mathrm{FS}}$) and the half-space BIE formulation ($N_{\mathrm{HS}}$) are such that $N_{\mathrm{FS}} \approx 7.25 N_{\mathrm{HS}}$. The non-dimensional frequency used was $\kappa_{\mathrm{S}} r = 2.5\pi$, leading respectively to $N_{\mathrm{FS}} = 38\ 934$ and $N_{\mathrm{HS}} = 7\ 686$. The total displacement computed on $S$ using the two approaches coincide within a relative discrepancy of about $10^{-3}$.

**Remarks on computational complexity.** The computational complexities of the full-space and half-space formulations are different. The former is known to be $\mathcal{O}(N_{\mathrm{FS}}\log N_{\mathrm{FS}})$. The latter is $\mathcal{O}(N_{\mathrm{HS}} n_\xi n_\alpha)$, where the GGQ size $(n_\xi, n_\alpha)$ cannot easily be evaluated by analytical means as (i) it is obtained using a numerical algorithm, and (ii) it depends on preset accuracy level, frequency, and on the size and depth of clusters of points $\boldsymbol{x}, \boldsymbol{y}$ (with the radial size $n_\xi$ increasing as clusters of points $\boldsymbol{x}, \boldsymbol{y}$ are closer to $\Gamma_F$). The half-space FM-BEM complexity is estimated in [8], using numerical experiments and for single-layer potentials, to be $\approx \mathcal{O}(N^{1.5})$ for clusters of points at shallow depth. This matter requires substantial additional investigation.

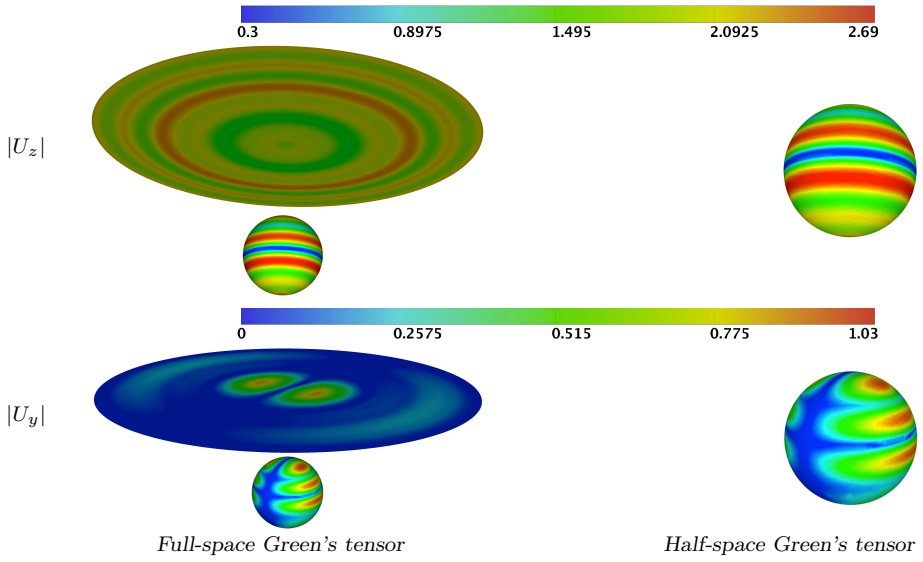


***Figure 2.3:*** *Comparison of the vertical and horizontal modulus of displacement obtained with the full-space formulation* (2.19) *and the half-space formulation* (2.18).

## 2.2 Wideband Fast Multipole Method for 3D acoustics

There is not one single FMM, but rather various algorithms with complementary advantages and drawbacks. In particular the approach we have developed for elastic waves is based on a plane wave expansion (PWFMM) and is only valid for the mid to high-frequencies (we call it the HF-PWFMM) due to some numerical instabilities in the low-frequency regime.

Other approaches have been proposed for the low-frequency regime. In [Greengard 1998] evanescent waves are added to the plane wave expansion, leading to the low-frequency PWFMM (LF-PWFMM). The LF-PWFMM has then been studied, and improved on, in several directions, for example in [Darve 2004a] or [Wallen 2007]. Although more computationally expensive than the HF-PWFMM, the LF-PWFMM produces stable computations for low frequency problems.

In some configurations such as high-frequency problems with very small geometric details or in the context of a mesh adaptation procedure (such as the one presented in Chapter 5), it is necessary to couple the low and high-frequency formulations. Since the HF-PWFMM accuracy decreases at low frequencies, while the LF-PWFMM increases with frequency, it is ineffective to use either formulation for all the frequencies. The idea is to couple the HF and LF formulations and to use the HF method whenever possible. Such formulations are called wideband or broadband FMMs. In [Cheng 2006], a wideband FMM is proposed and uses the original FMM proposed by Rokhlin [Rokhlin 1993][1]. To take advantage of the diagonal *far field to local* translation operators for the lower frequencies, a conversion between the traditional FMM and the LF-PWFMM is performed. A variant of this approach, avoiding the conversion to the LF-PWFMM is proposed in [Gumerov 2009]. All the previously-mentioned approaches are very complicated due to the use of two very different expansions to perform the factorisation in the FMM. As a result, they require involved implementations.

With Francis Collino (external collaborator at POEMS), we have proposed a wideband FMM which is based on plane wave expansions only and combines the advantages of the low and high-frequency formulations. We have revisited the method proposed in [Greengard 1998] devoted to the low-frequency regime and based on the splitting of the Green's function into a propagative and an evanescent part. The main advantage of this new formulation is its easy implementation compared to previously published approaches. This work is so far mainly theoretical (even though its efficiency has been checked numerically), and is also quite technical. I give in the following the

[1] Note that in [Darve 2004b], a detailed connection between the PWFMM and the FMM based on a multipole expansion is proposed.

main results and general ideas, and refer the interested reader to [6] for the complete proofs. In this preliminary step, we have only considered acoustic wave propagation, but the approach can be extended to elastic wave propagation.

**Principle of the PWFMM.** The PWFMM has been briefly presented in Chapter 1. We recall the basic ideas here to fix the notations. To simplify the explanation, we consider a cloud $X$ of $N$ points in $\mathbb{R}^3$ and a real wavenumber $\kappa$. The Helmholtz potential induced by the charges $\rho_i$ located at the points $\boldsymbol{x}_i \in X$ is given by

$$V_i = \sum_{j \neq i} \frac{e^{i\kappa|\boldsymbol{x}_i - \boldsymbol{x}_j|}}{|\boldsymbol{x}_i - \boldsymbol{x}_j|} \rho_j = \sum_{j \neq i} \mathbb{G}_{ij} \rho_j, \quad \boldsymbol{x}_i \in X. \tag{2.20}$$

In a first step, a 3D cubic grid of linear spacing $D$, embedding the cloud of points $X$, is created; the cubic cells are then recursively subdivided into eight smaller cubic cells; the cell-subdivision approach is systematized by means of an octree. At each level $\ell$, the linear cell size is $d = 2^{-\ell} D$, $\ell = 1, ..., \mathcal{L}$. The octree is used to derive a block decomposition of the matrix $\mathbb{G}$ (corresponding in this section to the discretization of the fundamental solution only). Generally speaking, the definition of an efficient PWFMM is based on the following three ingredients:

1. An approximation formula for the evaluation of the Green's function in terms of plane waves. If $\boldsymbol{x}_t \in B_t$ and $\boldsymbol{y}_s \in B_s$, the Green's function is sought under the form (i.e. (1.12) reformulated with more general notations)

$$\begin{gathered} \frac{e^{i\kappa|\boldsymbol{x}_t - \boldsymbol{y}_s|}}{|\boldsymbol{x}_t - \boldsymbol{y}_s|} \simeq \int_{\hat{\Lambda}} T(\boldsymbol{\kappa}; \mathbf{t})\, e^{i\boldsymbol{\kappa}\cdot((\boldsymbol{x}_t - \mathbf{c}_t) - (\boldsymbol{y}_s - \mathbf{c}_s))}\, d\hat{\Lambda}(\boldsymbol{\kappa}),\ \boldsymbol{x}_t \in B_t,\ \boldsymbol{y}_s \in B_s \\ \text{with } \hat{\Lambda} \subset \left\{ \boldsymbol{\kappa} = (\kappa_x, \kappa_y, \kappa_z) \in \mathbb{C}^3,\ \kappa_x^2 + \kappa_y^2 + \kappa_z^2 = \kappa^2 \right\} \end{gathered} \tag{2.21}$$

   where $\boldsymbol{\kappa}$ is a wave vector, $\mathbf{t} = \mathbf{c}_t - \mathbf{c}_s$ is the translation vector linking the centers of two interacting cells $(B_s, B_t)$ and $T$ is a translation function (defined in the following). Due to the octree structure, the translation vectors are defined by $\mathbf{t} = (id, jd, md)$ with $|i|, |j|, |m| \leq 3$, $|i| + |j| + |m| > 3$. As a result, the number of possible translation vectors at a given level is finite and not greater than 316.

2. Accurate quadrature rules for the evaluation of the integrals over $\hat{\Lambda}$. These quadrature rules will depend only on the size of the cells at a given level. Consequently there are as many quadrature rules as there are levels in the octree.

3. An interpolation formula allowing the evaluation of the plane waves at the level-$\ell$ quadrature points from their values at the level-$(\ell - 1)$ quadrature points. This last ingredient yields some additional factorizations of the computations, as the contributions at level-$\ell$ are reused to evaluate the contributions at level-$(\ell - 1)$ [Darve 2000a].

In the HF-PWFMM, the plane wave expansion is defined only in terms of propagative waves, reducing $\hat{\Lambda}$ in (2.21) to the unit sphere in $\mathbb{R}^3$. In this case, the translation function is a series involving spherical Hankel functions which are known to increase exponentially for small arguments. As a result, the HF-PWFMM suffers from numerical breakdowns in the low-frequency regime. In the LF-PWFMM, the evanescent plane waves are added to the expansion leading to a more expensive but also more stable method [Darve 2000b]. This extra cost is due to the introduction of six distinct factorizations in the LF-PWFMM instead of one in the HF-PWFMM [Greengard 1998]. Accordingly, the 316 translation vectors are dispatched into these six directions.

**New stable plane wave expansions.** The first ingredient to define an efficient PWFMM is the derivation of an approximation formula for the Green's function, in terms of plane waves. Let $\mathbf{w}$ be a vector with $z_w > 0$, with $(x_w, y_w, z_w)$ its Cartesian coordinates in $(0, \hat{\mathbf{x}}, \hat{\mathbf{y}}, \hat{\mathbf{z}})$, $(R_w = |\mathbf{w}|, \theta_w, \varphi_w)$ its spherical coordinates, and $(r_w = R_w \sin\theta_w, \varphi_w, z_w)$ its cylindrical coordinates. We choose to split the Green's function into the following two parts

$$\frac{e^{i\kappa|\mathbf{w}|}}{|\mathbf{w}|} = G_p(\mathbf{w}) + G_e(\mathbf{w}),$$

with the propagative part $G_p$, respectively the evanescent part $G_e$, given by

$$G_p(\mathbf{w}) = i\kappa \int_0^{\frac{\pi}{2}} J_0(\kappa r_w \sin\theta) e^{i\kappa z_w \cos\theta} \sin\theta d\theta, \tag{2.22}$$

$$G_e(\mathbf{w}) = \int_0^{\infty} J_0(\sqrt{\lambda^2+\kappa^2} r_w) e^{-\lambda z_w}\, d\lambda, \tag{2.23}$$

where $J_0(t)$ is the Bessel function of order 0.

The approach proposed in [Greengard 1998] to accelerate (and approximate) the evaluation of the Green's function in (2.20) is based on the integral representation of the Bessel function

$$J_0(t) = \frac{1}{2\pi} \int_0^{2\pi} e^{it\cos(\varphi-\psi)}\, d\varphi, \qquad \text{for any angle } \psi. \tag{2.24}$$

Taking $\psi = \varphi_w$ and plugging (2.24) into (2.22), the propagative part $G_p$ is found in terms of plane waves as

$$G_p(\mathbf{w}) = \frac{i\kappa}{2\pi} \int_0^{\frac{\pi}{2}} \int_0^{2\pi} e^{i\kappa R_w(\cos\theta\cos\theta_w + \sin\theta_w \sin\theta\cos(\varphi-\varphi_w))} \sin\theta d\theta d\varphi = \frac{i\kappa}{2\pi} \int_{S^2} \pi(\hat{\mathbf{s}}) e^{i\kappa\hat{\mathbf{s}}\cdot\mathbf{w}}\, d\sigma(\hat{\mathbf{s}}) \tag{2.25}$$

where $S^2$ is the unit sphere, and $\pi(\hat{\mathbf{s}})$ is the characteristic function of the upper hemisphere

$$\pi(\hat{\mathbf{s}}) = 1 \;\text{ if }\; \hat{\mathbf{s}}\cdot\hat{\mathbf{z}} \geq 0 \quad \text{ and } \quad = 0 \;\text{ if }\; \hat{\mathbf{s}}\cdot\hat{\mathbf{z}} < 0. \tag{2.26}$$

Similarly, the evanescent part $G_e$ may be recast as

$$G_e(\mathbf{w}) = \frac{1}{2\pi} \int_0^{\infty} \int_0^{2\pi} e^{i\boldsymbol{\kappa}(\lambda,\varphi)\cdot\mathbf{w}}\, d\varphi d\lambda \quad \text{ with } \quad \boldsymbol{\kappa} = \begin{bmatrix} \sqrt{\kappa^2+\lambda^2}\cos\varphi \\ \sqrt{\kappa^2+\lambda^2}\sin\varphi \\ i\lambda \end{bmatrix}. \tag{2.27}$$

In [6], we have proposed theoretical developments to speed-up the evaluation of the evanescent and propagative parts together with error estimates to check the accuracy of the accelerated method at all steps. These theoretical developments are then used to propose a wideband FMM based entirely on plane wave expansions.

### 2.2.1 Numerical evaluation of the propagative part

The difficulty to integrate numerically (2.25) is due to the discontinuity of $\pi$. The main idea (similarly to [Darve 2004a]) is to replace the upper hemisphere (2.26) with the complete sphere and to filter out the higher harmonic modes of the translation function. With this strategy, we reduce the number of plane wave expansions from six (for the six axes of evanescence) to one; as a consequence, the CPU time is also reduced. The second advantage is the possibility to use both the quadrature rules and the interpolation step designed for the HF-PWFMM [Darve 2000b]. Our main contributions in [6] to improve the evaluation of the propagative part concern the proposition of (i) a new expression of the translation function and (ii) estimates on the error introduced by the quadrature rule to perform the integration on the unit sphere.

Expression (2.25) of the propagative part defines a first expression of the translation function needed in (2.21), i.e. $T(\hat{\mathbf{s}},\mathbf{t}) = \frac{i\kappa}{2\pi}\pi(\hat{\mathbf{s}})e^{i\kappa\mathbf{t}\cdot\hat{\mathbf{s}}}$. It needs in practice to be truncated to reduce the number of quadrature points on the unit sphere. Since $\pi(\hat{\mathbf{s}})$ is discontinuous on the meridian circle $\hat{\mathbf{s}}\cdot\hat{\mathbf{z}} = 0$, it is very likely that the convergence of the expansion of the translation function, in terms of spherical harmonics will be slow, especially in the vicinity of the circular line of discontinuity. We give in Proposition 1 an alternative expression of the translation function to avoid this problem. It is first important to recall that the spherical harmonics are defined by

$$Y_n^m(\theta,\varphi) = \sqrt{\frac{2n+1}{4\pi}} \sqrt{\frac{(n-|m|)!}{(n+|m|)!}} P_n^{|m|}(\cos\theta) e^{im\varphi} \text{ for } m = -n,\ldots,n,\ n \geq 0 \tag{2.28}$$

(where $P_n^m(x)$ denotes the associated Legendre functions) and they form a complete orthonormal system in $L^2(S^2)$. Let $L$ be a non negative integer, the mapping $\Pi^L : L^2(S^2) \to L^2(S^2)$

$$\Pi^L f(\hat{\mathbf{s}}) = f^L(\hat{\mathbf{s}}) = \sum_{\ell=0}^{L} \sum_{m=-\ell}^{\ell} \left( \int_{S^2} f(\hat{\mathbf{d}}) \overline{Y_l^m(\hat{\mathbf{d}})}\, d\sigma(\hat{\mathbf{d}}) \right) Y_l^m(\hat{\mathbf{s}}) \tag{2.29}$$

defines an orthogonal projector in $L^2(S^2)$ onto the spherical harmonics of degree $\leq L$. The definition of the new translation function follows from this property.

**Proposition 1.** *Let $\pi$ be the characteristic function of the upper hemisphere (2.26) and $\Pi^L$ be the orthogonal projector (2.29) in $L^2(S^2)$. The translation function for the propagative part can be expressed as*

$$T^L(\hat{\mathbf{s}}, \mathbf{t}) = \Pi^L \left( \frac{i\kappa}{2\pi} e^{i\kappa \hat{\mathbf{s}}\cdot\mathbf{t}}\, \pi(\hat{\mathbf{s}}) \right)(\hat{\mathbf{s}}) = 2i\kappa \sum_{\ell=0}^{L} \sum_{m=-\ell}^{\ell} \left( \sum_{n=|m|}^{\infty} i^n j_n(\kappa t)\, \gamma_{n,\ell}^m \overline{Y_n^m(\hat{\mathbf{t}})} \right) Y_\ell^m(\hat{\mathbf{s}}) \tag{2.30}$$

*where $\mathbf{t} = t\,\hat{\mathbf{t}}$, the $Y_n^m$ are the spherical harmonics (2.28) and the $\gamma_{n,p}^m$ are the coupling parameters given in [6] (the detailed expressions are omitted since they do not give any information on the final algorithm).*

This new expression of the translation function can be evaluated in a fast way. In practice, it is necessary to truncate expansion (2.30) to some integer $L$ but it is possible to estimate the error introduced by this truncation, see [6, Lemma 4]. We have shown that the design of an accurate quadrature rule for the propagative part reduces to the choice of a quadrature rule exact for the spherical harmonics of degree less than or equal to $2L+1$. We choose the usual quadrature rule [Darve 2000a] with $N_\theta = L+1$ Gauss Legendre points in $\theta$ and $N_\varphi > 2L$ equidistributed points in $\varphi$. Finally the plane wave expansion of the propagative part is given by

$$G_p^L(\mathbf{t}, \mathbf{v}) = \fint_{S^2} \Pi^L \Big( \frac{i\kappa}{2\pi} \pi(\hat{\mathbf{s}}) e^{i\kappa\hat{\mathbf{s}}\cdot\mathbf{t}} \Big)\, e^{i\kappa\hat{\mathbf{s}}\cdot\mathbf{v}}\, d\sigma(\hat{\mathbf{s}}) \tag{2.31}$$

where $\fint_{S^2}$ denotes a quadrature rule over the unit sphere, exact for the spherical harmonics of degree less than or equal to $2L+1$.

### 2.2.2 Numerical evaluation of the evanescent part

Our main contribution concerns the evaluation of the evanescent part. The key point in the LF-PWFMM is the definition of accurate quadrature rules for (2.27). Such a numerical quadrature rule should be composed of a small number of quadrature points to optimize the computational costs. Since the phase of the integrand in (2.27) is nonlinear with respect to $\lambda$, deriving an optimal quadrature rule (in the sense of accuracy and number of points) is a difficult problem. There are various approaches in the literature [Cheng 2006, Yarvin 1998, Darve 2004a]. The minor drawback of these approaches is the need for each problem to pre-compute the appropriate quadrature rules.

With Francis Collino, we have proposed a method to avoid this drawback by simplifying the derivation of the quadrature rule and interpolation algorithm for the evanescent part. The idea is to reformulate (2.27) by using an appropriate change of variables. The starting point is to note that the integral representation (2.24) of the Bessel function is valid for any angle $\psi$. Instead of $\psi = \varphi_w$, we use the angle $\psi = \varphi_w + \psi_{\lambda,\kappa}$ with

$$\cos\psi_{\lambda,\kappa} = \frac{\kappa}{\sqrt{\lambda^2+\kappa^2}} \quad \text{and} \quad \sin\psi_{\lambda,\kappa} = \frac{\lambda}{\sqrt{\lambda^2+\kappa^2}}. \tag{2.32}$$

Inserting the formula (2.24) in (2.23), with $\psi$ given as above, and using simple trigonometric formulas; the evanescent part now reads

$$G_e(\mathbf{w}) = \frac{1}{2\pi} \int_0^\infty \int_0^{2\pi} e^{i\boldsymbol{\kappa}(\lambda,\varphi)\cdot\mathbf{w}}\, d\varphi d\lambda \quad \text{with} \quad \boldsymbol{\kappa} = \begin{bmatrix} \kappa\cos\varphi + \lambda\sin\varphi \\ \kappa\sin\varphi - \lambda\cos\varphi \\ i\lambda \end{bmatrix}. \tag{2.33}$$

This rotation by an angle $\psi_{\lambda,\kappa}$ (which depends on $\lambda$) leads to a phase which is linear with respect to $\lambda$. Some important simplifications follow from this new expression:

1. It is possible to use the optimal quadrature rules designed for the static case (for $\kappa = 0$).
2. A fast interpolation algorithm similar to the one proposed on the unit sphere for the HF-PWFMM is easily derived.
3. Error estimates on the main steps of the PWFMM are obtained.

**Reduction of the domain of definition.** In order to define the optimal quadrature rules, it is important to determine the domain of definition of the vector $\mathbf{w}$. In the context of the PWFMM, plane wave expansions are used to evaluate the contributions coming from interacting pairs of cells $(B_s, B_t)$. The formulas (2.25) and (2.27) are applied in the special case where $\mathbf{w} = \mathbf{t}+\mathbf{v}$, $\mathbf{t} = \mathbf{c}_t - \mathbf{c}_s$ and $\mathbf{v} = \mathbf{x}_t - \mathbf{c}_t - \mathbf{y}_s + \mathbf{c}_s$. This implies for example for the group associated to the evanescence axis $Oz$ that the 74 translation vectors are defined by $\mathbf{t} = (id, jd, md)$ with $|i|, |j| \leq m$ and $m = 2$ or 3 (where $d$ is the length of the edges of the cells). Since the three coordinates of the vector $\mathbf{v}$ lie between $-d$ and $d$, we have in addition $\mathbf{w} \in \Omega_d = d\hat{\Omega}$, and $\hat{\Omega}$ is the set given by (Fig. 2.4)

$$\hat{\Omega} = \left\{ (\hat{\mathbf{r}}_w, \hat{\mathbf{z}}_w) \in [0, 3\sqrt{2}] \times [1, 3] \cup [0, 4\sqrt{2}] \times [2, 4] \right\}. \tag{2.34}$$

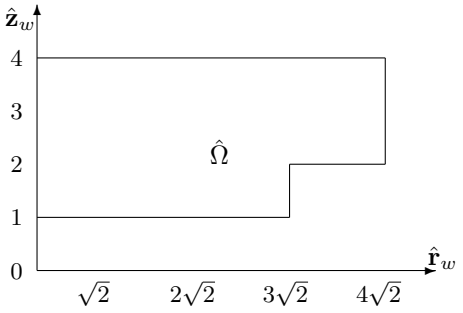


***Figure 2.4:*** *Definition of the normalised domain $\hat{\Omega}$ in which the vectors $\mathbf{w}/d$ lie, i.e. $\mathbf{w} \in \Omega_d$.*

**Efficient and accurate quadrature rule for the evanescent part.** Having reduced the size of the domain of definition of the vector $\mathbf{w}$, the key point in the LF-PWFMM is the definition of accurate quadrature rules to evaluate the integral in the $(\varphi, \lambda)$-space for all $\mathbf{w} \in \Omega_d$, with a small number of quadrature points (to optimize the computational costs). The linearisation of the phase introduced in (2.33) leads to some major simplifications in the derivation of an efficient quadrature rule. If we consider the angular integration over $\varphi$ independently from the integration over $\lambda$, the optimal choice is to use equidistributed angles (to perform the interpolation with the FFT). However, the optimal choice, in the sense of the smallest total number of points for an accurate integration in the $(\varphi, \lambda)$-space, is to consider a different quadrature over $\varphi$ for each value of $\lambda$.

Precisely, we have shown that the optimal quadrature rule with respect to $\lambda$ is a $P$-point quadrature rule with positive weights $(\tilde{\lambda}_p, \varpi_p)_{p=1,\ldots,P}$ such that

$$\max_{\xi \in \hat{\Omega}} \left| \sum_{p=1}^{P} \varpi_p e^{-\tilde{\lambda}_p \xi} - \frac{1}{\xi} \right| \leq \varepsilon_1'. \tag{2.35}$$

It is possible in practice to define a quadrature satisfying (2.35). It is simply a quadrature accurate for integrating $e^{-\lambda\xi}$ for any $\xi$, i.e. a quadrature for the static case for which quadrature points and weights are given in [Yarvin 1998]. The angular integration is then performed with $Q_{p,\kappa d} = 2L_p + 1$ equidistributed angles. The number of angular points thus depends on the wavenumber and the cell size.

**Filtering the translation function of the evanescent part.** The previous quadrature is not yet optimal for the PWFMM since it does not use the usual decomposition of the vector $\mathbf{w}$ in the FMM, i.e. $\mathbf{w} = \mathbf{t} + \mathbf{v}$ where $\mathbf{t}$ is the translation vector. The aim is to evaluate

$$G_e(\mathbf{t}+\mathbf{v}) = \frac{1}{2\pi}\int_0^\infty \int_0^{2\pi} e^{i(\kappa \mathbf{s}(\varphi)+\lambda \mathbf{t}(\varphi))\cdot \mathbf{t}}\, e^{i(\kappa \mathbf{s}(\varphi)+\lambda \mathbf{t}(\varphi))\cdot \mathbf{v}}\, d\varphi d\lambda$$

$$\text{with} \quad \left\{ \begin{array}{c} \mathbf{s}(\varphi) = \begin{bmatrix} \cos\varphi \\ \sin\varphi \\ 0 \end{bmatrix}, \qquad \mathbf{t}(\varphi) = \begin{bmatrix} \sin\varphi \\ -\cos\varphi \\ i \end{bmatrix}, \\ \mathbf{t} = d(i\hat{\boldsymbol{x}} + j\hat{\boldsymbol{y}} + m\hat{\mathbf{z}}),\ i,j,m \text{ relative integers}; \\ 3 \geq m \geq |i|,\ |j| \text{ and } i^2+j^2+m^2 > 3; \mathbf{v} \in d\hat{B} = d\left[-1,1\right]^3. \end{array} \right. \tag{2.36}$$

The idea is to filter out the Fourier modes of the plane wave expansion that do not contribute significantly to the value of the integral, to reduce computational times.

**Proposition 2.** *Let $\varepsilon_1'$, $\varepsilon_2'$ be two small positive numbers. Assume that there exists a $P$-point quadrature rule with positive weights $(\tilde{\lambda}_p, \varpi_p)_{p=1,,...,P}$ such that Condition (2.35) holds. For each $\tilde{\lambda}_p$, the angular integration is performed with $Q_{p,\kappa d} = 2L_p + 1$ equidistributed points $\varphi_{p,q} = \frac{2\pi q}{2L_p+1}$, $0 \leq q \leq 2L_p$. We define $T^L(\mathbf{t};\lambda,\varphi)$ the filtered translation function*

$$T^L(\mathbf{t};\lambda,\varphi) = e^{-\tilde{\lambda}\frac{z_t}{d}} \sum_{q=0}^{L} \varepsilon_q i^q J_q(\tau \frac{r_t}{d}) \cos(q(\varphi - \varphi_t - \psi_\lambda)) \tag{2.37}$$

*with $\tau = \sqrt{\tilde{\lambda}^2 + \kappa^2 d^2}$, $\kappa d = \tau \cos\psi_\lambda$, $\tilde{\lambda} = \tau \sin\psi_\lambda$. Then, for $\mathbf{t}$ and $\mathbf{v}$ satisfying (2.36) the filtered evanescent part $G_e^P$ with the previously defined quadrature rule*

$$G_e^P(\mathbf{t},\mathbf{v}) = \frac{1}{d}\sum_{p=1}^{P}\sum_{q=1}^{2L_p+1} \frac{\varpi_p}{2L_p+1}\, T^{L_p}(\mathbf{t};\tilde{\lambda}_p,\varphi_{p,q})\, e^{i(\kappa d \mathbf{s}(\varphi_{p,q}) + \tilde{\lambda}_p \mathbf{t}(\varphi_{p,q}))\cdot \frac{\mathbf{v}}{d}} \tag{2.38}$$

*satisfies the error estimate*

$$\max_{\mathbf{t}+\mathbf{v}\in\Omega_d} |\mathbf{t}+\mathbf{v}| \left| G_e^P(\mathbf{t},\mathbf{v}) - G_e(\mathbf{t}+\mathbf{v}) \right| \leq \varepsilon(\varepsilon_1,\varepsilon_2). \tag{2.39}$$

**Interpolation of the evanescent part.** The third ingredient listed in the introduction is the definition of a fast algorithm to perform the interpolation. Thus, some additional factorizations of the computations are obtained since the contributions at level-$\ell$ are used to evaluate the contributions at level-$(\ell-1)$. Let $\boldsymbol{x}_s$ be a point in a cell $b$ of the octree; assume $b$ is one of the eight children of the parent cell $B$; let $\mathbf{v}$ be the vector $\boldsymbol{x}_s - \mathbf{c}_B$, where $\mathbf{c}_B$ is the center of the cell $B$; The practical problem is to deduce

$$E(\mathbf{v};\lambda,\varphi) = e^{i(\kappa \hat{\mathbf{s}}(\varphi) + \lambda \hat{t}(\varphi))\cdot \mathbf{v}}$$

for any couple $(\lambda,\varphi)$ of the quadrature defined at level-$(\ell-1)$, from the values evaluated for the quadrature defined at level-$\ell$. The quadrature points at level-$\ell$ (cell of size $d$) and at level-$(\ell-1)$ (parent cell of size $2d$) are defined by

$$\mathcal{C}_\ell^{quad} = \left\{ \left(\frac{\tilde{\lambda}_p}{d}, \varphi_{q,p}\right), \begin{array}{l} 1 \leq p \leq P, \\ 1 \leq q \leq Q_{p,\kappa d} \end{array} \right\}; \quad \mathcal{C}_{\ell-1}^{quad} = \left\{ \left(\frac{\tilde{\lambda}_p}{2d}, \varphi_{q,p}\right), \begin{array}{l} 1 \leq p \leq P, \\ 1 \leq q \leq Q_{p,2\kappa d} \end{array} \right\}.$$

The number of points in the quadrature with respect to $\lambda$ is constant (equal to $P$) since it is defined for the static case. But the quadrature points and weights depend on the level (i.e. the cell size $d$). Assuming that the $\tilde{\lambda}_p$ are ordered by increasing values, the maximum value is achieved for $p = P$, i.e. $\tilde{\lambda}_P$. On the other hand, the quadrature with respect to $\varphi$ is composed of equidistributed points. The optimal quadrature is thus obtained by defining a different quadrature for each $\tilde{\lambda}_p$ $(p = 1, ..., P)$. The interpolation must address this problem.

Since the angles $\varphi$ are equidistributed, the FFT is an appropriate tool to perform the interpolation. But we have to take into account that a different quadrature with respect to $\varphi$ is defined for each $\tilde{\lambda}_p$. We denote by $Q = Q_{P,2\kappa d}$ the maximum number of angles in the finest discretization with respect to $\varphi$ (i.e. when $\tilde{\lambda}_p$ is equal to $\tilde{\lambda}_P$ and in the parent box). The idea is then to perform the interpolation independently for each $\tilde{\lambda}_p$. [6, Algorithm 2] presents the main three steps to perform the interpolation. For each $\tilde{\lambda}_p$, **Step 1** consists in interpolating $E : \varphi \to E(\mathbf{v}; \lambda, \varphi)$ to a uniform grid with $Q$ points. Then, in **Step 2** the interpolation is performed with respect to $\lambda$ for the $Q$ angles $\varphi$. Finally for each $\tilde{\lambda}_p$, **Step 3** is the transpose of **Step 1** to go back on a grid with $Q_{p,2\kappa d}$ angles.

### 2.2.3 A new wideband PWFMM based only on plane wave expansions

It is now possible to derive a wideband PWFMM. It combines the standard HF-PWFMM and the LF-PWFMM based on the plane wave expansions (2.31) and (2.38); together with the translation functions (2.30) and (2.37). The treatment of the fast multipole ("FM") contributions exploits expansion (2.21) in a manner suggested by their multiplicative form, i.e. in 3 steps labelled **(i)**-**(ii)**-**(iii)**. Accordingly in **step (i)** *multipole moments* defined by

$$\mathcal{F}^{B_s}(\boldsymbol{\kappa}) = \sum_{\boldsymbol{x}_s \in B_s} e^{-\mathrm{i}\boldsymbol{\kappa}.(\boldsymbol{x}_s - \mathbf{c}_{B_s})} \rho(\boldsymbol{x}_s) \tag{2.40}$$

are computed for each cell $B_s$. Then in **step (ii)**, *local expansions* for the cells $B_t$ are evaluated by applying the translation functions $T$ to the multipole moments according to

$$\mathcal{N}^{B_t}(\boldsymbol{\kappa}) = \sum_{\substack{B_s = \mathbf{t} + B_t \\ \mathbf{t} \in \mathcal{T}}} T(\boldsymbol{\kappa}; \mathbf{t}) \mathcal{F}^{B_s}(\boldsymbol{\kappa}) \tag{2.41}$$

where $\mathcal{T}$ denotes the set of translation vectors. Finally in **step (iii)**, replacing the integration over $\hat{\Lambda}$ in (2.21) by a numerical quadrature rule, the "FM" contributions to the potential are now expressed as

$$V^{B_t}(\boldsymbol{x}_t) = \int_{\hat{\Lambda}} \mathcal{N}^{B_t}(\boldsymbol{\kappa}) e^{\mathrm{i}\vec{k}.(\boldsymbol{x}_t - \mathbf{c}_{B_t})}, \quad \boldsymbol{x}_t \in B_t. \tag{2.42}$$

This is the single-level FMM. The computation of $V^{B_t}$ by the multi-level FMM consists of the following five steps:

- **(i)** *Initialization*: compute multipole moments for all lowest-level cells.
- **(ii)** *Upward pass*: recursively aggregate multipole moments by moving upward (via an interpolation and a shift of the cell center) in the tree until level 2 is reached.
- **(iii)** *Translation*: initialize local expansions for each level-$\ell$ cell and at each level $2 \leq \ell \leq \mathcal{L}$ by translating the multipole moments.
- **(iv)** *Downward pass*: for all levels $3 \leq \ell \leq \mathcal{L}$, the local expansion for each level-$\ell$ cell is updated (via a shift of the cell center and an inverse interpolation) with the contribution from the parent level-$(\ell - 1)$ cell.
- **(v)** When the leaf level $\ell = \mathcal{L}$ is reached, all local expansions have been computed. The contribution $V^{B_t}$ is evaluated with the level-$\mathcal{L}$ quadrature rule.

In the HF-PWFMM, $\hat{\Lambda}$ is the unit sphere $S^2$ of $\mathbb{R}^3$ and the filtered translation function is $T_L$ given by

$$T_L(\boldsymbol{\kappa}; \mathbf{t}) = \frac{i\kappa}{4\pi} \sum_{m=0}^{L} (2m+1) i^m h_m^{(1)}(\kappa|\mathbf{t}|) P_m(\cos(\hat{\boldsymbol{\kappa}}, \mathbf{t})) \quad \text{with } \boldsymbol{\kappa} = \hat{\boldsymbol{\kappa}}\kappa.$$

Now plugging the translation function defined in (2.30), i.e. the one associated to the propagative part, in (2.41) we obtain an approximation of

$$V_p^{B_t}(\boldsymbol{x}_t) = \sum_{x_s} G_p(|\boldsymbol{x}_t - \boldsymbol{x}_s|) \rho(\boldsymbol{x}_s)$$

which corresponds to the contribution of the propagative part of the LF-PWFMM. In other words, the only change of translation function in (2.41) amounts to computing the propagative part

$V_p^{B_t}(\boldsymbol{x}_t)$ in the LF-PWFMM instead of the " FM" contributions with the HF-PWFMM. This similarity between the two algorithms is true only because we have replaced the upper hemisphere by the complete sphere; hence, the same quadrature rule for the HF-PWFMM and the LF-PWFMM is used. In the case of the multi-level algorithm, the same remark remains valid. This relationship between the expansions of the Helmholtz Green's function in the HF-PWFMM and of the propagative part in the LF-PWFMM, is the basis of the combined HF/LF-PWFMM we have proposed.

The algorithm for the evanescent part is very similar. The main difference is that the 316 translation directions are dispatched into six groups (one for each axis of evanescence since $z_w > 0$). Consequently the PWFMM algorithm is now applied six times for the evanescent part, the total number of translations being unchanged. Due to the additional cost introduced by the evanescent part, the LF-PWFMM is stable at all frequencies but more expensive than the standard HF-PWFMM. It is thus natural to use the HF-PWFMM whenever possible, i.e. as long as sufficient accuracy is achieved.

In practice, it is possible to associate a boolean for each triplet $(\mathbf{t}, kd, \varepsilon)$ to define whether the HF-PWFMM can be safely applied (according to a prescribed accuracy $\varepsilon$). As a consequence, both the HF and LF approximations are used at any given level, depending on the values of the translation vector considered. Finally, the algorithm is decomposed into three groups: low-frequency formula for all translation vectors (for the small cells at the higher levels), high-frequency formula for all the translation vectors (for the large cells at the lower levels) and a combination of the two formulations for the intermediate levels.

### 2.2.4 Illustration of the accuracy of the wideband PWFMM

We consider 3 cylinders ($L_1$ is the length of the largest one) meshed with triangular surface elements (see Fig. 2.5). Starting from the initial mesh $C_1$, the meshed cylinders $C_2$ (resp. $C_3$) are obtained via a translation and a scaling with a factor 0.1 (resp. 0.01). Since the edge lengths in this mesh vary from 1 to 100, the HF-PWFMM used on this example would lead to inaccurate results. It is necessary to use a wideband FMM.

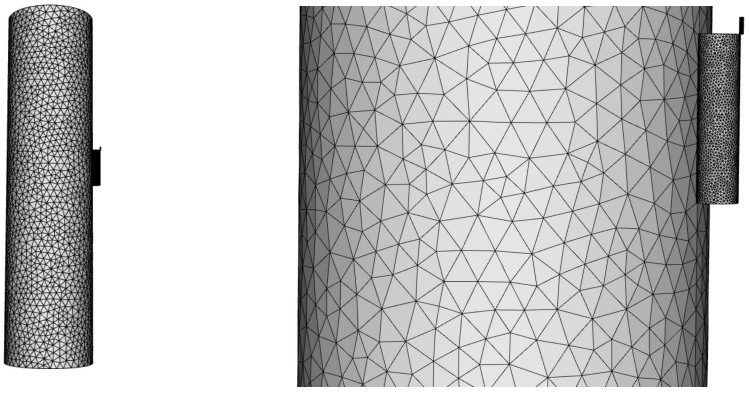

***Figure 2.5:*** *Geometry considered to illustrate the capabilities of the wideband PWFMM.*

The wavenumber $\kappa$ is automatically adapted to achieve 10 points per wavelength for the largest edge of the mesh. We discretize, then decompose the integral into near and far contributions. The near contributions are computed directly while the PWFMM is used for the far contributions. Similarly to what is done in [Cheng 2006], in Table 2.1 we compare the CPU times to evaluate the potential, with the direct method or with the wideband PWFMM; we consider two meshes and three prescribed accuracies. We report the relative 2-norm errors between the direct computations and the PWFMM on the complete mesh and also on the 3 different cylinders. The octree used by the combined LF/HF-PWFMM contains $\pounds = 15$ levels for both meshes. The HF-PWFMM (resp. LF-PWFMM) is applied for all the interactions between cells, from the level 3 up to the level $\ell_o - 1$ (resp. from $\ell_o + 1$ to $\pounds$). At level $\ell_o$, the HF-PWFMM is used except for the directions $(\pm 2, 0, 0), (0, \pm 2, 0), (0, 0, \pm 2)$. The corresponding level $\ell_o$ is reported in the last column

of Table 2.1. The method is shown to achieve the prescribed levels of accuracy with a drastic reduction of CPU time compared to the direct calculation. In addition, the ratios between the direct and PWFMM times are similar to the ones reported in [Cheng 2006].

| $N_t$ | $L_1$ | Time direct | Time FMM | 2−norm | 2−norm on $C_1$ | 2−norm on $C_2$ | 2−norm on $C_3$ | level $\ell_o$ LF/HF |
|---|---|---|---|---|---|---|---|---|
| 420 678 | $17\lambda$ | 2h02 | 28s | $3.3\ 10^{-3}$ | $6.7\ 10^{-4}$ | $5.2\ 10^{-4}$ | $1.0\ 10^{-2}$ | 12 |
| | | | 43s | $2.7\ 10^{-4}$ | $3.1\ 10^{-5}$ | $2.5\ 10^{-5}$ | $8.5\ 10^{-4}$ | 10 |
| | | | 87s | $1.3\ 10^{-5}$ | $1.3\ 10^{-6}$ | $7.4\ 10^{-7}$ | $4.2\ 10^{-5}$ | 7 |
| 1 008 102 | $23\lambda$ | 11h48 | 50s | $1.8\ 10^{-3}$ | $8.9\ 10^{-4}$ | $1.3\ 10^{-3}$ | $3.5\ 10^{-3}$ | 12 |
| | | | 78s | $1.8\ 10^{-4}$ | $5.7\ 10^{-5}$ | $1.6\ 10^{-4}$ | $3.2\ 10^{-4}$ | 11 |
| | | | 220s | $5.3\ 10^{-6}$ | $1.0\ 10^{-6}$ | $1.1\ 10^{-6}$ | $1.2\ 10^{-5}$ | 7 |

***Table 2.1:*** *Comparison of the CPU times to evaluate the potential, with the direct method or with the wideband PWFMM.*

## 2.3 Perspectives on the improvement of the FM-BEM solvers for wave propagation problems

We have illustrated in this Chapter the variety of possible FMMs for wave propagation problems. Each formulation has some advantages and drawbacks. First, we need to derive different kernel-dependent FMMs depending on which fundamental solution is used in the BIE. In the context of seismic wave propagation in the soil, the formulation of the BIE and FM-BEM with the full-space fundamental solution is probably not the most appropriate choice due to the need to artificially truncate the free surface. However, when starting with the FMM, the kernel-dependent FMM for the full-space fundamental solutions (used in Chapter 1) is the easiest approach to develop. A natural extension has then been to propose (with M. Bonnet) a new FMM to consider BIEs based on the half-space fundamental solutions [7, 8]. The difficulty in the case of 3D elastodynamics is that the method of images is not sufficient to obtain these fundamental solutions due to the vector nature of the problem. It is thus necessary to add a complementary term to the method of images and to propose a new methodology to evaluate it in a "FMM" fashion. If we keep increasing the difficulty gradually, the next step is to extend this method to the case of a layered elastic half-space [Kausel 2006]. We already have the methodology to propose this extension but the derivation will require involved implementation developments. Another important aspect is to couple the full-space fundamental solution based FM-BEM with the half-space fundamental solution based FM-BEM to be able to consider problems with a topography (e.g. mountains, hills, etc.). Thus so far, we have only considered buried obstacles since the half-space fundamental solution based FM-BEM is valid only for obstacles below the free surface.

The second difficulty when using the FMM for waves comes from the existence of low and high-frequency formulations. With Francis Collino, we have proposed in [6] a simple FMM stable at all frequencies. So far the method has been proposed and justified theoretically for Helmholtz problems. In the future, we want to extend the method to elastodynamic problems. There are no specific limitation on the theoretical point of view since the elastodynamic Green's tensors are only combinations of linear derivatives of the Helmholtz fundamental solution. The major involvement is on an implementation point of view. In a second step, the wideband FM-BEM will be tested in the context of the adapted fast BEM solvers (such as the one presented in Chapter 5).

# CHAPTER 3

# Reduction of the number of iterations in the FM-BEM with efficient preconditioners

## Contents



We have seen that the FMM allows to accelerate the iterative solution of the BEM system by evaluating in a fast and approximate way the matrix-vector product necessary at each iteration. The number of operations per iteration is thus reduced to $\mathcal{O}(N \log N)$. But linear systems arising from the discretization of the elastodynamic equations are known to be difficult to solve at mid- to high-frequencies since the matrix tends to be indefinite. It has been shown that the number of iterations can significantly hinder the overall efficiency of the FM-BEM [14, 13]. A crucial step in accelerating an iterative solver is thus to define an appropriate preconditioner that permits to modify the spectral properties of the initial system.

The proposition of an efficient preconditioner is currently the key point to increase the capabilities of fast BEMs for wave propagation problems. However, it is a delicate task in the framework of the FMM since the system matrix is never explicitly formed. The only matrix that can be used to define a preconditioner is the matrix of the near interactions. Traditional algebraic preconditioning approaches such as incomplete LU, SParse Approximative Inverse [Carpentieri 2000, Carpentieri 2005], multi-grid methods [Carpentieri 2006], nested GMRES algorithm [10] have been applied to acoustic, electromagnetic or elastodynamic FM-BEMs. In practice, numerical results show that all classical algebraic preconditioners used for example in the context of the Finite Element Method present the same moderate efficiency due to the availability of only a small part of the matrix.

To avoid this difficulty, an alternative approach consists in using the mathematical properties of the operators at the continuous level. This class of preconditioners is called analytic preconditioners, e.g. [Antoine 2005, Antoine 2007, Alouges 2007, Bruno 2012, Darbas 2013, Boubendir 2015]. Since it is not possible to have enough information at the discret level to precondition the system, the goal is to reformulate the problem at the continuous level such that the adequate preconditioner

is intrinsically present in the formulation. With Marion Darbas (LAMFA, Université de Picardie) and Frédérique Le Louër (LMAC, Université de Technologie de Compiègne) we have proposed an efficient analytic preconditioner to deal with scattering problems of time-harmonic elastic waves by 3-D rigid obstacles [3, 5].

We use an integral representation of the scattered field that naturally incorporates a regularizing operator. When considering Dirichlet boundary value problems, the regularizing operator is a high-frequency approximation of the exact Dirichlet-to-Neumann operator. The low-order approximation of the DtN is a linear combination of the tangential and normal parts (and it corresponds to the Kupradze radiation conditions at infinity). This approximation is shown to be very efficient for spherical obstacles but does not contain enough information to build an efficient preconditioner for more general shapes. A higher approximation of the DtN must be derived.

Before to consider the approximation of the DtN to derive analytic preconditioners, they are tested as radiation conditions on the boundary. In Section 3.1, I present a method to solve this scattering problem in a fast but approximate way with the On-Surface Radiation Condition (OSRC) method. Then in Section 3.2, I give a more accurate method based on the solution of well conditioned boundary integral equations. In both cases, the approximation of the DtN is the key point to derive fast algorithms. Finally in Section 3.3, I give some other possible uses of the approximation of the DtN.

**Problem definition.** So far, it is not possible to define analytic preconditioners for general configurations (e.g. for the diffraction of incident waves by an alluvial basin as mentioned in the introduction). We consider in this Chapter a bounded domain $\Omega^-$ in $\mathbb{R}^3$ representing an impenetrable body with a closed boundary $\Gamma := \partial\Omega^-$ of class $\mathscr{C}^2$ at least. $\Omega^+$ denotes the associated exterior domain $\mathbb{R}^3\backslash\overline{\Omega^-}$ and $\boldsymbol{n}$ the outer unit normal vector to the boundary $\Gamma$. Again, the Lamé parameters $\mu$ and $\lambda$ and the density $\rho$ are positive constants. The propagation of time-harmonic waves in a three-dimensional isotropic and homogeneous elastic medium is modeled by the Navier equation (1.1). The scattering problem is formulated as follows : Given an incident wave field $\boldsymbol{u}^{\text{inc}}$ which is assumed to solve the Navier equation in the absence of any scatterer, find the displacement $\boldsymbol{u}$ solution to the Navier equation (1.1) in $\Omega^+$ which satisfies the Dirichlet boundary condition on $\Gamma$

$$\boldsymbol{u}_{|\Gamma} + \boldsymbol{u}^{\text{inc}}_{|\Gamma} = 0. \tag{3.1}$$

In addition, the field $\boldsymbol{u}$ has to satisfy the Kupradze radiation conditions at infinity

$$\lim_{r\to\infty} r\left(\frac{\partial\psi_p}{\partial r} - i\kappa_p\psi_p\right) = 0, \qquad \lim_{r\to\infty} r\left(\frac{\partial\boldsymbol{\psi}_s}{\partial r} - i\kappa_s\boldsymbol{\psi}_s\right) = 0, \quad r = |\boldsymbol{x}|, \tag{3.2}$$

uniformly in all directions. These scatterers are illuminated by incident plane waves of the form

$$\boldsymbol{u}^{\text{inc}}(\boldsymbol{x}) = \frac{1}{\mu}\, e^{i\kappa_s\boldsymbol{x}\cdot\boldsymbol{d}}(\boldsymbol{d}\times\boldsymbol{p})\times\boldsymbol{d} + \frac{1}{\lambda+2\mu}\, e^{i\kappa_p\boldsymbol{x}\cdot\boldsymbol{d}}(\boldsymbol{d}\cdot\boldsymbol{p})\boldsymbol{d}\,, \quad \text{where } \boldsymbol{d}\in\mathbf{S}^2 \text{ and } \boldsymbol{p}\in\mathbb{R}^3. \tag{3.3}$$

When $\boldsymbol{p} = \pm\mathbf{e}^r$, the incident plane wave oscillates along the direction of propagation (pressure wave or P-wave). When the polarization $\boldsymbol{p}$ is orthogonal to the propagation vector $\mathbf{e}^r$, the incident plane wave oscillates in a direction orthogonal to the direction of propagation (shear wave or S-wave).

## 3.1 On-Surface Radiation Condition for elastic waves

The OSRC method allows to solve scattering problems in a very efficient but approximated way. A strategy, developed in acoustic and electromagnetic scattering [Antoine 2006, El Bouajaji 2014], to obtain accurate local approximations of the DtN map is to consider only its principal symbol. But its extension to 3D elastodynamics is not straightforward due to the presence of P and S waves and to the vector nature of the unknowns. In [5], we have shown that even though the OSRC method is an approximate method, the accuracy of the solution is high enough to be used as a preconditioner.

It is well-known that for a solution $\boldsymbol{u} \in \boldsymbol{H}^1_+(\Delta^*)$ to the Navier equation (1.1) in $\Omega^+$, that satisfies the Kupradze radiation conditions, the Somigliana integral representation of the field is given by

$$\boldsymbol{u}(\boldsymbol{x}) = \mathcal{D}\boldsymbol{u}_{|\Gamma}(\boldsymbol{x}) - \mathcal{S}\boldsymbol{t}_{|\Gamma}(\boldsymbol{x}), \quad \boldsymbol{x} \in \Omega^+, \tag{3.4}$$

where the single- and double-layer potential operators are defined by (2.20). The new unknowns of the scattering problem are thus the surface data $(\boldsymbol{u}_{|\Gamma}, \boldsymbol{t}_{|\Gamma})$. Several methods that are exact or approximate are proposed for computing the Neumann data $\boldsymbol{t}_{|\Gamma}$ knowing the Dirichlet one $\boldsymbol{u}_{|\Gamma}$, or inversely. Ideally, if we could explicit for a general shape the exact Dirichlet-to-Neumann map which is defined by

$$\begin{array}{rccc} \boldsymbol{\Lambda}^{\text{ex}} : & \boldsymbol{H}^{\frac{1}{2}}(\Gamma) & \to & \boldsymbol{H}^{-\frac{1}{2}}(\Gamma) \\ & \boldsymbol{u}_{|\Gamma} & \mapsto & \boldsymbol{t}_{|\Gamma} \end{array}, \tag{3.5}$$

the exterior problem (1.1)-(3.1)-(3.2) would be solved directly by the following representation

$$\boldsymbol{u}(\boldsymbol{x}) = -(\mathcal{D} - \mathcal{S}\boldsymbol{\Lambda}^{\text{ex}})\boldsymbol{u}^{\text{inc}}_{|\Gamma}(\boldsymbol{x}), \quad \boldsymbol{x} \in \Omega^+. \tag{3.6}$$

Unfortunately, using an exact expression of the DtN (in terms of elementary boundary integral operators) is too expensive. Instead, the idea is to derive a local approximate DtN map as accurate as possible. This approximation is usually reduced to a surface relation of the form

$$\mathcal{P}_1\boldsymbol{u}_{|\Gamma} + \mathcal{P}_2\boldsymbol{t}_{|\Gamma} = 0, \tag{3.7}$$

where $\mathcal{P}_1$ and $\mathcal{P}_2$ are two invertible local boundary operators. The advantage of such operators is to lead after discretization to sparse matrices.

### 3.1.1 Derivation of an approximate DtN for 3D elastodynamics

A key point to derive an approximation of the DtN map in 3D elastodynamics is to use the tangential Günter derivative $\boldsymbol{\mathcal{M}}$ defined by [Kupradze 1979]

$$\boldsymbol{\mathcal{M}} = \frac{\partial}{\partial \boldsymbol{n}} - \boldsymbol{n}\,\text{div} + \boldsymbol{n} \times \mathbf{curl}\,.$$

We also use the surface differential operators: the tangential gradient $\boldsymbol{\nabla}_\Gamma$, the surface divergence $\text{div}_\Gamma$, the surface scalar curl $\mathbf{curl}_\Gamma$, the tangential vector curl $\mathbf{curl}_\Gamma$, the scalar Laplace-Beltrami operator $\Delta_\Gamma$ and the vector Laplace-Beltrami operator $\boldsymbol{\Delta}_\Gamma$ [Nédélec 2001]. The tangential Günter derivative $\boldsymbol{\mathcal{M}}$ is then a surface derivative that can be rewritten

$$\boldsymbol{\mathcal{M}}\boldsymbol{u}_{|\Gamma} = \big([\boldsymbol{\nabla}_\Gamma \boldsymbol{u}_{|\Gamma}] - (\text{div}_\Gamma\, \boldsymbol{u}_{|\Gamma})\mathbf{I}_3\big)\boldsymbol{n}, \tag{3.8}$$

where $[\boldsymbol{\nabla}_\Gamma \boldsymbol{v}]$ is the matrix whose the $j$-th column is the tangential gradient of the $j$-th component of $\boldsymbol{v}$. In the following, it is convenient to rewrite the traction operator as

$$\mathbf{T} = \mathbf{2}\mu\boldsymbol{\mathcal{M}} + (\lambda + \mathbf{2}\mu)\,\boldsymbol{n}\,\text{div} - \mu\boldsymbol{n} \times \mathbf{curl}\,.$$

As a result, the Neumann trace of the displacement field $\boldsymbol{u}$ is expressed with the Dirichlet trace of $\boldsymbol{u}$ and of the Lamé potentials $\psi_p$ and $\boldsymbol{\psi}_s$ (1.3) as

$$\boldsymbol{t}_{|\Gamma} = 2\mu\boldsymbol{\mathcal{M}}\boldsymbol{u}_{|\Gamma} - \rho\omega^2\big(\boldsymbol{n}\,(\psi_p)_{|\Gamma} + \boldsymbol{n} \times (\boldsymbol{\psi}_s)_{|\Gamma}\big). \tag{3.9}$$

Then, (3.7) is considerably simplified if a surface relation between the data $\boldsymbol{u}_{|\Gamma}$ and $\boldsymbol{t}_{|\Gamma} - 2\mu\boldsymbol{\mathcal{M}}\boldsymbol{u}_{|\Gamma}$ of the form

$$\mathcal{Q}_1\boldsymbol{u}_{|\Gamma} + \mathcal{Q}_2(\boldsymbol{t}_{|\Gamma} - 2\mu\boldsymbol{\mathcal{M}}\boldsymbol{u}_{|\Gamma}) = 0 \tag{3.10}$$

is considered. It follows that $\mathcal{P}_1 = \mathcal{Q}_1 - 2\mu\mathcal{Q}_2\boldsymbol{\mathcal{M}}$, $\mathcal{P}_2 = \mathcal{Q}_2$. For an elastic half-space, we can derive exact non-local boundary relations of type (3.10) by using a Fourier analysis [5] and the exact DtN operator is given by

$$\boldsymbol{\Lambda}^{\text{ex}} = -\mathcal{P}_2^{-1}\mathcal{P}_1 = -\mathcal{Q}_2^{-1}\mathcal{Q}_1 + 2\mu\boldsymbol{\mathcal{M}}.$$

The following proposition gives two equivalent expressions for the DtN map.

**Proposition 3.1.1.** *For $\Gamma = \{\boldsymbol{x} \in \mathbb{R}^3 \mid x_1 = 0\}$, we have the following equivalent exact surface relations :*

*(i)* $\boldsymbol{u}_{|\Gamma} = \mathbf{V}\big(\boldsymbol{t}_{|\Gamma} - 2\mu\boldsymbol{\mathcal{M}}\boldsymbol{u}_{|\Gamma}\big)$, *with*

$$\mathbf{V} = \left(-\frac{1}{\rho\omega^2}\boldsymbol{\mathcal{M}} + \frac{1}{i\rho\omega^2}\left(\boldsymbol{n}(\Delta_\Gamma + \kappa_p^2\,\mathbf{I})^{\frac{1}{2}}\,\boldsymbol{n}\cdot\mathbf{I}_{\boldsymbol{n}} + (\boldsymbol{\Delta}_\Gamma + \kappa_s^2\,\mathbf{I}_{\boldsymbol{t}})^{-\frac{1}{2}}(\kappa_s^2\,\mathbf{I}_{\boldsymbol{t}} + \boldsymbol{\nabla}_\Gamma\,\mathrm{div}_\Gamma\,\mathbf{I}_{\boldsymbol{t}})\right)\right),$$

*(ii)* $\boldsymbol{\Lambda_1}\boldsymbol{u}_{|\Gamma} = (\mathbf{I} + \boldsymbol{\Lambda_2})\left(\boldsymbol{t}_{|\Gamma} - 2\mu\boldsymbol{\mathcal{M}}\boldsymbol{u}_{|\Gamma}\right)$, *with*

$$\boldsymbol{\Lambda_1} = i\rho\omega^2\left[\boldsymbol{n}\big(\Delta_\Gamma + \kappa_p^2\,\mathbf{I}\big)^{-\frac{1}{2}}\boldsymbol{n}\cdot\mathbf{I}_{\boldsymbol{n}} + \big(\boldsymbol{\Delta}_\Gamma + \kappa_s^2\,\mathbf{I}_{\boldsymbol{t}}\big)^{-\frac{1}{2}}\Big(\mathbf{I}_{\boldsymbol{t}} - \frac{1}{\kappa_s^2}\,\mathbf{curl}_\Gamma\,\mathbf{curl}_\Gamma\Big)\right], \tag{3.11}$$

*and*

$$\boldsymbol{\Lambda_2} = -i\Big(\boldsymbol{\nabla}_\Gamma\big(\Delta_\Gamma + \kappa_s^2\,\mathbf{I}\big)^{-\frac{1}{2}}\,\boldsymbol{n}\cdot\mathbf{I}_{\boldsymbol{n}} - \boldsymbol{n}\big(\Delta_\Gamma + \kappa_p^2\,\mathbf{I}\big)^{-\frac{1}{2}}\,\mathrm{div}_\Gamma\,\mathbf{I}_{\boldsymbol{t}}\Big), \tag{3.12}$$

*where we have defined* $\mathbf{I}_{\boldsymbol{n}} = \boldsymbol{n}\otimes\boldsymbol{n}$, $\mathbf{I}_{\boldsymbol{t}} = \mathbf{I} - \mathbf{I}_{\boldsymbol{n}}$.

These relations are non local and are valid only in the case of an elastic half-space. There exists two ways to construct such surface operators in the case of a general smooth surface: a formal one using a tangent plane approximation and a rigourous one applying the technique of microlocal diagonalization for hyperbolic systems [Engquist 1979]. These two approaches allow to obtain the surface approximations $(i)$ and $(ii)$ onto a general smooth surface $\Gamma$. In practice, we choose to consider the approximation $(ii)$ that is more judicious numerically speaking. Indeed, both surface relations require to invert some surface differential operators. The operator $\mathbf{V}$ in $(i)$ is of order $+1$ and the operator $(\mathbf{I} + \boldsymbol{\Lambda_2})$ in $(ii)$ is of order 0. The latter is thus more appropriate.

### 3.1.2 Regularization and localization of the approximate DtN map

Numerical experiments for the case of a spherical obstacle (for which analytical expressions of the solutions are available) have shown [5] that the approximation of the DtN map is very good for all the modes $m$, except in the transition zones for $m \approx \kappa_p$ and $m \approx \kappa_p$. These localized errors are due to the singularity that arises in the square-roots in (3.11) and (3.12). A solution to regularize the square-root operator consists in adding a small artificial damping parameter to the wavenumbers $\kappa_p$ and $\kappa_s$. We set $\kappa_{\alpha,\varepsilon} = \kappa_\alpha + i\varepsilon_\alpha$, with $\varepsilon_\alpha > 0$, $\alpha = p, s$. The new approximate DtN operator is written

$$\tilde{\boldsymbol{t}}_{|\Gamma} = \Big(\Big(\mathbf{I} + \boldsymbol{\Lambda}_{\mathbf{2},\varepsilon}\Big)^{-1}\boldsymbol{\Lambda}_{\mathbf{1},\varepsilon} + 2\mu\boldsymbol{\mathcal{M}}\Big)\boldsymbol{u}_{|\Gamma} \tag{3.13}$$

with

$$\boldsymbol{\Lambda}_{\mathbf{1},\varepsilon} = i\rho\omega^2\left[\boldsymbol{n}\big(\Delta_\Gamma + \kappa_{p,\varepsilon}^2\,\mathbf{I}\big)^{-\frac{1}{2}}\boldsymbol{n}\cdot\mathbf{I}_{\boldsymbol{n}} + \big(\boldsymbol{\Delta}_\Gamma + \kappa_{s,\varepsilon}^2\,\mathbf{I}_{\boldsymbol{t}}\big)^{-\frac{1}{2}}\Big(\mathbf{I}_{\boldsymbol{t}} - \frac{1}{\kappa_{s,\varepsilon}^2}\,\mathbf{curl}_\Gamma\,\mathbf{curl}_\Gamma\Big)\right], \tag{3.14}$$

and

$$\boldsymbol{\Lambda}_{\mathbf{2},\varepsilon} = -i\Big(\boldsymbol{\nabla}_\Gamma\big(\Delta_\Gamma + \kappa_{s,\varepsilon}^2\,\mathbf{I}\big)^{-\frac{1}{2}}\,\boldsymbol{n}\cdot\mathbf{I}_{\boldsymbol{n}} - \boldsymbol{n}\big(\Delta_\Gamma + \kappa_{p,\varepsilon}^2\,\mathbf{I}\big)^{-\frac{1}{2}}\,\mathrm{div}_\Gamma\,\mathbf{I}_{\boldsymbol{t}}\Big). \tag{3.15}$$

The question is then to choose the damping parameters in order to minimize the errors between the exact and approximate coefficients in the transition zone. Previous works in acoustics and electromagnetism have exhibited an optimal damping parameter by solving an optimization problem for a wavenumber sufficiently large. It seems natural to consider the same expression of the optimal parameters for elastodynamic problems as for the Helmholtz [Darbas 2004, Antoine 2006] and Maxwell [El Bouajaji 2014] exterior problems, given respectively by $\varepsilon_{p,A} = 0.39\kappa_p^{1/3}(\mathcal{H}^2)^{1/3}$ and $\varepsilon_{s,EM} = 0.39\kappa_s^{1/3}(\mathcal{H}^2)^{1/3}$, where $\mathcal{H}$ is the mean curvature of the boundary $\Gamma$. We have numerically observed that this choice improves the accuracy of the approximate DtN (3.13).

Another crucial point is to propose a local representation of the square-root operators involved in (3.14) and (3.15). To this end, we use complex rational Padé approximants of order $2L+1$ with

a rotating branch-cut technique of angle $\theta$ [Baker 1996, Lu 1998, Milinazzo 1997, Antoine 2006]: for $z \in \mathbb{C}$, one has

$$(1+z)^{-1/2} \approx \frac{P_L(z)}{Q_L(z)} = r_0 + \sum_{\ell=1}^{L} \frac{r_\ell}{z - q_\ell}$$

where $P_L$ and $Q_L$ are two polynomials of degree $L$. The complex coefficients $r_\ell$, $\ell = 0, \ldots, L$, and $q_\ell$, $\ell = 1, \ldots, L$ depend on the angle $\theta$. The notation $z^{1/2}$ designates the principal determination of the square-root of a complex number $z$ with branch-cut along the negative real axis. The use of Padé approximants leads to the following relation on a general surface $\Gamma$

$$\tilde{\boldsymbol{t}}_{|\Gamma}^{\text{Pade}} = \Big(\Big(\mathbf{I} + \widetilde{\boldsymbol{\Lambda}}_{\mathbf{2},\varepsilon}\Big)^{-1} \widetilde{\boldsymbol{\Lambda}}_{\mathbf{1},\varepsilon} + 2\mu\boldsymbol{\mathcal{M}}\Big)\boldsymbol{u}_{|\Gamma} \tag{3.16}$$

where the local representations of the operators $\boldsymbol{\Lambda}_{\mathbf{1},\varepsilon}$ and $\boldsymbol{\Lambda}_{\mathbf{2},\varepsilon}$ are given respectively by

$$\begin{aligned} \widetilde{\boldsymbol{\Lambda}}_{\mathbf{1},\varepsilon} &= i\rho\omega^2\Big[\frac{1}{\kappa_{p,\varepsilon}}\boldsymbol{n}\Big(r_0\mathbf{I} + \sum_{\ell=1}^{L} r_\ell\Big(\frac{\Delta_\Gamma}{\kappa_{p,\varepsilon}^2} - q_\ell\mathbf{I}\Big)^{-1}\Big)\boldsymbol{n}\cdot\mathbf{I}_{\boldsymbol{n}} \\ &+ \frac{1}{\kappa_{s,\varepsilon}}\Big(r_0\mathbf{I} + \sum_{\ell=1}^{L} r_\ell\Big(\mathbf{L} - q_\ell\mathbf{I}\Big)^{-1}\Big)\Big(\mathbf{I}_{\boldsymbol{t}} - \mathbf{curl}_\Gamma\frac{1}{\kappa_{s,\varepsilon}^2}\mathbf{curl}_\Gamma\Big)\Big] \text{ and} \end{aligned} \tag{3.17}$$

$$\begin{aligned} \widetilde{\boldsymbol{\Lambda}}_{\mathbf{2},\varepsilon} &= i\Big[-\frac{1}{\kappa_{p,\varepsilon}}\boldsymbol{\nabla}_\Gamma\Big(r_0\mathbf{I} + \sum_{\ell=1}^{L} r_\ell\Big(\frac{\Delta_\Gamma}{\kappa_{p,\varepsilon}^2} - q_\ell\mathbf{I}\Big)^{-1}\Big)\boldsymbol{n}\cdot\mathbf{I}_{\boldsymbol{n}} \\ &+ \frac{1}{\kappa_{s,\varepsilon}}\boldsymbol{n}\Big(r_0\mathbf{I} + \sum_{\ell=1}^{L} r_\ell\Big(\frac{\Delta_\Gamma}{\kappa_{s,\varepsilon}^2} - q_\ell\mathbf{I}\Big)^{-1}\Big)\ \mathrm{div}_\Gamma\,\mathbf{I}_{\boldsymbol{t}}\Big] \end{aligned} \tag{3.18}$$

with $\mathbf{L} := \boldsymbol{\nabla}_\Gamma\frac{1}{\kappa_{s,\varepsilon}^2}\mathrm{div}_\Gamma - \mathbf{curl}_\Gamma\frac{1}{\kappa_{s,\varepsilon}^2}\mathbf{curl}_\Gamma$.

### 3.1.3 Application of the approximate local DtN: the OSRC method for 3D elastodynamics

One possible application of the approximate DtN (3.16) is as an OSRC [Antoine 2001] [El Bouajaji 2014, Kriegsmann 1987] to solve approximately the exterior Navier problem (1.1)-(3.1)-(3.2). The method consists in considering the boundary differential equation

$$\tilde{\boldsymbol{t}}_{|\Gamma} = -\Big(\Big(\mathbf{I} + \widetilde{\boldsymbol{\Lambda}}_{\mathbf{2},\varepsilon}\Big)^{-1} \widetilde{\boldsymbol{\Lambda}}_{\mathbf{1},\varepsilon} + 2\mu\boldsymbol{\mathcal{M}}\Big)\boldsymbol{u}_{|\Gamma}^{\text{inc}}, \tag{3.19}$$

directly on the physical surface $\Gamma$. The approximation of the DtN map is evaluated by solving a set of local differential equations posed on $\Gamma$ (i.e. on the boundary similarly to BEMs). The solution of the sparse linear systems (contrary to BEMs that lead to dense systems) associated with the discretization of (3.32) gives an approximation of the trace $\tilde{\boldsymbol{t}}_{|\Gamma}$, and hence of the scattered field

$$\boldsymbol{u}(\boldsymbol{x}) \approx -\mathcal{D}\boldsymbol{u}_{|\Gamma}^{\text{inc}}(\boldsymbol{x}) - \mathcal{S}\tilde{\boldsymbol{t}}_{|\Gamma}(\boldsymbol{x}), \quad \boldsymbol{x} \in \Omega^+. \tag{3.20}$$

Similarly, the approximate far-field pattern is computed via the integral representation formula

$$\boldsymbol{u}^\infty(\hat{\boldsymbol{x}}) \approx -\mathscr{F}_{\text{D}}\boldsymbol{u}_{|\Gamma}^{\text{inc}}(\hat{\boldsymbol{x}}) - \mathscr{F}_{\text{S}}\tilde{\boldsymbol{t}}_{|\Gamma}(\hat{\boldsymbol{x}}) \tag{3.21}$$

where the far-field operators $\mathscr{F}_{\text{S}}$ and $\mathscr{F}_{\text{D}}$ are defined by

$$\mathscr{F}_{\text{S}}\boldsymbol{\varphi}(\hat{\boldsymbol{x}}) = \int_\Gamma \left(\frac{1}{\mu}[\mathbf{I}_{\mathbb{R}^3} - \hat{\boldsymbol{x}}\otimes\hat{\boldsymbol{x}}]\frac{e^{-i\kappa_s\hat{\boldsymbol{x}}\cdot\boldsymbol{y}}}{4\pi} + \frac{1}{\lambda+2\mu}[\hat{\boldsymbol{x}}\otimes\hat{\boldsymbol{x}}]\frac{e^{-i\kappa_p\hat{\boldsymbol{x}}\cdot\boldsymbol{y}}}{4\pi}\right)\boldsymbol{\varphi}(\boldsymbol{y})\,ds(\boldsymbol{y}) \quad \text{and}$$

$$\mathscr{F}_{\text{D}}\boldsymbol{\varphi}(\hat{\boldsymbol{x}}) = \int_\Gamma \left(\frac{1}{\mu}\left[\mathbf{T}_{\boldsymbol{y}}[\mathbf{I}_{\mathbb{R}^3} - \hat{\boldsymbol{x}}\otimes\hat{\boldsymbol{x}}]\frac{\mathbf{e}^{-\mathbf{i}\kappa_{\mathbf{s}}\hat{\mathbf{x}}\cdot\mathbf{y}}}{\mathbf{4}\pi}\right]^{\mathsf{T}} + \frac{1}{\lambda+2\mu}\left[\mathbf{T}_{\boldsymbol{y}}[\hat{\boldsymbol{x}}\otimes\hat{\boldsymbol{x}}]\frac{\mathbf{e}^{-\mathbf{i}\kappa_{\mathbf{p}}\hat{\mathbf{x}}\cdot\mathbf{y}}}{\mathbf{4}\pi}\right]^{\mathsf{T}}\right)\boldsymbol{\varphi}(\boldsymbol{y})\,ds(\boldsymbol{y}).$$

Obviously, the efficiency of the OSRC method is obtained at the expense of the accuracy. Thus it is less accurate than integral equation methods but it is extremely faster. Its numerical efficiency is related to the (limited) level of accuracy required in the approximate DtN operator. We have demonstrated in [5] that the OSRC method is nevertheless a very interesting tool to analyze high-frequency scattering phenomena.

As an illustration of the accuracy of the method, we consider the scattering of incident elastic plane waves of the form (3.3) by different obstacles. We compute the Neumann trace of the scattered field $\boldsymbol{u}$ (3.20) and the bistatic Scattering Cross Section (SCS) [Alves 1997]:

$$\mathrm{SCS}(\theta,\phi) = 10\log_{10}(4\pi|\boldsymbol{u}^{\infty}(\hat{\boldsymbol{x}}(\theta,\phi))|^2) \quad (\mathrm{dB}), \tag{3.22}$$

where the points $\hat{\boldsymbol{x}} \in \mathbf{S}^2$ are defined by $\hat{\boldsymbol{x}} := \hat{\boldsymbol{x}}(\theta,\phi) = (\sin(\theta)\cos(\phi), \sin(\theta)\sin(\phi), \cos(\theta))$. We consider several geometries: a unit sphere, an ellipsoid and a semi-concave sphere (Fig. 3.3a). We denote by $n_{\lambda_s} = \lambda_s/h$ the density of discretization points per S-wavelength where $h$ is the average length of the edges of the triangles. Table 3.1 summarises the parameters used in the simulations.

***Table 3.1:*** *Important Parameters of the OSRC and corresponding fixed values.*

| Parameters | $\varepsilon_s$ | $\varepsilon_p$ | $L$ | $\theta$ | tol |
|---|---|---|---|---|---|
| Values | $0.4\kappa_s^{1/3}(\mathcal{H}^2)^{1/3}$ | $0.4\kappa_p^{1/3}(\mathcal{H}^2)^{1/3}$ | 4 | $\pi/2$ | 1.e-03 |

We consider first the ideal configuration of a unit sphere and incident plane P-waves or S-waves. The OSRC-based solution is compared to the analytical solution. We also add the analytical OSRC-based solution, which represents the best solution that we can expect when using the OSRC. Figure 3.1 represents the $\mathrm{SCS}(\theta, 0)$ (for $\kappa_s = 8\pi$ and $\kappa_s = 16\pi$). We observe a good agreement between the analytical and computed OSRC-based surface fields. In addition, the OSRC method allows a correct approximation of the reference exact solution. In the case $\kappa_s = 16\pi$ (corresponding to $n_{\lambda_s} = 8$), some oscillations appear in the OSRC solution. This is due to the small density of points per wavelength. However, the principal informations on the SCS are still well reproduced

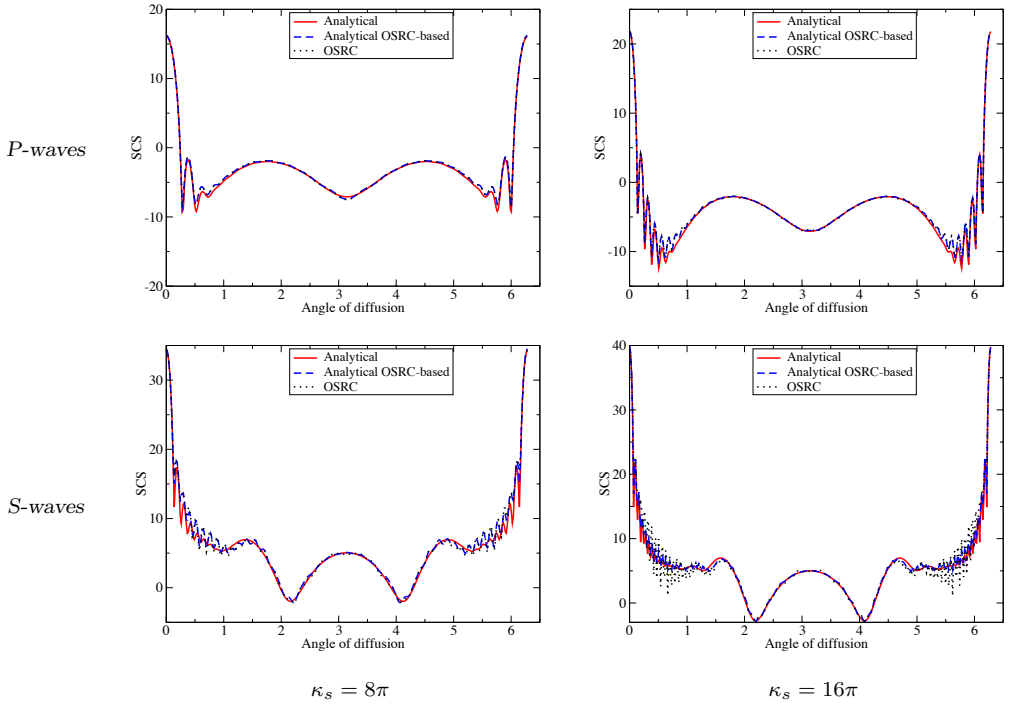


***Figure 3.1:*** *Diffraction of plane P-waves ($\boldsymbol{p} = \mathbf{e}^r = (0,0,1)^T$) and S-waves ($\mathbf{e}^r = (0,0,1)^T$, $\boldsymbol{p} = (1,0,0)^T$) by a unit sphere (for $\kappa_s = 8\pi,\ 16\pi$): comparison of the SCS for the analytical, analytical OSRC-based and the OSRC-based solutions.*

and a better accuracy is expected if a finer mesh is used.

We have then considered the scattering of plane waves by an ellipsoid (with $\kappa_s = 8\pi$, $N = 40\ 962$). We report in Figure 3.2 the SCS computed with a spectral method [Le Louër 2014] (considered as the reference one) and the SCS obtained with the OSRC method. Even for this more complex geometry of scatterer, the SCS is correctly reproduced. The only minor errors occur in the shadow zone.

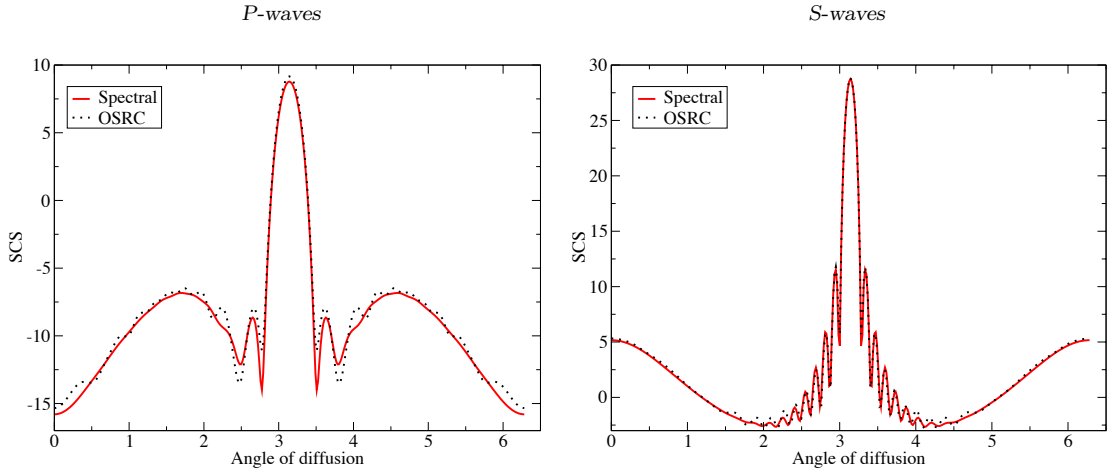


***Figure 3.2:*** *Diffraction of plane P-waves ($\mathbf{e}^r = (-1,0,0)^T$, $\boldsymbol{p} = (1,0,0)^T$) and S-waves ($\mathbf{e}^r = (0,0,-1)^T$, $\boldsymbol{p} = (0,1,0)^T$) by an ellipsoid ($\kappa_s = 8\pi$): comparison of the SCS for the OSRC-based solution and the spectral method-based solution.*

The last obstacle we have considered is the semi concave sphere. This trapping domain is known to be more difficult for the OSRC method [Antoine 2001, El Bouajaji 2014]. The data are incident plane P-waves with $\boldsymbol{p} = \mathbf{e}^r = (-1,0,0)^T$ and $\kappa_s = 8\pi$. This test corresponds to an incident wave that hits the concave part of the obstacle. The reference solution is computed using the FM-BEM [14] (presented in Chapter 1). We compute $\mathrm{SCS}(\theta, 0)$ with $\theta \in [0, 2\pi]$. We report in Fig. 3.3b the SCS. As expected, the accuracy on the SCS is better in the convex (sphere) part than in the cavity part.

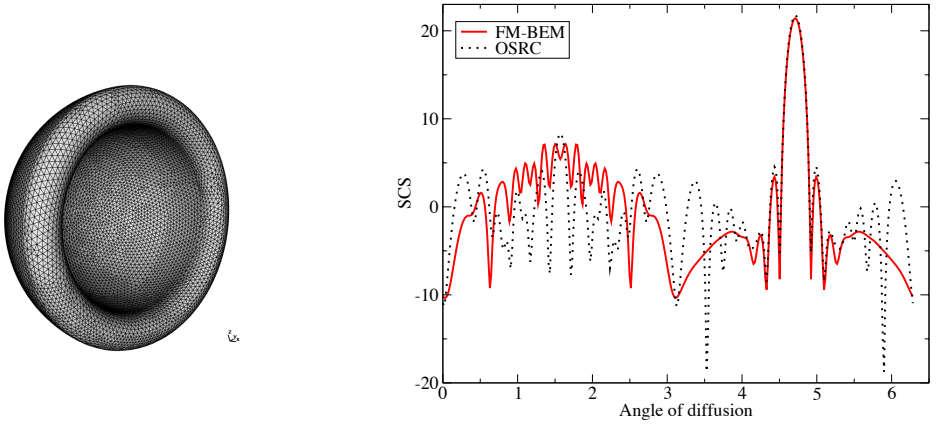


***(a)*** *Geometry of the semi-concave sphere* ***(b)*** *SCS*

***Figure 3.3:*** *Diffraction of incident plane P-waves by a semi concave sphere ($\kappa_s = 8\pi$).*

All these numerical experiments have demonstrated the potentialities of these approximations of the DtN to derive analytic preconditioners.

## 3.2 Analytic preconditioners for 3D elastodynamics FM-BEM

Once the OSRC validated for 3D elastodynamics, we have used the principal of high order approximations of the DtN to precondition the FM-BEM. The numerical efficiency of this combination between an OSRC-based preconditioner (i.e. analytic) and the FM-BEM solver has been validated for 3D high-frequency problems. The number of iterations is shown to be independent of the mesh density and frequency for various geometries (including complex geometries) in [3].

### 3.2.1 Approximation of the adjoint DtN operator for well-conditioned boundary integral equations

**Modified Boundary Integral Equations.** The DtN map introduced in [5] involves the need to invert the operator $\left(\mathbf{I}+\widetilde{\mathbf{\Lambda}}_{\mathbf{2},\varepsilon}\right)$. In the context of the OSRC it is not a major drawback since it is inverted only once. In the context of analytic preconditioners, it is a more serious problem since this inversion is needed at each iteration of GMRES. The approximation of the DtN (3.16) comes from a more general context presented in [Darbas 2015] that uses the modified theory of potentials. We introduce the modified Neumann trace $\boldsymbol{t}_\alpha \in \boldsymbol{H}^{-\frac{1}{2}}(\Gamma)$ defined for any real-valued constant $\alpha$ by

$$\boldsymbol{t}_\alpha = \boldsymbol{t}_{|\Gamma} - \alpha \boldsymbol{\mathcal{M}} \boldsymbol{u}_{|\Gamma} \ .$$

The double-layer potential operator is defined accordingly by

$$\mathcal{D}_\alpha \boldsymbol{\psi} = \int_\Gamma [(\mathbf{T}_{\boldsymbol{y}} - \alpha \boldsymbol{\mathcal{M}}) \mathbf{\Phi}(\cdot\,, \boldsymbol{y})]^{\mathsf{T}} \boldsymbol{\psi}(\boldsymbol{y}) ds(\boldsymbol{y}), \tag{3.23}$$

The traces of the single and double-layer potentials are given by applying the exterior Dirichlet and Neumann-type trace to $\mathcal{S}$ and $\mathcal{D}_\alpha$ such that we have [Darbas 2015]

$$\begin{aligned} \big((\mathbf{T} - \alpha \boldsymbol{\mathcal{M}}) \mathcal{S} \boldsymbol{\varphi}\big)_{|\mathbf{\Gamma}} &= -\frac{\mathbf{1}}{\mathbf{2}} \boldsymbol{\varphi} + \mathbf{D}_\alpha^{'} \boldsymbol{\varphi}, \\ (\mathcal{D}_\alpha \boldsymbol{\psi})_{|\Gamma} &= \frac{1}{2} \boldsymbol{\psi} + D_\alpha \boldsymbol{\psi}, \quad \text{and } \big((\mathbf{T} - \alpha \boldsymbol{\mathcal{M}}) \mathcal{D}_\alpha \boldsymbol{\psi}\big)_{|\mathbf{\Gamma}} = \mathbf{N}_\alpha \boldsymbol{\psi}, \end{aligned} \tag{3.24}$$

where I is the identity operator. Given vector densities $\boldsymbol{\varphi}$ and $\boldsymbol{\psi}$, the boundary integral operators $D_\alpha$, $D_\alpha^{'}$ and $N_\alpha$ are defined, for $\boldsymbol{x} \in \Gamma$, by

$$\begin{aligned} D_\alpha \boldsymbol{\psi}(\boldsymbol{x}) &= \int_\Gamma [(\mathbf{T}_{\boldsymbol{y}} - \alpha \boldsymbol{\mathcal{M}}) \mathbf{\Phi}(\boldsymbol{x}, \boldsymbol{y})]^{\mathsf{T}} \boldsymbol{\psi}(\boldsymbol{y})\, ds(\boldsymbol{y}), \\ D_\alpha^{'} \boldsymbol{\varphi}(\boldsymbol{x}) &= \int_\Gamma (\mathbf{T}_{\boldsymbol{x}} - \alpha \boldsymbol{\mathcal{M}}) \left\{ \mathbf{\Phi}(\boldsymbol{x}, \boldsymbol{y}) \boldsymbol{\varphi}(\boldsymbol{y}) \right\} \mathbf{ds}(\boldsymbol{y}), \\ N_\alpha \boldsymbol{\psi}(\boldsymbol{x}) &= \int_\Gamma (\mathbf{T}_{\boldsymbol{x}} - \alpha \boldsymbol{\mathcal{M}}) \left\{ [(\mathbf{T}_{\boldsymbol{y}} - \alpha \boldsymbol{\mathcal{M}}) \mathbf{\Phi}(\boldsymbol{x}, \boldsymbol{y})]^{\mathsf{T}} \boldsymbol{\psi}(\boldsymbol{y}) \right\} \mathbf{ds}(\boldsymbol{y}). \end{aligned}$$

The operators $D_\alpha$ and $D_\alpha^{'}$ are of order 0, i.e. they have a strongly singular kernel and are bounded from $\boldsymbol{H}^{\frac{1}{2}}(\Gamma)$ and $\boldsymbol{H}^{-\frac{1}{2}}(\Gamma)$ to themselves, respectively. The operator $N_\alpha$ is of order 1, i.e. it has a hypersingular kernel and is bounded from $\boldsymbol{H}^{\frac{1}{2}}(\Gamma)$ to $\boldsymbol{H}^{-\frac{1}{2}}(\Gamma)$. We consider again the direct method based on the following integral representation formula

$$\boldsymbol{u} = -\mathcal{S}\big(\boldsymbol{t}_{|\Gamma} + \boldsymbol{t}_{|\Gamma}^{inc}\big) \,,$$

with $\boldsymbol{t}_{|\Gamma}^{inc} = \mathbf{T}\boldsymbol{u}^{\mathbf{inc}}$. Taking the exterior Dirichlet and Neumann-type traces of the right hand side, we obtain on $\Gamma$

$$S\big(\boldsymbol{t}_{|\Gamma} + \boldsymbol{t}_{|\Gamma}^{inc}\big) = -\boldsymbol{u}_{|\Gamma} = \boldsymbol{u}_{|\Gamma}^{inc} \quad \text{and} \quad (-\frac{\mathbf{I}}{2} + D_\alpha^{'})\big(\boldsymbol{t}_{|\Gamma} + \boldsymbol{t}_{|\Gamma}^{inc}\big) = -\boldsymbol{t}_\alpha \Leftrightarrow (\frac{\mathbf{I}}{2} + D_\alpha^{'})\big(\boldsymbol{t}_{|\Gamma} + \boldsymbol{t}_{|\Gamma}^{inc}\big) = \boldsymbol{t}_\alpha^{inc} \,.$$

Combining the previous two equations, we construct the modified CFIE: find the physical unknown $\boldsymbol{\varphi} = -\big(\boldsymbol{t}_{|\Gamma} + \boldsymbol{t}^{inc}_{|\Gamma}\big) \in \boldsymbol{H}^{-\frac{1}{2}}(\Gamma)$ solution to

$$(\frac{\mathbf{I}}{2} + D^{'}_{\alpha} + i\eta S)\boldsymbol{\varphi} = -\big(\boldsymbol{t}^{inc}_{\alpha} + i\eta \boldsymbol{u}^{inc}_{|\Gamma}\big), \quad \text{on } \Gamma, \tag{3.25}$$

with $\eta$ a non-zero real constant. The integral equation (3.25) is well-posed for any frequency $\omega$ and any non-zero real parameter $\eta$ [Kupradze 1979]. The choice $\alpha = 0$ leads to the standard CFIE

$$(\frac{\mathbf{I}}{2} + D^{'} + i\eta S)\boldsymbol{\varphi} = -\big(\boldsymbol{t}^{inc} + i\eta \boldsymbol{u}^{inc}_{|\Gamma}\big), \quad \text{on } \Gamma, \tag{3.26}$$

which is the most stable integral equation and thus it is considered as the reference one in the following. The OSRC corresponds to the simpliest case $\alpha = 2\mu$. However, Hähner and Hsiao [Hähner 1993] have shown that for $\alpha = \alpha_{HH} := (2\mu^2)/(\lambda + 3\mu)$, the CFIE (3.25) (called Hähner-Hsiao CFIE in the sequel) is of the second-kind for any positive real-valued parameter $\eta$. It thus leads to the inversion of a perturbation of the identity.

**Well-conditioned Boundary Integral Equations.** It is well known that the standard CFIE is not suited for an iterative solution. Even though the Hähner-Hsiao CFIE is more adapted (because of second kind), CFIE (3.25) does not provide sufficiently good spectral properties at high frequencies. To expect an eigenvalue clustering and hence a fast convergence of GMRES, we need to derive well-conditioned boundary integral equations. Similarly to the OSRC method, we use an approximation of the adjoint DtN map. However, to improve the computational efficiency of the method, we use the modified integral equations to derive the high order approximation. The exact exterior Modified Dirichlet-to-Neumann (MDtN) map is defined by

$$\boldsymbol{\Lambda}^{\text{ex}}_{\alpha} : \boldsymbol{u}_{|\Gamma} \in \boldsymbol{H}^{\frac{1}{2}}(\Gamma) \mapsto \boldsymbol{\Lambda}^{\text{ex}}_{\alpha}\boldsymbol{u}_{|\Gamma} := \boldsymbol{t}_{\alpha} \in \boldsymbol{H}^{-\frac{1}{2}}(\Gamma)\,.$$

We consider the following boundary integral equation

$$\frac{\mathbf{I}}{2} + D^{'}_{\alpha} - \boldsymbol{\Lambda}^{\text{ex}'}_{\alpha} S = \mathbf{I}, \tag{3.27}$$

that is related to the CFIE (3.25). The adjoint MDtN map $\boldsymbol{\Lambda}^{\text{ex}'}_{\alpha} : \boldsymbol{H}^{\frac{1}{2}}(\Gamma) \to \boldsymbol{H}^{-\frac{1}{2}}(\Gamma)$ satisfies

$$\boldsymbol{\Lambda}^{\text{ex}'} = \boldsymbol{\Lambda}^{\text{ex}'}_{\alpha} + \alpha\boldsymbol{\mathcal{M}}. \tag{3.28}$$

Assume that $\omega$ is not an eigenfrequency of the Navier equation (1.1) in $\Omega^-$ with either the Dirichlet or the Neumann homogeneous boundary condition, the adjoint MDtN map is expressed in terms of boundary integral operators on $\Gamma$ by

$$\boldsymbol{\Lambda}^{\text{ex}'}_{\alpha} = -(\frac{1}{2}\mathbf{I} - D'_{\alpha})S^{-1} = (\frac{1}{2}\mathbf{I} + D'_{\alpha})^{-1}N_{\alpha}. \tag{3.29}$$

In the ideal configuration (3.27), the solution $\boldsymbol{\varphi} = -\big(\boldsymbol{t}^{inc}_{\alpha} - \boldsymbol{\Lambda}^{\text{ex}'}_{\alpha}\boldsymbol{u}^{inc}_{|\Gamma}\big)$ is obtained directly. However, it is too expensive to consider the exact operator (3.29) for a numerical purpose. Instead, an approximation $\boldsymbol{\Lambda}'_{\alpha}$ of $\boldsymbol{\Lambda}^{\text{ex}'}_{\alpha}$, given in terms of surface differential operators, is introduced to construct a preconditioned CFIE : Find $\boldsymbol{\varphi} = -\big(\boldsymbol{t}_{|\Gamma} + \boldsymbol{t}^{inc}_{|\Gamma}\big)$ solution to

$$(\frac{\mathbf{I}}{2} + D^{'}_{\alpha} - \boldsymbol{\Lambda}'_{\alpha}S)\boldsymbol{\varphi} = -\big(\boldsymbol{t}^{inc}_{\alpha} - \boldsymbol{\Lambda}'_{\alpha}\boldsymbol{u}^{inc}_{|\Gamma}\big), \quad \text{on } \Gamma. \tag{3.30}$$

Coming back to the standard case $\alpha = 0$, solving equation (3.30) is equivalent to solving

$$(\frac{\mathbf{I}}{2} + D^{'} - \boldsymbol{\Lambda}'S)\boldsymbol{\varphi} = -\big(\boldsymbol{t}^{inc}_{|\Gamma} - \boldsymbol{\Lambda}'\boldsymbol{u}^{inc}_{|\Gamma}\big), \quad \text{on } \Gamma, \tag{3.31}$$

where the approximate adjoint DtN map is given by the formula $\boldsymbol{\Lambda}' = \boldsymbol{\Lambda}'_{\alpha} + \alpha\boldsymbol{\mathcal{M}}$.

**Proposed approximations of the DtN operator.** The spectral properties of (3.31) depend on the choice of the approximate adjoint DtN map $\mathbf{\Lambda}'$. We want to compare several approximations of different orders. The idea is again to consider only the principal part of the exact adjoint operator $\mathbf{\Lambda}_\alpha^{\mathrm{ex}'}$ and the judicious decomposition (3.29). The approximation is defined by

$$\left\{\begin{array}{l} \mathbf{\Lambda}'_\alpha = \Big(\dfrac{\mathbf{I}}{2} + P(D'_\alpha)\Big)^{-1} P(N_\alpha), \\ \mathbf{\Lambda}' = \mathbf{\Lambda}'_\alpha + \alpha \boldsymbol{\mathcal{M}}, \end{array}\right. \tag{3.32}$$

where the operators $P(D'_\alpha)$ and $P(N_\alpha)$ are respectively the principal parts of the boundary integral operators $D'_\alpha$ and $N_\alpha$. The operator $\mathbf{\Lambda}'$ depends on $\alpha$ that has to be choosen to reduce the computational cost to obtain $\big(\frac{\mathbf{I}}{2} + P(D'_\alpha)\big)^{-1}$.

In [3], we provide explicit expressions of the principal parts $P(D'_\alpha)$ and $P(N_\alpha)$. The operator $P(D'_\alpha)$ is decomposed into two terms: $P(D'_\alpha) = I_1 + I_2$ with

$$\begin{aligned} I_1 &= \frac{i}{2}\Big(\boldsymbol{n}\big(\Delta_\Gamma + \kappa_p^2\mathbf{I}\big)^{-\frac{1}{2}} \operatorname{div}_\Gamma \mathbf{I}_{\boldsymbol{t}} - \boldsymbol{\nabla}_\Gamma\big(\Delta_\Gamma + \kappa_s^2\mathbf{I}\big)^{-\frac{1}{2}} \boldsymbol{n}\cdot\mathbf{I}_{\boldsymbol{n}}\Big) \\ I_2 &= \frac{i(2\mu-\alpha)}{2\rho\omega^2}\Big( -\boldsymbol{n}\big(\Delta_\Gamma + \kappa_s^2\mathbf{I}\big)^{\frac{1}{2}} \operatorname{div}_\Gamma \mathbf{I}_{\boldsymbol{t}} + \boldsymbol{n}\Delta_\Gamma\big(\Delta_\Gamma + \kappa_p^2\mathbf{I}\big)^{-\frac{1}{2}} \operatorname{div}_\Gamma \mathbf{I}_{\boldsymbol{t}} \\ &\qquad +\boldsymbol{\nabla}_\Gamma\big(\Delta_\Gamma + \kappa_p^2\mathbf{I}\big)^{\frac{1}{2}}\big(\boldsymbol{n}\cdot\mathbf{I}_{\boldsymbol{n}}\big) - \boldsymbol{\nabla}_\Gamma\big(\Delta_\Gamma + \kappa_s^2\mathbf{I}\big)^{-\frac{1}{2}}\Delta_\Gamma\big(\boldsymbol{n}\cdot\mathbf{I}_{\boldsymbol{n}}\big)\Big) \end{aligned} \tag{3.33}$$

where $\mathbf{I}_{\boldsymbol{n}} = \boldsymbol{n}\otimes\boldsymbol{n}$ and $\mathbf{I}_{\boldsymbol{t}} = \mathbf{I} - \mathbf{I}_{\boldsymbol{n}}$. The operator $P(N_\alpha)$ is decomposed into three terms $P(N_\alpha) = J_1 + J_2 + J_3$ by setting

$$\begin{aligned} J_1 &= \frac{i}{2}\Big((\lambda+2\mu)\kappa_p^2\,\boldsymbol{n}\big(\Delta_\Gamma + \kappa_p^2\mathbf{I}\big)^{-\frac{1}{2}}\boldsymbol{n}\cdot\mathbf{I}_{\boldsymbol{n}} + \mu\big(\boldsymbol{\Delta}_\Gamma + \kappa_s^2\mathbf{I}\big)^{-\frac{1}{2}}\Big(\kappa_s^2\mathbf{I}_{\boldsymbol{t}} - \mathbf{curl}_\Gamma\,\mathbf{curl}_\Gamma\Big)\Big) \\ J_2 &= -i(\alpha-2\mu)\Big(\boldsymbol{\nabla}_\Gamma\big(\Delta_\Gamma + \kappa_s^2\mathbf{I}\big)^{-\frac{1}{2}} \operatorname{div}_\Gamma \mathbf{I}_{\boldsymbol{t}} + \boldsymbol{n}\,\Delta_\Gamma\big(\Delta_\Gamma + \kappa_p^2\mathbf{I}\big)^{-\frac{1}{2}}\boldsymbol{n}\cdot\mathbf{I}_{\boldsymbol{n}}\Big) \\ J_3 &= \frac{i((\alpha-2\mu)^2}{2\rho\omega^2}\Big( -\boldsymbol{n}\big(\Delta_\Gamma + \kappa_s^2\mathbf{I}\big)^{\frac{1}{2}}\Delta_\Gamma\big(\boldsymbol{n}\cdot\mathbf{I}_{\boldsymbol{n}}\big) + \boldsymbol{n}\,\Delta_\Gamma\big(\Delta_\Gamma + \kappa_p^2\mathbf{I}\big)^{-\frac{1}{2}}\Delta_\Gamma\big(\boldsymbol{n}\cdot\mathbf{I}_{\boldsymbol{n}}\big) \\ &\quad -\boldsymbol{\nabla}_\Gamma\big(\Delta_\Gamma + \kappa_p^2\mathbf{I}\big)^{\frac{1}{2}} \operatorname{div}_\Gamma \mathbf{I}_{\boldsymbol{t}} + \boldsymbol{\nabla}_\Gamma\big(\Delta_\Gamma + \kappa_s^2\mathbf{I}\big)^{-\frac{1}{2}}\Delta_\Gamma \operatorname{div}_\Gamma \mathbf{I}_{\boldsymbol{t}}\Big). \end{aligned} \tag{3.34}$$

From (3.32), we derive three different preconditioned CFIEs:

- the *Low-Order preconditioned CFIE* (LO P-CFIE): we retain in (3.32) the informations associated to the first eigenmode of the scalar and vector Laplacian Beltrami operators only:

$$\mathbf{\Lambda}' := \mathbf{\Lambda}'_{\mathrm{LO}} = i((\lambda+2\mu)\kappa_p\mathbf{I}_{\boldsymbol{n}} + \mu\kappa_s\mathbf{I}_{\boldsymbol{t}}). \tag{3.35}$$

  The associated preconditioned integral equation is

$$(\frac{\mathbf{I}}{2} + D' - \mathbf{\Lambda}'_{\mathrm{LO}}S)\boldsymbol{\varphi} = -\big(\boldsymbol{t}^{inc}_{|\Gamma} - \mathbf{\Lambda}'_{\mathrm{LO}}\boldsymbol{u}^{inc}_{|\Gamma}\big), \quad \text{on } \Gamma. \tag{3.36}$$

  This preconditioner is easy to implement and this is its main advantage. By construction, this approximation provides a good clustering of the first eigenvalues (associated with propagating modes) only but we need high-order approximations to also cluster grazing and evanescent modes, and then to obtain a more efficient preconditioner.

- the *High-Order preconditioned CFIE with two terms* (HO(2) P-CFIE): the approximation $\mathbf{\Lambda}'$ (3.32) depends on the parameter $\alpha$ and thus provides an infinity of high-order approximate adjoint DtN maps. Among all the possible values of $\alpha$, we choose $\alpha = \alpha_{HH}$ for which the operator $D_\alpha$ and its adjoint are compact. This choice leads to good spectral properties of the corresponding preconditioned integral equations (3.31).

- the *High-Order preconditioned CFIE with one term* (HO(1) P-CFIE): previous investigations in acoustics would suggest that the use of the operator $P(N_\alpha)$, i.e

$$\mathbf{\Lambda}' = 2P(N_\alpha) + \alpha\boldsymbol{\mathcal{M}}, \tag{3.37}$$

  is sufficient to take into account all the modes. We will show that the operator $P(N_\alpha)$ enables the clustering of eigenvalues associated with the propagating and evanescent modes only, while the operator $(\mathbf{I}/2 + P(D'_\alpha))$ is necessary to deal with the grazing modes.

Similarly to the OSRC method, we add a small damping parameter to regularize and use Padé approximants with a rotating branch cut to localise the square root operator.

### 3.2.2 Numerical efficiency of the proposed analytical preconditioners

To study the efficiency of the different proposed preconditioned CFIEs, we consider several more or less complex geometries: a unit sphere, an ellipsoid, a cube and a sphere with cavity (Fig. 3.4). In all our simulations, the mechanical parameters are normalised and defined such that the wavenumbers satisfy $\kappa_s = 1.5\kappa_p$. The density of points per S-wavelength $\lambda_s = 2\pi/\kappa_s$ is fixed to about $n_{\lambda_s} = 10$, i.e. the usual criterion for high-frequency applications. The parameters of Padé approximants are fixed to $(L, \theta) = (35, \pi/3)$.

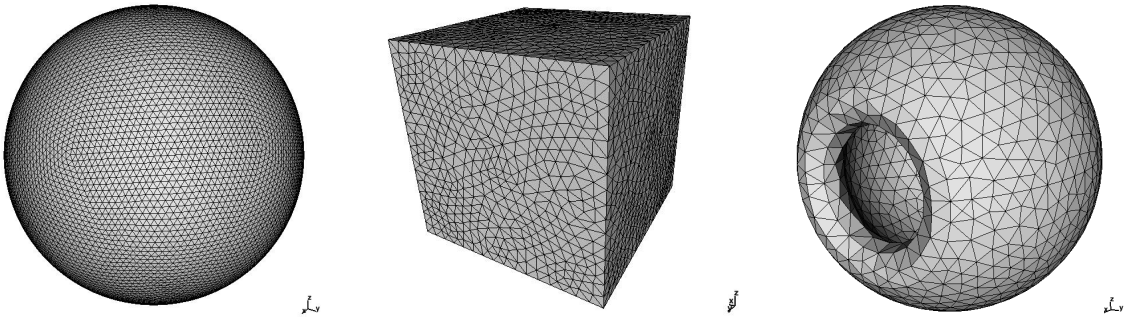

***Figure 3.4:*** *Illustration of the geometries considered: a unit sphere, a cube and a sphere with cavity.*

**Diffraction of incident plane waves by a unit sphere: numerical spectral analysis.** First, we consider the diffraction of incident plane waves by a unit sphere. A spectral decomposition, in terms of the vector spherical harmonics, of the elementary integral operators can be obtained [Darbas 2015]. This permits to perform a detailed spectral analysis of the standard and preconditioners CFIEs with respect to both physical and discretization parameters.

We compare in Figure 3.5 the distribution of the eigenvalues of the four CFIEs: the standard CFIE, the LO P-CFIE and the two High-Order P-CFIEs. For this spectral analysis, we consider the exact square-root operators in the approximation (3.32) of the adjoint DtN map. As expected, the eigenvalues of the LO P-CFIE operator are well-clustered in the hyperbolic zone only. The approximation (3.37) of the adjoint DtN map offers a better eigenvalue clustering than the low-order approximation. We observe an area of accumulation of the eigenvalues associated with the propagating and evanescent modes. However, these two approximations of the adjoint DtN map do not allow to shift the eigenvalues related to grazing modes around $(1, 0)$ as well as the others. The best spectral configuration is obtained by considering the approximation (3.32) of the adjoint DtN map.

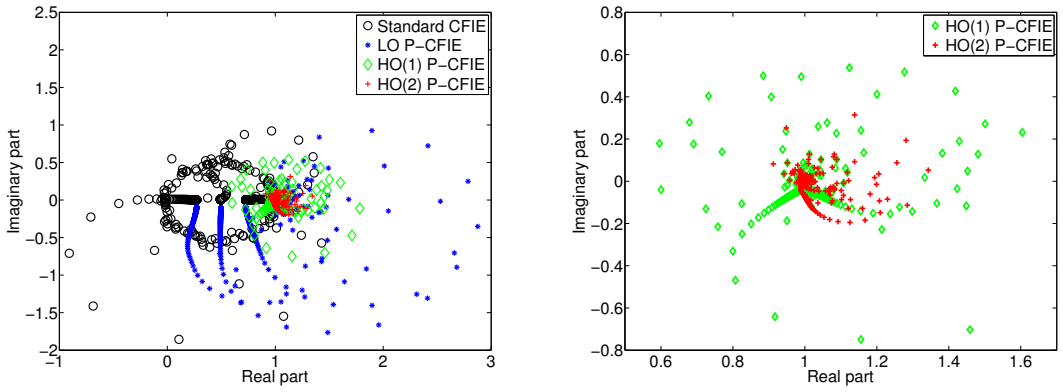


*(a)* *(b)*

***Figure 3.5:*** *Distribution of the eigenvalues of the standard and different P-CFIEs for a unit sphere ($\eta = 1$, $\kappa_s = 16\pi$ and $n_{\lambda_s} = 10$).*

**Diffraction of incident plane waves by a unit sphere: convergence of the fast iterative solver.** For all the tests, the tolerances of the inner and outer GMRES solvers are set to $10^{-4}$ and $10^{-3}$ respectively. We consider the scattering of incident plane P-waves with $\boldsymbol{p} = \boldsymbol{d} = (0, 0, 1)^T$. We compare the convergence of GMRES for the iterative solution of the different standard and P-CFIEs. The number of GMRES iterations with respect to the frequency $\omega$ are reported in Table 3.2. In the case of the HO P-CFIEs, inner iterations are indicated in parentheses.

| #DOFs | $\omega$ | # iter CFIE | # iter LO P-CFIE | # iter HO(1) P-CFIE | # iter HO(2) P-CFIE |
|---|---|---|---|---|---|
| 1 926 | 4 | 18 | 8 | 7 | 5 (11) |
| 7 686 | 8.25 | 27 | 8 | 6 | 4 (11) |
| 30 726 | 16.5 | 51 | 9 | 6 | 3 (13) |
| 122 886 | 33 | 180 | 9 | 6 | 3 (13) |
| 490 629 | 66.5 | $> 500$ | 9 | 6 | 3 (14) |

***Table 3.2:*** *Diffraction of P-waves by the unit sphere. Number of GMRES iterations for a fixed density of 10 points per wavelength.*

These results confirm that in the case of the scattering by a unit sphere, the number of iterations of the standard CFIE drastically increases with the frequency. The LO P-CFIE is very efficient. Finally, the two HO P-CFIEs require a number of iterations independent of the frequency, as expected in our context.

**Convergence of the fast iterative solver for non spherical scatterers.** To validate the good behavior of the HO P-CFIEs, we consider now non-spherical scatterers for which no analytical spectral analysis is available. We report again the convergence of GMRES for the diffraction of incident plane P-waves, for standard and P-CFIEs. The number of iterations with respect to the frequency $\omega$ are given in Table 3.3 for a cube. In the case of the HO P-CFIEs, inner iterations are indicated in parentheses.

For this geometry, the number of iterations without any preconditioner drastically increases with the frequency. Even for moderate problem sizes, the number of iterations is larger than 500. The three preconditioned CFIEs are very efficient. The number of iterations are reduced to around 10 iterations for a convergence fixed to $10^{-3}$ in GMRES. Similarly to what is noted on a sphere, the high order P-CFIEs slightly reduce the number of iterations compared to the LO P-CFIE.

Finally, we consider a more complex geometry: a sphere with cavity. This trapping domain is known to be difficult due to the numerous internal reflections of waves in the cavity and the propagation of creeping waves. In Table 3.4, we report the number of GMRES iterations with

| #DOFs | $\omega$ | # iter CFIE ($\eta = 1$) | # iter LO P-CFIE | # iter HO(1) P-CFIE | # iter HO(2) P-CFIE |
|---|---|---|---|---|---|
| 1 446 | 2.5 | 14 | 10 | 9 | 9 (13) |
| 6 630 | 5 | 40 | 12 | 10 | 9 (13) |
| 26 505 | 11 | 120 | 13 | 10 | 9 (12) |
| 105 990 | 22 | >500 | 14 | 11 | 9 (13) |

***Table 3.3:*** *Diffraction of P-waves by a cube. Number of GMRES iterations for a fixed density of 10 points per wavelength.*

respect to the frequency $\omega$ for two incidences of plane P-waves: $\boldsymbol{p}_1 = \boldsymbol{d}_1 = (-1, 0, 0)$ and $\boldsymbol{p}_2 = \boldsymbol{d}_2 = (0, 0, 1)$.

| #DOFs | $\omega$ | # iter LO P-CFIE | | # iter HO(1) P-CFIE | | # iter HO(2) P-CFIE | |
|---|---|---|---|---|---|---|---|
| 11 964 | 5 | 39 | 40 | 44 | 47 | 33 (54) | 34 (55) |
| 49 137 | 10 | 43 | 63 | 41 | 54 | 27 (42) | 30 (42) |
| 98 499 | 15 | 48 | 208 | 31 | 121 | 22 (28) | 103 (28) |
| 197 688 | 20 | 97 | > 500 | 48 | 283 | 36 (29) | 199 (29) |

***Table 3.4:*** *Diffraction of incident plane P-waves by the sphere with cavity. In each column, the first numbers give the number of GMRES iterations for $\boldsymbol{p}_1 = \boldsymbol{d}_1 = (-1, 0, 0)$ and the second numbers correspond to the incidence $\boldsymbol{p}_2 = \boldsymbol{d}_2 = (0, 0, 1)$.*

In the case of sound-soft acoustic scattering problems, estimates of the condition number of the combined field integral equations have been obtained [Betcke 2011b, Betcke 2011a] for different geometries of the scatterer. These studies show that the dependence of the condition number on the wavenumber is more pronounced for the case of trapping domains than for the case of a circle or a square. The same conclusion must apply in elastodynamics. The proposed preconditioner is very efficient and the GMRES iteration number for the solution of the HO(2) P-CFIE is quasi-independent on $\omega$ in the case of the sphere, the ellipsoid and the cube. The iteration number is less equal than 10 in each case. The HO(2) P-CFIE still offers an alternative to the usual CFIE when the scatterer is the sphere with cavity. As expected, the iteration number is higher than for the other scatterers but still efficiently decreased, particularly at high frequencies (36/199 against 97/ > 500 for $\omega = 20$, cf. Table 3.4). The iteration number is sensitive to the angle of incidence of the plane waves. The incidence $\boldsymbol{p}_2 = \boldsymbol{d}_2 = (0, 0, 1)$ normal to the cavity generates more trapping rays. Nevertheless, in the two cases considered the HO P-CFIEs are more efficient than the simple LO P-CFIE. For the second angle of incidence with $\omega = 20$, the convergence is not achieved after 500 iterations for the LO P-CFIE while it converges within 200 iterations with the HO(2) P-CFIE. It is worth noting that the number of inner GMRES iterations for the HO(2) P-CFIE is independent from the incidence of plane waves. To have a better understanding, we report in Figure 3.6 the number of iterations for the incidence $\boldsymbol{p}_2 = \boldsymbol{d}_2 = (0, 0, 1)$ for a large number of sample frequencies in the range 0-20. For all frequencies, the number of iterations is lower for the HO P-CFIEs than for the LO P-CFIE. Even if they all follow the same trend (i.e. existence of peaks at resonant frequencies of the cavity), the introduction of an accurate adjoint DtN approximation is important to keep the number of iterations reasonable at large frequencies. Close to a resonant frequency, the presence of small eigenvalues, distributed away from the cluster of eigenvalues at $(1, 0)$, slows down the convergence of the iterative solver. Nevertheless, the efficiency of the HO P-CFIEs is here again highlighted.

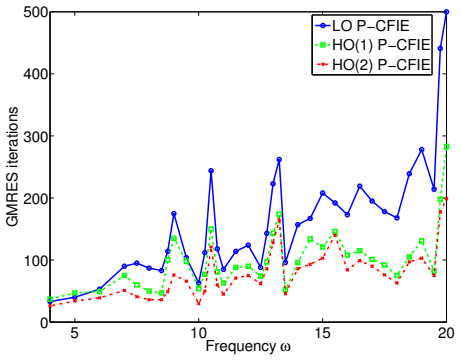


***Figure 3.6:*** *Diffraction of incident plane P-waves by a sphere with cavity. Number of GMRES iterations with respect to the frequency $\omega$ for the incidence $\boldsymbol{p}_2 = \boldsymbol{d}_2 = (0, 0, 1)$.*

## 3.3 Perspectives on the use of approximate DtNs

We have seen that the derivation of approximate DtNs is a very efficient method to define analytic preconditioners for fast BEMs. So far, with Marion Darbas and Frédérique Le Louër, we have considered Dirichlet problems. Ongoing work concerns the derivation of such preconditioners for Neumann elastic exterior problems. Contrary to the acoustic and electromagnetic cases, the definition of the Neumann-to-Dirichlet (NtD) preconditioner as the inverse of the DtN preconditioner is not sufficient to construct well-conditioned BIEs for Neumann scattering problems. A more extensive analysis of the DtN and NtD maps has to be realized in the transition region corresponding to the grazing modes. In addition to this numerical work, we are considering the theoretical proof of the number of iterations required to achieve convergence similarly to what have been done for 3D acoustics [Galkowski 2016].

It is worth noting that approximate DtN operators are not limited to the OSRC method or analytic preconditioners but find many applications. They are used to derive absorbing boundary conditions (ABCs) to truncate infinite domains in the context of volume methods. Our work on 3D elastodynamics has been used to derive very efficient high order absorbing boundary conditions for 2D elastodynamics [Mattesi 2018] (see e.g. the illustration in Fig. 3.7). These approximations play also a crucial role in Domain Decomposition Methods (DDM) [Gander 2002, Boubendir 2012] to ensure the transmission of the physical informations between the sub-domains. In the DDM context, algebraic approximations of the DtN have been proposed [Magoules 2004, Magoules 2006]

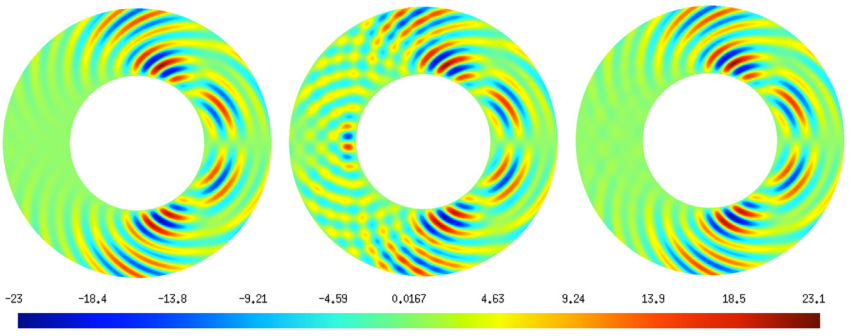


***Figure 3.7:*** *Illustration of the efficiency of the ABCs based on the approximate DtN operator in 2D elastodynamics. Comparisons of (from left to right) analytic solution, FEM solution with a low-order ABC and FEM solution with a high-order ABC, from [Mattesi 2018]. Similarly to what we have noticed in the context of analytic preconditioners, low-order approximations of the DtN are not sufficient to propose efficient ABCs.*

but these approaches show moderate efficiency in the high-frequency regime.

With Axel Modave, we are working on the improvement of the preconditioner for problems with corners similarly to what he has done for the derivation of high order absorbing boundary conditions for 3D Helmholtz problems [Modave ]. Finally, another application of this work will be to perform an efficient iterative FEM/BEM coupling with DtN approximations similarly to what has been done for 3D acoustics and electromagnetism in [Caudron 2018].

# CHAPTER 4

# Study of the potentialities of hierarchical matrix based fast BEMs for wave propagation problems

## Contents



Analytic preconditioners have been shown to be very efficient for 3D elastic exterior Dirichlet problems with homogeneous properties in Chapter 3. But these preconditioners are very intrusive in the code since they require to modify the BIE and, they are problem-dependent. So far, the extension of these analytic preconditioners to complex geological configurations with many layers or to anisotropic media is not straightforward.

However, FM-BEMs are not the only possible fast BEMs, other accelerated BEMs based on hierarchical matrices ($\mathcal{H}$-matrices) have been proposed in the literature [Hackbusch 1999]. To reduce storage requirements only the most significant and non redundant pieces of information are kept. When used in conjunction with an efficient rank revealing algorithm it leads to a data-sparse and memory efficient approximation of the original fully-populated BEM matrix. Contrary to the FM-BEM, it is a purely algebraic tool which does not require an *a priori* knowledge of the closed-form expression of the fundamental tensors. The advantage of the $\mathcal{H}$-matrix representation is the possibility to derive not only iterative but also direct solvers based on a $\mathcal{H}$-LU factorization and thus to avoid the need of an efficient preconditioner.

$\mathcal{H}$-matrix representations have been derived for some specific problems and will not result in efficient algorithms for all equations or matrices. The crucial point is to know *a priori* (i) if savings will be obtained when trying to approximate *admissible* blocks with a sum of separated variable functions and (ii) which blocks are *admissible* since the explicit computation of the rank of all blocks would be too expensive. A kernel is said to be a degenerate kernel when it can be approximated by a sum of functions with separated variables. In the case of an asymptotically smooth kernel $G(\boldsymbol{x}, \boldsymbol{y})$, it is proved that under some *a priori* condition on the distance between $\boldsymbol{x}$ and $\boldsymbol{y}$, the kernel is a degenerate kernel. After discretization, this property is reformulated as

the efficient approximation of blocks of the matrix by low-rank matrices. The Laplace Green's function is an example of asymptotically smooth kernel for which $\mathcal{H}$-matrix representations have been shown to be very efficient.

On the other hand, oscillatory kernels such as the Helmholtz or elastodynamic kernels, are not asymptotically smooth, which leads to frequency-dependent admissibility of blocks. In these cases, the method is not optimal [Banjai 2008]. To avoid the increase of the rank for high-frequency problems, directional $\mathcal{H}^2$-methods have been proposed [Börm 2017, Börm 2015]. $\mathcal{H}^2$-matrices are a specialization of hierarchical matrices. It is a multigrid-like version of $\mathcal{H}$-matrices that enables more compression, by factorizing some basis functions of the approximate separable expansion [Börm 2006]. But the implementation of $\mathcal{H}^2$ or directional methods is much more involved than the one of the standard $\mathcal{H}$-matrix. Since the 3D elastodynamic Green's tensor, similarly to the Helmholtz Green's function, is a linear combination of derivatives of the 3D Laplace Green's function with coefficients depending on the circular frequency $\omega$, it is important to determine the frequency-range within which the $\mathcal{H}$-matrices are efficient for elastodynamic problems and what can be expected of such an approach to solve problems encountered in mechanical engineering. Previous works on $\mathcal{H}$-matrices for oscillatory kernels have mostly been devoted to the direct application to derive fast iterative solvers for 3D acoustics [Brunner 2010, Stolper 2004], a direct solver for 3D electromagnetism [Lizé 2014] or iterative solvers for 3D elastodynamics [Milazzo 2012, Messner 2010, Coulier 2014b]. There is no discussion in these references on the capabilities and limits of the method for oscillatory kernels.

Our original direction of research with Patrick Ciarlet (POEMS), initiated in [2], is to show that even though the method is not optimal (in the sense that more efficient approaches can be proposed at the cost of a much more complex implementation effort), an efficient solver for mechanical engineering is easily developed. Our main contribution has been to study carefully the behaviour of the hierarchical algorithm in the context of oscillatory kernels. To do so, we have modified the algorithm to perform the low-rank approximations in an efficient way, the Adaptive Cross Approximation, to consider problems with vector unknowns (Section 4.1). Then, during the PhD of Luca Desiderio we have checked the efficiency of $\mathcal{H}$-matrix based direct and iterative solvers (Section 4.2). Since hierarchical matrices are a purely algebraic tool, it is easy to extend such fast solvers to a large class of mechanical engineering problems. In Section 4.3, I present some collaborations initiated recently to develop the use of hierarchical matrices and improve the capabilities of BEM solvers for a large range of applications.

## 4.1 Is the $\mathcal{H}$-matrix representation of a BEM matrix efficient for wave problems?

### 4.1.1 General description of $\mathcal{H}$- matrix representation

To illustrate the construction of an $\mathcal{H}$-matrix, we consider the matrix $\mathbb{G}_e$ resulting from the discretization of the 3D elastic Green's tensor $\mathbf{U}$ (1.6) for a cloud of points located on the plate $(x_1, x_2, x_3) \in [-a, a] \times [-a, a] \times \{0\}$. The plate is discretized uniformly with a fixed density of 10 points per S-wavelength. We fix the Poisson's ratio $\nu = 1/3$ and a non-dimensional frequency $\eta_S = \kappa_s a = 5\pi$ (e.g. $\rho\mu^{-1} = 1$, $\omega = 5\pi$, $\kappa_s = 5\pi$, $\kappa_p = \kappa_s/2$ and $a = 1$). As a result, the discretization consists of $N_d = 50$ points in each direction leading to $N = 2500$ points and a matrix of size $7500 \times 7500$. We recall that the numerical rank of a matrix $\mathbb{A}$ is

$$r(\varepsilon) := \min\{r \quad | \quad ||\mathbb{A} - \mathbb{A}_r|| \leq \varepsilon ||\mathbb{A}||\} \tag{4.1}$$

where $\mathbb{A}_r$ defines the singular value decomposition (SVD) of $\mathbb{A}$ keeping only the $r$ largest singular values and $\varepsilon > 0$ is a given parameter. In Fig. 4.1a, we report the decrease of the singular values of the matrix $\mathbb{G}_e$. As expected, the decay of the singular values is very slow such that the matrix cannot be globally approximated by a low-rank decomposition. Now, we partition the plate into two parts (here, two rectangles) of equal area and subdivide the matrix accordingly into 4 subblocks. Figure 4.1b gives the decrease of the singular values both for diagonal and off-diagonal blocks. It

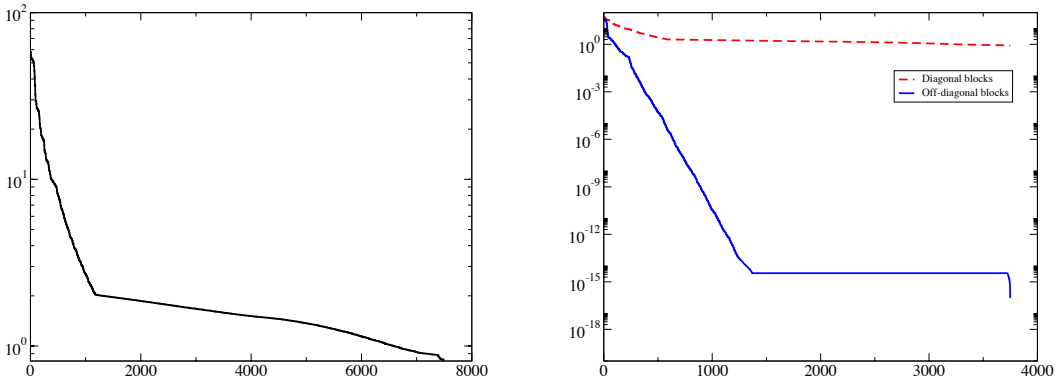


*(a)* *(b)*

***Figure 4.1:*** **(a)** *Decrease of the singular values of the complete matrix $\mathbb{G}_e$ corresponding to the discretization of the elastic Green's tensor for a cloud of 2 500 points.* **(b)** *Decrease of the singular values of the diagonal and off-diagonal blocks of the same matrix decomposed into a 2-by-2 block matrix.*

illustrates the possibility to accurately represent off-diagonal blocks by low-rank matrices while diagonal blocks cannot have low-rank representations.

If we keep subdividing the full rank blocks in a similar manner, we observe in Fig. 4.2 that diagonal blocks are always full rank numerically, i.e. with respect to (4.1) where we have chosen $\varepsilon = 10^{-4}$, while off-diagonal blocks become accurately approximated by a low-rank decomposition after some iterations of the subdivision process. This academic example illustrates the concept of data-sparse matrices used to derive fast algorithms. Using the hierarchical structure in addition to low-rank approximations, significant savings are obtained both in terms of computational times and memory requirements.

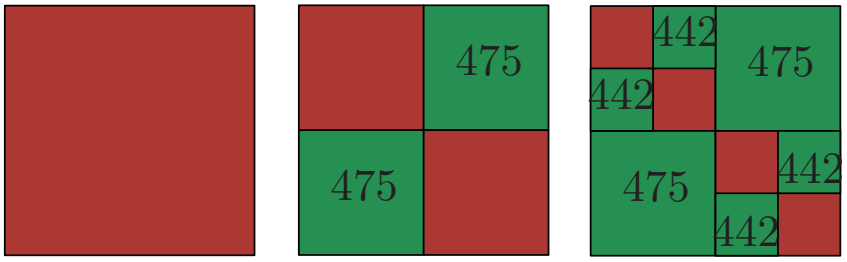


Entire matrix
Size block=7500

2 levels
Size block=3750

3 levels
Size block=1875

***Figure 4.2:*** *Computed numerical ranks of each block of the matrix $\mathbb{G}_e$ to achieve an accuracy of $10^{-4}$, i.e. if singular values smaller than $10^{-4}$ are neglected in the singular value decomposition.*

The key ingredient of hierarchical matrices is the recursive block subdivision. On the illustrative example, the subdivision of the matrix is conducted by a recursive subdivision of the geometry, i.e. a recursive subdivision of the plan into partitions of equal areas. The first step prior to the partition of the matrix is thus a partitioning based on the geometry of the set of row and column indices of the matrix $\mathbb{A}$. The purpose is to permute the indices in the matrix to reflect the physical distance and thus interaction between degrees of freedom. Consecutive indices should correspond to DOFs that interact at close range. For the sake of clarity, the system matrix $\mathbb{A}$ is defined by the same set of indices $I = \{1, \ldots, n\}$ for rows and columns. A binary tree $\mathcal{T}_I$ is used to drive the clustering. Each node of the tree defines a subset of indices $\sigma \subset I$ and each subset corresponds to a part in the partition of the domain, see Figure 4.3 for the case of the illustrative example.

After the clustering of the unknowns is performed, a block cluster representation $\mathcal{T}_{I\times I}$ of the

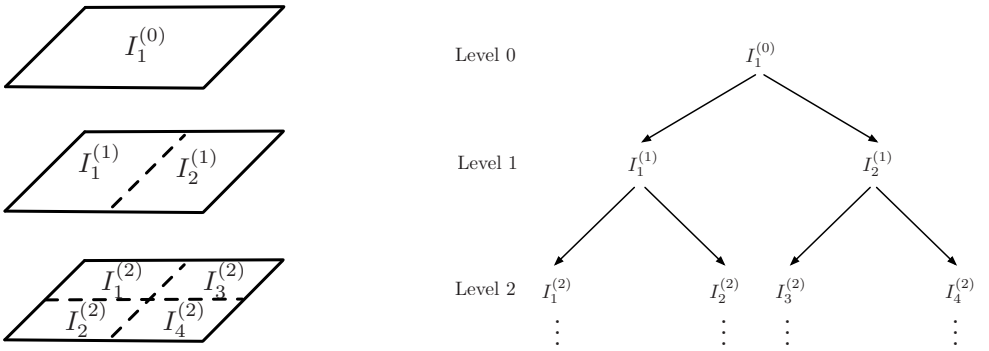


***(a)*** *Partition of the physical domain* ***(b)*** *Binary cluster tree $\mathcal{T}_I$*

***Figure 4.3:*** *Illustration of the clustering of the degrees of freedom:* **(a)** *partition of the degrees of freedom in the domain and* **(b)** *corresponding binary tree.*

matrix $\mathbb{A}$ is defined by going through the cluster tree $\mathcal{T}_I$. Each node of $\mathcal{T}_{I\times I}$ contains a pair $(\sigma, \tau)$ of indices of $\mathcal{T}_I$ and defines a block of $\mathbb{A}$. This uniform partition defines a block structure of the matrix with a full pattern (Figure 4.4a). Figure 4.1b shows that this partition is not optimal. As a matter of fact, some parts of the matrix $\mathbb{A}$ can accurately be approximated by a low-rank matrix at a higher level (i.e. for larger clusters). Such blocks are said to be *admissible*. Hence, a hierarchical representation $\mathcal{P} \subset \mathcal{T}_{I\times I}$ that uses the cluster tree $\mathcal{T}_I$ and the existence of *admissible* blocks is more appropriate (Figure 4.4b). Starting from the initial matrix, each block is recursively subdivided until it is either *admissible* or the leaf level is achieved. In the illustrative example, only diagonal blocks are subdivided due to the very simple 2D geometry (see again Fig. 4.2, red-colored blocks). For more complex 3D geometries, an admissibility condition based on the geometry and the interaction distance between points is used to determine *a priori* the *admissible* blocks. For more details on the construction of the block cluster tree, we refer the interested reader to [Börm 2003b]. The partition $\mathcal{P}$ is subdivided into two subsets $\mathcal{P}^{\text{ad}}$ and $\mathcal{P}^{\text{non-ad}}$ reflecting the possibility for a block $\tau \times \sigma$ to be either *admissible*, i.e. $\tau \times \sigma \in \mathcal{P}^{\text{ad}}$; or *non-admissible*, i.e. $\tau \times \sigma \in \mathcal{P}^{\text{non-ad}}$. It is clear that $\mathcal{P} = \mathcal{P}^{\text{ad}} \cup \mathcal{P}^{\text{non-ad}}$. To sum up, the blocks of the partition can be of 3 types: at the leaf level a block can be either an *admissible* block or a *non-admissible* block, at a non-leaf level a block can be either an *admissible* block or an $\mathcal{H}$-matrix (i.e a block that will be subsequently hierarchically subdivided).

***(a)*** ***(b)***

***Figure 4.4:*** **(a)** *Block cluster representation $\mathcal{T}_{I\times I}$ for the illustrative example (full structure);* **(b)** *Hierarchical partition $\mathcal{P} \subset \mathcal{T}_{I\times I}$ of the same matrix based on the admissibility condition (sparse structure).*

### 4.1.2 Extension of the Adaptive Cross Approximation to problems with vector unknowns

**ACA for scalar problems.** Once the *admissible* blocks are determined, an accurate rank-revealing algorithm is applied to determine low-rank approximations. Such an algorithm must be accurate (i.e. its result, the computed numerical rank, must be as small as possible) to avoid un-

necessary computational costs. The truncated Singular Value Decomposition (SVD) [Golub 2012] gives the best low-rank approximation (Eckart-Young theorem) for unitary invariant norms (e.g. Frobenius or spectral norm). Thus it produces an approximation with the smallest possible numerical rank for a given prescribed accuracy. But the computation of the SVD is expensive, i.e. in the order of $O(\max(m,n) \times \min(m,n)^2)$ for an $m \times n$ matrix, and in addition it requires the computation of all the entries of $\mathbb{A}$. In the context of the $\mathcal{H}$-matrices, the use of the SVD would induce the undesired need to assemble the complete matrix.

The adaptive cross approximation (ACA) [Bebendorf 2015, Bebendorf 2003] offers an interesting alternative to the SVD since it produces a quasi-optimal low-rank approximation without requiring the assembly of the complete matrix. The starting point of the ACA is that every matrix of rank $r$ is the sum of $r$ matrices of rank 1. The ACA is thus a greedy algorithm that improves the accuracy of the approximation by adding iteratively rank-1 matrices. At iteration $k$, the matrix is split into the rank $k$ approximation $\mathbb{B}_k = \sum_{\ell=1}^{k} \mathbf{u}_\ell \mathbf{v}_\ell^* = \mathbb{U}_k \mathbb{V}_k^*$ with $\mathbb{U}_k \in \mathbb{C}^{m\times k}$, $\mathbb{V}_k \in \mathbb{C}^{n\times k}$, and the residual $\mathbb{R}_k = \mathbb{A} - \sum_{\ell=1}^{k} \mathbf{u}_\ell \mathbf{v}_\ell^*$; $\mathbb{A} = \mathbb{B}_k + \mathbb{R}_k$. The information is shifted iteratively from the residual to the approximant.

There are various ACAs that differ by the choice of the best pivot at each iteration. The simplest approach is the so-called fully-pivoted ACA and it consists in choosing the pivot as the largest entry in the residual. But similarly to the SVD, it requires the computation of all the entries of $\mathbb{A}$ to compute the pivot indices. It is not an interesting option for the construction of $\mathcal{H}$-matrices. The partially-pivoted ACA proposes an alternative approach to choose the pivot avoiding the assembly of the complete matrix. The idea is to maximize alternately the residual for only one of the two indices and to keep the other one fixed. With this strategy, only one row and one column is assembled at each iteration. The complexity of the partially-pivoted ACA is reduced to $O(r_{\text{ACA}}^2(m+n))$ where $r_{\text{ACA}}$ is the numerical rank obtained with the ACA. Since the partially-pivoted ACA is a heuristic method, there exist counter-examples where ACA fails [Börm 2003a] and variants have been designed to improve the robustness of the method. Nevertheless, in all the numerical examples we have performed, we do not need them.

**Extension to elastodynamics.** One specificity of our work is to consider $\mathcal{H}$-matrices and ACA in the context of systems of partial differential equations with vector unknowns. There exist a lot of works both theoretical and numerical on the ACA for scalar problems, in particular on the selection of non-zero pivots. Indeed for scalar problems, it is straightforward to find the largest non-zero entry in a given column. For problems with vector unknowns in $\mathbb{R}^d$, the system has a block structure, i.e. each pair of nodes on the mesh does not define a single entry but rather a $d \times d$ subblock in the complete matrix. This happens for example for 3D elastodynamics where the Green's tensor is a $3 \times 3$ subblock.

Different strategies can be applied to perform the ACA on matrices with a block structure. The first strategy consists in ordering the system matrix such that it is composed of $9 = 3^2$ subblocks of size $N \times N$ where $N$ is the number of points in the cloud. In 3D elastodynamics, this corresponds to the following partitioning of the matrix (below the solution is represented with $\mathbf{U}$):

$$\begin{bmatrix} \mathbb{A}_{11} & \mathbb{A}_{12} & \mathbb{A}_{13} \\ \mathbb{A}_{21} & \mathbb{A}_{22} & \mathbb{A}_{23} \\ \mathbb{A}_{31} & \mathbb{A}_{32} & \mathbb{A}_{33} \end{bmatrix}, \quad (\mathbb{A}_{\alpha\beta})_{ij} = (\mathbf{U})_{\alpha\beta}(\boldsymbol{x}_i, \boldsymbol{y}_j) \;\; 1 \leq \alpha, \beta \leq 3, \; 1 \leq i, j \leq N_c.$$

Then each submatrix is approximated independently with the conventional scalar ACA. This strategy is used in [Messner 2010]. It is well suited for iterative solvers. But it cannot be adapted straightforwardly in the context of direct solvers since the recursive $2 \times 2$ block structure inherited from the binary tree is used.

The second naive approach consists in considering the complete matrix as a scalar matrix, i.e. to forget about the block structure. While appealing this approach fails in practice for 3D elastodynamics, whatever ordering is used, due to the particular structure of the matrix. Rewriting the Green's tensors (1.6) component-wise [Bonnet 1999] and using the Einstein summation convention,

it reads

$$(\mathbf{U})_{\alpha\beta}(\boldsymbol{x},\boldsymbol{y}) = \frac{1}{4\pi\varrho}(a_1\delta_{\alpha\beta} + a_2\varrho_{,\alpha}\varrho_{,\beta}),$$

$$(\mathbf{T})_{\alpha\beta}(\boldsymbol{x},\boldsymbol{y}) = \frac{1}{4\pi\varrho}\Big[2a_3\varrho_{,\alpha}\varrho_{,\gamma}\varrho_{,\beta} + a_4(\delta_{\alpha\beta}\varrho_{,\gamma} + \delta_{\gamma\beta}\varrho_{,\alpha}) + a_5\delta_{\alpha\gamma}\varrho_{,\beta}\Big]n_\gamma(\boldsymbol{y})$$

where the constants $a_1, ..., a_5$ depend only on the mechanical properties, $\varrho = ||\boldsymbol{x}-\boldsymbol{y}||$ and $\varrho_{,\alpha} = \frac{\partial}{\partial y_\alpha}\varrho(\boldsymbol{x},\boldsymbol{y})$. As a result, as soon as $\boldsymbol{x}$ and $\boldsymbol{y}$ belong to the same plane (let's say $x_3 = y_3$ for simplicity) the Green's tensors simplify to

$$\mathbf{U}(\boldsymbol{x},\boldsymbol{y}) = \frac{1}{4\pi\varrho}\begin{bmatrix} a_1+a_2\varrho_{,1}^2 & a_2\varrho_{,1}\varrho_{,2} & 0 \\ a_2\varrho_{,1}\varrho_{,2} & a_1+a_2\varrho_{,1}^2 & 0 \\ 0 & 0 & a_1 \end{bmatrix},\ \mathbf{T}(\boldsymbol{x},\boldsymbol{y}) = \frac{1}{4\pi\varrho}\begin{bmatrix} 0 & 0 & a_4\varrho_{,1} \\ 0 & 0 & a_4\varrho_{,2} \\ a_4\varrho_{,1} & a_4\varrho_{,2} & 0 \end{bmatrix}. \quad (4.2)$$

It is then clear that the complete matrix $\mathbb{A}$ composed of such subblocks is a reducible matrix (there are decoupled groups of unknowns after discretization). While the fully-pivoted ACA will succeed in finding the best pivot to perform low-rank approximations, the partially pivoted ACA will only cover parts of the matrix resulting in a non accurate approximation of the initial matrix. As a result, this approach cannot be applied for 3D elastodynamics. Another strategy would be to adapt the choice of the pivot to reducible matrices, i.e. to cover all the decoupled groups of unknowns. This is possible with the use of the ACA+ algorithm that defines a reference column and a reference row along which the pivots are looked for [Börm 2003b]. Even though this approach could fix the problem it does not seem to be the best suited one since it does not use the vector structure of 3D elastodynamic problems.

To sum up, it is now important to use an algorithm that takes into account the particular structure of our matrix such that the vector ACA does not rely anymore on a rank-1 update but instead on a rank-3 update. The central question is then how to find the pivot used for this rank-3 update instead. There are 3 possible strategies:

1. To look for the largest scalar pivot, determine the corresponding point in the cloud and update all 3 DOFs linked to this point simultaneously. This approach is not stable since the $3 \times 3$ subblock pivot may not be invertible (cf. a discretized version of (4.2)).
2. The second strategy is to look for the $3 \times 3$ subblock with the largest norm. Again this approach fails in practice since the $3 \times 3$ subblock pivot may not be invertible.
3. The third strategy proposed in [2] is to compute the singular values $\sigma_1 \geq \sigma_2 \geq \sigma_3$ of every candidate subblock. In order to achieve convergence and to avoid singular pivots, the safest approach consists in choosing the pivot corresponding to the subblock with the largest $\sigma_3$. A similar approach has been proposed during the same period for electromagnetic problems in [Rjasanow 2016].

### 4.1.3 Application of $\mathcal{H}$-matrices to oscillatory kernels: theoretical estimates

The efficiency of $\mathcal{H}$-matrix based solvers depends on the possible storage reduction obtained by low-rank approximations. It is thus important to estimate the memory requirements of the method in the context of 3D elastodynamics. At this point, we need to define the sparsity pattern introduced by L. Grasedyck [Grasedyck 2001]. For sparse matrices, the sparsity pattern gives the maximum number of non-zero entries per row. Similarly for a hierarchical matrix defined by the partition $\mathcal{P} \subset \mathcal{T}_{I\times I}$, the sparsity pattern of a row cluster $\tau \in \mathcal{T}_I$, resp. a column cluster $\sigma \in \mathcal{T}_I$, is

$$C_{sp}(\tau) = |\{\sigma \in \mathcal{T}_I : \tau \times \sigma \in \mathcal{P}\}|, \text{ resp. } C_{sp}(\sigma) = |\{\tau \in \mathcal{T}_I : \tau \times \sigma \in \mathcal{P}\}|.$$

It is convenient to define the overall sparsity pattern (for row and column clusters):

$$C_{sp} = \max\{\max_{\tau\in\mathcal{T}_I} C_{sp}(\tau),\ \max_{\sigma\in\mathcal{T}_I} C_{sp}(\sigma)\}.$$

We can then easily show that the storage requirement of a matrix of size $N \times N$ is bounded by

$$N_{st}(\mathbb{A}) \leq 2C_{sp}\max\{r_{\text{ACA}}^{\max}, N_{\text{leaf}}\}N(\log_2 N - \log_2 N_{\text{leaf}} + 1).$$

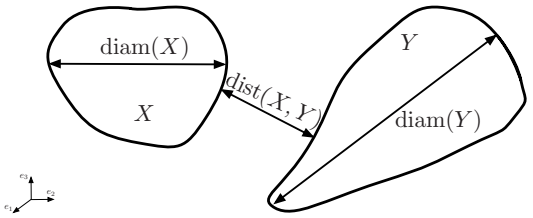


***Figure 4.5:*** *Definition of the distance and diameter.*

In this storage estimate, the parameters $N$ and $N_{\text{leaf}}$ (stopping criteria to build the binary tree) are known *a priori*. The sparsity pattern $C_{sp}$ depends on the partition $\mathcal{P}$, i.e. only on the problem geometry. In the context of oscillatory kernels, the maximum numerical rank observed among the admissible blocks $r_{\text{ACA}}^{\max}$ is known to depend on the frequency. One of our contributions in [2] has been to characterise this dependence.

The capability to produce low rank approximations is closely related to the concept of degenerate functions [Bebendorf 2008]. A kernel function is said to be degenerate if it can be well approximated (under some assumptions) by a sum of functions with separated variables. In other words, noting $X$ and $Y$ two domains of $\mathbb{R}^3$, we are looking for an approximation $s^r$ of $s$ on $X \times Y$ with $r$ terms such that it writes

$$s^r(\boldsymbol{x}, \boldsymbol{y}) = \sum_{\ell=1}^{r} u_\ell^{(r)}(\boldsymbol{x}) v_\ell^{(r)}(\boldsymbol{y}) \quad \boldsymbol{x} \in X, \quad \boldsymbol{y} \in Y.$$

$r$ is called the *separation rank* of $s^r$ and $s(\boldsymbol{x}, \boldsymbol{y}) = s^r(\boldsymbol{x}, \boldsymbol{y}) + R_s^r(\boldsymbol{x}, \boldsymbol{y})$ with $R_s^r$ the remainder. Such an approximation is obtained for instance with a Taylor expansion. A kernel function is said to be a separable expression in $X \times Y$ if the remainder converges quickly to zero uniformly on $X \times Y$, i.e. with an exponential decay. The main result for asymptotically smooth kernels presented in [Bebendorf 2008, Lemma 3.15] and [Hackbusch 2015, Theorem 4.17] is that the exponential convergence of the Taylor expansion over $X$ and $Y$ is constrained by the notion of $\eta$-admissibility. $X$ and $Y$ are said to be *$\eta$-admissible* if $\operatorname{diam} X \leq \eta \operatorname{dist}(X, Y)$ where $\eta > 0$ is a parameter of the method, dist denotes the euclidian distance, i.e.

$$\operatorname{dist}(X, Y) = \inf\{||\boldsymbol{x} - \boldsymbol{y}||, \ \boldsymbol{x} \in X, \ \boldsymbol{y} \in Y\} \tag{4.3}$$

and diam denotes the diameter of a domain (Fig. 4.5), i.e.

$$\operatorname{diam}(X) = \sup\{||\boldsymbol{x}_1 - \boldsymbol{x}_2||, \ \boldsymbol{x}_1, \ \boldsymbol{x}_2 \in X\}. \tag{4.4}$$

However, the Helmholtz Green's function $G(r; \kappa)$ defined in (1.7) is not asymptotically smooth [Banjai 2008]. On the other hand, noting that it holds $G(r; \kappa) = \exp(i\kappa||\boldsymbol{x} - \boldsymbol{y}||)G(r, 0)$ and since $G(r; 0)$ is asymptotically smooth [Bebendorf 2008, Hackbusch 2015], it is clear that in the so-called *low-frequency regime*, i.e. when $\kappa \ \max_{\boldsymbol{x},\boldsymbol{y} \in X \times Y}(||\boldsymbol{x} - \boldsymbol{y}||)$ is small, the Helmholtz Green's function behaves similarly to an asymptotically smooth kernel.

According to the previous discussion, we know that, for the asymptotically smooth kernel, the asymptotic smoothness allows to prove the exponential convergence of the Taylor series if $X$ and $Y$ are *$\eta$-admissible*. On the other hand for the Helmholtz kernel, we can show [2] that to ensure convergence of the series, $X$ and $Y$ must now be chosen in such a way that

$$\gamma_{\kappa,x} := \ (1 + \kappa||\boldsymbol{x}_0 - \boldsymbol{y}||)\frac{\max_{\boldsymbol{x} \in X} ||\boldsymbol{x} - \boldsymbol{x}_0||}{c_2||\boldsymbol{x}_0 - \boldsymbol{y}||} < 1, \tag{4.5}$$

where $c_2$ is the constant coming from the asymptotic smoothness of the Laplace kernel (see [2] for more details on the numerical evaluation of this constant). From now on, we say that $X$ and $Y$ are *$\eta_\kappa$-admissible* if (4.5) is satisfied. This result on the convergence of the Taylor expansion of the 3D Helmholtz Green's function is easily extended to 3D elastodynamics since the Green's tensors are linear combinations of the derivatives of the Helmholtz Green's function.

The definition of the $\eta_\kappa$-admissibility for oscillatory kernels could be modified in order to keep the separation rank constant while the frequency increases. It is the option followed for example in directional approaches [Messner 2012, Delamotte 2016]. The option we consider instead is to work with the $\eta$-admissibility condition defined for the asymptotically smooth kernels. In other words, we choose to keep $\eta$ constant for all frequencies and use the admissibility condition defined by:

$$\operatorname{diam} X \leq \eta \operatorname{dist}(X, Y). \tag{4.6}$$

Our goal is to determine what is the actual behaviour of the algorithm in that configuration. Following the study of the remainder of the Taylor expansion, it is clear that the method will not be optimal since the separation rank to achieve a given accuracy will increase with the frequency. Nevertheless, we are interested in determining the limit until which the low-frequency approximation is viable for oscillatory kernels such as the 3D Helmholtz Green's function or the 3D elastodynamic Green's tensors.

The relevant question to address is then to determine the law followed by the growth of the numerical rank if the $\eta$-admissibility condition (4.6) is used in the context of oscillatory kernels. From algebraic arguments, we have shown in [2] that if we consider a fixed geometry at a fixed frequency and we increase the density of discretization points per wavelength, and as a consequence the total number of discretization points, the maximum numerical rank of the blocks can be either small or large depending on the value of the product between the frequency and the diameter of the blocks (fixed by the geometry). However we expect that this rank will remain fixed if the density of discretization points per wavelength increases. On the other hand, if we consider a fixed geometry with a fixed density of points per S-wavelength, the maximum rank of the blocks is expected to grow linearly with the frequency until the *high-frequency regime* is achieved. This transition regime is in some sense a *pre-asymptotic regime* and we have demonstrated numerically its existence. In the *high-frequency* regime, the $\mathcal{H}$-matrix representation is expected to be suboptimal with a rank rapidly increasing.

### 4.1.4 Behaviour of hierarchical matrix representations for low and high-frequency elastodynamic kernels

We consider the diffraction of vertical incident plane P waves by a spherical cavity. The material properties are fixed to $\mu = \rho = 1$ and $\nu = 1/3$. In all the numerical examples, the binary tree $\mathcal{T}_I$ is built with a stopping criteria $N_{\text{leaf}} = 100$ and the constant in the admissibility condition is set to $\eta = 3$. Unless otherwise indicated, the required accuracy in the ACA is fixed to $\varepsilon_{\text{ACA}} = 10^{-4}$. In the following, we denote by $N$ the number of degrees of freedom.

**Storage requirements for the single and double-layer potentials for a fixed frequency.** We determine first the behaviour of the algorithm for a fixed frequency while the number of discretization points is increased (i.e. in the *low-frequency* regime). The circular frequency $\omega$ is thus fixed. As a result, the density of points per S-wavelength increases as the number of discretization points increases.

We have seen that the memory requirements are expected to be of the order of $O(\max(r_{\text{ACA}}^{\max}, N_{\text{leaf}})N \log_2 N)$. In addition, for a fixed frequency, $r_{\text{ACA}}^{\max}$ is expected to be constant. In Tables 4.1 and 4.2, we report the maximum numerical rank observed among all the *admissible* blocks for the case of a sphere for a fixed circular frequency ($\omega = 3$ or $\omega = 14$) and for various mesh sizes, for the single-layer and double-layer operators. The first rank corresponds to the numerical rank obtained by the partially pivoted ACA. The second rank corresponds to the numerical rank obtained after the recompression step. Thus, since the partially pivoted ACA is a heuristic method, the numerical rank is not the optimal one. In order to reduce this overestimation of the numerical rank, a recompression step is used. It consists in the application of the SVD to the already compressed block. The recompression step permits to recover the intrinsic numerical rank of the blocks (see [2] for more details on this step). In practice, as suggested by the study of the Taylor expansion, the two ranks are seen to be almost constant while the density of points is increasing. As expected, the numerical rank without the recompression step is much larger than after the optimization step. In addition, the maximum numerical rank increases with the frequency.

We will study in more details this dependence on the frequency in the following. Finally also as expected, similar numerical ranks are observed for the single and double layer potentials.

| $N$ | 7 686 | 30 726 | 122 886 | 183 099 | 490 629 | 763 638 | 985 818 |
|---|---|---|---|---|---|---|---|
| $\omega = 3$ | 63/39 | 72/39 | 75/39 | 69/37 | 75/39 | 69/40 | 78/39 |
| $\omega = 14$ | 99/73 | 105/75 | 108/76 | 99/67 | 114/76 | 111/76 | 111/76 |

***Table 4.1:*** *Maximum numerical rank observed (before/after the recompression step) for a fixed frequency, i.e. while increasing the density of points per S-wavelength, for* $\varepsilon_{\text{ACA}} = 10^{-4}$ *and the single-layer potential (1.9).*

| $N$ | 7 686 | 30 726 | 122 886 | 183 099 | 490 629 | 763 638 | 985 818 |
|---|---|---|---|---|---|---|---|
| $\omega = 3$ | 66/37 | 66/37 | 72/38 | 66/36 | 69/38 | 72/39 | 75/39 |
| $\omega = 14$ | 102/70 | 117/74 | 117/74 | 102/66 | 114/75 | 114/75 | 114/76 |

***Table 4.2:*** *Maximum numerical rank observed (before/after the recompression step) for a fixed frequency, i.e. while increasing the density of points per S-wavelength, for* $\varepsilon_{\text{ACA}} = 10^{-4}$ *and the double-layer potential (1.9).*

Ultimately we are not interested in the maximum numerical rank but rather on the memory requirements of the algorithm. In Figures 4.6, we report the memory requirements $N_s$ and the compression rate $\tau(\mathcal{H}) := N_s/N^2$ with respect to the number of degrees of freedom $N$ for $\varepsilon_{\text{ACA}} = 10^{-4}$ and the single-layer operator, before/after recompression. Since the rank is constant, $N_s$ is expected to be of the order of $N \log_2 N$ and $\tau(\mathcal{H})$ of the order of $\log_2 N/N$. We observe for the two frequencies a very good agreement between the expected and observed complexities of the compression rate and memory requirements. Note that the storage is reduced by more than 95%, i.e. $\tau(\mathcal{H}) \leq 5\ 10^{-2}$, as soon as $N \geq 10^5$.

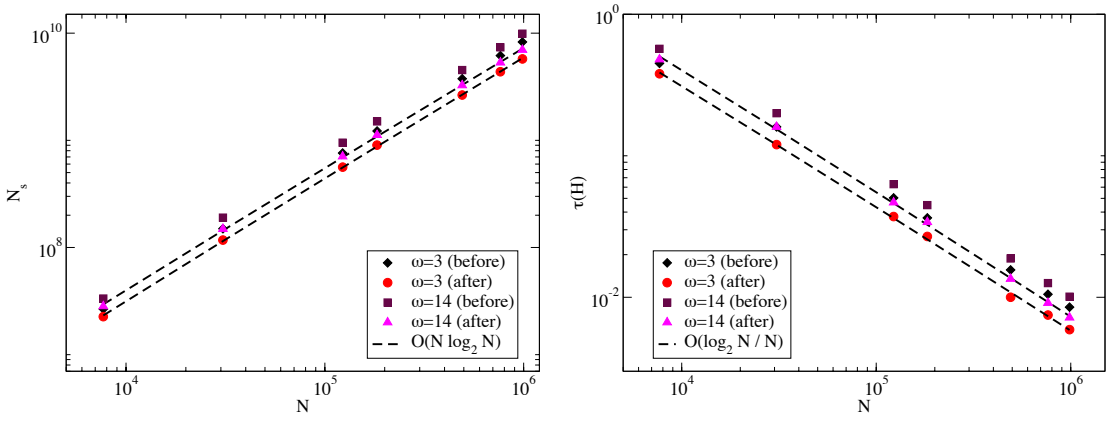


***(a)*** ***(b)***

***Figure 4.6:*** *Observed and estimated* **(a)** *memory requirements* $N_s$ *and* **(b)** *compression rate* $\tau(\mathcal{H})$ *with respect to the number of degrees of freedom* $N$ *for a fixed frequency* ($\omega = 3$ *or* $\omega = 14$) *for the single layer-operator and* $\varepsilon_{\text{ACA}} = 10^{-4}$.

**Storage requirements for the single and double-layer potentials for a fixed density of points per S-wavelength.** We now determine the behaviour of the algorithm for a given fixed density of points per S-wavelength while the number of discretization points is increased (i.e. in the *higher frequency* regime). The circular frequency $\omega$ is thus fitted to the mesh length to keep the density of points per S-wavelength fixed for the different meshes. In this case, an increase of the

number of degrees of freedom $N$ leads to an increase of the size of the body to be approximated. In Table 4.3 we report the number of degrees of freedom, corresponding circular frequencies and number of S-wavelengths spanned in the sphere diameter used in the examples.

| $\omega$ | 8.25 | 16.5 | 33 | 40 | 66 | 84 | 92 |
|---|---|---|---|---|---|---|---|
| $N$ | 7 686 | 30 726 | 122 886 | 183 099 | 490 629 | 763 638 | 985 818 |
| $n_{\lambda_s}$ | 2.6 | 5.2 | 10.5 | 12.6 | 21 | 26.6 | 29.1 |

***Table 4.3:*** *Number of degrees of freedom, corresponding number of wavenumbers spanned in the sphere diameter $D$ ($D = n_{\lambda_s}\lambda_s$) on the different meshes of spheres and corresponding circular frequencies used for a fixed density of points per S-wavelength.*

We have seen that for a fixed geometry and a fixed density of points per S-wavelength, the maximum rank of the $\eta$-*admissible* blocks is expected to grow linearly with the frequency until the *high-frequency regime* is achieved. The goal of this section is to observe numerically, and so to validate the existence of this pre-asymptotic regime. In Figure 4.7a, we report the maximum numerical rank observed among all the $\eta$-*admissible* blocks before and after the recompression step with respect to the circular frequency $\omega$, for both the single and double layer potentials. In accordance to the study of the Taylor expansion, the growth of the numerical rank after the recompression step (i.e. the intrinsic rank of the blocks) is seen to be linear with respect to the circular frequency. The behaviour of the single layer and double layer operators are again very similar (the symbols on the figure are overlapping).

In practice however, we are interested in the complexity with respect to the number of degrees of freedom. The number of discretization points is fitted to the circular frequency in order to keep 10 discretization points per S-wavelength. Since the density of points is fixed, the mesh size is $h = O(\lambda_S) = O(\omega^{-1})$. In addition since the mesh for the BEM is a surface mesh, the mesh size is $h = O(N^{-2})$. Hence, the maximum numerical rank is expected to be of the order of $O(N^{1/2})$ in the pre-asymptotic regime. In Figure 4.7b, we report the maximum numerical rank observed among all the $\eta$-*admissible* blocks before and after the recompression step with respect to the number of DOFs $N$, for both the single and double layer potentials. The growth of the numerical rank after the recompression step (i.e. the intrinsic rank of the blocks) is indeed seen to be of the order of $O(N^{1/2})$.

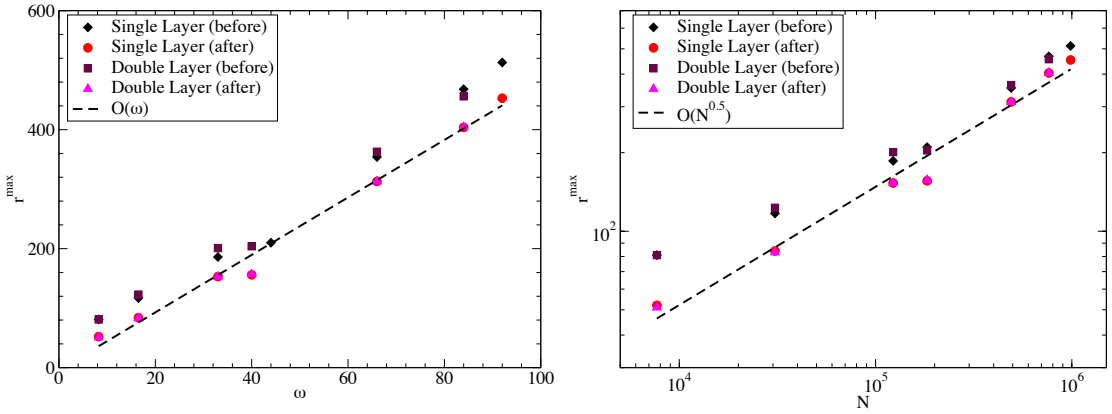


***(a)*** ***(b)***

***Figure 4.7:*** *Maximum numerical rank observed (before/after the recompression step) for a fixed density of points per wavelength, i.e. while increasing the circular frequency with the number of discretization points, for $\varepsilon_{\mathrm{ACA}} = 10^{-4}$:* **(a)** *with respect to the circular frequency and* **(b)** *with respect to the number of degrees of freedom.*

Ultimately we are not interested in the maximum numerical rank but rather on the memory requirements of the algorithm. In Figures 4.8, we report the memory requirements $N_s$ and

compression rate $\tau(\mathcal{H})$, with respect to the number of degrees of freedom $N$ for $\varepsilon_{\text{ACA}} = 10^{-4}$. Since the observed numerical rank is of the order of $O(N^{1/2})$, $N_s$ is expected to be of the order of $N^{3/2}\log_2 N$ and $\tau(\mathcal{H})$ of the order of $\log_2 N/N^{1/2}$. In practice, observed complexities are lower than the expected one in the order of $N^{5/4}\log_2 N$. The reason is that the estimation of the memory requirements gives only an upper bound based on the estimation of the maximum numerical rank. But, all the *admissible* blocks do not have the same numerical rank, as a result, the complexity is lower than the estimated one.

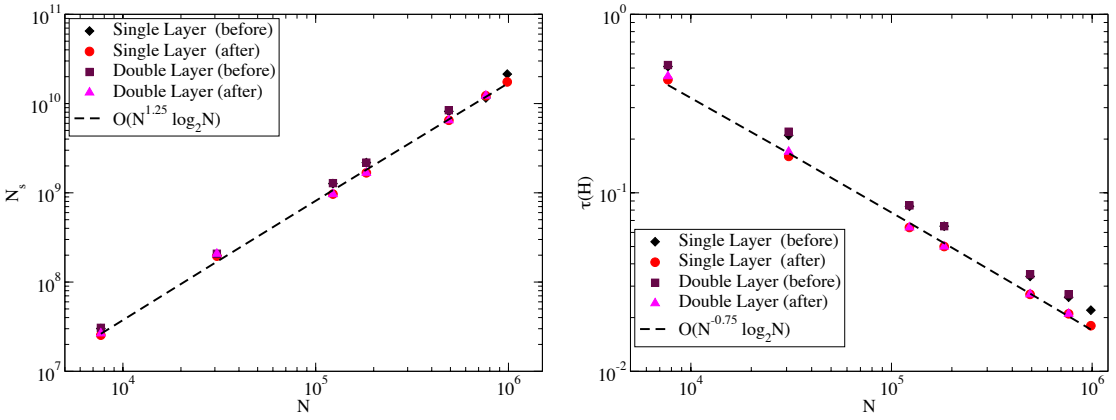


*(a)* *(b)*

***Figure 4.8:*** *Observed and estimated* **(a)** *memory requirements $N_s$ and* **(b)** *compression rate $\tau(\mathcal{H})$ with respect to the number of degrees of freedom $N$ for a fixed density of points per S-wavelength for the single and double layer-operators and $\varepsilon_{\text{ACA}} = 10^{-4}$.*

## 4.2 Hierarchical matrix based fast BEM solvers

During the PhD of L. Desiderio, funded by the company SHELL, and in collaboration with Patrick Ciarlet (POEMS), we have studied the capabilities of the $\mathcal{H}$-matrix based iterative and direct solvers for 3D elasticity [Desiderio 2017].

**Principle of Hierarchical solvers.** Once the $\mathcal{H}$-matrix representation of a matrix is computed, it is easy to derive an $\mathcal{H}$-matrix based iterative solver. The only operation required is an efficient matrix-vector product. It is performed hierarchically by going through the block cluster tree $\mathcal{P}$. For example at the leaf level, there are two possibilities. If the block of size $N_{\text{leaf}} \times N_{\text{leaf}}$ does not admit a low-rank approximation (*non-admissible* block), then the standard matrix-vector product is used with cost $O(N_{\text{leaf}}^2)$. Otherwise, the block is marked as *admissible* such that a low-rank approximation has been computed. The cost of this part of the matrix-vector product is then reduced from $O(N_{\text{leaf}}^2)$ to $O(r_{\text{ACA}}N_{\text{leaf}})$ where $r_{\text{ACA}}$ is the numerical rank of the block computed with the ACA.

One of the advantages of the $\mathcal{H}$-matrix representation is the possibility to derive a fast direct solver. Due to the hierarchical block structure of a $\mathcal{H}$-matrix, the LU factorization is performed recursively on 2×2 block matrices $\mathbb{A}_{(\tau_1\cup\tau_2)\times(\sigma_1\cup\sigma_2)}$ of the form

$$\begin{pmatrix} \mathbb{A}_{\tau_1\times\sigma_1} & \mathbb{A}_{\tau_1\times\sigma_2} \\ \mathbb{A}_{\tau_2\times\sigma_1} & \mathbb{A}_{\tau_2\times\sigma_2} \end{pmatrix} = \begin{pmatrix} \mathbb{L}_{\tau_1\times\sigma_1} & \mathbb{O} \\ \mathbb{L}_{\tau_2\times\sigma_1} & \mathbb{L}_{\tau_2\times\sigma_2} \end{pmatrix} \begin{pmatrix} \mathbb{U}_{\tau_1\times\sigma_1} & \mathbb{U}_{\tau_1\times\sigma_2} \\ \mathbb{O} & \mathbb{U}_{\tau_2\times\sigma_2} \end{pmatrix}$$

For such block matrices, we recall that the LU factorization is classically decomposed into 4 steps:

1. LU decomposition of $\mathbb{A}_{\tau_1\times\sigma_1}$ to compute $\mathbb{L}_{\tau_1\times\sigma_1}$ and $\mathbb{U}_{\tau_1\times\sigma_1}$: $\mathbb{A}_{\tau_1\times\sigma_1} = \mathbb{L}_{\tau_1\times\sigma_1}\mathbb{U}_{\tau_1\times\sigma_1}$;
2. Compute $\mathbb{U}_{\tau_1\times\sigma_2}$ from $\mathbb{A}_{\tau_1\times\sigma_2} = \mathbb{L}_{\tau_1\times\sigma_1}\mathbb{U}_{\tau_1\times\sigma_2}$;
3. Compute $\mathbb{L}_{\tau_2\times\sigma_1}$ from $\mathbb{A}_{\tau_2\times\sigma_1} = \mathbb{L}_{\tau_2\times\sigma_1}\mathbb{U}_{\tau_1\times\sigma_1}$;

4. LU decomposition to compute $\mathbb{L}_{\tau_2\times\sigma_2}$ and $\mathbb{U}_{\tau_2\times\sigma_2}$: $\mathbb{A}_{\tau_2\times\sigma_2} - \mathbb{L}_{\tau_2\times\sigma_1}\mathbb{U}_{\tau_1\times\sigma_2} = \mathbb{L}_{\tau_2\times\sigma_2}\mathbb{U}_{\tau_2\times\sigma_2}$. The obvious difficulty is the fact that the process is recursive (cf steps 1 and 4). In addition, Step 4 requires the addition and multiplication of blocks which may come in different formats. In more general terms, the difficulty is to evaluate

$$\mathbb{A}^{'''}_{\tau\times\sigma} \leftarrow \mathbb{A}_{\tau\times\sigma} + \mathbb{A}^{'}_{\tau\times\sigma'}\mathbb{A}^{''}_{\tau'\times\sigma}.$$

Since each block may belong to three different classes this results into 27 cases to take into account [Desiderio 2017].

**Parallelisation.** Another important aspect of $\mathcal{H}$-BEMs is their easy parallelization. During his internship, Shashank Anand (student from Indian Institute of Technology Roockee) has worked on the parallelization of the iterative $\mathcal{H}$-matrix based solver. The $\mathcal{H}$-matrix representation is based on a hierarchical of the partition of matrix. But in practice, all the operations to perform during a matrix-vector product are independent. As a result, it is easy to parallelize the code with OpenMP. The construction of the low-rank approximations of the partitioned blocks is performed in parallel to reduce the computational costs to compute the data-sparse representation of the matrix. The only difficulty is the load balancing since the sub-blocks do not have the same size. The next step is to perform the parallelization of the direct solver. It is a more involved operation since the $\mathcal{H}$-LU factorization is done hierarchically and it is necessary to determine the graph of dependences.

**Illustration in the context of seismic wave propagation.** To validate the implementation, we have considered the response of a homogeneous half-space to a time-harmonic load applied on the free surface (Fig. 4.9). The reference solution for this configuration is given by the half-space fundamental solution (presented in Chapter 2). We have then considered the same problem for hemi-spherical canyons (see [Desiderio 2017] for more details).

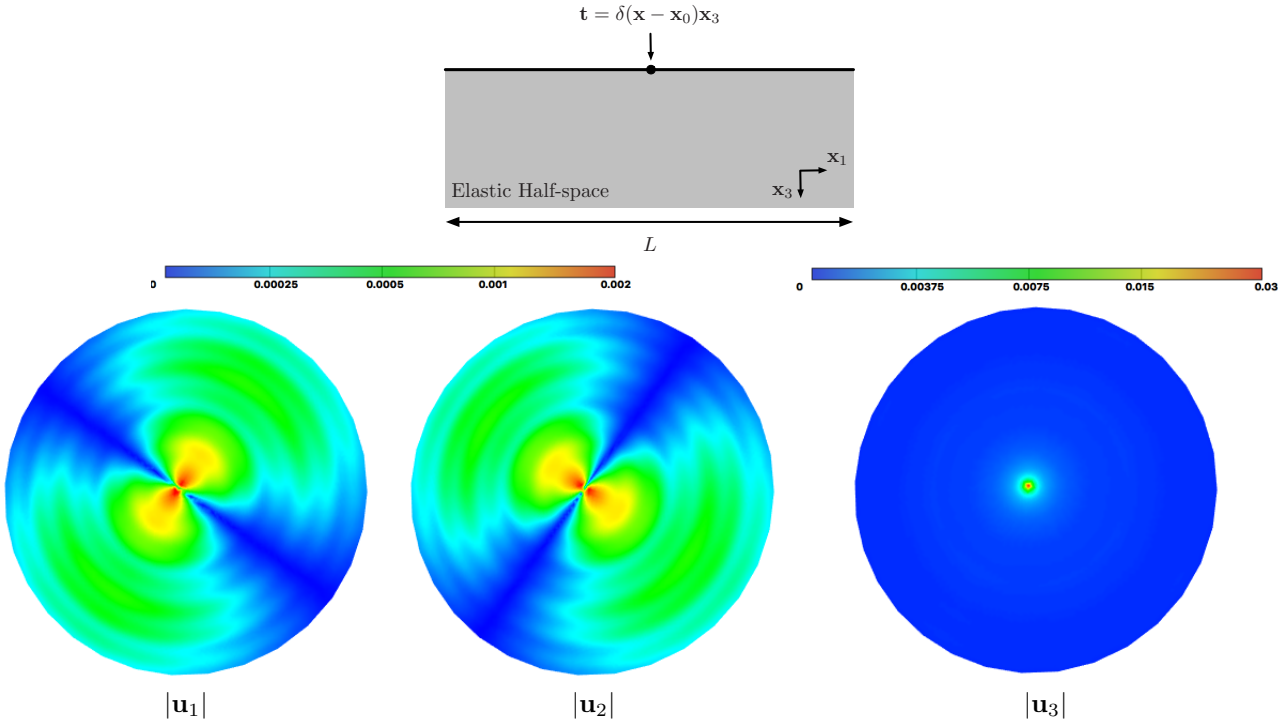


***Figure 4.9:*** *Response of a homogeneous half-space to a time-harmonic load applied on the free surface: modulus of the displacement on the free surface.*

The computational times of the iterative and direct solvers have not been compared due to the difficulty to perform a fair and exhaustive comparison. On the one hand, the iterative solver

can easily be optimized and parallelized but its performances depend largely on the quality of the preconditioner used to reduce the number of iterations. On the other hand, the optimization of the direct solver is a more involved operation that requires a task-based parallelization. Our experience with the two solvers is that the computational time of the direct solver is increasing very rapidly as a function of the number of DOFs if no parallelization is performed. However, the preconditioning of iterative BEM solvers for oscillatory problems is still an open question. Our point of view is that the two solvers have complementary advantages such that the optimal solution in the future will be to combine the iterative and direct solvers to propose new highly efficient solvers for oscillatory problems (this is part of the ongoing post-doc project of Félix Kpadonou).

## 4.3 Ongoing work: application of hierarchical matrices to mechanical engineering problems

**Better theoretical understanding.** Our first work on the application of hierarchical matrices for wave propagation problems has been to propose some algebraic arguments to explain the existence of this pre-asymptotic regime for which the method is still efficient. With Patrick Ciarlet and Félix Kpadonou, we are working on a more precise understanding of the phenomenon. We are comparing this pre-asymptotic regime with other more involved hierarchical matrix based approaches proposed for oscillatory kernels, e.g. directional $\mathcal{H}^2$-matrices and with the plane wave expansions used in the FMM. Another interesting but difficult question we try to address is to determine theoretically the limits of the pre-asymptotic regime.

**Extension to anisotropic media.** It is not sufficient to consider the soil as an isotropic viscoelastic medium. If the proposition of a FM-BEM for more complex media is difficult due to the need to derive analytically the separation of the variables in the Green's tensors, the extension of the $\mathcal{H}$-matrix based solvers is straightforward due to the algebraic nature of the method. During her internship, Aurore Texier (student from ENS Cachan) has worked on the extension of the $\mathcal{H}$-BEMs to 3D transverse isotropic elastic medium. The main difficulty lies in the complex form of the Green's tensors, based on the Radon transform [Wang 1995]. Aurore Texier has implemented these Green's tensors in COFFEE.

As an illustration, we consider the diffraction of an incident plane wave by a unit spherical cavity embedded in an either isotropic, or in a transverse isotropic medium

$$\mathbf{u}^{inc} = i\,\kappa_p\, e^{i\,\kappa_p\, x_3} \quad \text{with } \boldsymbol{x}_3 = x_3\mathbf{e}_3.$$

The mechanical parameter are set similarly to what is proposed in [Niu 2003] and [Milazzo 2012]. For the isotropic medium, we consider the non-dimensional frequency $\eta_p = \omega/c_P = 0.25\,\pi$. For the transverse isotropic medium (set to graphite-epoxy), we consider the non-dimensional frequency $\eta_p = \omega/c_P = 1$. Figures 4.10 (resp. 4.11) compare our numerical results with the results from [Milazzo 2012] for the isotropic (resp. transverse isotropic) cases. The radial and tangential displacements $\mathbf{u}_r$ and $\mathbf{u}_t$ are plotted in the $\mathbf{e}_2 - \mathbf{e}_3$ plane with respect to the angle $\theta$ (angle between $\mathbf{x}_3$ and $\mathbf{x}$). In the two cases, good agreements are obtained between the two implementations.

We now need to check the actual compression achieved with this $\mathcal{H}$-matrix representation. The extension to general anisotropy is possible but will need an involved implementation effort to code the Green's tensors.

**Fast algorithms to model quasi-dynamic earthquake cycles in complex fault networks.** Boundary Element Methods are a useful numerical tool to propagate seismic waves in the soil. But they are also used to understand the mechanism of generation of an earthquake, i.e. seismic cycle. An earthquake comes from a three-step process. First, large-scale plate movements locally generate stress accumulations with concentrated deformations on faults. When the resistance threshold of the rocks is reached, a sudden slip occurs along the fault plane; in a few seconds, the rupture spreads, then stops: it is the earthquake. The cycle can then start again.

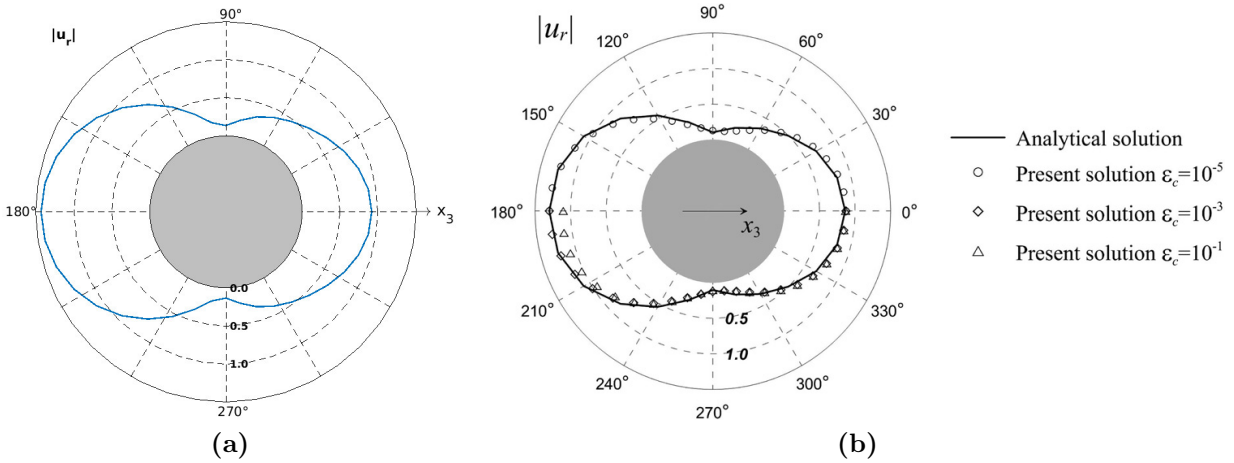


**(a)** **(b)**

***Figure 4.10:*** *Comparison of previously published and present radial displacements on the points lying in the $\mathbf{e}_2 - \mathbf{e}_3$ plane for the spherical cavity in an unbounded isotropic domain:* **(a)** *present solutions (with solid lines) and* **(b)** *results from [Milazzo 2012].*

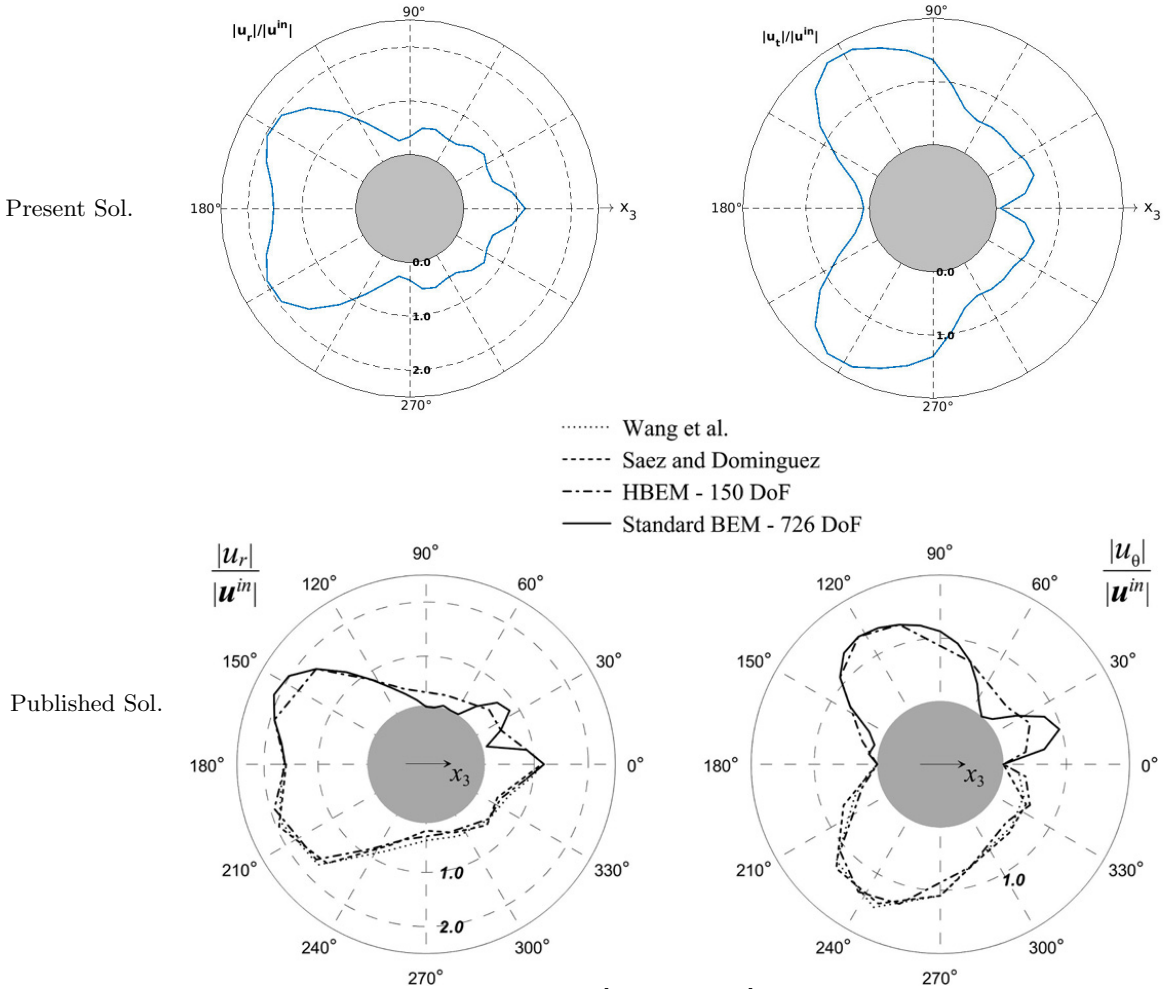


***Figure 4.11:*** *Comparison of previously published [Milazzo 2012] and present radial and tangential displacements on the points lying in the $\boldsymbol{x}_2 - \boldsymbol{x}_3$ plane for scattering by a spherical cavity in a graphite-epoxy (transverse isotropic) unbounded domain.*

Faults most often act as a network and have geometric complexities (roughness, branches ...) at all scales (see Fig. 4.12). However, the majority of seismic cycle models to date are limited to plane geometries with a unique fault in order to reduce the computational costs. One of the research axes of the group of Harsha Bhat at ENS Ulm is on the improvement of these seismic cycle models. In his PhD thesis [Romanet 2018], Pierre Romanet has developed the following new quasi-dynamic model of the seismic cycle.

- The quasi-static shear traction at a given point on the fault due to the slip distribution is computed with the Boundary Element Method.
- The shear traction is balanced by the strength of the fault, modelled by a rate-and-state friction law with ageing state evolution.
- The far-field tectonic loading rate is assumed to be constant.

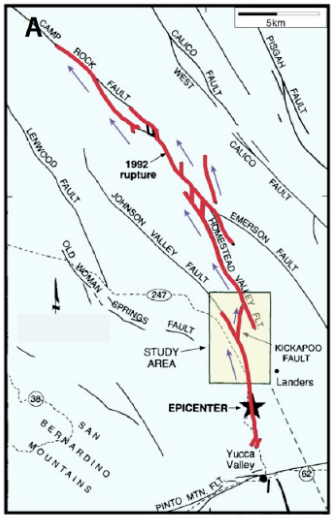


***Figure 4.12:*** *Illustration of the complexity of a fault network to model in the seismic cycle (from [Romanet 2018]).*

The most time consuming part in this model is due to the computation of the elastic stress interaction. In this context, we have adapted the hierarchical matrices to this problem to accelerate the BEM problem. With the capabilities of the improved algorithm, Pierre Romanet has been able to explore the behaviour of fault networks in mode II or III (whereas he was only able to consider mode II with the FMM). As an illustration of the accuracy of the method, Figure 4.13 represents the maximum velocity over time for a single fault with an imposed slip (for which an analytical solution is known). Both mode II and III are considered since it is a flat fault. The idea is to check if some error has accumulated over time (each time step having been checked previously). On this example, we note that after 8 cycles corresponding to 160 years, the earthquake is happening at the same time (up to a few seconds) for the approximated and analytical solutions, confirming the accuracy of the approach [Romanet 2018].

Once the code was validated, Pierre Romanet has shown that while a single fault gives rise to a periodic behaviour, with always the same repeating earthquake, the introduction of a second fault interacting with the first reveals a great complexity in the seismic cycle. An article on this first application of hierarchical matrices to model seismic cycles is under preparation [18]. From a computational point of view, in the future it would be interesting to quantify the compression rate achieved for this specific type of kernels. So far, we have simply observed the drastic reduction of the computational times without quantifying and analysing this improvement.

**Hydraulic fracturing.** The development of numerical methods for hydraulic fracture simulation is a timely topic [Lecampion 2017, Lecampion 2018]. The BEM is also particularly well-suited to model fracture problems in homogeneous (or piecewise homogeneous). With Brice Lecampion

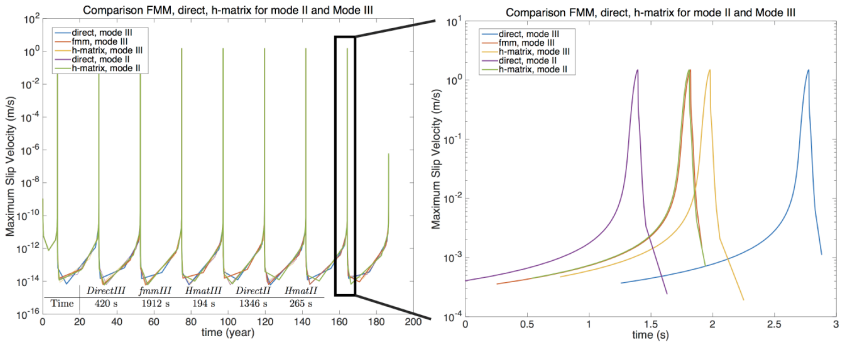


***Figure 4.13:*** *Validation of the accuracy of the H-matrix based solver (with respect to an analytical solution) to simulate a seismic cycle for a single fault. The zoom shows that after 8 cycles corresponding to* 160 *years, the earthquake is happening at the same time (up to few seconds), confirming the accuracy of the approach [Romanet 2018].*

(and in collaboration with François Fayard from the company InsideLoop), we are developing a library based on $\mathcal{H}$-matrices to speed-up the modelling of hydraulic fractures (see Fig. 4.14). The group of Brice Lecampion (EPFL) is interested in improving the efficiency and sustainability of fluid injection and withdrawal from porous reservoirs located in the upper earth crust. More specifically, the library will be used to speed up the modelling of the propagation of fluid-driven fractures. The main applications are to improve the performances of wells (both producers and injectors) and to engineer the hydraulic conductivity of enhanced geothermal system.

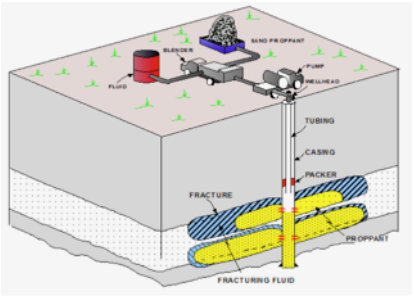


***Figure 4.14:*** *The hydraulic Fracturing Process, courtesy of B. Lecampion.*

So far, the library has been used to check the accuracy of a simple 2D elastostatic displacement discontinuity boundary element problem (i.e. a fracture problem). This elastic solver is part of a larger code (HPx2D) geared toward the solution of fluid-driven fracture propagation problems which exhibit a strongly non-linear hydro-mechanical coupling. $\mathcal{H}$-matrix representations are very efficient for elastostatic problems since the kernel is asymptotically smooth such that the expected compression rate is important. We have considered the standard Griffith crack test. It is a simple straight crack under a uniform mode I loading. The analytical solution of this problem is known such that we can check the accuracy of the method. To begin, we compare at all collocation points the numerical fracture opening with the analytical solution.

In Table 4.4, we report the first preliminary results. The $\mathcal{H}$-LU direct solver is used for a problem of size $N = 40\,000$ and an accuracy in the ACA fixed to $\varepsilon_{\text{ACA}} = 0.1$. We study the effect of the parameter $\eta$ in this configuration. As expected, if we increase $\eta$, more blocks are admissible and the compression rate is larger. But since the accuracy in the ACA is very low, the accuracy of the overall result decreases as $\eta$ increases. For 3D elastodynamics we have seen that the optimal results are obtained for $\eta = 3$. Interestingly, since in this work we consider elongated objects in the static case, the optimal parameter seems to be smaller. We will study in more details this aspect.

Nevertheless, these preliminary results show that for a given accuracy, the computational costs are drastically reduced (by a fact 7 on this example).

| $\eta$ | Mean rel. error | $\tau(\mathcal{H})$ | Matrix construction time (s) | Total time (s) |
|---|---|---|---|---|
| dense | $1.23\ 10^{-4}$ | - | 219 | 855 |
| 0.3 | $19.43\ 10^{-4}$ | $2.01\ 10^{-2}$ | 9 | 42 |
| 0.2 | $7.83\ 10^{-4}$ | $2.40\ 10^{-2}$ | 11 | 63 |
| 0.1 | $1.43\ 10^{-4}$ | $4.19\ 10^{-2}$ | 19 | 132 |

***Table 4.4:*** *Effect of the $\eta$ parameter in the admissibility condition on the relative error to the Griffith solution and computational costs for the case $N = 40\,000$ ($\mathbb{P}_0$ elements) and $\varepsilon_{\text{ACA}} = 0.1$.*

Future work will concern the exhaustive study of the parameters of the acceleration technique and the application to more complex configurations: an arc crack for which an analytical solution is available, an array of parallel cracks and then 3D examples.

# CHAPTER 5

# Anisotropic mesh adaptation for BEMs

## Contents



So far, most of the effort in the BEM community has been dedicated to the speed-up of the solution of the BIEs. However once fast BEMs are well developed, it is necessary to propose tools to guarantee a certain level of accuracy of the numerical results. Error estimates are an important tool for reliable and efficient BEM computations. In addition, an adaptive mesh procedure is a complementary way to reduce the computational time. The principle is to optimize (or at least improve) the positioning of a given number of degrees of freedom on the geometry of the obstacle, in order to yield simulations with superior accuracy compared to those obtained via the use of uniform refinements. Adaptation is particularly important for scattering obstacles that contain geometric singularities, i.e., corners and ridges, which lead to a rapid variation of the surface solution near these singularities. For such problems, meshes graded toward these singularities must be employed in order to obtain an optimal rate of convergence. In addition, for wave scattering problems, we may exploit the directionality of the waves in order to further reduce the number of DOFs. By choosing the optimal mesh to achieve a desired level of accuracy, the number of DOFs can be reduced. In the same way than for FEMs, error estimates need to be studied for fast BEMs. The number of publications on error estimates for BEMs is limited because of the high computational cost of standard BEMs. With the recent developments of fast BEMs, error estimates can be tested in the situations where they are really essential (i.e. large-scale problems). It was the main goal of the project RAFFINE funded by the French National Research Agency (ANR, 2013-2017).

In the BEM community, the majority of the research on mesh adaptation has been confined to isotropic techniques with a focus on the Laplace equation see, e.g., the exhaustive review [Feischl 2015] and extensions to the Helmholtz equation being made only fairly recently [Bakry 2016, Bakry 2017a, Bakry 2017b]. These isotropic techniques are usually based on *a posteriori* error analysis from which element-wise error indicators are derived. An indicator is then used to steer the mesh refinement by systematically marking and refining only elements where the error is above a specified threshold - a process known as Dörfler marking [Carstensen 2014]. The derivation of appropriate local error estimators [Faermann 1998] is a significant challenge owing to the non-locality of boundary integral operators. This difficulty is the main reason why adaptivity for the BEM is a much less well-explored research topic in comparison to adaptivity for the FEM where the relevant operators are local differential operators. In many works convergence rates for error estimates are proven rigorously, e.g., [Ferraz-Leite 2008, Carstensen 1997, Gantumur 2013].

However, it is seen that Dörfler refinement techniques do not usually recover the optimal convergence rates for 3D problems with anisotropic features [Aurada 2012]. The additional drawback of previously published works is the problem-dependent or integral equation-dependent nature of the error estimates. Also, the error analysis of these methods requires a Galerkin discretization and hence a higher computational cost than a collocation discretization.

With Samuel Groth, Faisal Amlani and in collaboration with Adrien Loseille (INRIA team Gamma3), we have introduced a metric-based anisotropic mesh adaptation strategy [Loseille 2010] for the FM-BEM for the three-dimensional Helmholtz equation [1] (the application to 3D elastodynamics is then straightforward). The first advantage of this method is to be independent of the discretization technique. In addition, it does not employ a Dörfler marking strategy but rather generates a sequence of non-nested meshes with a specified complexity (proportional to the number of vertices or elements). The different meshes are defined according to a metric field derived from the evaluation of the linear interpolation error of the (unknown) exact solution on the current mesh. From a theoretical point of view, a continuous metric is derived from the Hessian of the exact solution. From a practical point of view, an approximate metric is derived from the numerical solution (obtained via the BEM on a mesh) only on which a numerical Hessian-recovery procedure is applied. The metric-based anisotropic mesh adaptation (AMA) approach, as outlined above, has never been applied to the BEM and is presented in Section 5.1. This adaptation procedure results in anisotropic meshes. Numerical examples presented in Section 5.2 demonstrate that contrary to existing approaches, we recover the theoretical optimal convergence rates for domains that include geometric singularities such as corners and ridges. The potentialities of the anisotropic mesh adaptation for fast BEMs is first done for a $\mathbb{P}_1$ interpolation of the solution. If we want to consider curved elements, it is necessary to make some improvements presented in Section 5.3.

## 5.1 Metric-based anisotropic mesh adaptation for BEMs

In [1], we derive new estimates for the metric-based anisotropic mesh adaptation procedure in the case of 3D surface solutions. The metric-based mesh adaptation method we employ is connected to the linear interpolation error of the (unknown) exact solution on the mesh (interpolation with higher order functions is under investigation) within a specified norm. Then, given a number of degrees of freedom, meshes which minimize this interpolation error are designed in an anisotropic setting. Via arguments relating the BEM approximation error to this interpolation error, such meshes are seen to be close to optimal for BEM solutions. We report here the main results and refer the interested reader to [1] for the complete proofs.

### 5.1.1 Metric-based anisotropic mesh adaptation for a surface solution

A convenient framework to generate anisotropic meshes is based on Riemannian metric spaces. A Riemannian metric space is defined by a metric tensor $\mathcal{M}(\mathbf{x})$ (where $\mathcal{M}$ is a symmetric positive definite matrix), i.e., is a smoothly varying function of the physical variable $\mathbf{x}$. In the context of anisotropic mesh generation, each mesh vertex $\mathbf{x}$ has an assigned value $\mathcal{M}(\mathbf{x})$ which dictates the size and orientation of adjacent elements. By generating a unit mesh in the corresponding Riemannian metric space, we obtain an anisotropic mesh refined in Euclidean space according to the metric $\mathcal{M}$. This is the fundamental idea of metric-based mesh adaptation [George 1991].

A surface mesh, associated with a Riemannian metric space $\mathbf{M} = (\mathcal{M}(\mathbf{x}))_{\mathbf{x}\in\Gamma}$ is a triangulation of the surface $\Gamma$. A triangle $K$, which is defined by its edges $\{\mathbf{e}_i\}_{i=1}^3$, is *unit* with respect to $\mathcal{M}$ if the length of each edge is unit in this metric, i.e., if

$$||\mathbf{e}_i||_{\mathcal{M}} := \sqrt{{}^t\mathbf{e}_i\mathcal{M}\mathbf{e}_i} = 1, \quad \text{for} \quad i = 1, 2, 3. \tag{5.1}$$

At this point it is important to note that in the BEM context, the mesh is 3D but the elements are 2D. We need to introduce the operator $R_K$ that restricts a 3D quantity to the 2D local element frame. If the three edges of $K$ are of unit length with respect to the metric tensor $\mathcal{M}$, then the area of $K$ computed in the Riemannian ($|K|_{\mathcal{M}}$) or Euclidean ($|K|$) space is, respectively,

$$|K|_{\mathcal{M}} = \frac{\sqrt{3}}{4}, \quad \text{and} \quad |K| = \frac{\sqrt{3}}{4}\det(R_K(\mathcal{M}^{-1/2})).$$

The existence of a conforming *unit mesh* in which each triangle is perfectly unit with respect to a given Riemannian metric space is not guaranteed in general [Loseille 2017]. Hence the objective of seeking a unit mesh must be relaxed. We seek for a *quasi-unit* mesh with respect to $\mathcal{M}$, which is a mesh composed of quasi-unit triangles. A triangle $K$ is quasi-unit with respect to $\mathcal{M}$ if

$$\frac{1}{\sqrt{2}} \leq ||\mathbf{e}_i||_{\mathcal{M}} \leq \sqrt{2}, \quad \text{for} \quad i = 1, 2, 3, \quad \text{and} \quad |K|_{\mathcal{M}} = \frac{\sqrt{3}}{4}. \tag{5.2}$$

Using the above notion of a quasi-unit mesh, the generation of anisotropic meshes is simplified. The mesh generator is only required to generate a quasi-unit mesh in the prescribed Riemannian metric space, and this is shown to be always possible. The generated adapted mesh is anisotropic in Euclidean space.

The principle of AMA theory consists in minimizing the error coming from the linear interpolation of the (unknown) exact solution. In the BEM context, we cannot directly apply the results proposed for 2D or 3D volume solutions as we only have the solution on the boundary. In particular, we cannot recover the Hessian of the numerical solution which is needed for the AMA procedure. One alternative would be to extend the theory for 3D volume solutions by considering the covariant derivatives. This approach would involve complex developments of differential geometry. In addition, we only focus on a linear approximation of the surface. These developments are mainly relevant for higher order approximations. A more natural and simple approach in the BEM context is to extend the surface solution in a tubular neighborhood, i.e., for a collection of points whose distance to the surface is smaller than $\varepsilon$ [Nédélec 2001]. More precisely, to any solution $u_s$ defined on the surface $\Gamma$, we associate the lifting $u$ defined on the tubular neighborhood $\Gamma_\varepsilon$ by

$$u(\mathbf{x}) = u_s(\mathcal{P}(\mathbf{x}))$$

where $\mathcal{P}(\mathbf{x})$ is the projection onto the surface $\Gamma$. The function $u$ is now a 3D volume solution and we can define its Hessian.

### 5.1.2 Controlling the linear interpolation error

We note $\Pi_h$ the discrete linear interpolation operator, i.e., $\Pi_h u$ is the linear interpolant of $u$ on the mesh $\mathcal{H}_N$ (with $N$ nodes). The starting point is to show that the interpolation error in the $L^1$ norm of the solution $u$ on a triangular element $K$ is

$$||u - \Pi_h u||_{L^1(K)} = \frac{|K|}{24} |\sum_{i=1}^{3} {}^t\mathbf{e}_i \, H \, \mathbf{e}_i| \; \leq \frac{|K|}{24} \sum_{i=1}^{3} {}^t\mathbf{e}_i \, |H| \, \mathbf{e}_i, \tag{5.3}$$

where the $\mathbf{e}_i$ are the edges of the triangle $K$ provided in the local element frame and for every symmetric Hessian matrix $H$, $|H|$ denotes the positive symmetric matrix deduced from H by taking the absolute values of its eigenvalues. The proof is based on the evaluation of the pointwise interpolation error within the element, i.e., $(u - \Pi_h u)(\mathbf{x})$ for $\mathbf{x} \in K$. It uses only the mapping onto the reference element and the knowledge that the solution is a quadratic function. This error is then integrated over the element.

So far, we have not used the fact that all elements $K$ are unit with respect to the metric $\mathcal{M}$. Using this information, we can show that

$$\sum_{i=1}^{3} {}^t\mathbf{e}_i \, H \, \mathbf{e}_i = \frac{3}{2} \text{trace}(R_K(\mathcal{M}^{-\frac{1}{2}} \, H \, \mathcal{M}^{-\frac{1}{2}})).$$

Finally, using that $|K| = \frac{\sqrt{3}}{4} \det(R_K(\mathcal{M}^{-1/2}))$, the interpolation error (5.3) is expressed for a surface solution by:

$$||u - \Pi_h u||_{L^1(K)} = \frac{\sqrt{3}}{64} \det(R_K(\mathcal{M}^{-\frac{1}{2}})) \, |\text{trace}(R_K(\mathcal{M}^{-\frac{1}{2}} \, H \, \mathcal{M}^{-\frac{1}{2}}))|. \tag{5.4}$$

Importantly, (5.4) implies that the interpolation error does not depend on the element shape. The metric alone contains enough information to describe completely the linear interpolation error

in the $L^1$ norm. In addition, this interpolation error can be expressed with continuous quantities only. The restriction $R_K$ is replaced by its continuous counterpart $R_s$, i.e., the tangent plane restriction. We thus define a continuous linear interpolation error, independent from the discrete mesh

$$2\frac{||u-\Pi_h u||_{L^1(K)}}{|K|} = \frac{1}{8}\,|\mathrm{trace}(R_s(\mathcal{M}^{-\frac{1}{2}}\,H\,\mathcal{M}^{-\frac{1}{2}}))| \leq \frac{1}{8}\,\mathrm{trace}(R_s(\mathcal{M}^{-\frac{1}{2}}\,|H|\,\mathcal{M}^{-\frac{1}{2}})).$$

Then, we define the upper bound of the continuous interpolation error by

$$e_{R_s(\mathcal{M})}(\mathbf{x}) = \frac{1}{8}\,\mathrm{trace}(R_s(\mathcal{M}^{-\frac{1}{2}}\,|H|\,\mathcal{M}^{-\frac{1}{2}})). \tag{5.5}$$

Finally, the continuous interpolation error calculated on the continuous mesh $\mathbf{M}$ is given by

$$E_p(\mathbf{M}) = \int_\Gamma \Big(e_{R_s(\mathcal{M})}(\mathbf{x})\Big)^p d\mathbf{x}, \quad p \geq 1. \tag{5.6}$$

### 5.1.3 Deriving the optimal continuous mesh

The introduction of the continuous interpolation is very important to find the optimal mesh, i.e., the mesh minimizing the error introduced in the BEM solution. Indeed, the initial discrete optimization problem is to find the to find the surface mesh $\mathcal{H}_N^{opt}$ with $N$ nodes minimising the discrete interpolation error in the $L^p$ norm:

$$\text{Given a number of nodes } N\text{, find } \mathcal{H}_N^{opt}\text{, minimising } ||u-\Pi_h u||_{L^p(\Gamma_h)}, \tag{$\mathcal{P}_d$}$$

where $\Gamma_h$ is the discrete support representing $\Gamma$. This problem is generally intractable practically and would require some simplifications. By replacing the discrete interpolation error with its continuous equivalent, we do not have anymore to deal with discrete quantities. Using the mathematical tools defined on the continuous mesh space instead of the discrete one, the optimization problem is simplified. We consider in the following the continuous interpolation error controlled in $L^p$ norm (with $p \geq 1$). The global optimization problem becomes to find the optimal continuous mesh $\mathbf{M}^*$ minimizing the continuous interpolation error in the $L^p$ norm:

$$\text{Given a complexity } \mathcal{N}\text{, find } \mathbf{M}^* = \mathrm{argmin}_{\mathbf{M}}\ \Big(\int_\Gamma \Big(e_{R_s(\mathcal{M})}(\mathbf{x})\Big)^p d\mathbf{x}\Big)^{1/p}. \tag{$\mathcal{P}_c$}$$

The optimization problem ($\mathcal{P}_c$) is well-posed and the interpolation error is expressed continuously without the need to define a discrete support.

We need to introduce some concepts of the continuous mesh framework [Loseille 2011]. These meshes are represented by a Riemannian metric space $\mathbf{M} = (R_s(\mathcal{M})(\mathbf{x}))_{\mathbf{x}\in\Gamma}$. Locally, the spectral decomposition of $R_s(\mathcal{M})(\mathbf{x})$ is

$$R_s(\mathcal{M})(\mathbf{x}) = \mathcal{R}(\mathbf{x})\Lambda(\mathbf{x})^t\mathcal{R}(\mathbf{x}),$$

where $\mathcal{R}(\mathbf{x})$ is an orthonormal matrix that provides the local orientation given by the eigenvectors $(\mathbf{v}_i(\mathbf{x}))_{i=1,2}$. The $(\lambda_i(\mathbf{x}))_{i=1,2}$ are the corresponding eigenvalues. As a result, the diagonal matrix $\Lambda$ is either

$$\begin{bmatrix} \lambda_1(\mathbf{x}) & 0 \\ 0 & \lambda_2(\mathbf{x}) \end{bmatrix} \quad \text{or} \quad \begin{bmatrix} h_1^{-2}(\mathbf{x}) & 0 \\ 0 & h_2^{-2}(\mathbf{x}) \end{bmatrix}.$$

Introducing the density $d = (h_1h_2)^{-1}$ and the anisotropic quotients $r_i = h_i^2(h_1h_2)^{-1}$, we can write

$$R_s(\mathcal{M})(\mathbf{x}) = d(\mathbf{x})\mathcal{R}(\mathbf{x}) \begin{bmatrix} r_1^{-1} & \\ & r_2^{-1} \end{bmatrix}{}^t\mathcal{R}(\mathbf{x}).$$

It follows from (5.5) that

$$e_{R_s(\mathcal{M})} = \frac{1}{8}\Big(d^{-1}(\mathbf{a})\sum_{i=1}^{2} r_i(\mathbf{a})^t\mathbf{v}_i(\mathbf{a})|R_s(H)|\mathbf{v}_i(\mathbf{a})\Big),$$

where $\mathbf{v}_i$ denotes the eigenvectors of the metric $R_s(\mathcal{M})$.

It is then possible to solve the continuous optimization problem. We introduce $\gamma_i = {}^t\mathbf{v}_i(\mathbf{a})|R_s(H)|\mathbf{v}_i(\mathbf{a})$, i.e., the directions of the continuous mesh. The first step in the solution of $(\mathcal{P}_c)$ is to fix $\gamma_1$ and $\gamma_2$. We have shown in [1] using the calculus of variations that the optimal continuous mesh $\mathbf{M}^*$ obtained by solving $(\mathcal{P}_c)$ is described by

$$\lambda_i^* = (h_i^*)^{-2} = \mathcal{N}\left(\int_\Gamma (\gamma_1\,\gamma_2)^{\frac{p}{2(p+1)}}\right)^{-1} (\gamma_1\,\gamma_2)^{-\frac{1}{2(p+1)}}\ \gamma_i\,, \quad \text{and } r_i^* = \frac{(\gamma_1\,\gamma_2)^{\frac{1}{2}}}{\gamma_i}\ \ \forall i = 1,2\,. \tag{5.7}$$

It is also possible to prove that the optimal continuous mesh $\mathbf{M}^*$ given by (5.7) is the unique solution of $(\mathcal{P}_c)$ verifying $E_p(\mathbf{M}^*)^p < E_p(\mathbf{M})^p$ for all $\mathbf{M}$ having the same fixed $(\gamma_i)_{i=1,2}$.

The last step consists in deriving the optimal directions of the continuous mesh $\mathbf{M}^*$. Our main result is that the optimal metric both in sizes and directions is given by the following theorem.

**Theorem 5.1.1.** *Let $u$ be a twice continuously differentiable function and $H$ its Hessian, the optimal continuous mesh $\mathbf{M}^*$ minimizing Problem $(\mathcal{P}_c)$ reads locally:*

$$R_s(\mathcal{M}^*) = D^*\ \det(|R_s(H)|)^{\frac{-1}{2(p+1)}}\ |R_s(H)|,\ \textit{with } D^* = \mathcal{N}\left(\int_\Gamma \det(|R_s(H)|)^{\frac{p}{2(p+1)}}\right)^{-1}. \tag{5.8}$$

*$\mathbf{M}^*$ is unique, locally aligned with the eigenvectors basis of $R_s(H)$ and has the same anisotropic quotients as $R_s(H)$. In addition, $\mathbf{M}^*$ provides an optimal explicit bound of the interpolation error in the $L^p$ norm (with $p \geq 1$):*

$$E_p(\mathbf{M}^*) = \frac{\mathcal{N}^{-1}}{4}\left(\int_\Gamma \det\left(|R_s(H)|\right)^{\frac{p}{2(p+1)}}\right)^{\frac{p+1}{p}}. \tag{5.9}$$

We now have all the tools to generate in practice a discrete mesh approximating the continuous optimal solution. We can use any metric-based adaptive mesh generator as soon as the generated mesh is quasi-unit. In addition, we provide bounds on the discrete interpolation error when the continuous mesh is projected into the space of discrete meshes by means of an adaptive mesh generator. If the mesh generator achieves a quasi-unit mesh with respect to $\mathbf{M}^*$, the following bounds for the discrete interpolation error are obtained:

$$\frac{1}{2}\,E_p(\mathbf{M}^*) \quad \leq \|u - \Pi_h u\|_{L^p(\Gamma_h)} \leq \quad 2\,E_p(\mathbf{M}^*)\,,$$

or equivalently,

$$\frac{1}{8}\,\mathcal{N}^{-1}\left(\int_\Gamma \det\left(|R_s(H)|\right)^{\frac{p}{2(p+1)}}\right)^{\frac{p+1}{p}} \quad \leq \|u - \Pi_h u\|_{L^p(\Gamma_h)} \leq \quad \frac{1}{2}\,\mathcal{N}^{-1}\left(\int_\Gamma \det\left(|R_s(H)|\right)^{\frac{p}{2(p+1)}}\right)^{\frac{p+1}{p}} \tag{5.10}$$

In other words, $\mathbf{M}^*$ defined by (5.8) allows us to generate an optimal adapted mesh to control the interpolation error in the $L^p$ norm. One main advantage of this approach is to be completely generic, independent from the PDE and the numerical scheme.

### 5.1.4 Refinement strategy

All our numerical examples use the same refinement strategy. Given a user-prescribed sequence of complexity $\mathbf{N} = [\mathcal{N}_1, \ldots, \mathcal{N}_k]$, we seek for the sequence of corresponding optimal meshes $\mathbf{H} = [\mathcal{H}_1, \ldots, \mathcal{H}_k]$. This process is non-linear, i.e., both the mesh and the solution have to be converged. The following iterative algorithm is used to generate $\mathcal{H}_i$:

Start from the mesh $\mathcal{H}_i^0 = \mathcal{H}_{i-1}$ (or from the initial uniform mesh $\mathcal{H}_0$ at iteration 0).
**for all** k=0 : $n_{iter}$ **do**
Compute the approximation $u^h$ on the mesh $\mathcal{H}_i^k$ with the iterative FM-BEM solver (software COFFEE).

Compute the recovered Hessian from $u^h$ and deduce Metric (5.8) at the nodes of the mesh, with complexity $\mathcal{N}_i$.
From (5.8), a new quasi-unit mesh $\mathcal{H}_i^{k+1}$ of complexity $\mathcal{N}_i$ is generated with FEFLO.A [Loseille 2017].
**end for**

For each case, the complexity sequence is always defined as $\mathcal{N}_{i+1} = 2\mathcal{N}_i$ with $n_{iter} = 3$ or $n_{iter} = 5$.

## 5.2 Validation of the adaptive mesh strategy for 3D acoustic FM-BEM

We report in this section two illustrations of the capabilities of the adaptive mesh strategies presented in [1].

**Planar screen.** We consider the scattering of plane waves (with unit amplitude and direction $\mathbf{d} = (-1, 0, 0)$) by a sound-soft unit screen centered at the origin, i.e., the screen occupies the region $\left[-\frac{1}{2}, \frac{1}{2}\right] \times \left[-\frac{1}{2}, \frac{1}{2}\right]$. Such configurations lead to surface solutions with the most severe singular behavior, and are a good illustration of the capabilities of an adaptive mesh strategy. It is well known (see, e.g., [Juhl 1998]) that at the edge of a screen, we have

$$\left[\frac{\partial u}{\partial \mathbf{n}}\right] \sim (\kappa r)^{-0.5} \quad \text{as } \kappa r \to 0, \tag{5.11}$$

where $r$ is the distance from the edge. At the corner of the screen, this singularity is more severe, and is shown in [Bažant 1974] to take the form

$$\left[\frac{\partial u}{\partial \mathbf{n}}\right] \sim (\kappa r)^{-0.704} \quad \text{as } \kappa r \to 0.$$

The optimal convergence rate here (for our $\mathbb{P}_1$ discretization) is $\mathcal{O}(N^{-1})$. Owing to the singular behavior, the approximated solution on a sequence of uniformly refined meshes should yield a sub-optimal convergence rate.

We have employed our adaptive strategy for three wavenumbers ($\kappa = 5,\ 20,\ 80$) and compared the results to those obtained with a sequence of uniformly refined meshes. In figures 5.1b-d, we present the relative $L^2$ errors in the scattered field evaluated on a circle in the $(x, y)$-plane of radius 2 (Figure 5.1a). We observe that the use of the anisotropic adaptive strategy improves the computational efficiency for this scattering problem by almost an order of magnitude. For example, for $\kappa = 80$, to achieve an accuracy of $1.12\ 10^{-2}$ with a uniform refinement 55 224 DOFs are required while the anisotropic refinement produced an approximation with an accuracy of $7.9\ 10^{-3}$ with only 4 672 DOFs. In addition, for all three wavenumbers the uniform refinement yields a convergence rate of approximately $\mathcal{O}(N^{-0.5})$ in the relative $L^2$ error. This sub-optimality is related to the prominent edge singularities of the form (5.11). While, with the adaptive mesh strategy, the optimal convergence rate of $\mathcal{O}(N^{-1})$ is recovered. In fact, it appears that we even improve slightly on this rate, especially at the higher wavenumbers. This improvement can be attributed to the exploitation of the directionality of the wave propagation.

In Figure 5.2, we depict the final surface mesh for $\kappa = 5$ and $\kappa = 20$. For $\kappa = 5$ (resp. $\kappa = 20$), the mean anisotropic ratio is around 30 (resp. 60). If an isotropic error estimate was used, the obtained mesh would contained 55 608 DOFs, i.e., 15 times more DOFs than the anisotropic mesh for $\kappa = 20$ at 5th iteration. This also emphasizes the advantage of using anisotropic estimates over isotropic estimates.

Finally, the level of anisotropy on the sides of the screen increases with the complexity, see Figure 5.3, showing the strong directionality of the error.

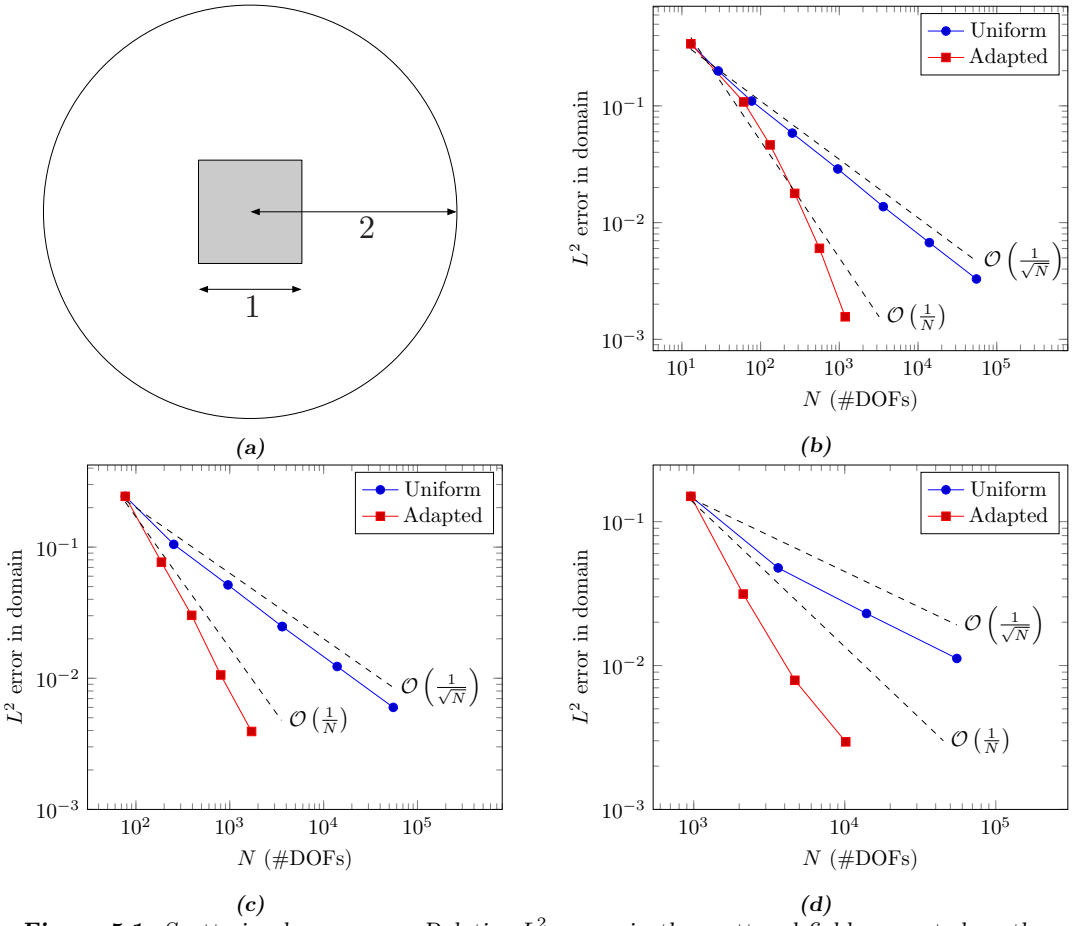


***Figure 5.1:*** *Scattering by a screen: Relative $L^2$ errors in the scattered field computed on the circle* **(a)** *for uniform and adapted meshes for three wavenumbers:* **(b)** $\kappa = 5$, **(c)** $\kappa = 20$ *and* **(d)** $\kappa = 80$.

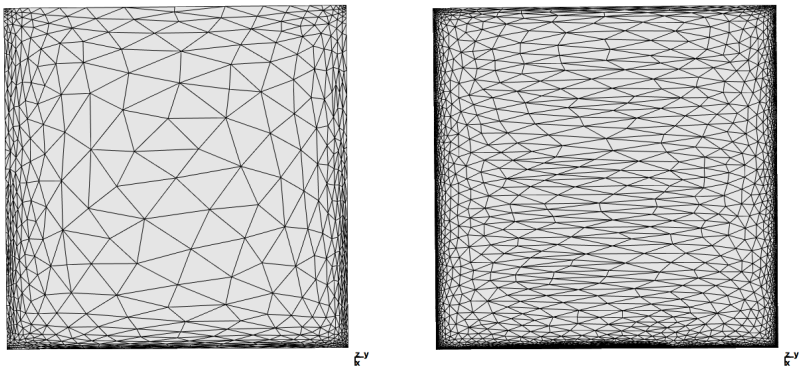

***Figure 5.2:*** *Screen case: final adapted meshes for $\kappa = 5$ (left) and $\kappa = 20$ (right).*

**F15 aircraft.** In this test case, we illustrate the robustness of the technique with respect to the complexity of the input geometry. We consider the geometry of an unarmed F15 aircraft. The computation is started with a uniform mesh composed of almost 80 000 vertices and 163 000 triangles. The incident plane wave has direction $\mathbf{d}^i = (1/2, 1, 0)$ and wavenumber $\kappa = 6$. In this numerical experiment, 15 adapted meshes are generated. The imposed complexity is kept constant for 3 iterations, and then it is multiplied by a factor 2. The prescribed complexities are $\{10\,000, 20\,000, 40\,000, 80\,000, 160\,000\}$.

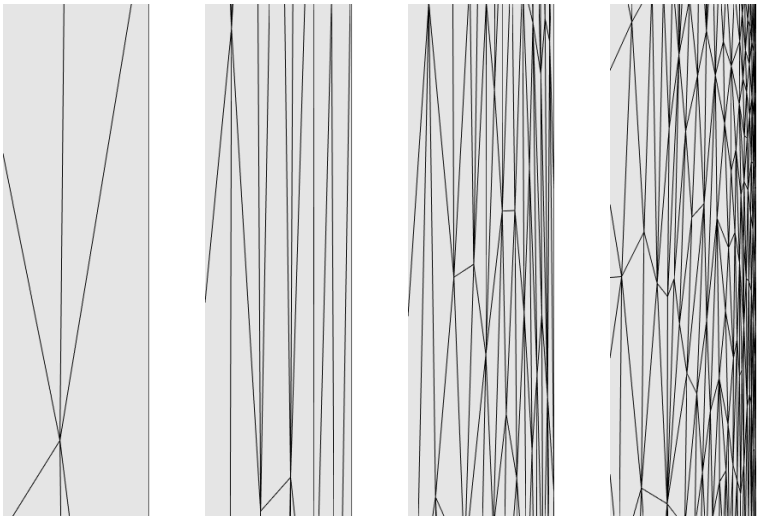


***Figure 5.3:*** *Screen case: evolution of the anisotropic ratio from 2nd to 5th iteration for $\kappa = 20$ at side $x = 0.5$.*

The real part of the boundary solution is represented in Figure 5.4a. We see the high directionality of the diffracted waves with different patterns for the front and back part of the aircraft. In Table 5.2, we report the sizes of the generated meshes. We observe that the size is almost doubled at each sequence of fixed complexity. The meshing CPU time is the combined time taken to evaluate the error estimate, generate the adapted mesh, and interpolate the solution from the previous mesh to the current mesh. In term of sizes, we report in Table 5.1 the minimal size of the anisotropic mesh. To evaluate the gain of using an anisotropic approach, an isotropic and uniform mesh have been generated with the same level of discretization as its anisotropic counterpart. The factors provided in Table 5.1 are the multiplication factors needed to obtain the sizes of the isotropic and uniform meshes, respectively. We observe that if an isotropic approach was used, the size of the meshes would be approximately 3 times greater. And if uniform meshes were employed, the size of the meshes to achieve the same accuracy would be between 300 and 6 million times greater! For instance, the uniform mesh having the same accuracy than the 15th mesh is composed of more than 500 million vertices. This illustrates the optimality of the anisotropic approach in term of ratio accuracy/CPU time. Finally in Figure 5.4c-d, we display the total field in the planes defined by $y = 0$ and $z = 0$.

| Iteration | Minimal Size | Gain over isotropic | Gain over uniform |
|---|---|---|---|
| 3 | $9 \cdot 10^{-3}$ | 3.9 | 378 |
| 6 | $4 \cdot 10^{-3}$ | 4.9 | 2 535 |
| 9 | $1.3 \cdot 10^{-3}$ | 3.0 | 47 572 |
| 12 | $5.6 \cdot 10^{-4}$ | 3.2 | 377 246 |
| 15 | $1.8 \cdot 10^{-4}$ | 3.5 | 6 195 211 |

***Table 5.1:*** *F15 aircraft: Expected gain in terms of DOFs of using an anisotropic approach compared to isotropic or uniform refinement. The size of the corresponding isotropic or uniform mesh has to be multiplied by the factor given in the 3rd and 4th column respectively.*

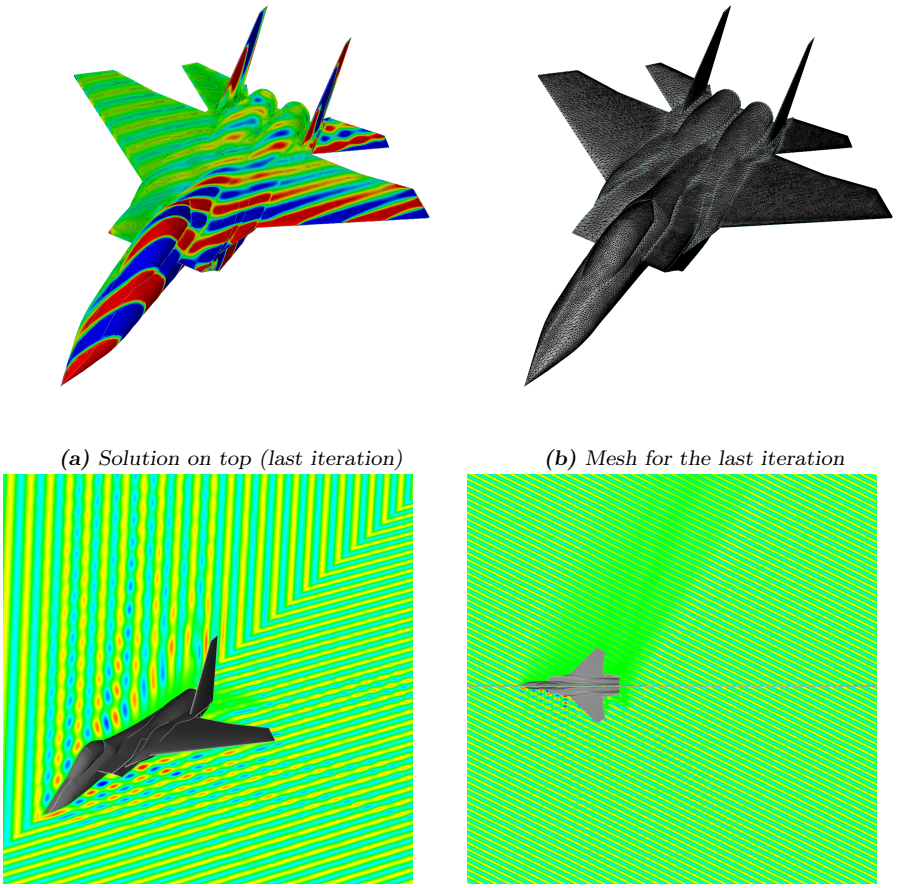

**(a)** *Solution on top (last iteration)*

**(b)** *Mesh for the last iteration*

**(c)** *Cut in the planes $z = 0$*

**(d)** *Cut in the planes $y = 0$*

***Figure 5.4:*** *F15 aircraft geometry: illustration of the adaptive mesh strategy.*

| Iteration | # vertices | # triangles | # Solver iterations | Meshing CPU Time | Solver CPU time |
|---|---|---|---|---|---|
| 3 | 10 562 | 21 120 | 392 | 42 s | 19 mn 47 s |
| 6 | 15 687 | 31 370 | 521 | 57 s | 30 mn 36 s |
| 9 | 25 428 | 50 852 | 707 | 1 mn 34 s | 52 mn 25 s |
| 12 | 43 217 | 86 430 | 593 | 2 mn 44 s | 65 mn 38 s |
| 15 | 80 611 | 161 218 | 364 | 5 mn 13 s | 70 mn 53 s |

***Table 5.2:*** *F15 aircraft statistics of the adapted meshes, solver iteration and CPU times.*

## 5.3 Ongoing work: Extension to higher order BEMs

The metric-based anisotropic mesh adaptation strategy is very efficient for the 3D Helmholtz BEM. We consider now the case of a spherical resonator (Figure 5.5a). Such objects are of interest in the context of anisotropic mesh adaptation because they require the retention of some level of isotropy in the refinement in order to maintain a good approximation of the surface by planar triangles. The incident wave is a plane wave travelling in the negative $x$-direction with a wavenumber of $\kappa = 10$. In Figure 5.5b, we represent the modulus of the solution computed in a 2D planar slice of the domain (the screen in the $(x, y)$ plane with $z = 0$) using the boundary integral representation.

Since this example is an isotropic example, we perform an experiment demonstrating the capabilities of our mesh adaptation technique with three configurations: with full anisotropy (similarly to what is presented in previous examples), and two additional ones with different levels of isotropy

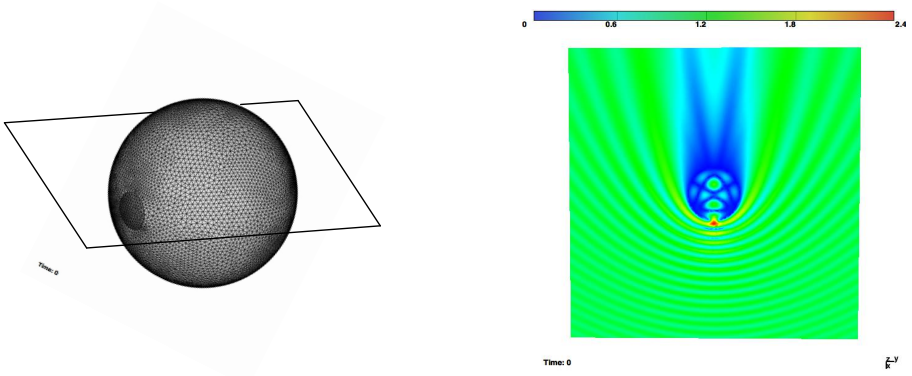


*(a) Uniform mesh with 9 120 vertices* *(b) Volume solution*

***Figure 5.5:*** *Spherical resonator: (a) Uniform mesh of the spherical resonator and screen where the volume solution is computed; (b) corresponding modulus of total field in the $(x, y)$-plane.*

enforced. The first level is called "semi-isotropy" and the second one is a fully isotropic case. For the semi-isotropy approach, the maximum dimension of the adapted triangles is limited accordingly to the complexity. Precisely, we enforce

$$\max(h) = \frac{C}{\sqrt{\mathcal{N}}},$$

where $h$ is the maximum dimension of each triangle. This restricts the elongation of the elements but still permits some elongation controlled by the parameter $C$. In this work, $C$ is set to 3.5 after some numerical experimentation.

In Figure 5.6, we give some meshes and corresponding solutions obtained during the adaptation process for the anisotropic and semi-anisotropic strategies.

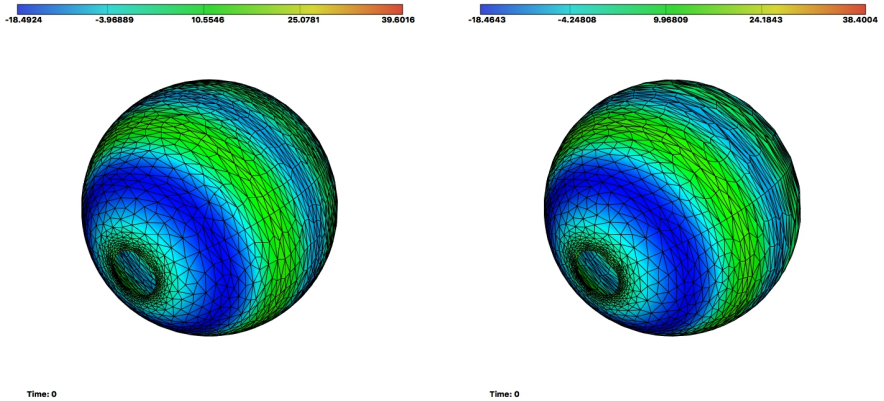


*(a) Semi-isotropic adaptation* *(b) Fully anisotropic adaptation*

***Figure 5.6:*** *Spherical resonator: Adapted meshes with real part of the surface solution for (a) semi-isotropic, (b) fully anisotropic.*

In Figure 5.7, we report the relative $L^2$ errors for uniform and (anisotropic, isotropic and semi-isotropic) adapted meshes with $\kappa = 5$. Similarly to the case of the planar screen, a uniform refinement yields a convergence rate of $\mathcal{O}(N^{-\frac{1}{2}})$. The anisotropic and semi-isotropic adaptive strategies initially achieve a rate of $\mathcal{O}(N^{-\frac{3}{2}})$ which is super optimal, however this rate begins to slow as higher accuracies are reached. The reason is that the shape to which the refinement is leading is not the correct one due to the elongated elements, see Figure 5.6. By enforcing some

isotropy the convergence rate of $\mathcal{O}(N^{-\frac{3}{2}})$ is maintained up to a larger mesh. However, it still slows once the relative error falls below approximately $10^{-3}$. On the other hand, for the fully isotropic refinement, which restricts the height to width ratio of the triangles, at first the convergence rate is similar to the one obtained by a uniform refinement then for accuracies smaller than $10^{-2}$, the convergence rate is $\mathcal{O}(N^{-\frac{3}{2}})$. Furthermore, it appears that the isotropic refinement maintains this rate asymptotically since it is also refining towards the spherical shape accurately as well as resolving the edge singularity. Nevertheless, it appears that if one is interested in achieving accuracies of the order of $10^{-2}$ or $10^{-3}$, the anisotropic adaptive strategy is superior.

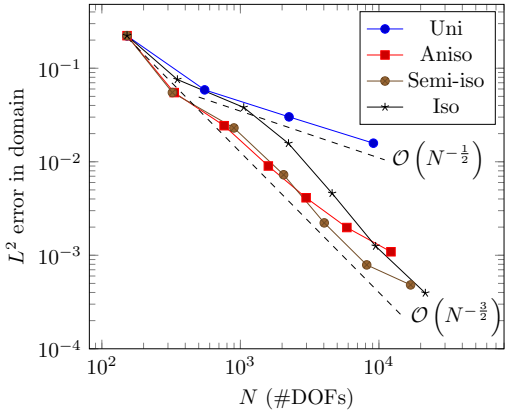


***Figure 5.7:*** *Scattering by a spherical resonator: Relative $L^2$ errors for uniform and (anisotropic, isotropic and semi-isotropic) adapted meshes with $\kappa = 5$.*

This spherical example illustrates the limitations of the current approach. The potential anisotropy, provided by the error estimate, has to comply with the surface principal curvatures. In this example, the full anisotropic error estimate implies a deformed sphere that the solver is not able to recover. The semi-anisotropic approach reduces the anisotropy to limit this artefact. For more complex geometries, it is then necessary to intersect the metric provided by the error estimate with a geometric metric representing the surface curvatures, see [Loseille 2017]. It is clear from this example that defining a high-order adaptive mesh strategy, for instance for $\mathbb{P}_2$ interpolation, is necessary to recover anisotropy while preserving the geometry. We are currently working on this subject with Faisal Amlani and a publication is in preparation [20].

In order to improve the accuracy of the solver, we have first introduced the possibility to use $\mathbb{P}_2$ interpolation in the solver COFFEE. Figure 5.8 presents a validation of the orders of convergence for the three available orders of elements: $\mathbb{P}_0$, $\mathbb{P}_1$ and $\mathbb{P}_2$ in the case of the diffraction of an incident plane wave by a unit sphere ($\kappa = 10$).

Before to develop new error estimates for a $\mathbb{P}_2$ interpolation, similarly to what is done in [Coulaud 2016], we have checked the efficiency of the mesh adaptation procedure based on the minimisation of the linear interpolation error in the case of $\mathbb{P}_2$ elements. Figure 5.9 presents the order of convergence in the case of a planar screen (to remove the effect of the curvature) for $\mathbb{P}_2$ and $\mathbb{P}_1$ interpolations. Two wavenumbers are considered: $\kappa = 5$ and $\kappa = 200$. Since no exact solution is available for this case, the error is a relative error with respect to a reference solution computed on a finer mesh. The first observation is that if a uniform refinement is used, the gain of using $\mathbb{P}_2$ interpolation is reduced, similar accuracy being obtained for the same number of DOFs in both cases. We also see that the use of the mesh adaptation strategy enables to obtain a better order of convergence with the $\mathbb{P}_2$ interpolation than with the $\mathbb{P}_1$ interpolation. These results are still preliminary and we need to consider larger examples to check the asymptotic behavior.

Another important point to highlight is that high anisotropy ratios tend to increase the number of iterations to solve the linear system. However, the mesh adaptation framework naturally provides a good initial guess for the iterative solver by simply interpolating the solution of the previous mesh onto the current mesh. This has been shown in [1] to decrease the number of iterations at very little expense but the number of iterations is still a limiting factor. We are currently working on a

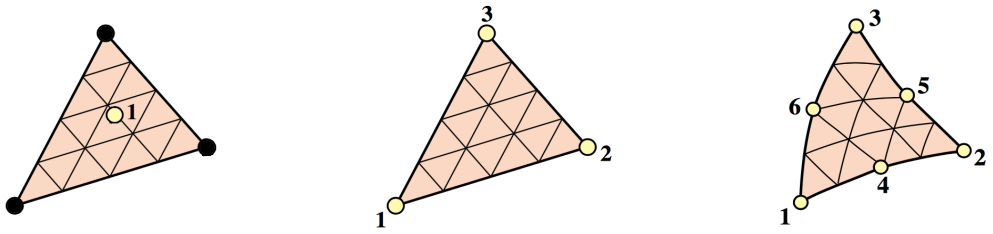


| # DOF | $L^2$ error | $\mathcal{O}\left(L^2\right)$ |
|---|---|---|
| 230 | 3.2e-1 | – |
| 798 | 8.8e-2 | 1.0 |
| 1750 | 4.48e-2 | 0.9 |
| 3018 | 2.98e-2 | 0.8 |

***(a)*** *$\mathbb{P}_0$ interpolation*

| # DOF | $L^2$ error | $\mathcal{O}\left(L^2\right)$ |
|---|---|---|
| 117 | 8.2e-1 | – |
| 401 | 1.7e-1 | 1.3 |
| 877 | 7.8e-2 | 1.0 |
| 1511 | 4.5e-2 | 1.0 |

***(b)*** *$\mathbb{P}_1$ interpolation*

| # DOF | $L^2$ error | $\mathcal{O}\left(L^2\right)$ |
|---|---|---|
| 682 | 5.8e-2 | – |
| 1598 | 1.2e-2 | 1.9 |
| 3502 | 3.2e-3 | 1.7 |
| 6038 | 1.0e-3 | 2.1 |

***(c)*** *$\mathbb{P}_2$ interpolation*

***Figure 5.8:*** *Illustration of the triangular elements developed in the code and validation of the order of convergence for a sphere.*

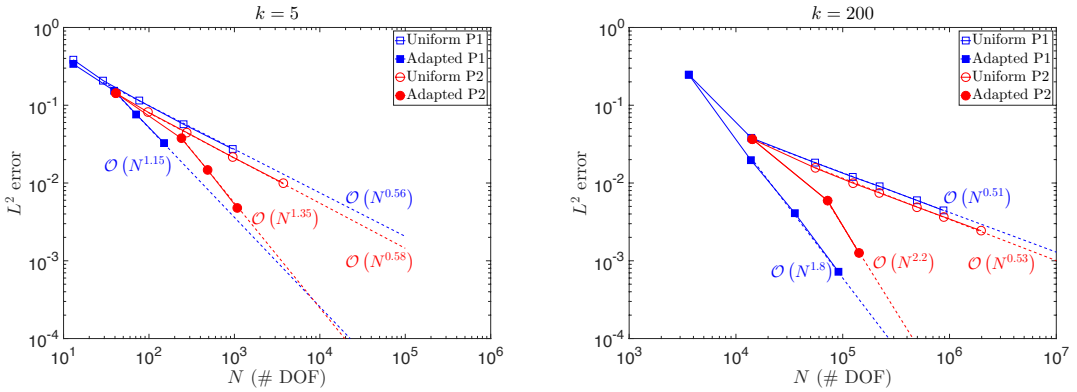


***Figure 5.9:*** *Planar screen geometry: verification of the efficient of the mesh adaptation procedure in the case of a $\mathbb{P}_2$ interpolation.*

combination of the FM and the $\mathcal{H}$-matrix based solvers to propose an efficient high-order adapted fast BEM for wave propagation problems [20].

# CHAPTER 6

# Future research directions

Developing fast solvers for wave propagation problems requires to investigate and improve several components: (i) data-sparse representation of the system, (ii) reduction of the number of DOFs on the domain boundary (to obtain a prescribed accuracy) and (iii) acceleration of the system solution. In order to validate and show the efficiency of the numerical method I develop, I always consider its application to realistic problems. Figure 6.1 gives an overview of my major contributions (together with the names of my industrial partners and academic collaborators).

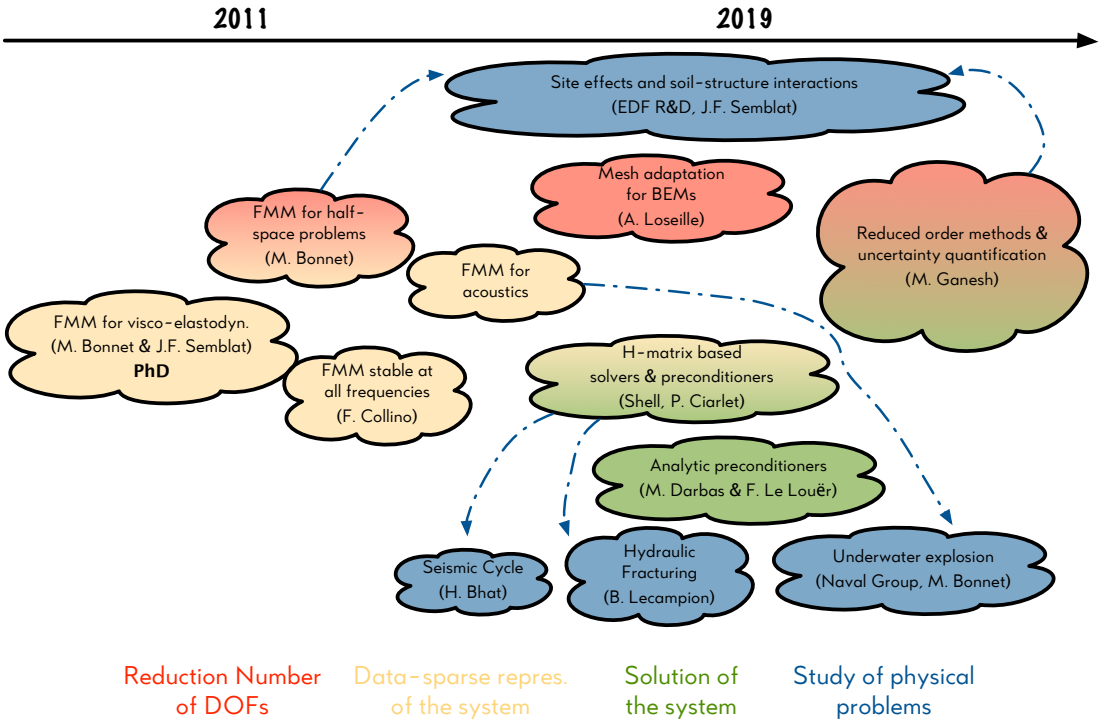


***Figure 6.1:*** *Overview of my major contributions. The main connections between numerical methods and mechanical engineering problems are represented with blue arrows. Interactions between different numerical aspects are omitted to lighten the diagram (they are all connected).*

I have presented in the previous Chapters some short term directions to improve the work begun. In addition, I have recently started three new projects.

1. Numerical simulation of long-period ground motion;
2. Development of reduced order and uncertainty quantification methods for fast BEMs;
3. Modelling of fluid-structure interaction during an underwater explosion.

**Numerical simulation of long-period ground motion.** I am involved in the project *Modeling lOng-perioD groUnd motions, and assessment of their effects on Large-scale infrAsTructurEs* (MODULATE, 11/2018-11/2022) funded by the French National Agency (ANR). The originality and main goal of the project is to model **long period ground motions**, and their effects on large-scale infrastructures (see Fig. 6.2 for an example from the 2003 Tokachi-oki, Japan earthquake [Koketsu 2005]). Intense long-period ground motions are usually generated at large distances from the source and consist primarily of surface waves that arise when seismic waves encounter sedimentary deposits. The project aims at developing a methodology based on the physics of surface waves, to describe the evolution of the spectral content of the ground motion at a site located in a sedimentary basin. 3D numerical soil-structure models that capture the particular dynamic characteristics of real large-scale structures will be developed for assessments of their performance when subjected to the ground motion model. The results of the project will allow the development of tools and guidelines to be used by the earthquake engineering community for more resilient designs of large-scale infrastructures.

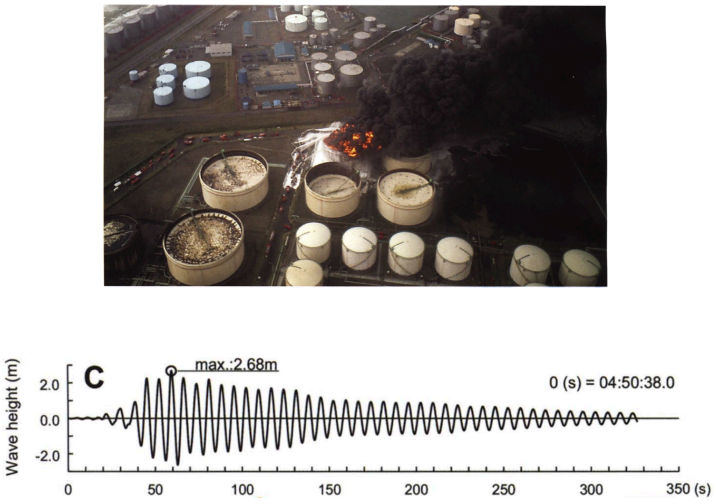


***Figure 6.2:*** *Aerial view of the fire in the oil tank damaged by long-period ground motions from the 2003 Tokachi-oki earthquake and corresponding time history [Koketsu 2005].*

To date there are no technique for ground motion simulation which consider the non-stationary and dispersive nature of surface waves so as to generate time histories of realistic longer durations and amplitudes. Accordingly, modern simulation techniques are not capable to take into account the important physical parameters of the basin-structure setting (such as basin depth, source depth, station location relative to the basin, etc.). This project aims at developing a physical model for surface waves. It will be based on a systematic analysis of strong ground motions recorded on the floor of sedimentary basins using evolutionary stochastic processes [Meza-Fajardo 2015].

With Jean-François Semblat (ENSTA, UME) and a post-doctoral student (to start January 2019 for two years), we will participate to the task "Numerical simulation of long-period ground motion". We will first apply fast BEMs to study generic sedimentary basin models to provide a useful guidance to assess the effect of the near-surface (around 100 m) soft deposits on long period motions. In a second time, we will study the physics of surface wave propagation on basins with realistic geometries and heterogeneities. This project will be the occasion to gather all the efforts made in the last couple of years on fast BEMs and to evaluate the capacities of the fast BEM solver on realistic configurations and with real data. To achieve this goal, we will have to improve the FM-BEM based on the half-space fundamental solutions and its coupling with the FM-BEM based on the full-space fundamental solutions. In addition, a large effort will be devoted to the porting of the numerical method to high performance computing facilities.

**Reduced order models and uncertainty quantification for BEMs.** Another important aspect I will consider in a near future is the definition of (i) reduced order models for BEMs and (ii) efficient tools to quantify uncertainties in BEMs. It is clear that the mechanical characteristics of the geological medium are inevitably polluted by some error since they define complex multiscale domains and are indirectly determined by inverse methods, partial in situ and laboratory testing. It is thus important to take into account these uncertainties in the numerical method and in the soil-structure interaction [Papadopoulos 2018].

Input uncertainties can be modeled with independent random variables. But in that case, the computational costs will be prohibitive. However, it is clear that dependencies exist between these variables. Model reduction methods use this parametric dependence of the inputs to reduce the overall size of the numerical problem. This idea is very general: if a problem is too expensive to be solved as a whole, an approximation of the initial problem, in which the redundant information is removed, is formulated to reduce the computational cost. More precisely the principle is to avoid the sampling of the complete space of parameters, defined here as the possible values of the mechanical parameters of the piecewise homogeneous domain, by finding an adequate approximation subspace (as small as possible). The dimension of the subspace depends on the prescribed accuracy for the approximation. The algorithm is decomposed into two (offline and online) steps. In the offline part, the reduced basis for the approximation space is computed. Then in the online procedure, the evaluation of the parameter-dependent solution is computed with a negligible cost, for any new parameter value. So far, investigations have mostly concerned partial differential equations. Recent theoretical works have however shown that model reductions can also be applied in some cases to BIEs [Casenave 2015, Fares 2011]. If BEMs are well-suited to derive efficient model reduction methods, there are still a lot of additional theoretical and numerical developments required to make them applicable to real-life configurations.

To start working in this field, I am collaborating with M. Ganesh from Colorado School of Mines who is already well established in this field [Ganesh 2015]. Our first problem consists in studying the influence on the surface motion, of the uncertainty on the damping parameters in each layer of a sedimentary basin. We are developing a forward uncertainty quantification algorithm to compute statistical moments of the quantity of interest, i.e. the output surface displacement, by modelling the damping parameters as random variables with known probability distributions. We use an offline/online algorithm to study epistemic uncertainties in our uncertainty quantification model arising from the lack of precise knowledge in modelling the input probability distributions.

This problem is simple in the sense that the only random parameters are the damping factors in each layers. The number of these variables is thus limited. However this problem is very interesting in practice for two reasons. First, it is clear that the soil properties present a spatial variability with respect to the mean homogeneous soil deposits [Baecher 2005]. In addition, it is very difficult to measure experimentally the damping parameters of the soils. And it is not clear if the damping parameters are due to the viscoelastic behavior of the soil or the presence of heterogeneities.

**Modelling the fluid-structure interaction during a far-field underwater explosion.** I have recently started to work on fluid-structure interactions. The shock-resistance capability estimation of battle ships or submarines against a far-field underwater explosion (Fig. 6.3) is a major issue in naval shipbuilding. Numerical simulations are important to study the behaviour of a mechanical structure in some specific situations, under some known loads. Thus, once the numerical method has been validated through comparisons with experimental tests, the simulation can be used as an alternative to numerous costly and difficult experimental tests to validate some specific criteria. The modelling of the fluid-structure interaction between a structure (a submarine) and an acoustic medium (water) caused by a far-field underwater explosion is the subject of the PhD thesis of Damien Mavaleix-Marchessoux funded by Naval Group.

The main difficulty in this work is due to the complex solicitations transmitted by the fluid to the structure. An underwater explosion usually involves two phenomena of different time scales: a primary acoustic wave or shock wave with a stiff front, followed by a slower motion of heavy fluid produced by the oscillation of a hot gaz bubble. The shock wave and the oscillating bubble are very different by nature but are intrinsically linked since they both emerge from the same explosion. In [Geers 1992], approximations are proposed to model these fluid-structure interactions.

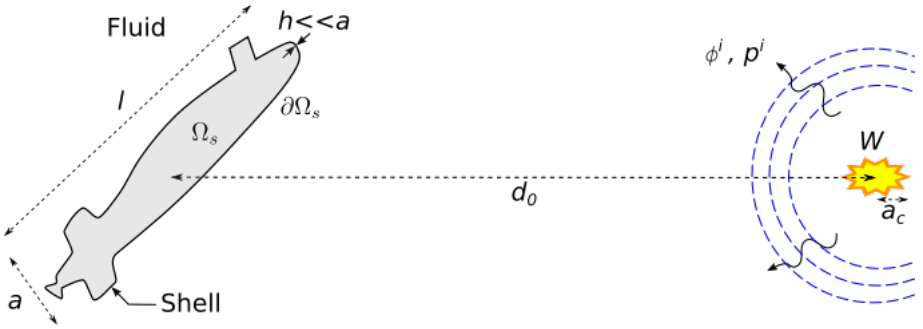


***Figure 6.3:*** *Submarine subjected to an underwater explosion.*

By construction, they are accurate in the very high and very low-frequency regimes. These approaches (called Doubly Asymptotic Approximations) are currently used at Naval Group but do not produce accurate enough results when compared with experimental results. In this context, we are developing an alternative approach based entirely on numerical simulations. After having modelled the two phenomena separately, we will need to propose a multi-scale approach to unify them.

Since the fluid domain is unbounded, it is natural to use the BEM to model this part of the problem. The Convolution Quadrature Method (CQM) [Lubich 1988, Hassell 2016] will be used to develop a fast BEM solver in the time domain. The structure part is then studied with the FEM due to the complexity of the mechanical behaviour to be modelled. This aspect is well controlled at Naval Group. An important issue is to propose an efficient fluid-structure coupling algorithm and to determine a priori its convergence rate.

An important aspect of this collaboration is that numerical results will be compared to experimental data obtained at Naval Group in order to validate the improved accuracy of the method compared to the actual used strategies.

# Author's bibliography

Articles in international journals


[1] S. Chaillat, S. Groth, and A. Loseille. Metric-based anisotropic mesh adaptation for 3D acoustic boundary element methods. *Journal of Computational physics*, 372:473–499, 2018.

[2] S. Chaillat, L. Desiderio, and P. Ciarlet. Theory and implementation of $\mathcal{H}$-matrix based iterative and direct solvers for Helmholtz and elastodynamic oscillatory kernels. *Journal of Computational physics*, 351:165–186, 2017.

[3] S. Chaillat, M. Darbas, and F. Le Louër. Fast iterative boundary element methods for high-frequency scattering problems in 3D elastodynamics. *Journal of Computational Physics*, 341:429–446, 2017.

[4] K. Meza-Fajardo, J.F. Semblat, S. Chaillat, and L. Lenti. Seismic Wave Amplification in 3D Alluvial Basins: 3D/1D Amplification Ratios from Fast Multipole BEM Simulations. *Bulletin of the Seismological Society of America*, 106:1267–1281, 2016.

[5] S. Chaillat, M. Darbas, and F. Le Louër. Approximate local Dirichlet-to-Neumann map for three-dimensional elastic waves. *Computer Methods in Applied Mechanics and Engineering*, 297:62–83, 2015.

[6] S. Chaillat and F. Collino. A Wideband Fast Multipole Method for the Helmholtz Kernel: Theoretical Developments. *Computers and Mathematics with Applications*, 70:660–678, 2015.

[7] S. Chaillat and M. Bonnet. A new Fast Multipole Formulation for the elastodynamic half-space Green's tensor. *Journal of Computational physics*, 258:787–808, 2014.

[8] S. Chaillat and M. Bonnet. Recent advances on the fast multipole accelerated boundary element method for 3D time-harmonic elastodynamics. *Wave Motion*, 50(7):1090–1104, 2013.

[9] E. Grasso, S. Chaillat, M. Bonnet, and J.F. Semblat. Application of the multi-level time-harmonic fast multipole BEM to 3-D visco-elastodynamics. *Engineering Analysis with Boundary Elements*, 36:744–758, 2012.

[10] S. Chaillat, J.F. Semblat, and M. Bonnet. A preconditioned 3-D multi-region fast multipole solver for seismic wave propagation in complex geometries. *Communications in Computational Physics*, 11:594–609, 2012.

[11] S. Chaillat and G. Biros. FaIMS: A fast algorithm for the inverse medium problem with multiple frequencies and multiple sources for the scalar Helmholtz equation. *Journal of Computational Physics*, 231:4403–4421, 2012.

[12] H.D. Bui, S. Chaillat, A. Constantinescu, and E. Grasso. Identification of a planar crack in Zener type viscoelasticity . *Annals of Solid and Structural Mechanics*, 1:3–8, 2010.

[13] S. Chaillat, M. Bonnet, and J.F. Semblat. A new fast multi-domain BEM to model seismic wave propagation and amplification in 3D geological structures. *Geophysical Journal International*, 177:509–531, 2009.

[14] S. Chaillat, M. Bonnet, and J.F. Semblat. A multi-level fast multipole BEM for 3-D elastodynamics in the frequency domain. *Computer Methods in Applied Mechanics and Engineering*, 197:4233–4249, 2008.

[15] S. Chaillat, M. Bonnet, and J.F. Semblat. A Fast Multipole accelerated BEM for 3-D elastic wave computation. *European Journal of Computational Mechanics*, 17:701–712, 2008.

[16] S. Chaillat and H.D. Bui. Resolution of linear viscoelastic equations in the frequency domain using real Helmholtz boundary integral equations. *C. R. Mecanique*, 335:746–750, 2007.

[17] S. Chaillat, M. Bonnet, and J.F. Semblat. A Fast Multipole Method formulation for 3D elastodynamics in the frequency domain. *C. R. Mecanique*, 335:714–719, 2007.

Articles in preparation

[18] P. Romanet, H.S. Bhat, S. Chaillat, and R. Madariaga. Fast seismic cycle model in geometrically complex fault system. In preparation.

[19] S. Chaillat, P. Ciarlet, and F. Kpadonou. Efficient preconditioner for $\mathcal{H}$-matrix based iterative solvers for 3d acoustic and elastodynamic problems. In preparation.

[20] F. Amlani, S. Chaillat, and A. Loseille. Metric-based anisotropic mesh adaptation for high-order boundary element methods in acoustic scattering. In preparation.

[21] Z. Adnani, V. Alves Fernandes, M. Bonnet, S. Chaillat, and G. Devesa. Fast Multipole Boundary Element Method for site effects and soil-structure interactions. In preparation.

Book chapter

[22] M. Bonnet, S. Chaillat, and J.F. Semblat. Multi-level fast multipole BEM for 3-D elastodynamics. In D. Polyzos and G. Manolis, editors, *Recent Advances in BEM*. 2009.

PhD Thesis

[23] S. Chaillat. *Fast Multipole Method (FMM) for boundary element method in 3D elastodynamics. Application to seismic wave propagation.* PhD thesis, ENPC, 2008.

# Bibliography


[Adnani 2018] Z. Adnani. *Three-dimensional numerical modelling of site effects in Soil-Structure Interaction for large scale seismic problems.* PhD thesis, Université Paris-Saclay, 2018.

[Alouges 2007] F. Alouges, S. Borel and D. P. Levadoux. *A stable well-conditioned integral equation for electromagnetism scattering.* J. Comput. Appl. Math., vol. 204, no. 2, pages 440–451, 2007.

[Alves 1997] C.J.S. Alves and T. Ha Duong. *On the far field amplitude for elastic waves.* Modern Mathematical Methods in Diffractions Theory and its Applications in Engineering, pages 49–67, 1997.

[Antoine 2001] X. Antoine. *Fast approximate computation of a time-harmonic scattered field using the OSRC method.* IMA J. Appl. Math., vol. 66, pages 83–110, 2001.

[Antoine 2005] X. Antoine and M. Darbas. *Alternative integral equations for the iterative solution of acoustic scattering problems.* Quart. J. Mech. Appl. Math., vol. 58, pages 107–128, 2005.

[Antoine 2006] X. Antoine, M. Darbas and Y.Y. Lu. *An improved surface radiation condition for high-frequency acoustic scattering problems.* Comput. Methods Appl. Mech. Engrg., vol. 195, no. 33-36, pages 4060–4074, 2006.

[Antoine 2007] X. Antoine and M. Darbas. *Generalized combined field integral equations for the iterative solution of the three-dimensional Helmholtz equation.* ESAIM: Math. Modell. Numer. Anal., vol. 41, pages 147–167, 2007.

[Arias 2004] I. Arias and J.D. Achenbach. *Rayleigh wave correction for the BEM analysis of two-dimensional elastodynamic problems in a half-space.* International journal for numerical methods in engineering, vol. 60, no. 13, pages 2131–2146, 2004.

[Aurada 2012] M. Aurada, S. Ferraz-Leite and D. Praetorius. *Estimator reduction and convergence of adaptive BEM.* Applied Numerical Mathematics, vol. 62, no. 6, pages 787–801, 2012.

[Baecher 2005] G.B. Baecher and J.T. Christian. Reliability and statistics in geotechnical engineering. John Wiley & Sons, 2005.

[Baker 1996] G.A. Baker and P.R. Graves-Morris. Padé approximants. Encyclopedia of Mathematics and its Applications. Cambridge University Press, UK, 1996.

[Bakry 2016] M. Bakry. *Fiabilité et optimisation des calculs obtenus par des formulations intégrales en propagation d'ondes.* PhD thesis, Université Paris-Saclay, 2016.

[Bakry 2017a] M. Bakry. *A goal-oriented a posteriori error estimate for the oscillating single layer integral equation.* Applied Mathematics Letters, vol. 69, pages 133–137, 2017.

[Bakry 2017b] M. Bakry, S. Pernet and F. Collino. *A new accurate residual-based a posteriori error indicator for the BEM in 2D-acoustics.* Computers & Mathematics with Applications, vol. 73, no. 12, pages 2501–2514, 2017.

[Banjai 2008] L. Banjai and W. Hackbusch. *Hierarchical matrix techniques for low-and high-frequency Helmholtz problems.* IMA journal of numerical analysis, vol. 28, no. 1, pages 46–79, 2008.

[Bard 1985] P.Y. Bard and M. Bouchon. *The two-dimensional resonance of sediment-filled valleys.* Bulletin of the Seismological Society of America, vol. 75, no. 2, pages 519–541, 1985.

[Bažant 1974] Zdeněk P Bažant. *Three-dimensional harmonic functions near termination or intersection of gradient singularity lines: a general numerical method.* International Journal of Engineering Science, vol. 12, no. 3, pages 221–243, 1974.

[Bebendorf 2003] M. Bebendorf and S. Rjasanow. *Adaptive low-rank approximation of collocation matrices.* Computing, vol. 70, no. 1, pages 1–24, 2003.

[Bebendorf 2008] M. Bebendorf. Hierarchical matrices. Springer, 2008.

[Bebendorf 2015] M. Bebendorf, C. Kuske and R. Venn. *Wideband nested cross approximation for Helmholtz problems.* Numerische Mathematik, vol. 130, no. 1, pages 1–34, 2015.

[Beskos 1993] D.E. Beskos. *Applications of the boundary element method in dynamic soil-structure interaction.* In Developments in dynamic soil-structure interaction, pages 61–90. Springer, 1993.

[Betcke 2011a] T. Betcke, S.N. Chandler-Wilde, I.G. Graham, S. Langdon and M. Lindner. *Condition number estimates for combined potential integral operators in acoustics and their boundary element discretization.* Numerical Methods for Partial Differential Equations, vol. 27, no. 1, pages 31–69, 2011.

[Betcke 2011b] T. Betcke and E.A. Spence. *Numerical estimation of coercivity constants for boundary integral operators in acoustic scattering.* SIAM Journal on Numerical Analysis, vol. 49, no. 4, pages 1572–1601, 2011.

[Bonnet 1999] M. Bonnet. Boundary integral equation methods for solids and fluids. Wiley, 1999.

[Börm 2003a] S. Börm, L. Grasedyck and W. Hackbusch. *Hierarchical matrices.* Technical report, Max Planck Institute for Mathematics in the Sciences, 2003.

[Börm 2003b] S. Börm, L. Grasedyck and W. Hackbusch. *Introduction to hierarchical matrices with applications.* Engineering analysis with boundary elements, vol. 27, no. 5, pages 405–422, 2003.

[Börm 2006] S. Börm. *$\mathcal{H}^2$-Matrix Arithmetics in Linear Complexity.* Computing, vol. 77, no. 1, pages 1–28, 2006.

[Börm 2015] S. Börm. *Directional $\mathcal{H}^2$-matrix compression for high-frequency problems.* arXiv preprint arXiv:1510.07087, 2015.

[Börm 2017] S. Börm and J.M. Melenk. *Approximation of the high-frequency Helmholtz kernel by nested directional interpolation: error analysis.* Numerische Mathematik, vol. 137, no. 1, pages 1–34, 2017.

[Boubendir 2012] Y. Boubendir, X. Antoine and C. Geuzaine. *A quasi-optimal non-overlapping domain decomposition algorithm for the Helmholtz equation.* Journal of Computational Physics, vol. 231, no. 2, pages 262–280, 2012.

[Boubendir 2015] Y. Boubendir, O. Bruno, D. Levadoux and C. Turc. *Integral equations requiring small numbers of Krylov-subspace iterations for two-dimensional smooth penetrable scattering problems.* Applied Numerical Mathematics, vol. 95, pages 82–98, 2015.

[Bremer 2010] J. Bremer, Z. Gimbutas and V. Rokhlin. *A nonlinear optimization procedure for generalized gaussian quadrature.* SIAM J. Sci. Comp., vol. 32, pages 1761–1788, 2010.

[Brunner 2010] D. Brunner, M. Junge, P. Rapp, M. Bebendorf and L. Gaul. *Comparison of the fast multipole method with hierarchical matrices for the Helmholtz-BEM.* Computer Modeling in Engineering & Sciences, vol. 58, no. 2, pages 131–160, 2010.

[Bruno 2001] O.P. Bruno and L.A. Kunyansky. *A fast, high-order algorithm for the solution of surface scattering problems: basic implementation, tests, and applications.* Journal of Computational Physics, vol. 169, no. 1, pages 80–110, 2001.

[Bruno 2012] O.P. Bruno, T. Elling and C. Turc. *Regularized integral equations and fast high-order solvers for sound-hard acoustic scattering problems.* Int. Journal Numerical Methods in Engineering, vol. 91, no. 10, pages 1045–1072, 2012.

[Bruno 2018] Oscar P Bruno and Emmanuel Garza. *A Chebyshev-based rectangular-polar integral solver for scattering by general geometries described by non-overlapping patches.* arXiv preprint arXiv:1807.01813, 2018.

[Carpentieri 2000] B. Carpentieri, I.S. Duff and L. Giraud. *Some sparse pattern selection strategies for robust Frobenius norm minimization preconditioners in electromagnetism.* Numer. Linear Algebra Appl., vol. 7, pages 667–685, 2000.

[Carpentieri 2005] B. Carpentieri, I.S. Duff, L. Giraud and G. Sylvand. *Combining fast multipole techniques and an approximate inverse preconditioner for large parallel electromagnetics calculations.* SIAM J. Sci. Comp., vol. 27, pages 774–792, 2005.

[Carpentieri 2006] B. Carpentieri. *A matrix-free two-grid preconditioner for solving Boundary Integral Equations in Electromagnetism.* Computing, vol. 77, pages 275–296, 2006.

[Carstensen 1997] C. Carstensen. *An a posteriori error estimate for a first-kind integral equation.* Mathematics of Computation of the American Mathematical Society, vol. 66, no. 217, pages 139–155, 1997.

[Carstensen 2014] C. Carstensen, M. Feischl, M. Page and D. Praetorius. *Axioms of adaptivity.* Computers & Mathematics with Applications, vol. 67, no. 6, pages 1195–1253, 2014.

[Casenave 2015] F. Casenave, A. Ern and T. Lelièvre. *A nonintrusive reduced basis method applied to aeroacoustic simulations.* Advances in Computational Mathematics, vol. 41, no. 5, pages 961–986, 2015.

[Caudron 2018] B. Caudron. *Couplages FEM-BEM faibles et optimisés pour des problèmes de diffraction harmoniques en acoustique et en électromagnétisme.* PhD thesis, Université de Liège, 2018.

[Chaljub 2010] E. Chaljub, P. Moczo, S. Tsuno, P.Y. Bard, J. Kristek, M. Käser, M. Stupazzini and M. Kristekova. *Quantitative comparison of four numerical predictions of 3D ground motion in the Grenoble Valley, France.* Bulletin of the Seismological Society of America, vol. 100, no. 4, pages 1427–1455, 2010.

[Cheng 2006] H. Cheng, W.Y. Crutchfield, Z. Gimbutas, L.F. Greengard, J.F. Ethridge, J. Huang, V. Rokhlin, N. Yarvin and J. Zhao. *A wideband fast multipole method for the Helmholtz equation in three dimensions.* Journal of Computational Physics, vol. 216, no. 1, pages 300–325, 2006.

[Choi 2001] J.S. Choi, C.B. Yun and J.M. Kim. *Earthquake response analysis of the Hualien soil–structure interaction system based on updated soil properties using forced vibration test data.* Earthquake engineering & structural dynamics, vol. 30, no. 1, pages 1–26, 2001.

[Clouteau 2001] D. Clouteau and D. Aubry. *Modifications of the ground motion in dense urban areas.* Journal of Computational Acoustics, vol. 9, no. 04, pages 1659–1675, 2001.

[Clouteau 2003] D. Clouteau and D. Aubry. *Computational soil-structure interaction.* In Boundary element methods for soil-structure interaction, pages 61–125. Springer, 2003.

[Clouteau 2013] D. Clouteau, R. Cottereau and G. Lombaert. *Dynamics of structures coupled with elastic media: a review of numerical models and methods.* Journal of Sound and Vibration, vol. 332, no. 10, pages 2415–2436, 2013.

[Coulaud 2016] O. Coulaud and A. Loseille. *Very High Order Anisotropic Metric-Based Mesh Adaptation in 3D.* Procedia Engineering, vol. 163, pages 353–365, 2016.

[Coulier 2014a] P. Coulier, A. Dijckmans, S. François, G. Degrande and G. Lombaert. *A spatial windowing technique to account for finite dimensions in 2.5 D dynamic soil–structure interaction problems.* Soil Dynamics and Earthquake Engineering, vol. 59, pages 51–67, 2014.

[Coulier 2014b] P. Coulier, S. François, G. Lombaert and G. Degrande. *Coupled finite element–hierarchical boundary element methods for dynamic soil–structure interaction in the frequency domain.* International Journal for Numerical Methods in Engineering, vol. 97, no. 7, pages 505–530, 2014.

[Darbas 2004] M. Darbas. *Préconditionneurs analytiques de type Calderón pour les formulations intégrales des problèmes de diffraction d'ondes.* PhD Thesis, INSA, Toulouse, 2004.

[Darbas 2013] M. Darbas, E. Darrigrand and Y. Lafranche. *Combining OSRC preconditioning and Fast Multipole Method for the Helmholtz equation.* J. Comput. Phys., vol. 236, pages 289–316, 2013.

[Darbas 2015] M. Darbas and F. Le Louër. *Well-conditioned boundary integral formulations for high-frequency elastic scattering problems in three dimensions.* Mathematical Methods in the Applied Sciences, vol. 38, no. 9, pages 1705–1733, 2015.

[Darve 2000a] E. Darve. *The fast multipole method: I. Error analysis and asymptotic complexity.* SIAM J. Numer. Anal., vol. 38, pages 98–128, 2000.

[Darve 2000b] E. Darve. *The fast multipole method: numerical implementation.* Journal of Computational Physics, vol. 160, no. 1, pages 195–240, 2000.

[Darve 2004a] E. Darve and P. Havé. *Efficient fast multipole method for low-frequency scattering.* J. Comput. Phys., vol. 197, no. 1, pages 341–363, 2004.

[Darve 2004b] E. Darve and P. Havé. *A fast multipole method for Maxwell equations stable at all frequencies.* Philosophical Transactions of the Royal Society of London A: Mathematical, Physical and Engineering Sciences, vol. 362, no. 1816, pages 603–628, 2004.

[Delamotte 2016] K. Delamotte. *Une étude du rang du noyau de l'équation de Helmholtz: application des $\mathcal{H}$-matrices à l'EFIE.* PhD thesis, Paris 13, 2016.

[Desiderio 2017] L. Desiderio. *$\mathcal{H}$-matrix based Solvers for 3D Elastodynamic Boundary Integral Equations.* PhD thesis, Université Paris-Sacaly, 2017.

[Dravinski 2003] M. Dravinski. *Scattering of elastic waves by a general anisotropic basin. Part 2: a 3D model.* Earthquake engineering & structural dynamics, vol. 32, no. 5, pages 653–670, 2003.

[El Bouajaji 2014] M. El Bouajaji, X. Antoine and C. Geuzaine. *Approximate Local Magnetic-to-Electric Surface Operators for Time-Harmonic Maxwell's Equations.* Journal of Computational Physics, vol. 279, pages 241–260, 2014.

[Elleithy 2003] W.M. Elleithy and M. Tanaka. *Interface relaxation algorithms for BEM–BEM coupling and FEM–BEM coupling.* Computer Methods in Applied Mechanics and Engineering, vol. 192, no. 26-27, pages 2977–2992, 2003.

[Engquist 1979] B. Engquist and A. Majda. *Radiation boundary conditions for acoustic and elastic wave calculations.* Comm. Pure Appl. Math., vol. 32, no. 3, pages 314–358, 1979.

[Engquist 2007] B. Engquist and L. Ying. *Fast directional multilevel algorithms for oscillatory kernels.* SIAM J. Sci. Comp., vol. 29, pages 1710–1737, 2007.

[Epton 1995] M.A. Epton and B. Dembart. *Multipole translation theory for the three-dimensional Laplace and Helmholtz equations.* SIAM J. Sci. Comp., vol. 16, pages 865–897, 1995.

[Eringen 1975] A.C. Eringen and E.S. Suhubi. Elastodynamics, Vol. II-Linear Theory. Academic Press, 1975.

[Faermann 1998] B. Faermann. *Local a-posteriori error indicators for the Galerkin discretization of boundary integral equations.* Numerische Mathematik, vol. 79, no. 1, pages 43–76, 1998.

[Fares 2011] M. Fares, J.S. Hesthaven, Y. Maday and B. Stamm. *The reduced basis method for the electric field integral equation.* Journal of Computational Physics, vol. 230, no. 14, pages 5532–5555, 2011.

[Feischl 2015] M. Feischl, T. Fuhrer, N. Heuer, M. Karkulik and D. Praetorius. *Adaptive Boundary Element Methods: A Posteriori Error Estimators, Adaptivity, Convergence, and Implementation.* Arch. Computat. Methods Eng., vol. 22, no. 3, pages 309–389, 2015.

[Ferraz-Leite 2008] S. Ferraz-Leite and D. Praetorius. *Simple a posteriori error estimators for the h-version of the boundary element method.* Computing, vol. 83, no. 4, pages 135–162, 2008.

[Fischer 2005] M. Fischer and L. Gaul. *Fast BEM-FEM mortar coupling for acoustic–structure interaction.* International Journal for Numerical Methods in Engineering, vol. 62, no. 12, pages 1677–1690, 2005.

[Fong 2009] W. Fong and E. Darve. *The black-box fast multipole method.* J. Comp. Phys., vol. 228, pages 8712–8725, 2009.

[François 2015] S. François, P. Coulier and G. Degrande. *Finite element–boundary element coupling algorithms for transient elastodynamics.* Engineering Analysis with Boundary Elements, vol. 55, pages 104–121, 2015.

[Galkowski 2016] J. Galkowski, E.H. Müller and E.A. Spence. *Wavenumber-explicit analysis for the Helmholtz h-BEM: error estimates and iteration counts for the Dirichlet problem.* arXiv preprint arXiv:1608.01035, 2016.

[Gander 2002] M.J. Gander, F. Magoules and F. Nataf. *Optimized Schwarz methods without overlap for the Helmholtz equation.* SIAM J. Sci. Comput., vol. 24, no. 1, pages 38–60, 2002.

[Ganesh 2004] M. Ganesh and I.G. Graham. *A high-order algorithm for obstacle scattering in three dimensions.* Journal of Computational Physics, vol. 198, no. 1, pages 211–242, 2004.

[Ganesh 2015] M. Ganesh and S.C. Hawkins. *A high performance computing and sensitivity analysis algorithm for stochastic many-particle wave scattering.* SIAM Journal on Scientific Computing, vol. 37, no. 3, pages A1475–A1503, 2015.

[Gantumur 2013] T. Gantumur. *Adaptive boundary element methods with convergence rates.* Numerische Mathematik, vol. 124, no. 3, pages 471–516, 2013.

[Geers 1992] T.L. Geers, P. Zhang and B.A. Lewis. *Advanced DAA methods for shock response analysis.* Technical report, Colorado Univ. at Boulder, 1992.

[George 1991] P.L. George, F. Hecht and M.G. Vallet. *Creation of internal points in Voronoi's type method. Control adaptation.* Advances in engineering software and workstations, vol. 13, no. 5-6, pages 303–312, 1991.

[Golub 2012] G.H. Golub and C.F. Van Loan. Matrix computations. JHU Press, 3rd edition, 2012.

[Grasedyck 2001] L. Grasedyck. *Theorie und Anwendungen Hierarchischer Matrizen*. PhD thesis, Christian-Albrechts Universität Kiel, 2001.

[Grasso 2012] E. Grasso. *Modelling visco-elastic seismic wave propagation: a fast-multipole boundary element method and its coupling with finite elements*. PhD thesis, Université Paris-Est, 2012.

[Greengard 1987] L. Greengard and V. Rokhlin. *A fast algorithm for particle simulations*. Journal of Computational physics, vol. 73, no. 2, pages 325–348, 1987.

[Greengard 1998] L. Greengard, J. Huang, V. Rokhlin and S. Wandzura. *Accelerating fast multipole methods for the Helmholtz equation at low frequencies*. IEEE Computational Science and Engineering, vol. 5, no. 3, pages 32–38, 1998.

[Guiggiani 1990] M. Guiggiani and A. Gigante. *A general algorithm for multidimensional Cauchy principal value integrals in the boundary element method*. Journal of Applied Mechanics, vol. 57, no. 4, pages 906–915, 1990.

[Gumerov 2009] N.A. Gumerov and R. Duraiswami. *Wideband fast multipole accelerated boundary element methods for the three-dimensional Helmholtz equation.* The Journal of the Acoustical Society of America, vol. 125, no. 4, pages 2566–2566, 2009.

[Hackbusch 1999] W. Hackbusch. *A Sparse Matrix Arithmetic Based on $\mathcal{H}$-Matrices. Part I: Introduction to $\mathcal{H}$-Matrices*. Computing, vol. 62, pages 89–108, 1999.

[Hackbusch 2015] W. Hackbusch. Hierarchical matrices: algorithms and analysis, volume 49. Springer, 2015.

[Hähner 1993] P. Hähner and G.C. Hsiao. *Uniqueness theorems in inverse obstacle scattering of elastic waves*. Inverse Problems, vol. 9, no. 5, pages 525–534, 1993.

[Hassell 2016] M. Hassell and F.J. Sayas. *Convolution quadrature for wave simulations*. In Numerical simulation in physics and engineering, pages 71–159. Springer, 2016.

[Hsiao 1990] G.C. Hsiao. *The coupling of boundary element and finite element methods*. Zeitschrift fur Angewandte Mathematik Und Mechanik, vol. 70, pages T493–T503, 1990.

[Hsiao 2008] G.C. Hsiao and W.L. Wendland. Boundary integral equations. Springer, 2008.

[Isbiliroglu 2015] Y. Isbiliroglu, R. Taborda and J. Bielak. *Coupled soil-structure interaction effects of building clusters during earthquakes*. Earthquake Spectra, vol. 31, no. 1, pages 463–500, 2015.

[Jiang 1988] T. Jiang and E. Kuribayashi. *The three-dimensional resonance of axisymmetric sediment-filled valleys*. Soils and Foundations, vol. 28, no. 4, pages 130–146, 1988.

[Jingbo 1998] L. Jingbo and L. Yandong. *A direct method for analysis of dynamic soil-structure interaction based on interface idea*. In Developments in geotechnical engineering, volume 83, pages 261–276. Elsevier, 1998.

[Juhl 1998] P. Juhl. *A note on the convergence of the direct collocation boundary element method*. Journal of Sound and Vibration, vol. 212, no. 4, pages 703–719, 1998.

[Kausel 2006] E. Kausel. Fundamental solutions in elastodynamics. Cambridge University Press, 2006.

[Kim 1993] J. Kim and A.S. Papageorgiou. *Discrete wave-number boundary-element method for 3-D scattering problems*. Journal of engineering mechanics, vol. 119, no. 3, pages 603–624, 1993.

[Koketsu 2005] K. Koketsu, K. Hatayama, T. Furumura, Y. Ikegami and S. Akiyama. *Damaging long-period ground motions from the 2003 Mw 8.3 Tokachi-oki, Japan earthquake*. Seismological Research Letters, vol. 76, no. 1, pages 67–73, 2005.

[Komatitsch 1998] D. Komatitsch and J.P. Vilotte. *The spectral element method: an efficient tool to simulate the seismic response of 2D and 3D geological structures.* Bulletin of the seismological society of America, vol. 88, no. 2, pages 368–392, 1998.

[Kriegsmann 1987] G.A. Kriegsmann, A. Taflove and K.R. Umashankar. *A new formulation of electromagnetic wave scattering using the on-surface radiation condition method.* IEEE Trans. Antennas Propag., vol. 35, pages 153–161, 1987.

[Kupradze 1963] V.D. Kupradze and T.G. Gegelia. Dynamical problems in elasticity. Progress in solid mechanics, vol. III, North Holland, 1963.

[Kupradze 1979] V.D. Kupradze, T.G. Gegelia, M.O. Basheleĭshvili and T.V. Burchuladze. Three-dimensional problems of the mathematical theory of elasticity and thermoelasticity, volume 25 of *North-Holland Series in Applied Mathematics and Mechanics*. North-Holland Publishing Co., Amsterdam, russian edition, 1979. Edited by V. D. Kupradze.

[Le Louër 2014] F. Le Louër. *A high order spectral algorithm for elastic obstacle scattering in three dimensions.* Journal of Computational Physics, vol. 279, pages 1–17, 2014.

[Lecampion 2017] B. Lecampion, A. Bunger and X. Zhang. *Numerical methods for hydraulic fracture propagation: a review of recent trends.* Journal of Natural Gas Science and Engineering, 2017.

[Lecampion 2018] B. Lecampion, A. P. Bunger and X. Zhang. *Numerical methods for hydraulic fracture propagation: A review of recent trends.* Journal of Natural Gas Science and Engineering, vol. 49, pages 66–83, 2018.

[Lee 1978] V.W. Lee. Displacements near a three-dimensional hemispherical canyon subjected to incident plane waves. University of Southern California, Department of Civil Engineering, 1978.

[Liao 2004] W.I. Liao, T.J. Teng and C.S. Yeh. *A series solution and numerical technique for wave diffraction by a three-dimensional canyon.* Wave Motion, vol. 39, no. 2, pages 129–142, 2004.

[Lin 1996] C.C. Lin, E.C. Lawton, J.A. Caliendo and L.R. Anderson. *An iterative finite element-boundary element algorithm.* Computers & Structures, vol. 59, no. 5, pages 899–909, 1996.

[Lizé 2014] B. Lizé. *Résolution directe rapide pour les éléments finis de frontière en électromagnétisme et acoustique : $\mathcal{H}$-matrices. Parallélisme et applications industrielles.* PhD thesis, Paris 13, 2014. in french.

[Loseille 2010] A. Loseille. *Fully anisotropic goal-oriented mesh adaptation for 3D steady Euler equations.* Journal of Computational Physics, vol. 229, no. 8, pages 2866 – 2897, 2010.

[Loseille 2011] A. Loseille and F. Alauzet. *Continuous mesh framework part I: well-posed continuous interpolation error.* SIAM Journal on Numerical Analysis, vol. 49, no. 1, pages 38–60, 2011.

[Loseille 2017] A. Loseille. *Chapter 10 - Unstructured Mesh Generation and Adaptation.* In R. Abgrall and C.-W. Shu, editeurs, Handbook of Numerical Methods for Hyperbolic Problems, volume 18 of *Handbook of Numerical Analysis*, pages 263 – 302. Elsevier, 2017.

[Lu 1998] Y.Y. Lu. *A complex rational approximation of $\sqrt{1+x}$.* Applied Numerical Mathematics, vol. 27, pages 141–154, 1998.

[Lubich 1988] C. Lubich. *Convolution quadrature and discretized operational calculus. I.* Numerische Mathematik, vol. 52, no. 2, pages 129–145, 1988.

[Magoules 2004] F. Magoules, F.X. Roux and S. Salmon. *Optimal discrete transmission conditions for a non- overlapping domain decomposition method for the Helmholtz equation.* SIAM Journal on Scientific Computing, vol. 25, no. 5, pages 1497–1515, 2004.

[Magoules 2006] F. Magoules, F.X. Roux and L. Series. *Algebraic approximation of Dirichlet-to-Neumann maps for the equations of linear elasticity.* Comput. Methods Appl. Mech. Engrg., vol. 195, pages 3742–3759, 2006.

[Mattesi 2018] V. Mattesi, M. Darbas and C. Geuzaine. *A high-order absorbing boundary condition for 2D time-harmonic elastodynamic scattering problems.* Computers & Mathematics with Applications, 2018.

[Messner 2010] M. Messner and M. Schanz. *An accelerated symmetric time-domain boundary element formulation for elasticity.* Engineering Analysis with Boundary Elements, vol. 34, no. 11, pages 944–955, 2010.

[Messner 2012] M. Messner, M. Schanz and E. Darve. *Fast directional multilevel summation for oscillatory kernels based on Chebyshev interpolation.* Journal of Computational Physics, vol. 231, no. 4, pages 1175–1196, 2012.

[Meza-Fajardo 2015] K.C. Meza-Fajardo, A.S. Papageorgiou and J.F. Semblat. *Identification and extraction of surface waves from three-component seismograms based on the normalized inner product.* Bulletin of the Seismological Society of America, vol. 105, no. 1, pages 210–229, 2015.

[Milazzo 2012] A. Milazzo, I. Benedetti and M.H. Aliabadi. *Hierarchical fast BEM for anisotropic time-harmonic 3-D elastodynamics.* Computers & Structures, vol. 96, pages 9–24, 2012.

[Milinazzo 1997] F.A. Milinazzo, C.A. Zala and G.H. Brooke. *Rational square-root approximations for parabolic equation algorithms.* J. Acoust. Soc. Am., vol. 101, no. 2, pages 760–766, 1997.

[Moczo 2002] P. Moczo, J. Kristek, V. Vavrycuk, R.J. Archuleta and L. Halada. *3D heterogeneous staggered-grid finite-difference modeling of seismic motion with volume harmonic and arithmetic averaging of elastic moduli and densities.* Bulletin of the Seismological Society of America, vol. 92, no. 8, pages 3042–3066, 2002.

[Modave ] A. Modave, C. Geuzaine and X. Antoine. *Corner treatments for high-order absorbing boundary conditions in high-frequency acoustic scattering problems.* Under review.

[Nédélec 2001] J.C. Nédélec. Acoustic and Electromagnetic Equations: Integral Representations for Harmonic Problems. Springer, New York, 2001.

[Nieto-Ferro 2013] A. Nieto-Ferro. *Interaction sol-structure non-linéaire en analyse sismique.* PhD thesis, Ecole Centrale Paris, 2013.

[Niu 2003] Y. Niu and M. Dravinski. *Three-dimensional BEM for scattering of elastic waves in general anisotropic media.* International journal for numerical methods in engineering, vol. 58, no. 7, pages 979–998, 2003.

[Olsen 2000] K.B. Olsen, R. Nigbor and T. Konno. *3D viscoelastic wave propagation in the Upper Borrego Valley, California, constrained by borehole and surface data.* Bulletin of the Seismological Society of America, vol. 90, no. 1, pages 134–150, 2000.

[Pan 1998] L. Pan, F. Rizzo and P.A. Martin. *Some efficient boundary integral strategies for time-harmonic wave problems in an elastic halfspace.* Comput. Meth. Appl. Mech. Eng., vol. 164, pages 207–221, 1998.

[Paolucci 1999] R. Paolucci. *Shear resonance frequencies of alluvial valleys by Rayleigh's method.* Earthquake Spectra, vol. 15, no. 3, pages 503–521, 1999.

[Papadopoulos 2018] M. Papadopoulos, S. François, G. Degrande and G. Lombaert. *The influence of uncertain local subsoil conditions on the response of buildings to ground vibration.* Journal of Sound and Vibration, vol. 418, pages 200–220, 2018.

[Rjasanow 2016] S. Rjasanow and L. Weggler. *Matrix valued adaptive cross approximation.* Mathematical Methods in the Applied Sciences, 2016.

[Rodríguez-Zúñiga 1995] J.L. Rodríguez-Zúñiga, F.J. Sánchez-Sesma and L.E. Pérez-Rocha. *Seismic response of shallow alluvial valleys: The use of simplified models.* Bulletin of the Seismological Society of America, vol. 85, no. 3, pages 890–899, 1995.

[Rokhlin 1993] V. Rokhlin. *Diagonal Forms of Translation Operators for the Helmholtz Equation in three dimensions.* Applied and Computational Harmonic Analysis, vol. 1, pages 82–93, 1993.

[Romanet 2018] P. Romanet. *Fast algorithm to model quasi-dynamic earthquake cycles in complex fault networks.* PhD thesis, Université Sorbonne Paris Cité, 2018.

[Saad 1986] Y. Saad and M.H. Schultz. *GMRES: a Generalized Minimal Residual Algorithm for solving nonsymmetric linear systems.* SIAM Journal on Scientific Computing, vol. 7, pages 856–869, 1986.

[Sánchez-Sesma 1983] F.J. Sánchez-Sesma. *Diffraction of elastic waves by 3D surface irregularities.* Bull. seism. Soc. Am., vol. 73, pages 1621–1636, 1983.

[Sánchez-Sesma 1995] F.J. Sánchez-Sesma and F. Luzon. *Seismic response of three-dimensional alluvial valleys for incident P, S, and Rayleigh waves.* Bulletin of the Seismological Society of America, vol. 85, no. 1, pages 269–284, 1995.

[Sauter 2011] S.A. Sauter and C. Schwab. *Boundary element methods.* In Springer Series in Computational Mathematics, volume 39. Springer-Verlag, 2011.

[Semblat 2009] J.F. Semblat and A. Pecker. Waves and vibrations in soils: earthquakes, traffic, shocks, construction works. Iuss Press, 2009.

[Semblat 2010] J.F. Semblat, N. Lokmane, L. Driad-Lebeau and G. Bonnet. *Local amplification of deep mining induced vibrations Part. 2: Simulation of ground motion in a coal basin.* Soil Dynamics and Earthquake Engineering, vol. 30, no. 10, pages 947–957, 2010.

[Seo 2007] C.G. Seo, C.B. Yun and J.M. Kim. *Three-dimensional frequency-dependent infinite elements for soil–structure interaction.* Engineering Structures, vol. 29, no. 11, pages 3106–3120, 2007.

[Sieffert 1992] J.G. Sieffert and F. Cevaer. Manuel des fonctions d'impédance: Handbook of impedance functions. Ouest editions, 1992.

[Smerzini 2011] C. Smerzini, R. Paolucci and M. Stupazzini. *Comparison of 3D, 2D and 1D numerical approaches to predict long period earthquake ground motion in the Gubbio plain, Central Italy.* Bulletin of Earthquake Engineering, vol. 9, no. 6, pages 2007–2029, 2011.

[Song 1995] J.M. Song and W.C. Chew. *Multilevel fast-multipole algorithm for solving combined field integral equations of electromagnetic scattering.* Microw. Opt. Technol. Lett., vol. 10, pages 14–19, 1995.

[Stolper 2004] M. Stolper. *Computing and compression of the boundary element matrices for the Helmholtz equation.* Journal of Numerical Mathematics, vol. 12, no. 1, pages 55–75, 2004.

[Tanaka 1994] M. Tanaka, V. Sladek and J. Sladek. *Regularization techniques applied to boundary element methods.* Appl. Mech. Rev., vol. 47, pages 457–499, 1994.

[Wallen 2007] H. Wallen, S. Jarvenpaa, P. Yla-Oijala and J. Sarvas. *Broadband Müller-MLFMA for Electromagnetic Scattering by Dielectric Objects.* IEEE Transactions on Antennas and Propagation, vol. 55, pages 1423–1430, May 2007.

[Wang 1995] C.Y. Wang and J.D. Achenbach. *Three-dimensional time-harmonic elastodynamic Green's functions for anisotropic solids.* In Proceedings of the Royal Society of London A: Mathematical, Physical and Engineering Sciences, volume 449, pages 441–458. The Royal Society, 1995.

[Wirgin 1996] A. Wirgin and P.Y. Bard. *Effects of buildings on the duration and amplitude of ground motion in Mexico City.* Bulletin of the Seismological Society of America, vol. 86, no. 3, pages 914–920, 1996.

[Xiao 2012] J. Xiao, W. Ye, Y. Cai and J. Zhang. *Precorrected FFT accelerated BEM for large-scale transient elastodynamic analysis using frequency-domain approach.* Int. J. Num. Meth. Eng., vol. 90, pages 116–134, 2012.

[Xu 2001] X.M. Xu and Q.H. Liu. *Fast spectral-domain method for acoustic scattering problems.* IEEE transactions on ultrasonics, ferroelectrics, and frequency control, vol. 48, no. 2, pages 522–529, 2001.

[Yan 2010] Z.Y. Yan, J. Zhang and W. Ye. *Rapid solution of 3-D oscillatory elastodynamics using the pFFT accelerated BEM.* Eng. Anal. Bound. Elem., vol. 34, pages 956–962, 2010.

[Yang 1992] S.C. Yang and C.B. Yun. *Axisymmetric infinite elements for soil-structure interaction analysis.* Engineering Structures, vol. 14, no. 6, pages 361–370, 1992.

[Yarvin 1998] N. Yarvin and V. Rokhlin. *Generalized Gaussian Quadratures and singular value of integral operators.* SIAM J. Sci. Comput., vol. 20, no. 2, pages 699–718, 1998.

[Yokoi 2003] T. Yokoi. *The higher order Born approximation applied to improve the solution of seismic response of a three-dimensional canyon computed by the Indirect Boundary Method.* Physics of the Earth and Planetary Interiors, vol. 137, no. 1-4, pages 97–106, 2003.

[Zhao 1999] J.S. Zhao and W.C. Chew. *MLFMA for solving integral equations of 2-D electromagnetic problems from static to electrodynamic.* Microw. Opt. Technol. Lett., vol. 20, pages 306–311, 1999.